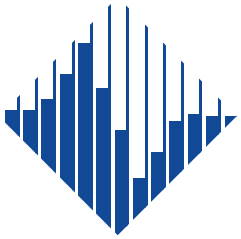

PACIFIC EARTHQUAKE ENGINEERING
RESEARCH CENTER

Seismic Design and Detailing of Bridge Columns to Account for Ground-Motion Duration

S. Mojtaba Alian Amiri
Mohamed A. Moustafa
David H. Sanders

Department of Civil and Environmental Engineering
University of Nevada, Reno

PEER Report No. 2021/08

Pacific Earthquake Engineering Research Center
Headquarters at the University of California, Berkeley
September 2021

PEER 2021/08 September 2021

Disclaimer

The opinions, findings, and conclusions or recommendations expressed in this publication are those of the author(s) and do not necessarily reflect the views of the study sponsor(s), the Pacific Earthquake Engineering Research Center, or the Regents of the University of California.

Seismic Design and Detailing of Bridge Columns to Account for Ground-Motion Duration

S. Mojtaba Alian Amiri

Mohamed A. Moustafa

David H. Sanders

Department of Civil and Environmental Engineering
University of Nevada, Reno

PEER Report 2021/08
Pacific Earthquake Engineering Research Center
Headquarters at the University of California, Berkeley

September 2021

ABSTRACT

Devastating, long-duration earthquakes such as 2011 Tohoku, Japan, earthquake, and 2010 Maule, Chile, earthquake have proved the importance of considering the duration of ground motion in conducting a seismic demand assessment. This research focuses on using both analytical and experimental methods to study the effect of different design details—confinement spacing ratio and longitudinal bar debonding—and different reinforcement strategies—conventional and high-strength reinforcement—on the seismic response of reinforced concrete (RC) bridge columns under long-duration ground motions. In this study, six large-scale RC bridge column specimens were designed, constructed, and tested in two phases on the shake table at the University of Nevada, Reno.

The first phase included three specimens designed using conventional Grade 60 ASTM 706 reinforcing bars tested under a sequence of long-duration earthquakes (2011 Tohoku earthquake). All three columns had the same longitudinal reinforcement ratio. Column #2 had a different confinement spacing ratio compared to Column #1. In contrast, Column #3 considered debonding of longitudinal reinforcement at the footing interface. Columns #4, 5, and 6 tested in the second phase were reinforced longitudinally with high-strength grade 100 ASTM A1035 MMFX steel. These columns were tested under short- and long-duration motions to study the cyclic deterioration of high-strength reinforcement and quantify the response of bridge columns under seismic events. Presented herein are the pre-test analyses, design, and construction of the specimens, the results of the shake table tests, and a comparison of the global and local seismic response of the six columns tested. The global responses include the force and displacement capacities and mode of failure. Local responses include the strain in both transverse and longitudinal rebars and the curvature of the columns within the plastic hinge zone. The experimental results demonstrate that although both the higher concrete confinement (i.e., smaller tie spacings) and longitudinal bars debonding are effective in improving the performance of columns subjected to long-duration earthquakes, the smaller tie spacings is more effective.

The pre-test analysis was conducted using a computational model that was initially calibrated against a previous experimental study. The model was then assessed using the shake table test data, refinements were conducted, and new modeling values/parameters/equations were obtained and proposed as modifications to the model. In addition, a set of material tests was conducted to refine the high-strength reinforcement material to investigate the effect of high strain rates on these reinforcing bars. The results revealed a significant increase in the yield stress and reduction in fracture strain due to high-strain-rate effect.

Finally, an analytical study on two-span, two-column bent archetype bridges was conducted with recommendations to amend the current seismic provisions in the design of the bridges at those sites with potential for long-duration earthquakes. To mitigate the damage from long-duration seismic events and spectral shape effects, new site-specific design criteria were developed for multi-column bent bridges located at sites in the U.S. Pacific Northwest and Alaska. The results of the experimental and analytical studies can help assess the effectiveness of the varied

design details and provide a foundation for future design guidelines to account for longer duration earthquakes.

ACKNOWLEDGMENTS

The authors would like to acknowledge the generous support of the Pacific Earthquake Engineering Research Center (PEER). This research was funded under Grant # NCTRDS (RFP 2017-01). The opinions, findings, conclusions, or recommendations expressed in this publication are those of the authors and do not necessarily reflect the views of the study's sponsor (PEER), or the Regents of the University of California.

The authors also thank the Earthquake Engineering Laboratory staff of the University of Nevada, Reno (UNR): Dr. Patrick Laplace, Chad Lyttle, and Todd Lyttle for their assistance in the shake table tests. Special thanks go to the collaborative team at Stanford University: Professor Greg Deierlein and Dr. Kuanshi Zhong.

CONTENTS

LIST OF TABLES

LIST OF FIGURES

1 Introduction

Long-duration earthquakes, such as 2010 Maule (Chile), 2011 Tohoku (Japan), 2014 Iquique (Chile), and 2015 Illapel (Chile) earthquakes, caused substantial damage in structures including bridges. Previous studies have demonstrated that—compared to the shorter duration motions upon which most design models and criteria are based—earthquake duration can have a significant effect on structural performance in terms of decreasing displacement capacity and increasing the risk of structural collapse. Current seismic design codes do not explicitly take earthquake duration into consideration. Thus, understanding the design implications of long-duration earthquakes is critical for highly seismic regions of the world capable of generating large-magnitude long-duration earthquakes. This research is focused on using both analytical and experimental methods to study the effect of different reinforcement and design details on the seismic response of reinforced concrete (RC) bridge columns under long-duration ground motions. This introduction includes discussion of long-duration earthquakes, strong-motion duration, and the motivating factors prompting this study. The objectives, scope of the work, and outline of the report are also included.

1.1 LONG-DURATION EARTHQUAKES

Large-scale tectonic movements in the plate boundaries are the main cause of the earth's largest and longest earthquakes. These plate boundaries are known as subduction zones. Figure 1.1 shows a map of the subduction zones and tectonic plates located around the world. Subduction zones exist and form where a plate with thinner oceanic crust descends beneath a plate with a thicker continental crust. The associated earthquakes are produced by the rupturing of the plates interface. In the Pacific Northwest region of the United States, the boundary where the Juan de Fuca oceanic plate and the North American continental plate meet is the Cascadia Subduction Zone (CSZ). Cascadia is a tectonically active region that is capable of producing mega-earthquakes with durations of several minutes [Heaton and Kanamori 1984; Kramer et al. 1998]. The potential of such earthquakes occurring is approximately every 500 years [Mazzotti and Adams 2004]. The CSZ extends from northern California into Canada's British Columbia; see Figure 1.2. The states of Washington and Oregon, and parts of Idaho, Montana, and southeast Alaska are included in the Cascadia subduction zone.

Generally, the magnitude of an earthquake increases with longer ruptures, thus increasing an earthquake's magnitude. The depth of an earthquake is also a factor in its magnitude. The

distance of the site from the zone of energy release of the causative earthquake also increases the duration of the earthquake due to the propagating surface waves arriving from long distances. A higher impedance ratio in soft soils may also cause an additional long-period portion in the earthquake records that is not been seen in seismograms of rock sites [Salmon et al. 1992].

The structural components subjected to such long-duration earthquakes would experience numerous displacement reversals [Marsh and Gianotti 1994]. Long-duration earthquakes could be more damaging due to the increased number of response cycles, leading to more significant structural damage. Strength and stiffness degradation of RC components, and low-cycle fatigue damage in the reinforcing bars result in higher collapse risk [Kunnath et al. 1997]. Also, imposing larger hysteretic energy demands due to the longer period of shaking, requires greater ability to dissipate energy within structural components [Hancock and Bommer 2005].

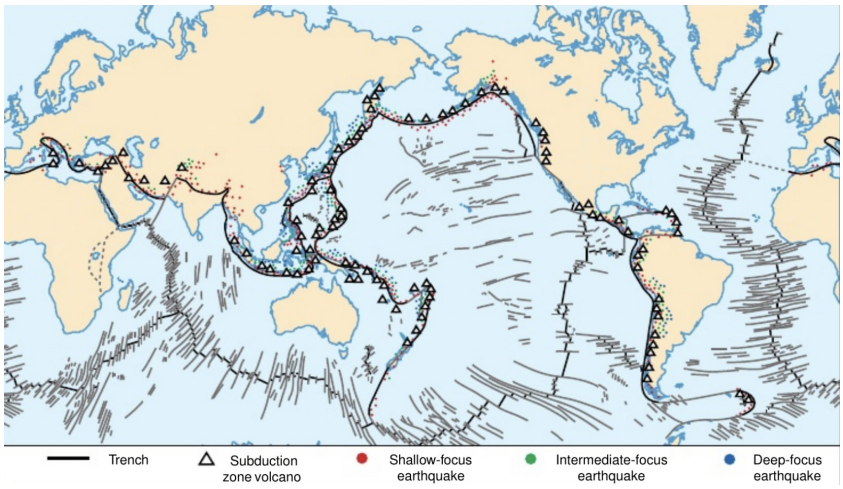

Figure 1.1 **Map of the Earth's subduction zones and tectonic plates [Hamblin and Christiansen 2003].**

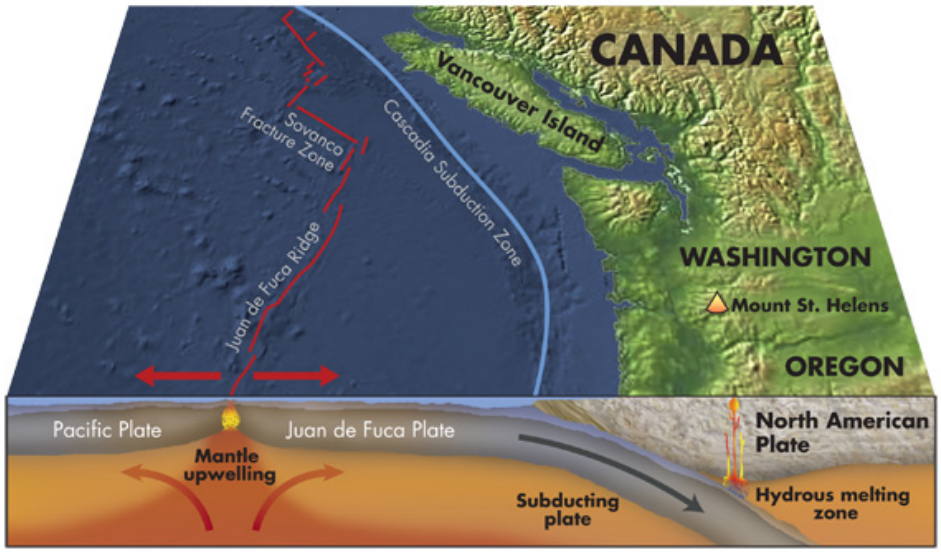

Figure 1.2 **Cascadia subduction zone (Credit: Kathleen Cantner, AGI).**

1.2 STRONG-MOTION DURATION

The total time of ground shaking from the arrival of seismic waves until the return to ambient conditions is defined as the "earthquake duration." The shaking amplitudes for many earthquakes are relatively low, with negligible effect on the seismic response of the structure and on the potential for damage. Those earthquakes that occur in highly seismic regions with the potential for major structural damage to structures and infrastructure require a specific parameter: strong-motion duration. Various researchers have developed a large variety of definitions and empirical relationships to measure strong-motion duration. These definitions are based upon two factors: (1) the damage potential of an earthquake as a function of the energy of the earthquake; and (2) the majority of the total energy of any earthquake contained in portions of the earthquake time history, which is much shorter than the total duration [Salmon et al. 1992].

Bommer and Martinez-Pereira [1999] classified the definitions into three generic groups including: (1) bracketed durations (D_b), defined as the total time elapsed between the first and last exceedance of a specified threshold; (2) uniform durations (D_u), defined as the sum of the time intervals during which the acceleration is greater than the threshold; and (3) significant durations (D_s), defined based on the accumulation of energy.

Foschaar et al. [2012] and Chandramohan et al. [2016] showed that the significant duration, specifically 5–75% or $Ds_{5–75\%}$, was the most suitable parameter in quantifying the structural damage due to longer duration earthquakes. This parameter depends on the energy content of the ground motions and does not change due to scaling of the record or changing the frequency content. The significant duration of a ground motion is defined as the time interval to accumulate a specific percentage range of the ground-motion acceleration, as per the integral shown in Equation (1.1).

$$\int_0^{t\max} a^2(t)\,dt \tag{1.1}$$

where $a(t)$ is the ground acceleration, and t_{max} is the length of the record. The percent range could be taken as 5–95% or 5–75% of the above integral. Thus, this duration includes 90% or 70% of the total cumulative energy, respectively. To compute the significant duration ($Ds_{5–95\%}$) for a ground motion, the differences between the strong-motion duration and the total duration are illustrated in Figure 1.3.

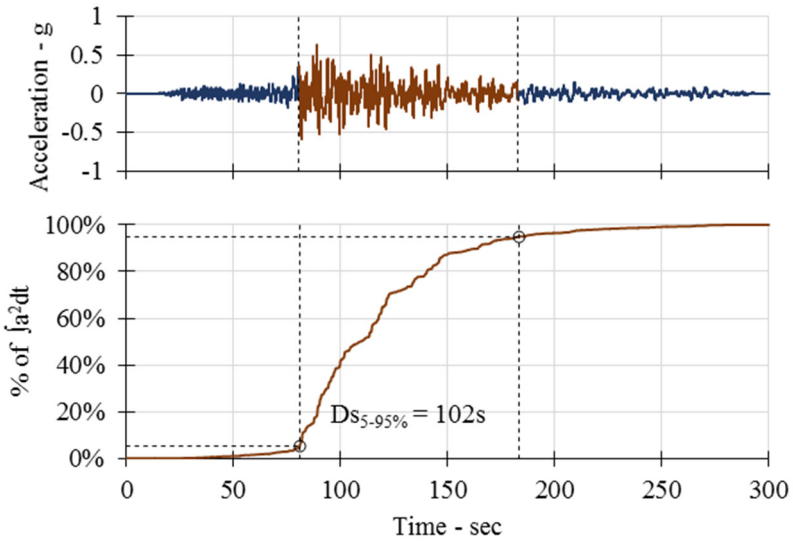

Figure 1.3 Computation of the 5–95% significant duration of a ground motion.

1.3 BACKGROUND AND MOTIVATION

This study is focused on RC bridges and columns in particular, along with the implication of design and reinforcement detailing in mitigating duration effects. Several emerging design details such as incorporating high strength reinforcement or reinforcing bars debonding are considered herein. Thus, a brief overview of relevant literature on duration effects on bridge columns, the use of high-strength reinforcement in design, and debonding is presented below.

1.3.1 Effect of Earthquake Duration on Bridge Columns

Several experimental studies have been conducted to examine the effect of duration on bridge columns. Kunnath et al. [1997] investigated cumulative damage in twelve 1/4-scale RC circular bridge columns using a series of monotonic and cyclic excitations. The failure mode in the columns subjected to large displacement amplitudes in excess of 5% drift was longitudinal bar rupture due to low-cycle fatigue. Under larger number of smaller amplitude cycles, confinement failure due to spiral rupture was observed. Ranf et al. [2005] tested six identical RC circular bridge columns to evaluate the effect of number of cycles on damage progression. The columns were lightly confined and tested under cyclic loadings. The results showed a 30% reduction in the maximum displacement at the final damage states occurred by increasing the number of cycles from 1 to 15 at each displacement level.

Ou et al. [2013] studied seismic behavior of flexural-dominated RC bridge columns under long-duration motions. Two identical columns were tested using two cyclic loading protocol. The first column load protocol represented the number of cycles expected in a long-duration earthquake, while the second column loading protocol was a baseline with one cycle for each drift loading. The main observation was 24% reduction in ductility capacity for the column subjected to the long-duration loading protocol. Mohammed [2016] investigated the effect of earthquake

duration on collapse capacity of RC bridge columns. Shake table tests were conducted on five 1/3-scale identical columns utilizing a set of five spectrally similar or close ground motions including one short-duration and four long-duration motions. The experimental study showed a significant effect of duration on the collapse capacity of the columns. Longitudinal bars in the columns subjected to the longer motions were fractured at lower displacements (32% lower) compared to the one under the short-duration motion. The general conclusion obtained from these studies was that longer duration earthquakes with larger number of inelastic cycles caused more damage in the plastic hinges. This was mainly attributed to the damage accumulation associated with low-cycle fatigue in the column reinforcing bars.

Recent analytical studies showed a similar trend. Mohammed [2016] and Chandramohan et al. [2016] studied the effect of duration by developing fragility curves for bridge columns. They used models that captured the deterioration of structural strength and stiffness. The former considered the fatigue failure in reinforcing bars of a 1/3-scale bridge column under study as the collapse index; the latter indicated an unbounded increase in peak chord rotations, above a threshold of 0.16 as collapse. Mohammed [2016] and Chandramohan et al. [2016] noted 25% and 17% reduction in the median collapse capacity under long-duration motions, respectively. Another study by Hancock and Bommer [2005] demonstrated that the effect of ground-motion duration on structural response depends on the response parameter used and whether or not deterioration and destabilization effects are incorporated in the model.

Since lower magnitude crustal earthquakes occur much more frequently than larger magnitude subduction earthquakes, short-duration ground motions recorded from low and moderate earthquakes dominate the ground-motion databases used in the development of seismic design provisions. The studies mentioned above show the importance of considering the effect of duration on seismic performance of the bridges. Given the current seismic design philosophies, the potential of active subduction zones to generate long-duration earthquakes in the CSZ in the United States, or other places such as Mexico, Chile, Japan, will result in a lower margin of safety against collapse for long-duration earthquakes. Such design codes need to be revised. This research is aimed at providing data to motivate code bodies to address this gap.

1.3.2 High-Strength Reinforcing Bars

High-strength reinforcing bars (HSRBs) discussed herein refers to reinforcement having a nominal yield stress of 80 ksi (550 MPa) or more, an elongation at rupture of at least 7%, and have potential economic and environmental benefits as they can reduce the amount of reinforcement required in the design of concrete members. ACI 318-14 [ACI Committee 2014] has imposed an upper limit of 60 ksi on yield stress of longitudinal reinforcement in concrete members resisting earthquake-induced forces. This limit was established based on tests of beams [Hognestad 1961] and concentrically loaded columns [Richart and Brown 1943; Todeschini et al. 1964]. The reason for this limitation is due to the low tensile-to-yield strength (T/Y) ratio of HSRBs and uncertainties about low-cycle fatigue life of newly developed HSRBs [Ghannoum and Slavin 2016]. Starting with ACI 318-19 [ACI 318 2019], ASTM A706 Grades-80 and -100 reinforcement is permitted to be used in special structural walls to resist moments, axial, and shear forces. ASTM A706 Grade-80 reinforcement is also permitted in special moment frames. To allow the use of HSS

reinforcement, ACI 318-19 [ACI 318 2019] includes limits for spacing of transverse reinforcement to control longitudinal bar buckling by providing adequate longitudinal bar support.

Recent experimental studies have demonstrated that at any given deformation level, HSRBs in concrete members experience higher strain concentration and demands compared to regular Grade-60 bars [Aoyama 2001; Macchi et al. 1996; Sokoli 2014; Sokoli and Ghannoum 2016; Sokoli et al. 2017; and Sokoli 2018]. This is attributed to low *T/Y* ratio of HSRBs. Furthermore, according to Slavin and Ghannoum [2015], low-cycle fatigue life of bars reduces exponentially with strain demands. This is exacerbated under long-duration earthquakes, which tend to impose higher number of strain cycles in reinforcing bars.

Rautenberg [2013] conducted a series of tests on eight RC columns reinforced using either ASTM A706 Grade-60, A706 Grade-80, or A1035 Grade-120 longitudinal bars designed to have similar moment capacity. The authors reported that as long as the fracture strain of the longitudinal reinforcement exceeded 7% for a reference gauge length of 203 mm (8 in), and the amount and detailing of the transverse reinforcement is sufficient to prevent shear failure, bond failure, and bar buckling, then the area of reinforcement can be decreased proportionally to the increase in yield strength. Test results were further used to calibrate numerical tools for investigating the effects of using HSRBs as longitudinal reinforcement in the columns of multi-story moment-resisting frame buildings. Results demonstrated that columns longitudinally reinforced with Grade-80 to Grade-120 reinforcement had comparable drift capacities to those of similar columns reinforced with Grade-60 reinforcement. Energy dissipation of the columns with HSRBs was lower than comparable columns with Grade-60 steel.

The smaller energy dissipation in the columns built with HSRBs was mainly attributed to the reduction in flexural stiffness as a result of the smaller amount of reinforcement when compared with the Grade-60 reinforced columns, because conventional steel reinforcement and HSS reinforcement have the same Young's modulus. This reduction in stiffness is accompanied by an increase in the displacement at yield (which may translate into a reduction in the ratio of maximum displacement to yield displacement) and a reduction in hysteretic energy dissipation. Numerical simulations indicated that multi-story moment-frame buildings with columns reinforced with Grade-120 longitudinal reinforcement did not produce roof drifts consistently larger than the roof drifts computed for models of buildings with columns having twice as much Grade-60 longitudinal reinforcement.

In a similar study, Barbosa et al. [2015] investigated the seismic performance of circular RC bridge columns constructed with A706 Grade-80 reinforcement. Columns were constructed using either A706 Grade-60 or A706 Grade-80 reinforcement and tested under lateral cyclic loading. Results indicated that the columns constructed with HSRBs achieved similar resistance, similar maximum lateral displacements, and similar curvature ductility values when compared with the control columns constructed with Grade-60 reinforcement. Note that the column constructed with HSRBs had approximately 75% of the amount of longitudinal reinforcement compared to the Grade-60 reinforcement. However, columns constructed with Grade-80 reinforcement exhibited lower hysteretic energy dissipation than the control columns. Results also indicate that independently of the steel grade, as the moment–shear span ratio decreases, the

maximum drift ratio decreases, despite an increase in the displacement ductility. Column failure mode (bar fracture due to buckling of longitudinal bars) was consistent across both grades of steel. Columns constructed with Grade-80 reinforcement exhibited lower overstrength factors than columns reinforced with regular strength reinforcement; this observation was attributed to smaller material overstrength of Grade-80 reinforcement and smaller reinforcement ratios.

Zhong and Deierlein [2019] investigated the effect of high-strength reinforcement on the nonlinear system response and risk of bar fracture in concrete moment frames and walls subjected to earthquake ground motions, including the effects of degradation associated with reinforcing bar yielding, buckling, and fracture. The authors developed a fatigue-fracture model based on a Manson–Coffin formulation to relate cumulative effective plastic strains to bar fracture. The model was described by a lognormal probabilistic distribution calibrated to represent the median estimate of fracture with a dispersion of 0.5. The performance of special moment frame and wall systems incorporating the fatigue-fracture model were evaluated under incremental dynamic analysis (IDA). Sensitivity studies revealed that fracture behavior is more influenced by the T/Y ratio followed by tie spacing (s/d_b ratio) and yield strength. Moreover, the risk of collapse under risk-targeted maximum considered earthquake (MCE_R) ground motions in systems with Grade-60 steel was comparable with systems with Grade-80 or -100 steel, provided that the $T/Y > 1.2$ and tie spacing $s/d_b < 5$ in cases with HSRBs.

Given these findings, there is concern about the application of HSRB in seismic zones with higher potential for long-duration earthquakes. Special attention needs to be given to assessing the performance of HSRBs under seismically induced low-cycle fatigue and the collapse risk of bridge columns utilizing HSRBs, especially when there is greater risk for long-duration motions. This study explore feasibility of using HSRBs in bridge columns susceptible to short- and long-duration ground motions.

1.3.3 Intentional Debonding of Longitudinal Reinforcement

Many researchers have incorporated partially debonded steel reinforcement as a technique to mitigate seismic damage, especially in precast concrete (PC) beams at beam-to-column connections and PC bridge columns at their connections to the footing or cap beam. In this technique, the reinforcing bar is debonded from the surrounding concrete along a specific length. The intent is to spread locally induced strains and deformations over larger reinforcing bar lengths, thereby preventing early reinforcing bar yielding and fracture, and improving the seismic performance of the columns [Pandey et al. 2008; Nikoukalam and Sideris 2017].

With unbonding the longitudinal bars from surrounding concrete, no flexural cracking will occur inside the unbonded shear span, and hence the concrete body remains under diagonal compression with a straight thrust line resembling a tied arch mechanism. The altered stress distribution can effectively prevent diagonal shear failure, thus enhancing the seismic performance of the column under shear [Pandey and Mutsuyoshi 2005]. This behavior is illustrated in Figure 1.4

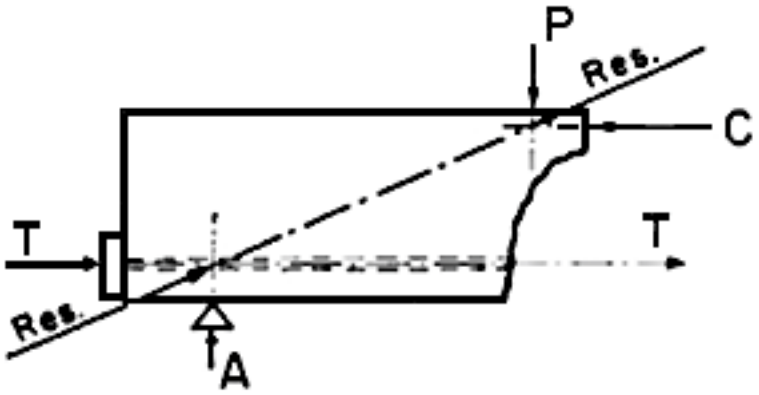

Figure 1.4 Debonded reinforcement direct shear strut [Kani 1964].

Kawashima et al. [2001] investigated the effect of full and partial debonding of reinforcement through cyclic tests on five cast-in-place bridge columns with span-to-depth ratio of 3.6. Test data showed reduced concrete damage and a dominant rocking response at the bottom of the columns. Also, as a result of debonding, ductility capacity of the columns increased slightly, but their lateral stiffness and energy dissipation capabilities were slightly reduced.

Pandey et al. [2008] utilized controlling the bond of reinforcement instead of the conventional sole reliance on shear reinforcement to enhance seismic performance of RC columns. The authors tested square RC columns with bonded and completely unbonded reinforcement under reversed cyclic loading. Although unbonding reinforcement was proved to be effective by changing the mode of failure from shear to ductile flexural, the hysteretic force-displacement relationship of these columns was completely different compared to columns with ordinary bonded reinforcement.

Aviram et al. [2014] used debonded reinforcement at the column-footing interface of a high-performance fiber-reinforced concrete (HPFRC) circular cantilever bridge column to force most of the inelastic deformations in the column. The debonding was applied over a short length (equivalent to 25% of the column diameter) and did not allow for sufficient spreading of locally induced strains. This demonstrated the importance of the proper selection of the debonding length.

Nikoukalam and Sideris [2017] investigated the effect of partial debonding of longitudinal reinforcement at the location of the plastic hinge on the performance of RC columns in special moment-resisting frames. The authors conducted quasi-static cyclic testing of three nearly full-scale cantilever columns with various debonded reinforcement lengths. It was concluded that the extent of concrete damage reduced with the debonded length, which was due to the strain incompatibility between the debonded reinforcement and the concrete. Debonding alleviated strain localizations in the reinforcement for drift ratios below 2%. The peak strength and initial elastic stiffness decreased with the debonded length. Energy dissipation and the equivalent viscous damping ratio increased with the debonded length for drift ratios below 2% and decreased with the debonded length for drift ratios exceeding 3%. Self-centering improved with the debonded length.

1.4 OBJECTIVES AND SCOPE

This research project employed comprehensive analytical and experimental simulations to study the effect of different reinforcement strength and design details on the seismic response of RC bridge columns under long-duration ground motions. The overarching goal of this study was to develop models and recommendations for considering earthquake duration in the performance assessment and design of bridges. The experimental part of the study was carried out at the Earthquake Engineering Laboratory (EEL) at the University of Nevada, Reno. The specific task-oriented objectives of this study were as follows:

1. Conduct preliminary analytical studies including nonlinear static and dynamic analyses for full-scale and reduced-scale bridge columns to explore the validity of various modeling assumptions and to provide data for the experimental phase (e.g., finalize earthquake loading protocols for the shake table tests).
2. Conduct six shake-table bridge column tests to examine how different detailing configurations (transverse reinforcement ratio and debonding details) and high-strength reinforcement impact column performance under long-duration ground motions.
3. Carry out post-test analytical studies that utilize the experimental results to carefully calibrate and inform modeling assumptions (e.g., fatigue and fracture models for reinforcing bars) and relate the damage, deformations, and collapse safety of bridges to design parameters and earthquake ground-motion duration.
4. Perform a comprehensive analytical parametric study on archetype bridges with varying design details and parameters to compute hazard-consistent collapse fragility curves employing a framework that incorporates ground-motion duration and response spectral shape.
5. Develop recommendations for design and performance assessment of concrete bridges that utilize the experimental and analytical results.

This study included two experimental phases: three 1/3-scale cantilever bridge column designed using conventional Grade-60 reinforcing bars, and three columns with high-strength Grade-100 longitudinal bars. In Phase I of the experimental program, three bridge column models were designed and tested on a shake table subjected to a sequence of long-duration earthquakes. All three columns had same longitudinal reinforcement ratio. Column #2 had different confinement and transverse reinforcement ratio compared to Column #1. Column #3 utilized debonding of longitudinal reinforcement at the column-footing interface, while the transvers steel ratio remained the same as Column #1. The experimental program in Phase II included three more columns reinforced longitudinally using high-strength Grade-100 reinforcement. The columns were tested under short- and long-duration motions to study the HSRB cyclic deterioration and quantify the use of high-strength reinforcement in seismic design of bridges. The test specimens were geometrically identical to the specimens in Phase I. The columns were designed such that they had a similar moment capacity as the columns tested in Phase I.

This report presents the details of the specimen's design, pre-test analyses, construction, and testing of the column models. The results of the shake table tests and a comparison of the global and local seismic response of the six columns are presented herein. The global response is discussed in terms of force and displacement capacities and mode of failure. The local response is discussed in terms of the strain in both longitudinal and transverse reinforcing bars, and the curvature of the columns within the plastic-hinge zone. The test results were used to assess the effectiveness of various design details, i.e., confinement, debonding and the use of high-strength steel, and provide a foundation for future design guidelines to account for long-duration earthquakes. Post-test analysis was then performed to propose recommendations on numerical modeling with emphasis on improving the models to better simulate cyclic deterioration due to low-cycle fatigue.

This study was performed in part through a collaborative PEER-funded project with Stanford University. All the experimental work was exclusively part of the scope at the University of Nevada, Reno, with some interaction with Stanford on the fatigue modeling aspects. However, the comprehensive analytical study on archetype bridges that is presented in Chapter 8 was heavily collaborative and was led by Stanford. The overall procedure and methodology used was adopted from what was conducted at Stanford University on single-column bent bridges by Zhong [2020]. Thus, the collaborative team at Stanford focused on developing the framework and used only simplified bridge prototype for demonstration. At UNR, a more realistic bridge configuration, modeling assumptions and features, accurate bridge components, and representative bi-directional earthquake excitations were used as discussed in this chapter. For completeness, all results obtained at UNR for multi-span bridges were compared to those from the simplified single-column bridges for a complete assessment. The results of this analytical study were then employed to construct a structural reliability framework that incorporates ground-motion duration and response spectral shape to develop design-domain surrogate models. Such surrogate models were used to develop recommendations that could be used to update the current seismic provisions for the design or retrofit of the bridges susceptible to large-magnitude and long-duration earthquakes.

1.5 OUTLINE OF THE REPORT

Chapter 1 includes an introduction on the long-duration earthquakes and strong-motion duration. Past studies on the effect of earthquake duration on bridge column performance, high-strength reinforcing bars, and intentional debonding of longitudinal reinforcement plus the objectives of this study are presented. Chapter 2 describes the preliminary modeling, design, pre-test analyses, and loading protocol selected for the shake table tests. Chapter 3 explains the construction stages, material properties, instrumentation, and setup of the test models in both Phases I and II of the experimental program. Chapter 4 and 5 present the experimental results—such as damage observations and measured data for the column tests—in Phases I and II, respectively. Chapter 6 focuses on a comparative discussion of the test results. Chapter 7 discusses the post-test analysis and compares the measured results of the shake table tests with the response predicted using the analytical model. Refinements made to the analytical model for calibration and modeling recommendations are also included. Chapter 8 includes the prototype bridge study on several

versions of two-span two-column bent archetype bridges. The site-specific design recommendations and strategies to consider the duration effects are also provided. Finally, a summary and conclusions of this study are presented in Chapter 9.

2 Preliminary Analytical Studies

2.1 OVERVIEW

This chapter presents the preliminary analytical studies that motivated the overall project and the experimental component of the study. Current state-of-the-practice modeling assumptions were employed to investigate the effect of earthquake duration on bridge columns using an IDA analysis to further confirm the results from previous studies. The experimental program included two phases. The design concepts and details of the column models tested in the two phases is presented first, as a pre-test analysis was conducted on the test models. The design of all components of the specimens was influenced by the test setup, where the specimens were placed on a shake table for uniaxial testing. The final testing procedure and loading protocol based on the pre-test analysis are also discussed in this chapter.

2.2 PRELIMINARY MODELING AND IMPETUS FOR THIS STUDY

Previous studies that investigated the effect of ground-motion duration on bridge-column collapse capacity considering the low-cycle fatigue life are very limited. Low-cycle fatigue, which is known to cause significant damage in structures subjected to long-duration earthquakes, needs to be accurately accounted for in the collapse analysis of structures. Fragility curves are one of the popular tools that have been extensively used in performance-based and vulnerability assessment of structures, buildings, and bridges. Thus, prior to designing the test specimens, an analytical study was carried out to conduct the first round of model calibration and develop fragility curves utilizing two sets of short- and long-duration spectrally equivalent earthquakes. These fragility curves were then compared to evaluate the effect of duration on the collapse capacity of bridge columns.

For this purpose, a finite-element model of a full-scale bridge column that represents a common RC bridge column located in highly seismic regions was developed in OpenSees [McKenna 2011]. The model considered the low-cycle fatigue behavior of reinforcing steel, cyclic deterioration of strength and stiffness, and the destabilizing P-Δ effects of gravity loads. Incremental dynamic analysis (IDA) was conducted on the prototype bridge column model, which involves nonlinear dynamic analyses of the structural model under a suite of ground-motion records. All ground motions are scaled to several intensity levels to force the structure all the way from elasticity to final global dynamic instability [Vamvatsikos and Cornell 2002]. The analysis

was conducted using a set of 156 spectrally equivalent long- and short-duration record pairs to study the effect of earthquake duration. Results from both short- and long-duration ground-motion sets were employed to develop fragility curves, which used the fatigue fracture index and spectral acceleration at fundamental period as the response and intensity parameters, respectively. Details of the model and analysis results are explained next.

2.2.1 Description of the Bridge Column

The bridge column used in this study was built with the same details as the full-scale column previously tested at the University of California, San Diego [Schoettler et al. 2015] to represent a single-column bent commonly used in California. The column was designed in accordance with the California Department of Transportation's (Caltrans) *Seismic Design Criteria* [2019] and AASHTO's LRFD Bridge Design Specifications [2014]. The cantilever column was fixed at the base and free at the top, i.e., the setup used to accommodate the additional mass did not constrain the column top. This boundary condition corresponded to a bent subjected to ground excitation in the transverse direction of the bridge deck. The column was subjected to uniaxial shake table excitations in east–west direction of the shake table. Figure 2.1 shows the column experimental setup. The clear height of the column was 288 in. The column had a circular section with eighteen 48 in.-diameter #11 bars as the longitudinal steel and a 2-in. clear cover. The reinforcement corresponded to 1.55% longitudinal reinforcement ratio. The volumetric transverse reinforcement ratio was 0.95%, which consisted of butt-welded, double #5 hoops, spaced at 6 in. The superstructure consisted of five cast-in-place concrete blocks that were post-tensioned together on-center. The axial load ratio was 5.3% of the column axial capacity. The considered bridge column specimen details and dimensions are shown in Figure 2.2.

Figure 2.1 Full-scale bridge column test setup [Schoettler et al. 2015].

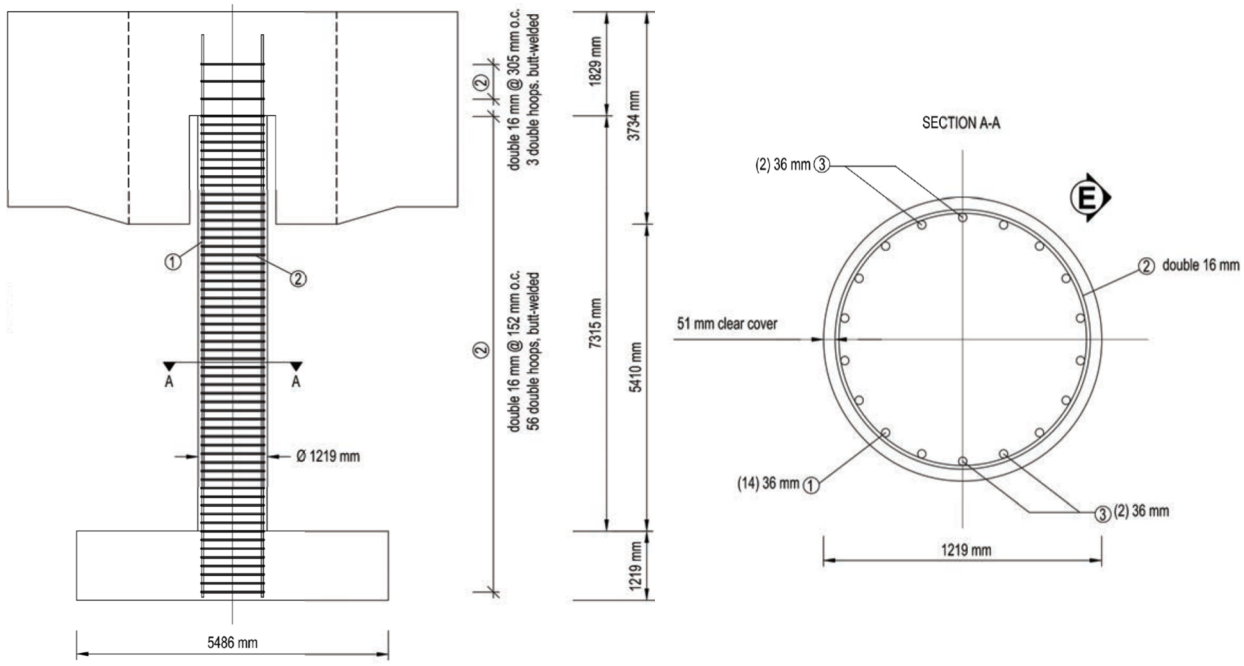

Figure 2.2 Full-scale bridge column details and dimensions [Schoettler et al. 2015].

2.2.2 Finite-Element Model

A two-dimensional analytical model of the bridge column was developed in OpenSees [Mckenna 2011] to conduct the IDA. OpenSees is an object-oriented software framework for simulation of structural and geotechnical systems subjected to seismic excitations. Figure 2.3 shows a schematic view of the OpenSees model. The column was modeled using a nonlinear *forceBeamColumn* element with a fiber section and five *Gauss-Lobatto* integration points that allows for the spread of plasticity along the element length. The fiber section incorporates nonlinear uniaxial materials, which captures the interaction between the axial and flexural response, and the nonlinear hysteretic behavior of the column. The cross section is divided into three parts to define the uniaxial materials, including concrete core and cover, and reinforcing steel in the RC section. Concrete core, cover, and longitudinal reinforcing bars were modeled using *Concrete02* and *ReinforcingSteel* uniaxial materials, respectively. These materials and their specific input parameters were selected based on the results of the model calibration explained in the next section.

The *Concrete02* material constructs the stress–strain relationship of concrete in compression and tension with linear tension softening; in this study reported herein, the concrete tensile strength was ignored in the model for simplicity's sake. The initial slope for this model is ($2f_c'/\varepsilon_0$). The parameters that must be defined for *Concrete02* include: concrete compressive strength (f_c'); strain at compressive strength (ε_0); concrete crushing strength (f_{cu}); strain at crushing strength (ε_{cu}); the ratio between unloading slope at ε_{cu} and initial slope (λ); tensile strength (f_t); and tension softening stiffness (E_{ts}) . Mander's model [Mander et al. 1988] was utilized to

determine confined properties of the core concrete in the column. The defined input parameters for the concrete material are shown in Table 2.1.

The *ReinforcingSteel* material is based on the Chang and Mander [1994] uniaxial steel model that uses the backbone curve as a bounding surface for the reinforcing bar simulation. The defined constants for this material are as follows: yield stress in tension (f_y); ultimate stress in tension (f_u); Initial elastic tangent (E_s); tangent at initial strain hardening (E_{sh}); strain corresponding to initial strain hardening (ε_{sh}); and strain at peak stress (ε_u). The defined input parameters for the steel material are shown in Table 2.2.

A dead load of 570 kips resulting in a 5.3% axial load index was applied on the column. For geometric transformation definition, the P-Δ option was utilized to account for the *P*- Δ effect in the analyses. The mass was lumped at the upper node of the column with only transitional mass defined, i.e. rotational inertial masses were not included in this analysis. A 5% Rayleigh damping ratio was considered in the dynamic analyses.

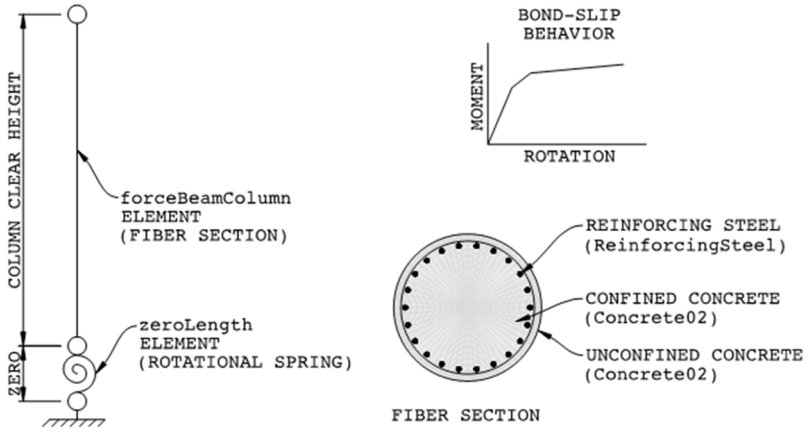

Figure 2.3 Schematic view of the OpenSees model.

Table 2.1 Parameters used to define *Concrete02* material for concrete core and cover in the preliminary full-scale OpenSees model.

Parameter	f'_c (ksi)	ε_{c0}	f'_{cu} (ksi)	ε_{cu}	λ	f_t (ksi)	E_{ts} (ksi)
Cover	6.1	0.002	0.0	0.005	0.4	0.0	0.0
Core	7.73	0.0047	4.35	0.0152	0.4	0.0	0.0

Table 2.2 Parameters used to define *ReinforcingSteel* material in the preliminary full-scale OpenSees model.

Parameter	f_y (ksi)	f_u (ksi)	E_s (ksi)	E_{sh} (ksi)	ε_{sh}	ε_u
#11 Bar	75.2	102.4	28,426	800	0.011	0.122

To define the bond-slip effects, a moment-rotation (M-θ) curve at the column-footing connection was defined using the bond-slip model proposed by Wehbe et al. [1997]. Thus, a hysteretic tri-linear material was assigned to a *zeroLength* element to simulate a rotational spring at the bottom of the column. The zero-length element is defined by two coincident nodes incorporating a uniaxial material that is implemented on each degree-of-freedom at the nodes to represent the force-deformation relationship. The column shear deformations were ignored in the analysis because of the relatively large column aspect ratio, indicating that the column is dominated by flexure.

To account for the failure of reinforcing bars due to low-cycle fatigue, the parent steel material assigned to the reinforcing bars was wrapped by the *Fatigue* material developed in OpenSees. The low-cycle fatigue parameters were determined by the fatigue-fracture model developed by Zhong and Deierlein [2018], which are defined using the Equations (2.1) to (2.4). Note that these equations were the preliminary versions that were available at the time of pre-test analysis and were later updated by Zhong and Deierlein [2019]. The final version of the fatigue-fracture model is provided in Chapter 7 and used for post-test analysis.

$$\varepsilon_p = C_f \left(2N_f\right)^{-\alpha_f} \tag{2.1}$$

$$\alpha_f = 0.729 - 0.075\left(f_y/60\text{ ksi}\right) + 0.038\left(s/d_b\right) - 0.217\left(T/Y\right) \tag{2.2}$$

$$C_f = 0.5^{\alpha_f}\left(\varepsilon_f - f_y/E\right) \tag{2.3}$$

$$\varepsilon_f = f_y/E - 0.029\left(f_y/60\text{ ksi}\right) + 0.127\left(T/Y\right) \tag{2.4}$$

where f_y is plastic strain amplitude; $2N_f$ is number of half cycles; C_f and α_f are material properties; f_y is steel yield strength; s is the clear spacing of reinforcing bar; d_b is the nominal size of reinforcing bar; T/Y is steel ultimate strength to yield strength ratio; ε_f is the fracture strain amplitude; and E is modulus of elasticity.

The *Fatigue* material in OpenSees uses a linear strain accumulation model that follows Miner's Rule [Miner 1945] through a modified rainflow cycle counting algorithm to accumulate damage in the utilized material (herein the *ReinforcingSteel* material). In addition, Coffin–Manson log-log relationships are used in this material to describe low-cycle fatigue failure [Manson and Hirschberg 1963; Coffin 1962]. When the damage level in the fatigue material model reaches 1.0, the force (or stress) of the parent material becomes zero. The collapse capacity is estimated when the accumulated damage, as defined by the fracture index (FI) defined below in Equation (2.5), where the reinforcing bars reaches a value of 1.0.

$$\text{FI} = \sum_{i=1}^{N}\left(\varepsilon_{pi}/C_f\right)^{1/\alpha_f} \tag{2.5}$$

where FI is fracture index in reinforcing bar; and N is number of full strain cycles in the reinforcing bar. A nonlinear response history analysis example showing the accumulation of the damage in a reinforcing bar is presented in Figure 2.4. Note: the *Fatigue* material is commonly used for other structural applications, such as capturing the fatigue-induced rupture of structural braces in steel braced frames [Hammad and Moustafa 2019; 2020a]. In this study, initial values for the fatigue model parameters are based on the model proposed by Zhong and Deierlein [2018]. Later in the study, such a model is assessed using shake table tests, which is a similar approach to what was reported for braced frames in Hammad and Moustafa [2020b].

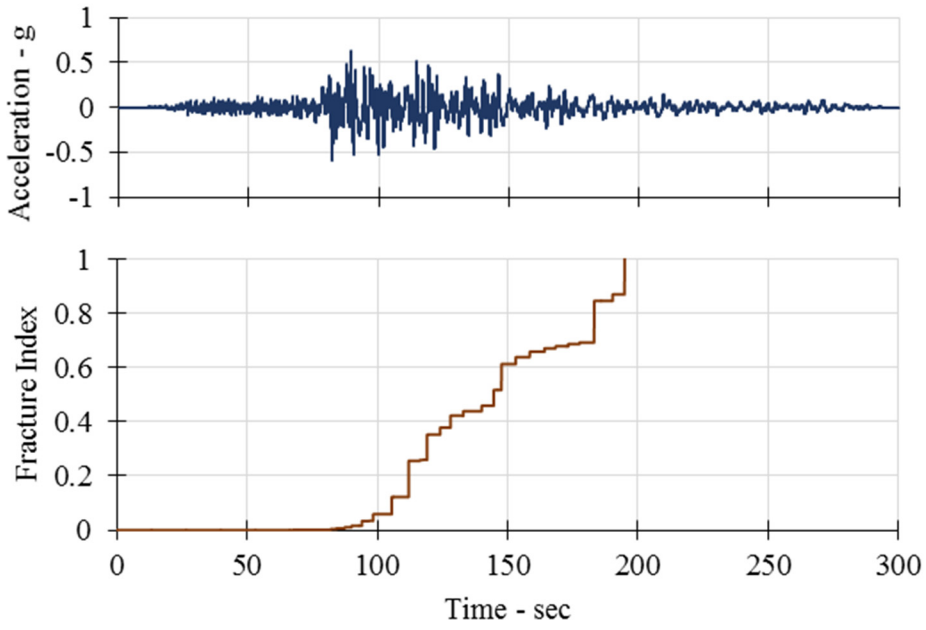

Figure 2.4 An example of the damage accumulation in a bar due to low-cycle fatigue.

2.2.3 Model Calibration

Several sets of modeling calibration have been conducted in this study. The first set presented here in this section is for the analytical model of the UC San Diego column, which was calibrated against the shake table experimental results. To improve agreement between the measured and calculated responses, several refinements were made on the numerical model. The modifications included the use of actual earthquake loading and adjusting the boundary conditions as well as material models and properties. The actual shake table feedback acceleration history was used as input motion for a nonlinear response history analysis for model calibration. The concrete and steel properties measured on test-day were utilized in the nonlinear beam–column element that represented the column (see Table 2.1 and Table 2.2 for actual values used in the refined model).

A sectional analysis was conducted to determine the bond-slip hysteretic tri-linear material parameters. The correlation between the measured and calculated results were then assessed by comparing two main seismic responses including column top displacement and base shear. Other responses such as the base rotation and strains in the longitudinal bars of the column were also

compared. Refinements were made on the materials parameters in the model to improve the accuracy of capturing bond-slip effects. After the correlation was deemed sufficiently satisfactory, the parameters of *Fatigue* material in the model were modified to predict the onset of bar rupture. The initial calculated parameters for the bond-slip model and fatigue material as well as the refined parameters after calibration are summarized in Table 2.3 and Table 2.4, respectively.

Figure 2.5 and Figure 2.6 compare the experimental and analytical displacement and strain histories for the column model during runs 5 and 6. These results indicate that the global and local responses were in a good agreement in terms of the peak points and the overall pattern, which gave confidence in using similar modeling assumptions throughout this study.

Table 2.3 Initial calculated and modified bond-slip model parameters after calibration of the preliminary full-scale model.

Parameter	M_1 (kip.in.)	θ_1 (rad)	M_2 (kip.in)	θ_2 (rad)	M_3 (kip.in)	θ_3 (rad)
Initial	32,100	0.0009	43,200	0.0032	53,700	0.031
Modified	34,000	0.0015	45,000	0.004	55,000	0.025

Table 2.4 Initial calculated and modified fatigue material parameters after calibration of the preliminary full-scale model.

Parameter	C_f	α_f
Initial	0.103	-0.49
Modified	0.11	-0.47

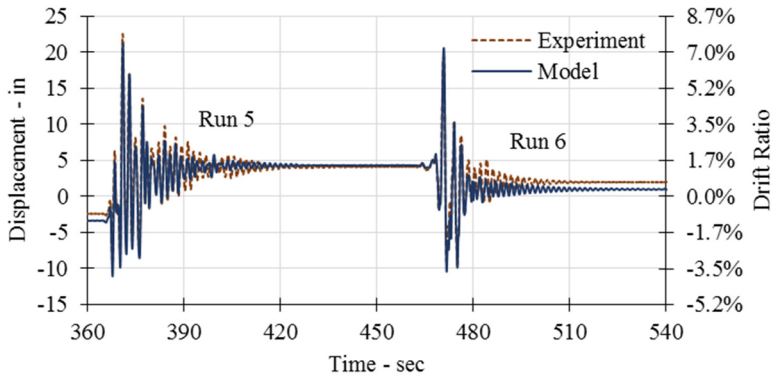

Figure 2.5 Comparison of experiment and model displacement histories for the bridge column during runs 5 and 6.

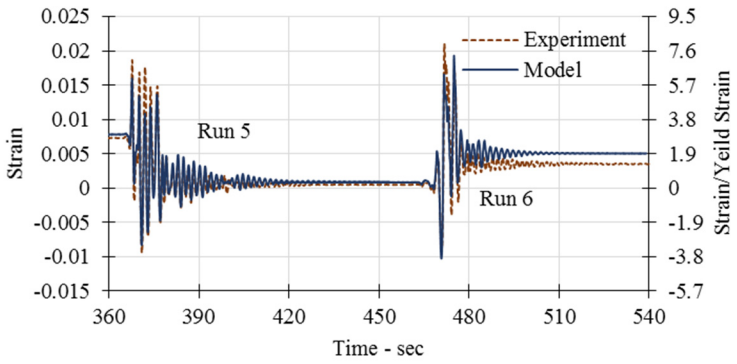

Figure 2.6 **Comparison of experiment and model strain histories for a sample reinforcing bar during runs 5 and 6.**

2.2.4 Ground-Motion Selection

The input records for the conducted IDA comprised two suites of spectrally matched ground motions: long-duration and short-duration suites. Each suite included 156 ground-motion records. Out of the 156 matched pairs, 112 pairs (hereafter referred to as "Group A" records) were selected to be similar to a set previously used by Mohammed [2016]. For each long-duration record, a corresponding short-duration ground-motion record with a closely matching response spectrum was selected from the PEER NGA-West2 database [Ancheta et al. 2013]. Short-duration ground motions were scaled by a factor such that the mean squared error (MSE) between the spectrum of the scaled motion (short duration) and the target spectrum (long duration) was minimized [Mohammed 2016]. The other 44 ground-motion pairs (hereafter referred to as "Group B" records) follow similar trend as Group A and were adopted from Chandramohan [2016]. Note: the short-duration motions in Group B comprised the FEMA-P695 [Kircher et al. 2010] far-field set of ground motions, which were accounted for as the target motions. In turn, Group B long-duration motions were selected such that their response spectra matched those of the equivalent short-duration motions. In addition, short-duration records remained unscaled, while the long-duration motions were scaled to minimize the MSE. For completeness, Appendix A provides the list of Group A and Group B ground-motion pairs and relevant scaling.

The long-duration records in both groups were selected from various subduction and crustal earthquakes. Each of the long-duration records belonged to one of the following large magnitude earthquake events: 1974 Lima (Peru), 1979 Imperial Valley (USA), 1985 Valparaiso (Chile), 1985 Michoacan (Mexico),1992 Landers (USA), 1999 Chi-Chi (Taiwan), 2002 Denali (USA), 2003 Hokkaido (Japan), 2007 Kepulauan Mentawai (Indonesia), 2008 Wenchuan (China), 2010 Maule (Chile), 2011 Tohoku (Japan), 2012 Kamaishi (Japan), 2014 Iquique (Chile), and 2015 Illapel (Chile). The ground motions were baseline corrected and filtered following the recommendations by Boore [2005] and Boore and Bommer [2005].

Different criteria have been considered by researchers to differentiate between long- and short-duration ground motions. Long-duration motions may be specified based on the significant duration. Chandramohan et al. [2013; 2016] used motions with significant duration Ds(5–95%) > 45 sec and Ds(5–75%) > 25 sec. Ou et al. [2013] specified long-duration motions such that the 5%

PGA levels are crossed more than 600 times. For both Group A and B ground motions utilized in this study, a combination of these three criteria was used to determine the long- and short-duration motions [Mohammed 2016]. The long- and short-duration record suites have geometric means of Ds(5–95%) of 79 and 14 sec, respectively. Figure 2.7 shows the distribution of Ds(5–95%) for the spectrally equivalent long- and short-duration sets. Comparisons of the response spectra and time histories of an example spectrally equivalent long- and short-duration motion pair is shown in Figure 2.8(a). Figure 2.8(b) compares the geometric mean response spectra of the long- and short-duration records.

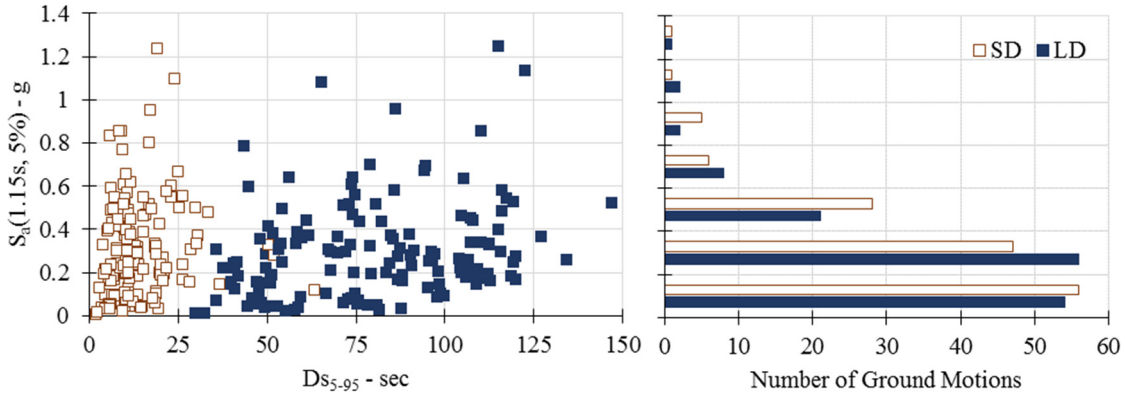

Figure 2.7 **Distribution of significant duration Ds_{5-95} for the ground motion suites (LD: long-duration motions, SD: short-duration motions).**

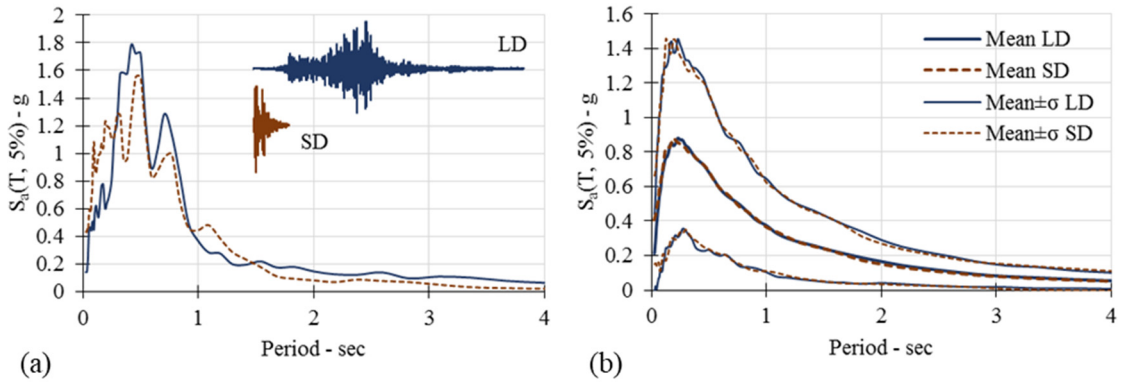

Figure 2.8 **Comparison of the response spectra: (a) example for spectrally equivalent long- and short-duration motion pair; and (b) geometric mean of all spectrally matched long- and short-duration motions.**

2.2.5 Analytical Fragility Curves

The IDA was conducted to develop fragility curves utilizing spectrally equivalent long and short-duration records, previously discussed in Section 1 above. All the ground motions were incrementally scaled until collapse was captured, or in other words, until the FI reached a value of 1. The fragility curves were developed by fitting a lognormal cumulative distribution to the

analysis results, and the final collapse fragility curves for short- and long-duration motions are shown in Figure 2.9. Spectral acceleration at collapse was used to compare the results from the long- and short-duration ground motion suites. Distribution of the data was examined by a Kolmogorov–Smirnov test for goodness of fit [Massey 1951] as the acceptance criterion. The median collapse capacities estimated for the short- and long-duration suites were 1.7*g* and 1.2*g*, respectively, which shows a 30% reduction in the collapse capacities under long-duration motions. This preliminary analytical study demonstrated a higher effect of duration on collapse capacity of bridge columns compared to the previous studies: 25% and 17% reductions reported by Mohammed [2016] and Chandramohan et al. [2016], respectively. This might be attributed to the use of a more reliable model to compute the low-cycle fatigue behavior of the reinforcing bars. Nonetheless, the results confirm previous observations on the adverse effects of longer duration but highlights the sensitivity of the results to the modeling assumptions, especially when considering low-cycle fatigue and limit states.

Figure 2.10 shows a log–log plot of the spectral acceleration of the bridge column at collapse versus ground motion Ds(5–95%) significant duration as fitted into the results from individual ground-motion runs. The figure suggests an obvious trend of reduction in the collapse capacity of the bridge column as the duration of the ground motion is increased. To further investigate the duration effect using spectrally-equivalent short- and long-duration motion pairs, the ratio of the collapse capacity under each long-duration motion to the spectrally-equivalent short-duration motion, referred to as "collapse capacity ratio," was plotted versus the similar ratio for Ds(5–95%), referred to as "duration ratio"; see Figure 2.11.

It can be seen from the figures that within each pair of matched ground motions, larger duration ratios correspond to lower collapse capacity ratios. In addition, the rate of decrease in the collapse capacity ratio is higher for smaller values of duration ratio. For example, if the duration ratio is increased from 2 to 6, the reduction on collapse capacity ratio is 17% (from 87% to 70%). When the duration ratio increases from 10 to 14, the collapse capacity ratio only decreases by 5% (from 63% to 58%).

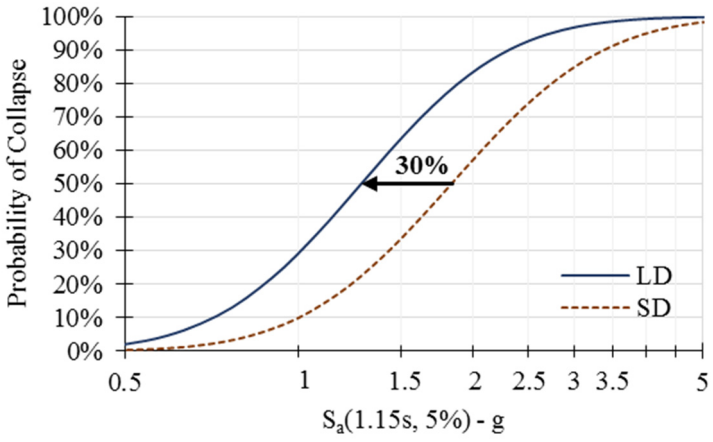

Figure 2.9 Collapse fragility curves for the short- and long-duration suites.

Overall, the results show that it is important to consider earthquake duration in the design and vulnerability assessment of new and existing bridge columns in regions that have higher risk for occurrence of long-duration earthquakes, such as subduction zones. It is also noted that the effect of the earthquake duration demonstrated in this study seems to be more significant compared to previous analytical studies. This can be attributed to the fact that most of the previous studies did not consider or underestimated the effects of low-cycle fatigue in the reinforcing steel as it relates to damage accumulation and earthquake duration. Thus, this study pays special attention to the low-cycle fatigue effects in modeling, as discussed throughout this report.

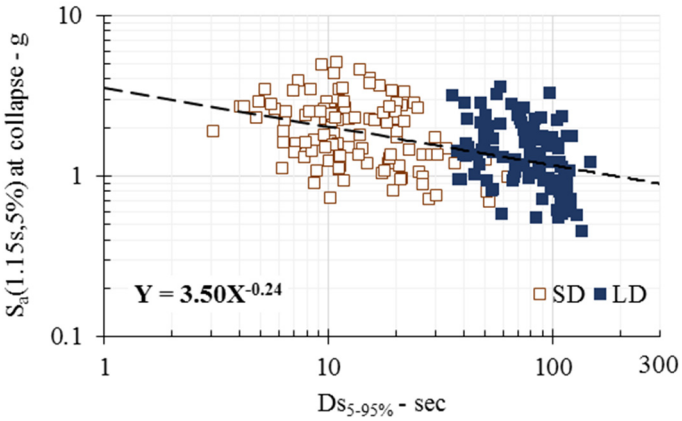

Figure 2.10 Collapse capacity of the column versus significant duration Ds(5–95%).

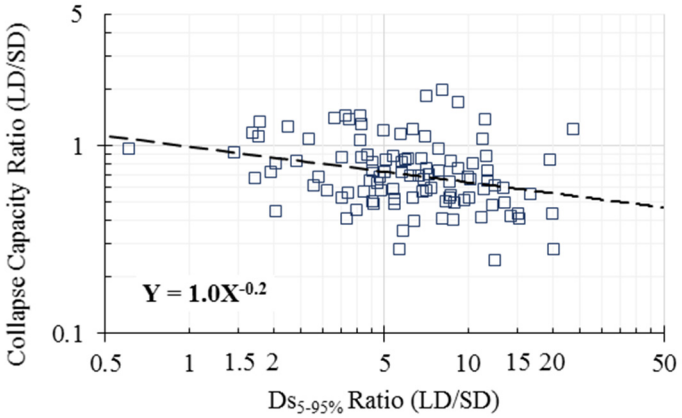

Figure 2.11 Collapse capacity ratio from matched long- and short-duration runs versus significant duration ratio.

2.3 SPECIMENS DESIGN

Section 2.2 stressed the importance of obtaining a preliminary understanding of critical modeling aspects worthy of additional study. An additional preliminary analysis is considered but with a different objective: to conduct careful pre-test assessment whose results should be included in the experimental program. Full details on the experimental program are discussed in Chapters 3–6.

The design of the test specimen design is provided here first since it is needed for the pre-test analysis.

Six one-third-scale cast-in-place (CIP) RC bridge column models were designed to be constructed and tested on the UNR shake table in two phases. The experimental specimens were adopted from a previous study by Phan et al. [2005], in which columns were designed based on AASHTO [2002]. The design presented herein still meets the requirements of recent AASHTO versions, i.e., AASHTO [2014]. The column named as NF-2, was selected as the base design for this study. The full-scale prototype columns were designed first and then scaled down to a size that is compatible with the shake table. Table 2.5 summarizes the details of the prototype and scaled column.

Column NF-2 was tested under a loading protocol until failure on a shake table using a sequence of the Rinaldi ground motions. This specimen configuration was also utilized in the previous study on the effect of duration at UNR conducted by Mohammed et al. [2017]. This NF-2 column was selected because its basic failure mode and displacement capacity were already known from previous research. The failure mode of NF-2 was reinforcing steel rupture as one longitudinal bar fractured at 135% of the Rinaldi ground motion. Also, the peak measured displacement capacity of the column was reported to be 9.8 in. Figure 2.12 shows the dimensions details of the column considered for all the specimens. The columns were circular with 16 in. diameter and a clear height of 72 in. An 80-kips axial load was applied on top of the columns, which corresponded to 8% of the column axial capacity $\left(A_g f_c'\right)$.

Table 2.5 Details of the prototype and scaled model columns.

	Prototype	Phase I Specimens	Phase II Specimens
Column height (in.)	216	72	
Column diameter (in.)	48	16	
Long. reinforcement	25 #11 (2.15%)	22 #4 Gr60 (2.2%)	14 #4 Gr100 (1.4%)
Trans. reinforcement	#7 @ 5 in. (1.1%)	#3 @ 3 in. or 1.5 in. (1% or 2%)	
Concrete cover (in.)	2	0.75	
Axial load (kips)	720	80	

2.3.1 Design Concepts

Current design codes mostly require ductile modes of failure. For example, the shear capacity of the column must be always larger than maximum plastic shear (the lateral load associated to the maximum flexural capacity) to avoid brittle shear failure. The structure is designed to resist the internal forces generated when the structure reaches its collapse limit state based on plastic mechanisms. The collapse limit state is defined as the condition when a sufficient number of plastic hinges have formed within the structure [Caltrans 2013]. Footings and bent caps are categorized as capacity protected members, which are designed to remain essentially elastic with no yielding or damage. Therefore, the footing and loading head should be designed to remain elastic when the column undergoes large plastic deformations.

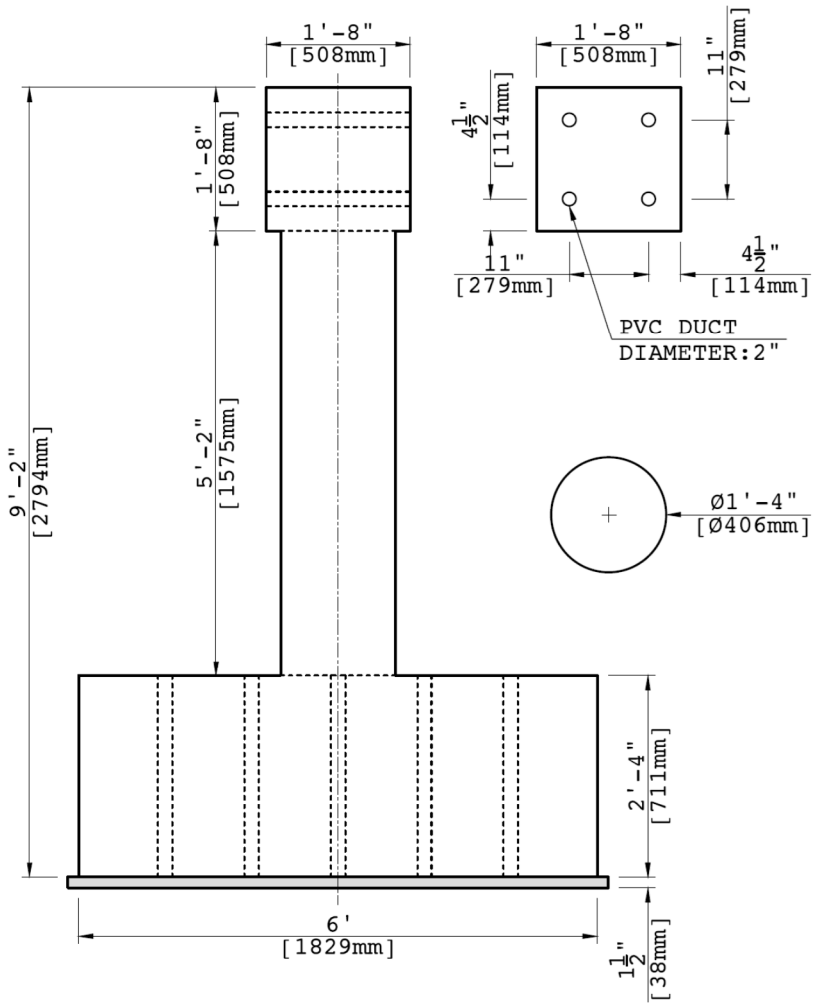

Figure 2.12 Concrete and overall dimensions of all six specimens.

2.3.2 Phase I: Columns Design

The first three column models, tested in the first phase of the experimental program had similar geometry and longitudinal bar arrangements but varied in other details. The longitudinal reinforcement consisted of twenty-two #4 (equivalent to 2.2% reinforcement ratio) Grade-60 bars in a circular pattern. The reference column had transverse steel volumetric ratio of 1.04% (#3@3 in.). The spiral spacing was determined such that the transverse reinforcement ratio be close to the minimum required ratio dictated by AASHTO (0.12 $f_c'/f_y = 1.15\%$) while still meeting the minimum AASHTO [2014] requirements for spacing, i.e., largest of: Dc/4; 4 in.; and six times the longitudinal bar diameter (= 3 in.). This column will hereafter be referred to as LD-S3-G60. In the second column (referred to as LD-S1.5-G60), the transverse reinforcement ratio was doubled (2.08%, #3@1.5 in.) to investigate the effect of tie spacing on column seismic performance under long-duration earthquakes. In the third column (referred to as LD-S3-G60D), the transverse steel was the same as the reference column LD-S1.5-G60, but the longitudinal bars were debonded at column-footing interface with an intent to spread the bar yielding and to potentially enhance the displacement capacity. To debond the longitudinal reinforcement, a total of 12 in. of each bar was

wrapped by duct tape with 8 in. of the debonded length inside the footing. Table 2.6 lists reinforcement details of the specimens considered in this study. Figure 2.13 through Figure 2.15 show the reinforcing details of the three specimens in Phase I. The detailed drawings and bidding document of the specimens are provided in Appendix B. All the columns were designed to behave as cantilever columns, representative of single-column bridge piers. The columns also had equal moment capacities. The footings were designed to be capacity protected and to be stiff enough to provide adequate fixity for the cantilever column.

Table 2.6 Phase I: reinforcing configuration of specimens.

Specimens	LD-S3-G60	LD-S1.5-G60	LD-S3-G60D
Long. reinforcement	22 #4 (2.2%) Gr. 60	22 #4 (2.2%) Gr. 60	22 #4 (2.2%) Gr. 60
Trans. reinforcement	#3 @ 3 in. (1.04%)	#3 @ 1.5 in. (2.08%)	#3 @ 3 in. (1.04%)
Tie spacing	6 db	3 db	6 db

2.3.3 Phase II: Column Design

In the second phase, three more 1/3-scale RC bridge column models were designed, constructed, and tested on the UNR shake table. The major difference between the two experimental phases is the use of high-strength reinforcement in the second phase. The experimental specimens were geometrically identical to the Phase I specimens but reinforced by 14 #4 Grade-100 ASTM A1035 bars that provides 1.4% reinforcement ratio. The Chrome 9100 bars from MMFX were intended to be used, so the design and pre-test analysis followed accordingly. The first column had transverse reinforcement spaced at 1.5 in. ($3d_b$) and was labeled as Column LD-S1.5-G100 since it was planned to be tested under long-duration earthquake. In the two other columns, the tie spacing was 3 in. ($6d_b$). These specimens were named as Columns SD-S3-G100 and LD-S3-G100, which were planned to be tested under short- and long-duration motions, respectively. The design details of the specimens are provided in Table 2.7. Figure 2.16 and Figure 2.17 show the reinforcing details of the specimens in Phase II.

Table 2.7 Phase II: reinforcing configuration of specimens.

Specimens	LD-S1.5-G100	SD-S3-G100	LD-S3-G100
Long. reinforcement	14 #4 (1.4%) Gr. 100	14 #4 (1.4%) Gr. 100	14 #4 (1.4%) Gr. 100
Trans. reinforcement	#3 @ 1.5 in. (2.08%)	#3 @ 3 in. (1.04%)	#3 @ 3 in. (1.04%)
Tie spacing	3 db	6 db	6 db

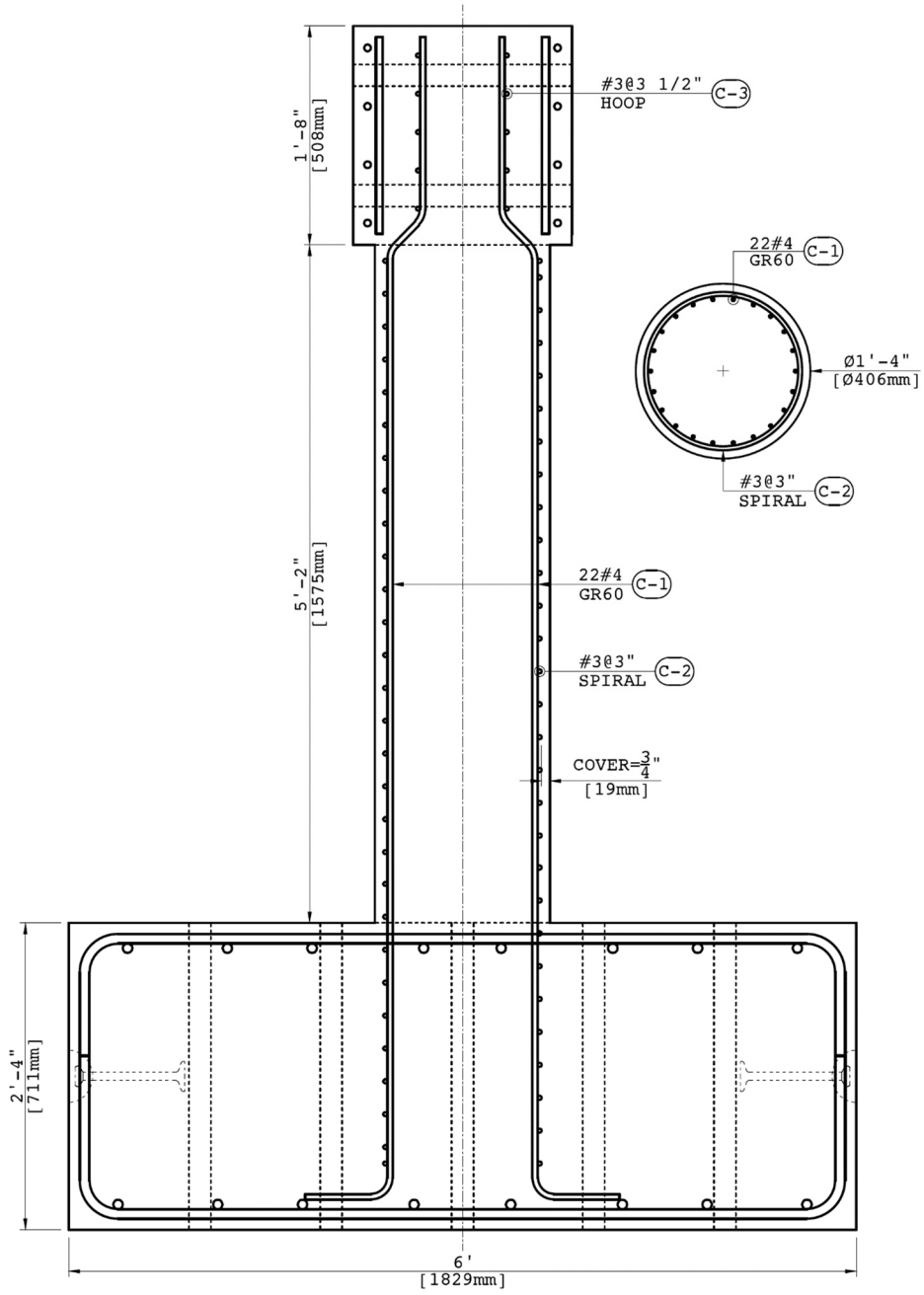

Figure 2.13 Column LD-S3-G60: reinforcement details.

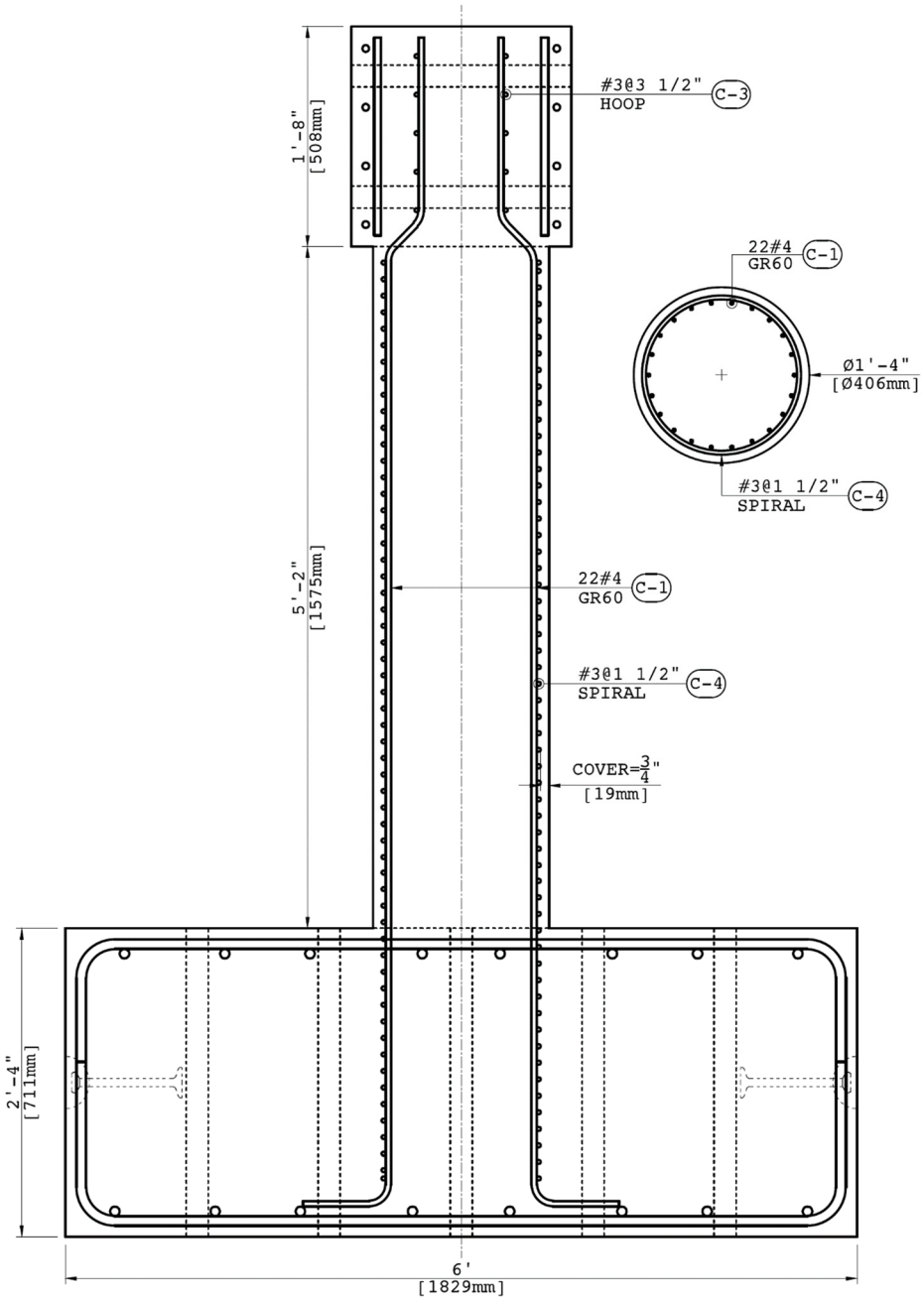

Figure 2.14 Column LD-S1.5-G60: reinforcement details.

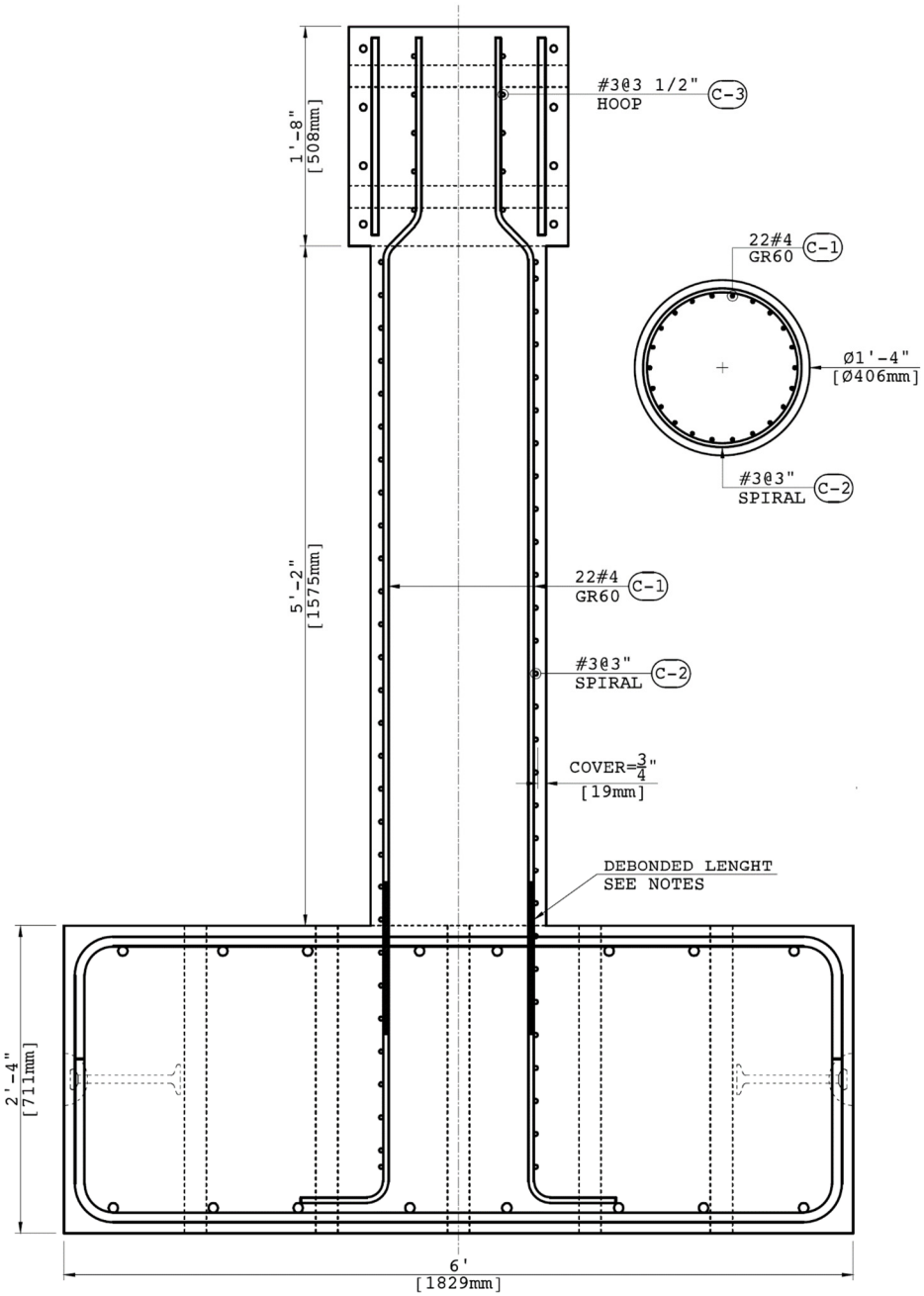

Figure 2.15 Column LD-S3-G60D: reinforcement details.

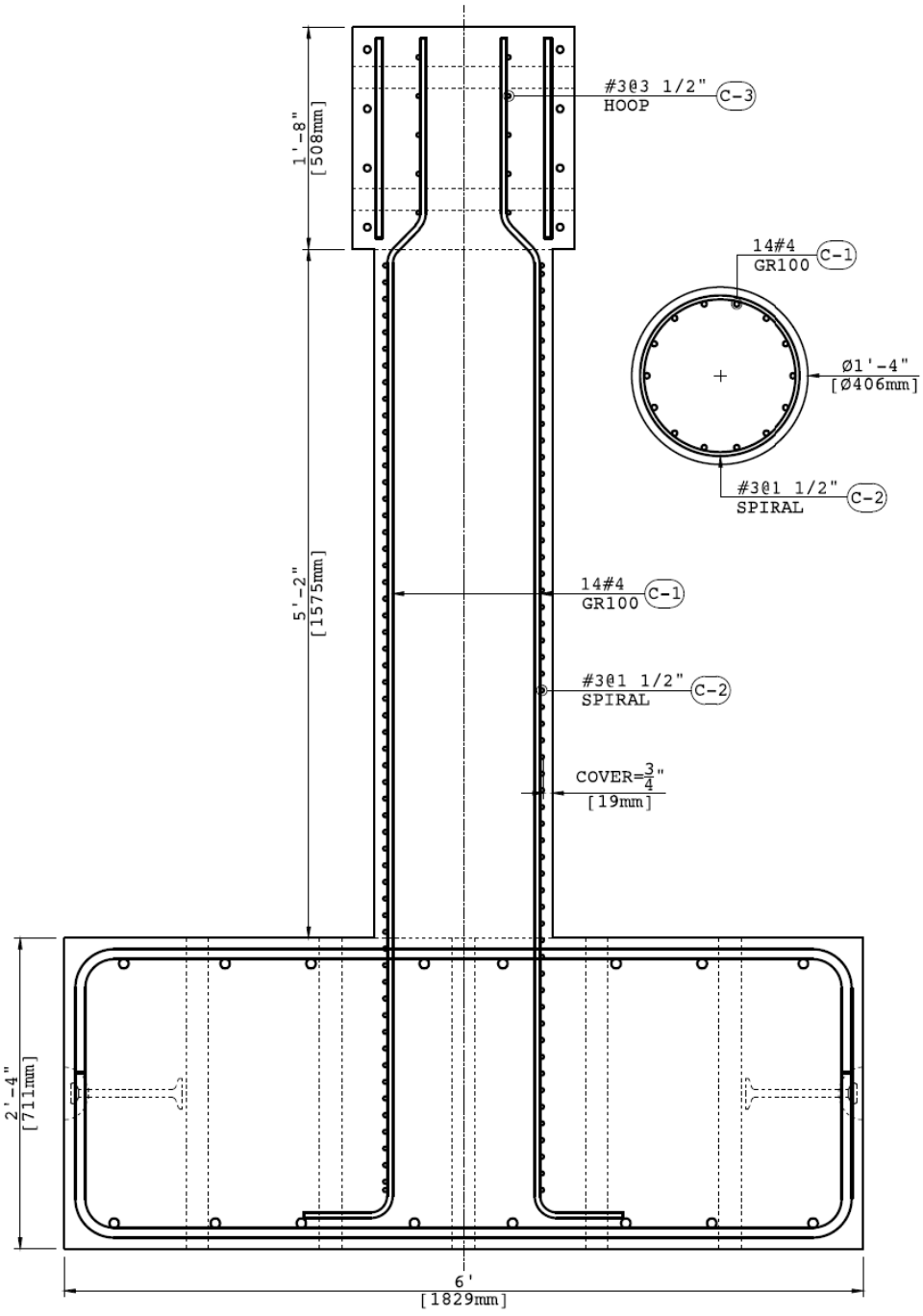

Figure 2.16 Column LD-S1.5-G100: reinforcement details.

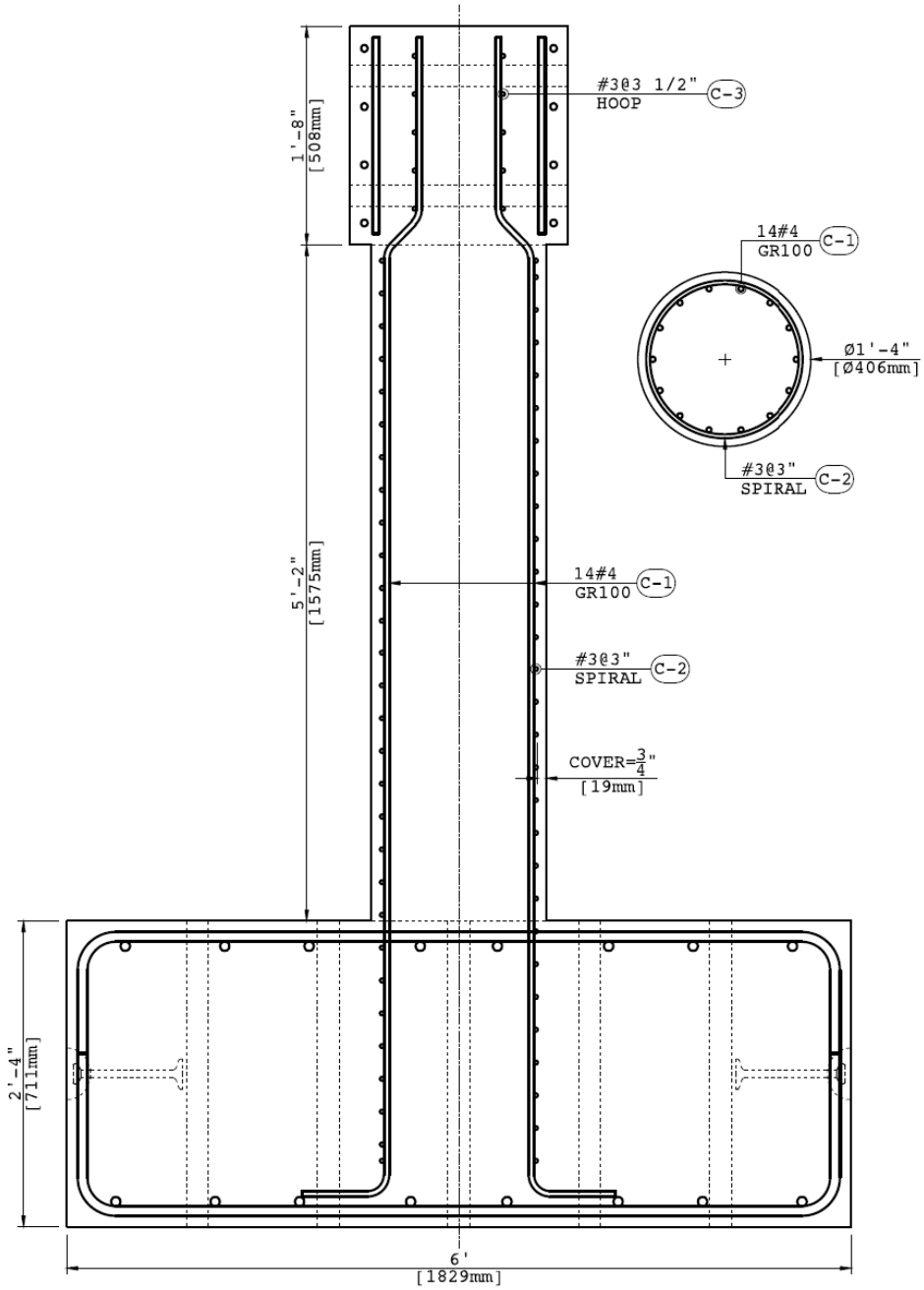

Figure 2.17 Columns SD-S3-G100 and LD-S3-G100: reinforcement details.

2.3.4 Footing Design

A 72-in.-square and 28-in.-high footing was used identically for all the specimens; see Figure 2.18. The height of the footing was determined such that the scaled column could be properly connected to the inertial mass rig system; see Chapter 3. To avoid any deformation and damage in the footing, the footings were designed to remain essentially elastic under applied loads through full plastic-hinge formation in the columns. Part of the design considered the setup where the footings were to be post-tensioned to the shake table using fourteen threaded rods. Threaded rods that connect

the footing to the table are typically post-tensioned up to 30 kip; therefore, sliding of the footings during testing was not a matter of concern. The reinforcement consisted of two top and bottom mats of #7 bars with a 1-in.-clear cover. Cross ties at each joint connected the top and bottom reinforcement meshes. Four lifting anchors for each specimen were considered as part of the design for lifting and transporting purposes. In addition, 16 PVC pipes were laid out in each footing to accommodate the post-tensioning rods (rods fed through pipes) needed to attach the experimental specimens to the shake table.

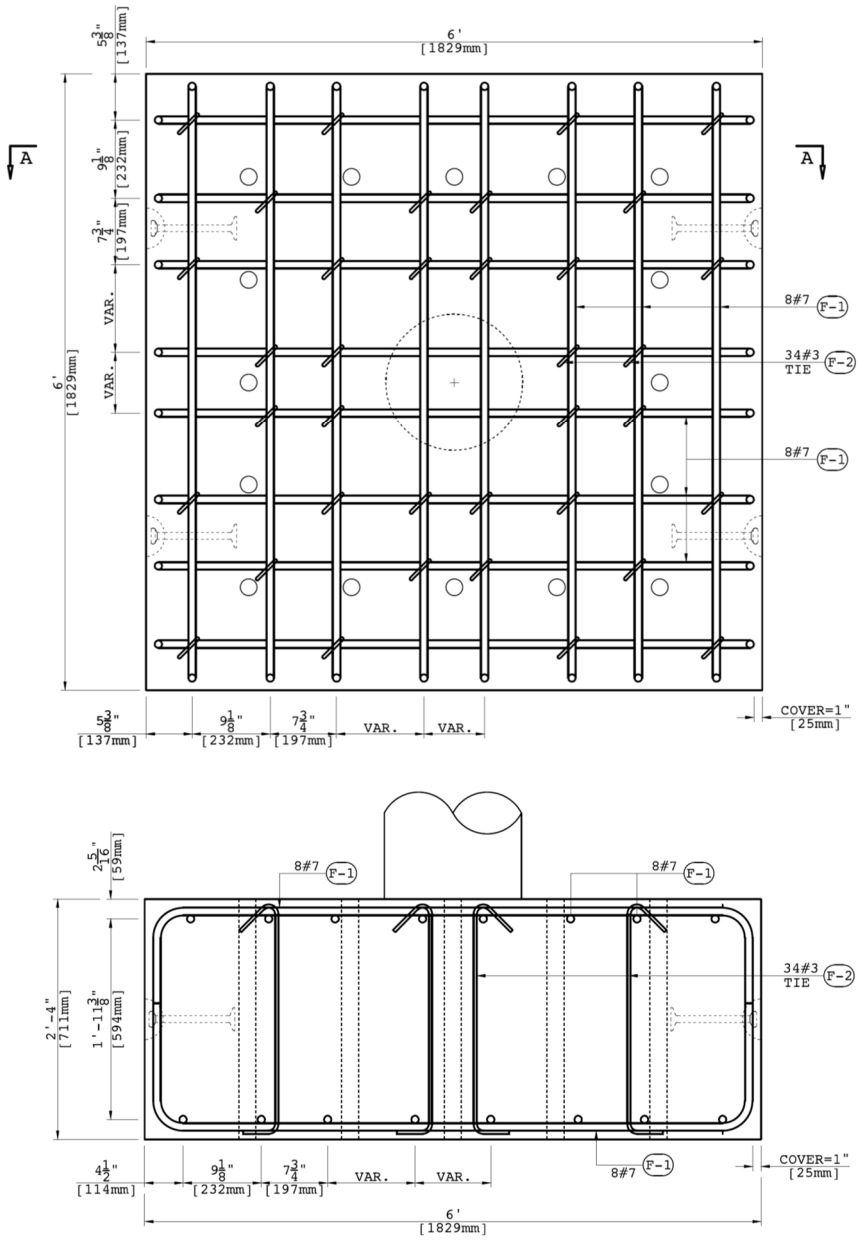

Figure 2.18 Reinforcement details of the footing.

2.4 PRE-TEST ANALYSIS

This section presents all the pre-test analysis work and blind prediction for the two phases of tests. The main specific objectives of the pre-test work were as follows: (1) estimate the dynamic response of the experimental specimens; and (2) ensure that the demand on the testing equipment is within the allowable limits; and (3) develop/finalize the earthquake loading protocol for the shake table tests.

2.4.1 Loading Head Design

Since the columns were designed to behave as cantilever members, minimal stresses were expected to be produced in the column head region and remain essentially elastic and damage free. The loading heads were 20 in. in length, width, and height. Each head was reinforced by four #4 vertical bars and four #4 ties. Four 2-in.-diameter PVC pipes were laid out in each loading head to allow for passing the rods that are needed to connect the inertial mass system to the specimen; see Figure 2.19. To make space for the PVC pipes, the longitudinal bars in the column were detailed as shown in the figure, i.e., bent in the head region.

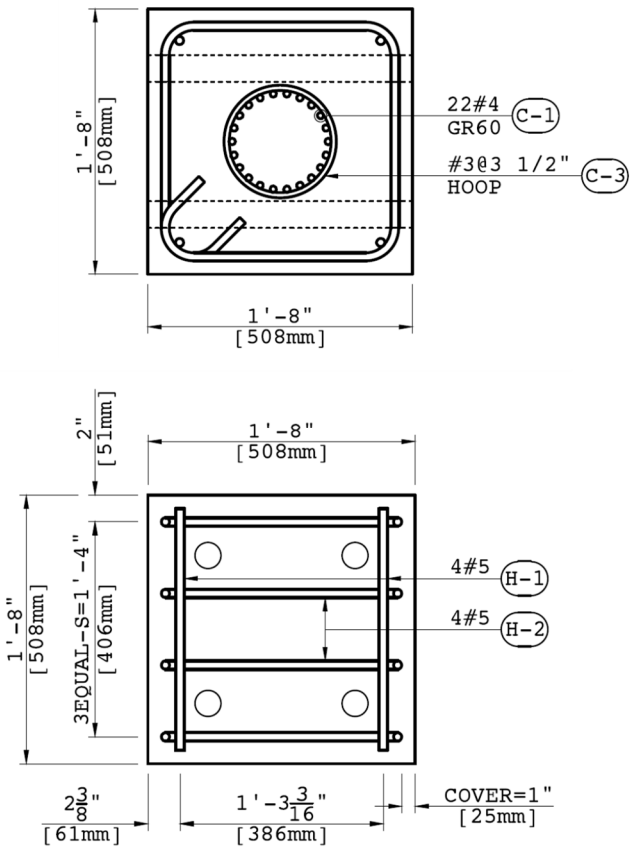

Figure 2.19 Reinforcement details of the loading head.

2.4.2 Analytical Model

For the pre-test analysis, the analytical modeling approach and assumptions described in Section 2.2.2 were refined after applying some modifications on the geometry, material properties, and bond-slip and fatigue material parameters. The model consisted of a nonlinear *forceBeamColumn* element with a fiber section, with the expected material properties. Note: the HSS bars in Phase II columns, the actual typical mechanical properties provided by the manufacturer from monotonic tests were used since current codes do not yet provide expected material properties for such reinforcement. The *Concrete02*, *ReinforcingSteel*, and *Steel02* uniaxial materials were used to model concrete core and cover, and conventional Grade-60 and high-strength Grade-100 longitudinal bars, respectively. The confined properties of the core concrete were determined based on Mander's model [Mander et al. 1988].

The specified 28-day concrete compressive strength $\left(f'_c\right)$ was 5 ksi. Thus, an expected unconfined strength $\left(f'_{ce}\right)$ and corresponding strain $\left(\varepsilon_{cc}\right)$ of 6.5 ksi and 0.2%, respectively, were used for the cover concrete. For core concrete of the columns with 3-in. tie spacing, the confined compressive strength $\left(f'_{cc}\right)$ and strain $\left(\varepsilon_{cc}\right)$ were determined to be 8.7 ksi and 0.53%, respectively, and the ultimate compressive strength and strain were 7.2 ksi and 1.83%, respectively. For the columns with 1.5-in. tie spacing, these former four values were determined to be 10.4 ksi and 0.81%, and 9.1 ksi and 2.79%, respectively. No tensile strength was assumed for the cover or core concrete. The specified yield strength $\left(f_y\right)$ and expected yield strength $\left(f_{ye}\right)$ for the Grade-60 reinforcement were 60 and 68 ksi, respectively. The modulus of elasticity $\left(E_s\right)$ was 29,000 ksi. The tangent strain-hardening modulus was assumed as $0.04E_s$. For the Grade-100 reinforcement, the actual measured mechanical properties from monotonic tensile tests were utilized in the numerical model, as previously mentioned. The actual yield strength $\left(f_y\right)$ of the HSS Grade-100 bars was 124 ksi. Other properties of the HSS bars are listed in Table 2.8.

The debonded bars in Column LD-S3-G60D were modeled using *trussSection* elements with length equal to the debonded length that were connected at the end of the debonded regions to the main element by *rigidLink* elements per Kennedy [2015]. A section with area of one bar that incorporated reinforcement steel uniaxial material was assigned to the *trussSection* elements. The column element inside the debonded region was modeled by a *dispBeamColumn* element with a fiber section incorporating concrete core and cover without steel bars. Figure 2.20 shows a sketch of the numerical model details.

Table 2.8 High-strength reinforcing steel properties.

	f_y (ksi)	ε_y	E (ksi)	F_u (ksi)	T/Y	ε_u	F_f (ksi)	ε_f
Long. Gr100	124*	0.0064*	28,000	163	1.31	0.055	105	0.09

* Defined by the 0.2%–offset method.

A dead load of 80 kips resulting in an 8% axial load index was applied on the top of the column. A mass of 0.207 kip.sec^2/in. was lumped at the upper node *Fatigue* of the column. The bond-slip model and *Fatigue* material input parameters were defined based on the methods described in Section 2.2.2. The calculated parameters of the bond-slip model and *Fatigue* material for the columns in both Phase I and Phase II are tabulated in Table 2.9 through Table 2.12, respectively.

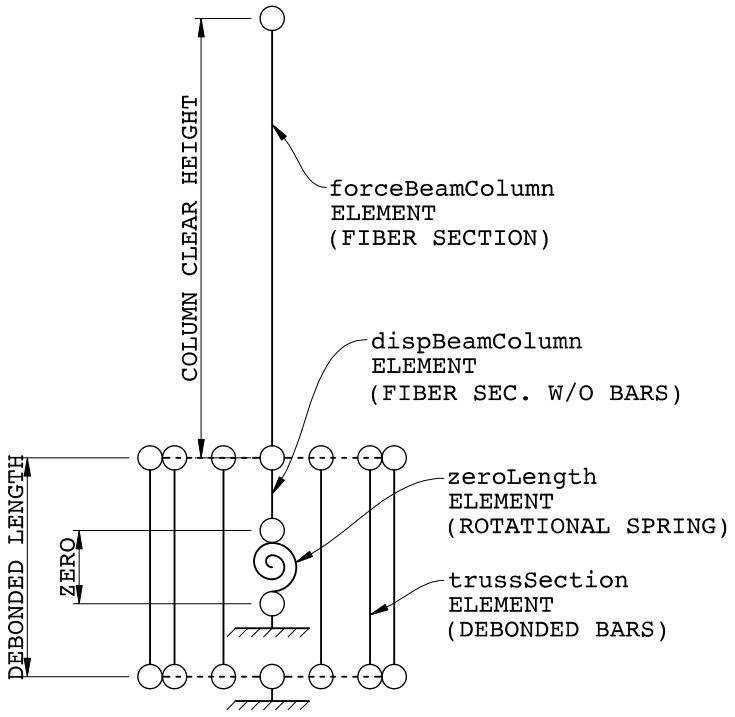

Figure 2.20 Schematic view of the OpenSees model for the column with debonding details.

Table 2.9 Phase I: bond-slip model parameters used in the pre-test model.

Parameter	M_1 (kip.in.)	θ_1 (rad)	M_2 (kip.in.)	θ_2 (rad)	M_3 (kip.in.)	θ_3 (rad)
Value	720	0.0001	2450	0.0063	2885	0.033

Table 2.10 Phase II: fatigue material parameters used in the pre-test model.

Parameter	C_f	α_f
LD-S3-G60 / LD-S3-G60D	0.097	-0.56
LD-S1.5-G60	0.105	-0.45

Table 2.11 Phase II: bond-slip model parameters used in the pre-test model.

Parameter	M_1 (kip.in.)	θ_1 (rad)	M_2 (kip.in.)	θ_2 (rad)	M_3 (kip.in.)	θ_3 (rad)
Value	700	0.0018	2,370	0.0065	2790	0.0295

Table 2.12 Phase II: fatigue material parameters used in the pre-test model.

Parameter	C_f	α_f
LD-S1.5-G100	0.086	-0.39
SD-S3-G100 / LD-S3-G100	0.080	-0.50

2.4.3 Model Calibration

For the pre-test analysis on the Phase I columns, the OpenSees model was calibrated against results from a shake table test of a similar, but not identical, bridge column from the previous study by Mohammed et al. [2017]. Column LD-J2 from the previous study was chosen for the calibration purposes. Note: this is the second set of calibration and model refinement conducted in this study. This column had the same longitudinal and transverse steel ratios as Column LD-S3-G60, but tighter tie spacing (wire #2@1.25 in). Similar to the calibration procedure explained in Section 2.2.3, refinements were made on the numerical model to improve agreement between the measured and calculated responses. The modifications included updating the input excitation, boundary conditions, and material properties. The actual shake table feedback acceleration was used as the input motion in the OpenSees model. The concrete and steel properties measured on test-day were used to update the materials in the model summarized in Table 2.13 and Table 2.14, respectively.

Table 2.13 Column LD-J2: actual concrete compressive strength on test-day.

	Footing (92 days)	Column (82 days)
Compressive strength f_c' (ksi)	6.00	6.05

Table 2.14 Column LD-J2: actual mechanical properties of longitudinal and transverse steel.

	Longitudinal	Transverse
Yield stress f_y (ksi)	74	90
Ultimate stress f_y (ksi)	103	101

The correlation between the measured and calculated results was then assessed by comparing seismic responses including column top displacement, base shear, base rotation, and strains in the longitudinal bars. The parameters of the *Fatigue* material model were then modified to accurately predict the onset of bar rupture. Figure 2.21 shows the strain history and accumulative damage for the northern bar, indicating a reasonable prediction of bar fracture compared to the actual test result. Table 2.15 and Table 2.16 llist the initially calculated and the modified parameters after calibration process used for the bond-slip model and *Fatigue* material, respectively. Since the modified parameters were within 5% of the initially computed ones, the equations for bond-slip model (Wehbe's model) and *Fatigue* material were used to obtain the intended parameters in the pre-test model, with no further modification. Figure 2.22 and Figure 2.23 compare the experimental and model displacement history, and force-displacement relationships for the column model, respectively. Results indicate that forces and displacements are in a good agreement in terms of the peak points and the overall pattern, which provided confidence in using the calibrated model for the pre-test analysis of the six columns analyzed herein.

For the pre-test analysis on the columns in Phase II, i.e., columns with high-strength steel, the same numerical OpenSees model was employed. Due to lack of any experimental study on bridge columns with HSS, the same input based on the conducted model calibration described above was incorporated to develop the bond-slip model and *Fatigue* material in the model. Such values will be revisited in the post-test analysis in Chapter 7, using results from the conducted shake table tests.

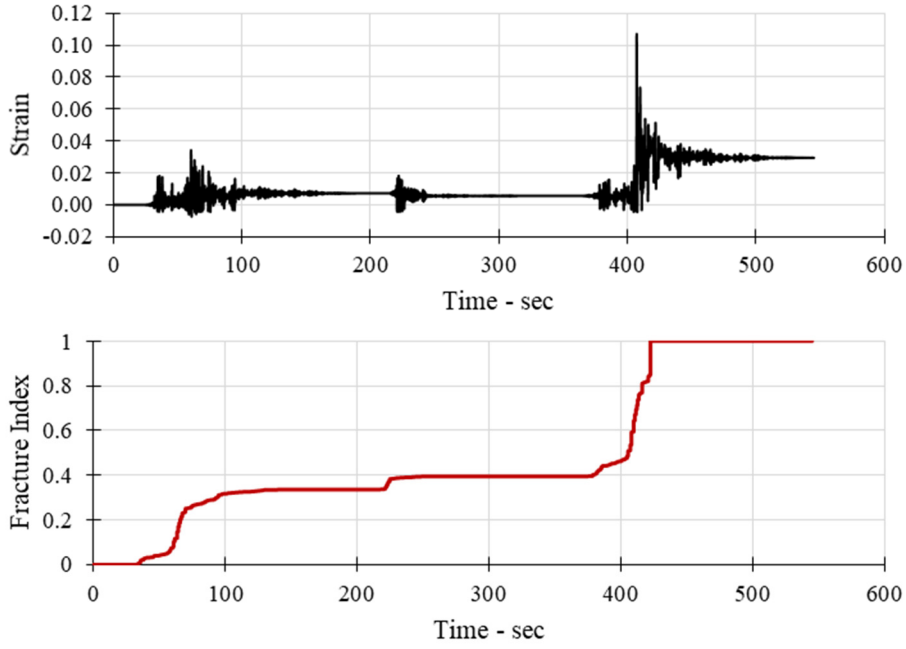

Figure 2.21 **Column LD-J2: strain history and accumulated damage in the northern bar.**

Table 2.15 **Column LD-J2: initial calculated and modified bond-slip model parameters after pre-test model calibration process.**

Parameter	M_1 (kip.in.)	θ_1 (rad)	M_2 (kip.in.)	θ_2 (rad)	M_3 (kip.in.)	θ_3 (rad)
Initial	1650	0.0011	2060	0.0018	2300	0.0082
Modified	1700	0.0016	2180	0.0022	2335	0.0076

Table 2.16 **Column LD-J2: initial calculated and modified fatigue material parameters after pre-test model calibration process.**

Parameter	C_f	α_f
Initial	0.105	-0.43
Modified	0.110	-0.42

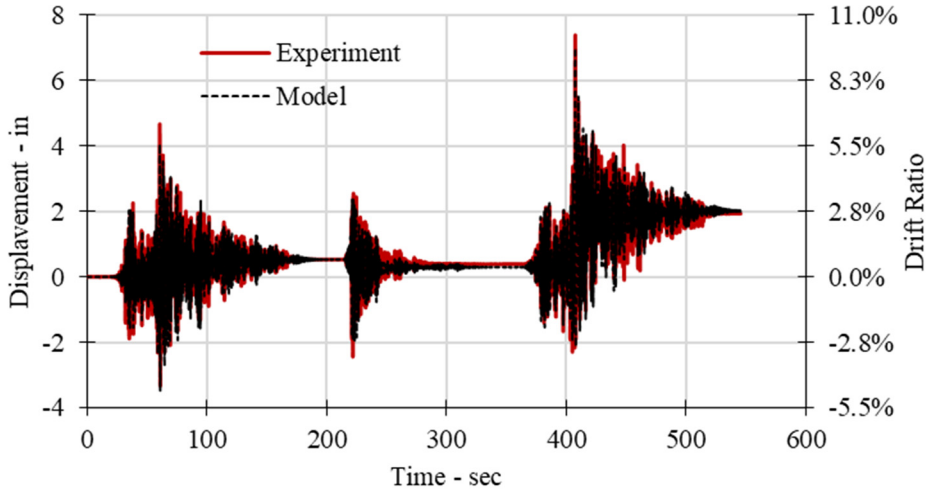

Figure 2.22 **Column LD-J2: comparisons of the experimental and model displacement history.**

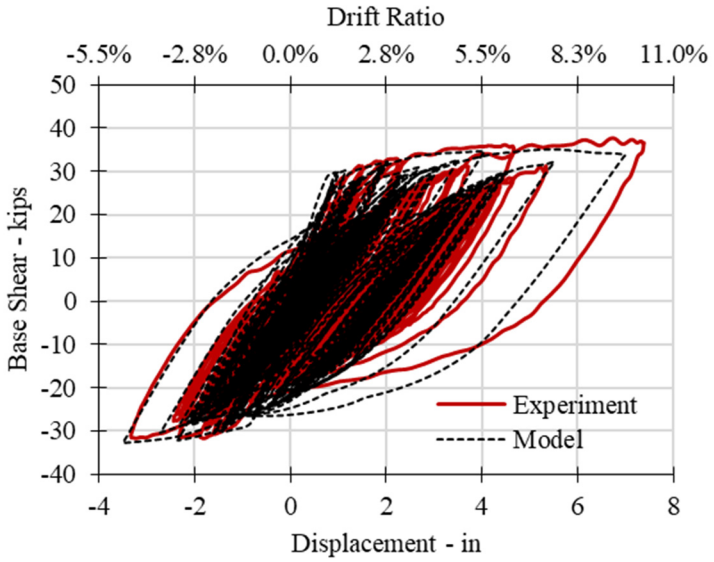

Figure 2.23 Column LD-J2: comparisons of the experimental and model force-displacement relationships.

2.4.4 Nonlinear Static Analysis

After calibrating the OpenSees model with previous experimental results, six models were developed for the specimens. Nonlinear static analysis, i.e., a pushover analysis, was conducted to determine the dominant failure mode, displacement capacity, and initial stiffness used in calculating the fundamental period of the columns. The pushover curves were idealized with an elastic-perfectly plastic response. The elastic portion of the idealized curve passed through the point marking the first yielding of the longitudinal column bars. The ultimate displacement (Δ_u) was defined as the point when the core concrete extreme fiber in the direction of loading reached 1.25 times the ultimate compressive strain (ε_{cu}) or when the strain in the reinforcing bar reached the expected ultimate strain (ε_{su}), 12%. The 25% increment in the ultimate concrete strain accounts for the underestimation of the maximum strain by the Mander's model, a factor that has been observed in previous bridge component tests [Johnson et al. 2006].

The idealized yield strength (F_y) and the displacement at effective yield (Δ_y) were determined by balancing the areas between the calculated and idealized pushover curves. The equivalent reinforcement fracture was the dominant mode of failure in the models. The pushover curves along with the idealized curves are shown in Figure 2.24. Table 2.17 and Table 2.18 show the results of pushover analysis for the columns in Phases I and II, respectively. The results showed that debonding the longitudinal bars resulted in 28% increase in the displacement ductility capacity of the column. Also, the columns with HSS demonstrated about 45% lower displacement ductility.

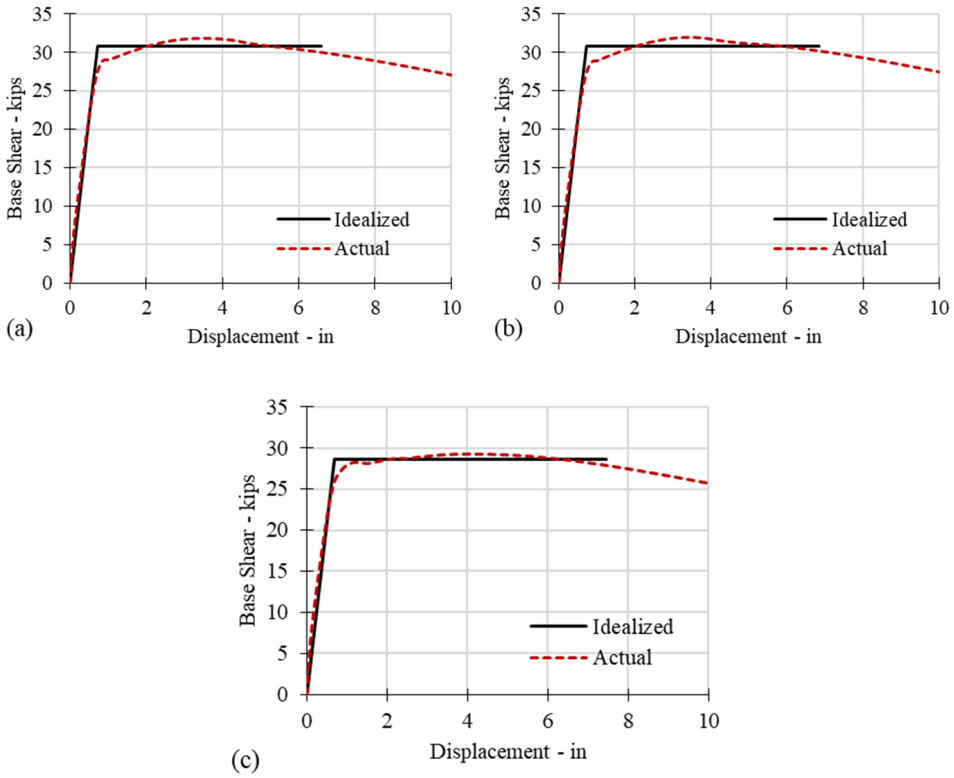

Figure 2.24 **Actual and idealized pushover curves for (a) LD-S3-G60; (b) LD-S1.5-G60; and (c) LD-S3-G60D.**

Table 2.17 Phase I results of pushover analysis.

Specimens	Yield disp. (in.)	Ultimate disp. (in.)	Disp. ductility	Plastic moment (kip/in.)	Effective stiffness (kip/in.)	Initial period (sec)
LD-S3-G60	0.72	6.53	9.05	2220	42.8	0.44
LD-S1.5-G60	0.73	6.74	9.23	2232	42.5	0.44
LD-S3-G60D	0.69	7.33	11.5	2112	42.1	0.44

Table 2.18 Phase II results of pushover analysis.

Specimens	Yield disp. (in.)	Ultimate disp. (in.)	Disp. ductility	Plastic moment (kip/in.)	Effective stiffness (kip/in.)	Initial period (sec)
LD-S1.5-G100	0.86	4.47	5.20	2,256	36.4	0.47
SD-S3-G100	0.85	4.32	5.08	2,210	36.1	0.48

2.4.5 Nonlinear Dynamic Analysis

Nonlinear dynamic response history analysis (NRHA) under a given loading protocol was conducted on the columns. The ground motions and initial loading protocol were adopted from the previous study by Mohammed et al. [2017]. This loading protocol was found to be appropriate for this study; see Section 2.5.1. The Park and Ang Damage Index (DI) [1985] was used along with experimental fragility curves to predict the seismic performance and damage states of the columns. This DI expresses seismic damage as a linear combination of the damage caused by the maximum deformation and the cumulative damage resulting from the repeated cycles as follows:

$$\mathrm{DI} = \frac{\delta_m}{\delta_u} + \beta \frac{\int E_h}{F_y \delta_u} \tag{2.6}$$

where δ_m is the maximum displacement demand for a specific damage state; δ_u is the ultimate displacement sustained by a column from an experimental; β is a non-negative parameter representing the effect of cyclic loading and taken as 0.15 [Fajfar 1992; Cosenza et al. 1993; Karim and Yamazaki 2001; and Hancock and Bommer 2007]; F_y is the yield force; and E_h is the dissipated hysteretic energy.

The Park and Ang DI was then correlated with five apparent damage states for bridge columns using the experimental fragility curves developed by Mohammed et al. [2017]. The experimental fragility curves were developed utilizing the data of over 25 bridge column models designed based on modern seismic design specifications and had been tested on shake tables or under lateral quasi-static loads. The considered damage states are as follows: minor spalling (M.S.); extensive spalling (E.S.); exposed reinforcement (E.R.); longitudinal bar buckling (B.B.); and longitudinal bar fracture (B.F.).

Figure 2.25 shows the experimental fragility curves considered for the assessment. The results of dynamic analyses and expected damage conditions for each column of Phases I and II in each run are summarized in Table 2.19 and Table 2.20, respectively. The results demonstrate that in Phase I, the two specimens without debonding detail are predicted to fail during run 3 (125% of the 2011 Tohoku earthquake). The failure of the specimens with debonding detail is expected to occur during run 4 (150% of 2011 Tohoku earthquake). Therefore, it was expected that the effect of debonding the longitudinal bars at interface of the column and footing would be more significant than reducing the transverse reinforcements spacing. For the Phase II columns, it was predicted to have first bar fracture during the third run (125% of the 2011 Tohoku earthquake) for the columns subjected to the long-duration motion. Column SD-S3-G100 under the short-duration motion was expected to sustain more demands and survive until run 4 (150% of the 2011 Tohoku earthquake) before failure. The accuracy of such predictions and associated modeling validity are assessed later in the study based on the experimental results. Chapter 7 provides such assessment as part of the post-test analysis.

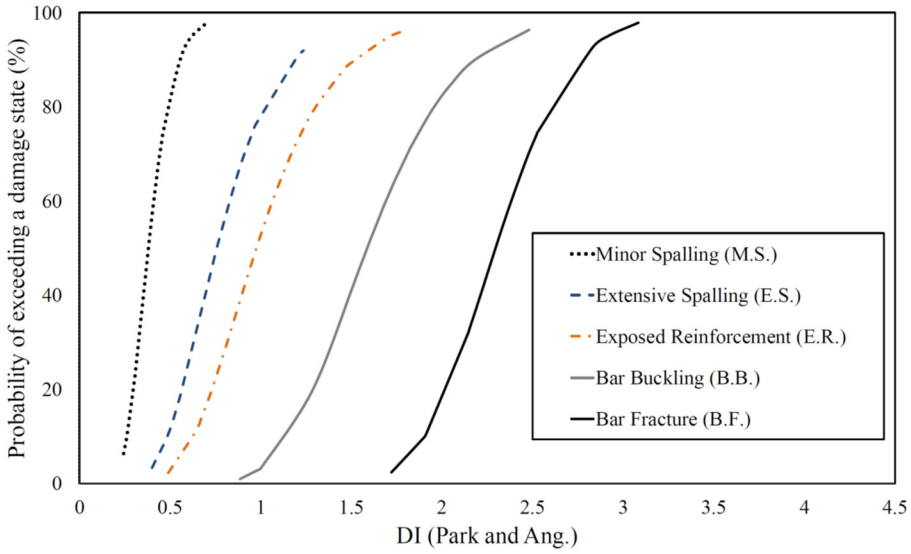

Figure 2.25 Experimental fragility curves correlating damage index (DI) with different damage states [Mohammed et al. 2017].

Table 2.19 Phase I: predicted performance of the test models.

Specimen	Run 1 (100%)[1]		Run 2 (AS)[2]		Run 3 (125%)[1]		Run 4 (150%)[1]	
	DI†	DS†	DI	DS	DI	DS	DI	DS
LD-S3-G60	1.3	80% E.R.‡	1.5	90% E.R.	2.8	95% B.F.	Not applicable	
LD-S1.5-G60	1.3	80% E.R.	1.4	85% E.R.	2.7	90% B.F.	Not applicable	
LD-S3-G60D	1.1	75% E.R.	1.2	75% E.R.	2.2	90% B.B.	>3	100% B.F.

[1] Tohoku EQ as the mainshock.
[2] An aftershock a month after the 2011 Tohoku earthquake.
† DI: Park and Ang DI; DS: Estimated Damage State.
‡ Minor Spalling (M.S.); Extensive Spalling (E.S.); Exposed Reinforcement (E.R.); Longitudinal Bar Buckling (B.B.); and Longitudinal Bar Fracture (B.F.).

Table 2.20 Phase II: predicted performance of the test models.

Specimen	Run 1 (100%)[1]		Run 2 (AS)[2]		Run 3 (125%)[1]		Run 4 (150%)[1]	
	DI	DS	DI	DS	DI	DS	DI	DS
LD-S1.5-G100	1.4	85% E.R.	1.6	95% E.R.	>3	100% B.F.	Not applicable	
SD-S3-G100	1.0	70% E.R.	1.2	80% E.R.	2.2	90% B.B.	2.8	95% B.F.
LD-S3-G100	1.5	75% E.R.	1.7	75% E.R.	>3	100% B.F.	Not applicable	

2.5 LOADING PROTOCOLS FOR SHAKE TABLE TESTS

2.5.1 Phase I: Columns with Conventional Steel

Based on the outcomes of the pre-test analyses, the same ground motion and loading protocol used by Mohammed et al. [2017] for testing column LD-J2, were deemed appropriate to use in Phase I of the experimental program. The 2011 Tohoku earthquake acceleration history recorded at MYG006 E-W station was selected as the main motion for the simulation in the shake table tests. This record was chosen because its response spectrum without any modifications or adjustments was close to the Crescent City response spectrum (2475-year return period) as the target spectrum. Additionally, the maximum displacement of the column imposed by the motion was expected to be about half the peak displacement capacity of the column (9.8 in), which imposes sufficient displacement demands while meeting the limits of the shake table. The time axis of the records was compressed by a factor of 0.577 ($\sqrt{1/3}$) corresponding to the square root of the dimensional scale length factor to account for the similitude requirements. The acceleration history of the 2011 Tohoku earthquake before and after time scaling is shown in Figure 2.26.

The loading protocol for all the columns in Phase I started with 100% of the 2011 Tohoku earthquake with significant duration (5–75%) of 58 sec, followed by an aftershock from the *Mw* 7.1 earthquake that occurred in Japan one month after the Tohoku earthquake. The PGA for the mainshock and the aftershock were 0.42*g* and 0.41*g*, respectively. Next, 125% and 150% of the mainshock were then applied to the test model. If failure did not occur up to the 150% run, an extra run at 160% of the main motion was also applied. The second test specimen with tight transverse reinforcement underwent the extra 160% run. Thus, for completeness and for the convenience of the reader, the actual loading protocols for each specimen are tabulated in Table 2.21.

In addition to the ground-motion tests, low-amplitude white-noise tests with frequency content from 0.5 Hz to 30 Hz were part of the loading protocol and conducted before each run and after the last seismic run for a frequency domain analysis to determine any changes in the fundamental period of the columns due to the progression of damage. The white-noise motions had a root-mean-square (RMS) acceleration of 0.015*g* and were applied to the columns over 70 sec.

Table 2.21 Phase I: loading protocol for shake table tests.

Specimen	LD-S3-G60	LD-S1.5-G60	LD-S3-G60D
Run 1	100% of Tohoku Earthquake		
Run 2	100% of Aftershock		
Run 3	125% of Tohoku Earthquake		
Run 4	150% of Tohoku Earthquake		
Run 5	Not Applicable	160% of Tohoku EQ	Not Applicable

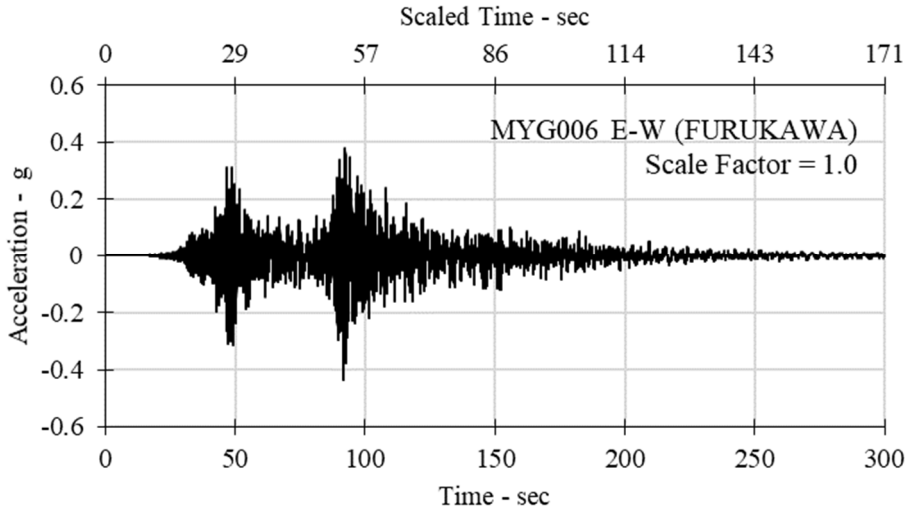

Figure 2.26 Acceleration history of the 2011 Tohoku earthquake recorded at MY006 station.

2.5.2 Phase II: Columns with High-Strength Steel

The columns in Phase II were tested under short- and long-duration motions to encourage research on cyclic deterioration and enrich the literature to help qualify the use of HSS reinforcement in seismic design of bridges. A similar loading protocol in terms of the mainshock/aftershock sequence and incremental mainshock ground motions was intended for two of the Phase II columns under long-duration motions and one column under short-duration motions. Unfortunately, the first two columns with HSS failed during the first run when tested under the 100% mainshock, requiring modification of the final column's loading protocol; the modified loading protocol used for the actual tests is explained here for convenience.

Column LD-S1.5-G100 was subjected to 100% of the 2011 Tohoku earthquake. Column SD-S3-G100 was tested under a short-duration motion recorded form 1999 Kocaeli earthquake at station IZN090. This motion was selected because its response spectrum is close to the Tohoku earthquake after modification by a factor of 3.68. Since the two first columns experienced bar ruptures during the first run, Column LD-S3-G100 was tested under a different sequence of the 2011 Tohoku earthquake to investigate damage progression in the column. The loading protocol started with 25% of the motion and incrementally scaled to 50% and 100% for the second and third runs, respectively. Table 2.2 lists the loading protocols used for each specimen in Phase II. More details about Phase II testing and HSS performance are discussed in following chapters. As for Phase I, before each run and after the last seismic run in Phase II, a white-noise test with frequency content from 0.5 Hz to 30 Hz was conducted to determine changes in the fundamental periods of the columns.

Table 2.22 Phase II: loading protocol for shake table tests.

Specimen	LD-S1.5-G100	SD-S3-G100	LD-S3-G100
Run 1	100% of Tohoku EQ	368% of Kocaeli EQ	25% of Tohoku EQ
Run 2	Not Applicable	Not Applicable	50% of Tohoku EQ
Run 3			100% of Tohoku EQ

3 Experimental Program Development

3.1 OVERVIEW

The design of the experimental test specimens was provided in Chapter 2. This chapter further describes the experimental program including the construction, actual material properties, instrumentation, and test setup of the columns test specimens in both phases. The entire process of construction as well as all material testing were conducted at the University of Nevada, Reno.

3.2 CONSTRUCTION

The two phases of the experimental program were conducted almost a year a part, and the construction of the columns done separately per phase. In each phase, three specimens were constructed in parallel following the same construction sequences. The specimens were constructed on a concrete slab outside EEL's fabrication yard at UNR. Construction of each specimen began by building the footing formwork followed by fabrication of the footing reinforcement cage and placement of 14 PVC pipes at specified locations. The PVC pipes were used for passing clamping threaded rods to securely attach the footing to the shake table. Four swift lift anchors were placed and fixed on two sides of each footing for the lifting of the specimens and transportation purposes. The reinforcing cages of the columns were constructed using a template board for alignment of the longitudinal bars and placed at the center of the footings.

For Column LD-S3-G60D (see Chapter 0 for details) the longitudinal bars were wrapped in 12-in.-long duct tape (out of this debonded length, 8 in. were inside the footing as shown in Figure 3.1). The spirals were then spaced and tied, and the strain gauge wires were grouped. Note: the reinforcing bars were carefully instrumented before the construction began. Subsequently, the concrete footings were cast. After casting of the concrete, the top surface was finished. Sonotubes were used for the column formwork. Four 3/4-in.-diameter rods were placed in the holes made on south and north sides of the columns at the specified locations to be used later for installation of the displacement transducers. Afterwards, the loading head formwork and the reinforcing cage were fabricated. Four PVC pipes were placed in the loading head for passing threaded rods. Concrete was then poured from the top of the columns. All concrete used in this project was provided by a local ready-mix concrete supplier. Curing blankets were used after placing the concrete to avoid shrinkage cracks. Since the concrete cover was relatively small, a maximum aggregate size of 0.375 in. was used. The formworks were removed after seven days. The various

stages of construction of the specimens are shown in Figure 3.2. The columns were whitewashed before the tests to help better locate and mark the cracks.

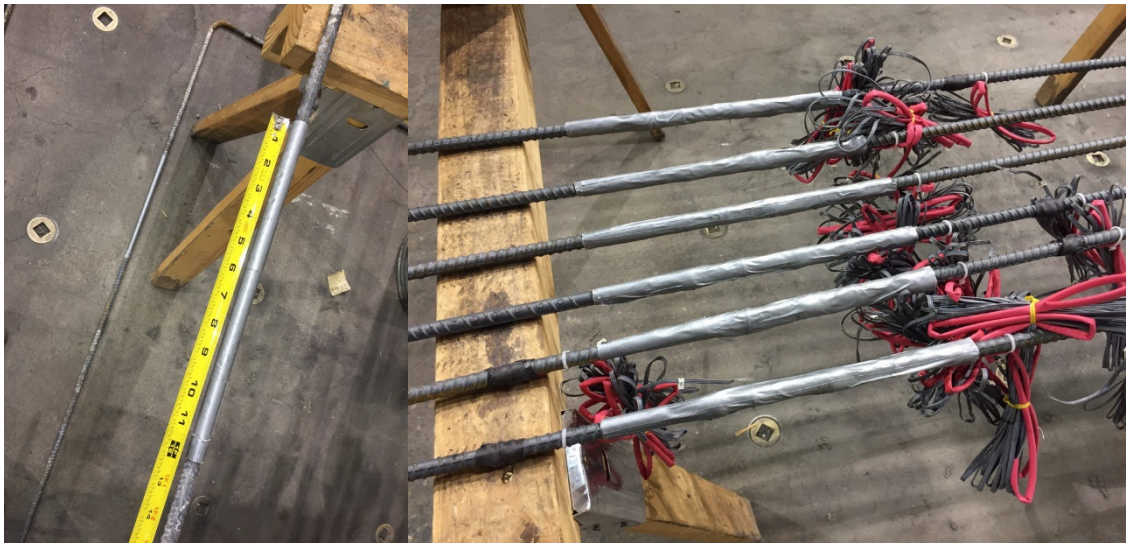

Figure 3.1 Column LD-S3-G60D: longitudinal bars debonded by duct tape.

Figure 3.2 Phase I: construction stages of the specimens.

3.3 MATERIAL PROPERTIES

Samples of the materials were taken during the construction and were tested to determine the actual mechanical properties of interest to assure that they were in the range of the expected properties. The reinforcing steel yield strain was determined to identify the yielding of the bars during the shake table tests. Furthermore, the actual concrete properties of the material on the days of testing were utilized to update the numerical models in the post-test analytical studies.

3.3.1 Reinforcement

All the columns in Phase I used Grade-60 longitudinal reinforcement, meeting the requirements of ASTM A706. Phase II columns were reinforced with Grade-100 longitudinal bars, meeting the requirements of ASTM A1035. All other reinforcement including spirals, footings, and loading head cages were Grade-60 ASTM A706. The actual stress–strain relationships for longitudinal bars and spirals were determined by conducting monotonic tension tests following ASTM A370. The samples were subjected to tension until rupture. The test setup is shown in Figure 3.3.

The force response of the bar was recorded during each test and divided by the nominal bar area to calculate stresses. Axial strains were measured using a high-resolution optical extensometer over an 8-in. gauge length per ASTM A370. The modulus of elasticity, yield strength, yield strain, tensile strength, tensile-to-yield strength (*T/Y*) ratio, uniform strain, and fracture strain were determined from the measured stress–strain relationships. The slope of the initial elastic region of the stress–strain curve was measured as the modulus of elasticity. Because the tested bars did not exhibit a clear yield plateau, the end of this elastic region was not clear for high-strength reinforcing bars. Thus, the yield stress and yield strain were calculated by the 0.2% offset method per ASTM E8. The maximum stress recorded in the test was considered as the ultimate tensile strength. The ratio of the ultimate tensile strength to the yield strength was taken as the tensile-to-yield strength ratio, i.e., *T/Y* ratio. The uniform strain is defined as the strain reached at the tensile strength. Finally, the fracture strain was measured just prior to loss of load-carrying capacity. Table 3.1 lists the measured properties of the longitudinal and transverse reinforcing steels. A comparison between the measured stress–strain relationship of the conventional and high-strength steel is shown in Figure 3.4.

Table 3.1 Reinforcing steel properties.

	f_y (ksi)	ε_y	E (ksi)	ε_{sh}	F_u (ksi)	T/Y	ε_u	f_f (ksi)	ε_f
Long. Gr60	72.3	0.0025	29000	0.0045	113.3	1.57	0.092	100	0.144
Long. Gr100	124*	0.0064*	28000	--	167	1.31	0.055	105	0.09
Transverse	70.0	0.0024	29000	--	95.0	--	--	--	0.105

* Defined by the 0.2%-offset method.

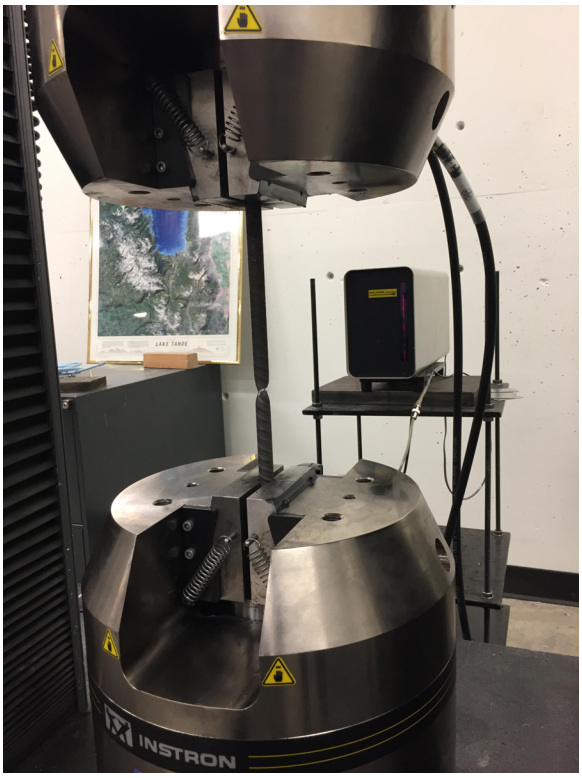

Figure 3.3 Reinforcing bar tensile test setup.

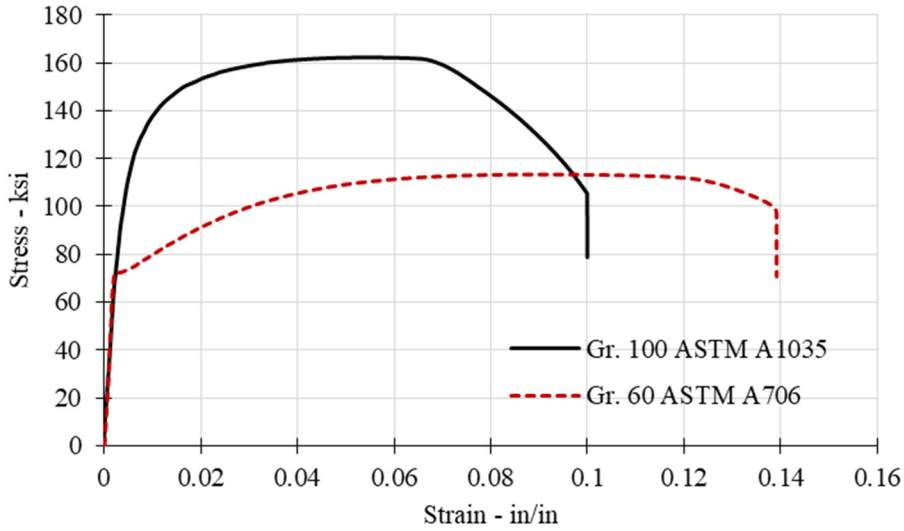

Figure 3.4 Stress–strain relationship curves for conventional and high-strength steel.

3.3.2 Concrete

As mentioned earlier, concrete was placed in two stages for each specimen: first the footing and then the column and loading head. The columns were designed for a specified and expected 28-

day compressive strength of 5000 and 6500 psi, respectively. The actual concrete compressive strength was determined by testing at least three 6 × 12 in. cylindrical samples at each age and test date per ASTM C39. The concrete was placed in a mold in three layers, and each layer was consolidated by rodding 25 times. The samples were tested at 7 days, 28 days, and the test day. To measure the concrete workability, a slump test was also conducted per ASTM C143 before each casting. Figure 3.5 shows the process of the slump test, and sampling and testing of the concrete coupons/specimens. Table 3.2 and Table 3.3. summarize the average measured 7-day, 28-day, and the test-day compressive strength data for the concrete poured in the footings and columns in both Phase I and II, respectively. Note: the test-day strength reported here were determined on the same day of the corresponding shake table test or on the day after if testing on same day was not possible.

Figure 3.5 **Photos of slump test, taking concrete samples, and a typical concrete cylinder compressive test.**

Table 3.2 **Phase I: concrete compressive strength.**

	7 days (psi)	28 days (psi)	Test day (psi)		
			107 days LD-S3-G60	120 days LD-S1.5-G60	126 days LD-S3-G60D
Column	3310	5240	7220	7510	7770
Footing	3180	4280	5920		

Table 3.3 **Phase II: concrete compressive strength.**

	7 days (psi)	28 days (psi)	Test day (psi)		
			86 days LD-S1.5-G100	93 days SD-S3-G100	100 days LD-S3-G100
Column	3620	4710	5260	5500	5600
Footing	2840	4400	5130		

3.4 INSTRUMENTATION

Various aspects of each specimen behavior were monitored using 65 channels of data from strain gauges, Novotechnik displacement transducers, string potentiometers, and load cells. High-definition video cameras were used to capture damage propagation. More details on the various utilized instrumentation and layout are presented below.

3.4.1 Strain Gauges

The channels included 26 strain gauges that were installed at seven levels, on six of the extreme northern and southern longitudinal bars, as illustrated in Figure 3.6 and Figure 3.7. The strain gauges were distributed and used to track the following: (1) the strain in the longitudinal bars, (2) the extent of yielding in the longitudinal bars, and (3) the length of the potential plastic hinge at the base of the column. In addition, three layers of strain gauges, including two strain gauges in each layer, were installed on the spiral. For completeness, the utilized strain gauges were of the type YEFLA-5-5LJCT distributed by Texas Measurements, Inc. These strain gauges are typically able to measure large and dynamic strains up to 15%.

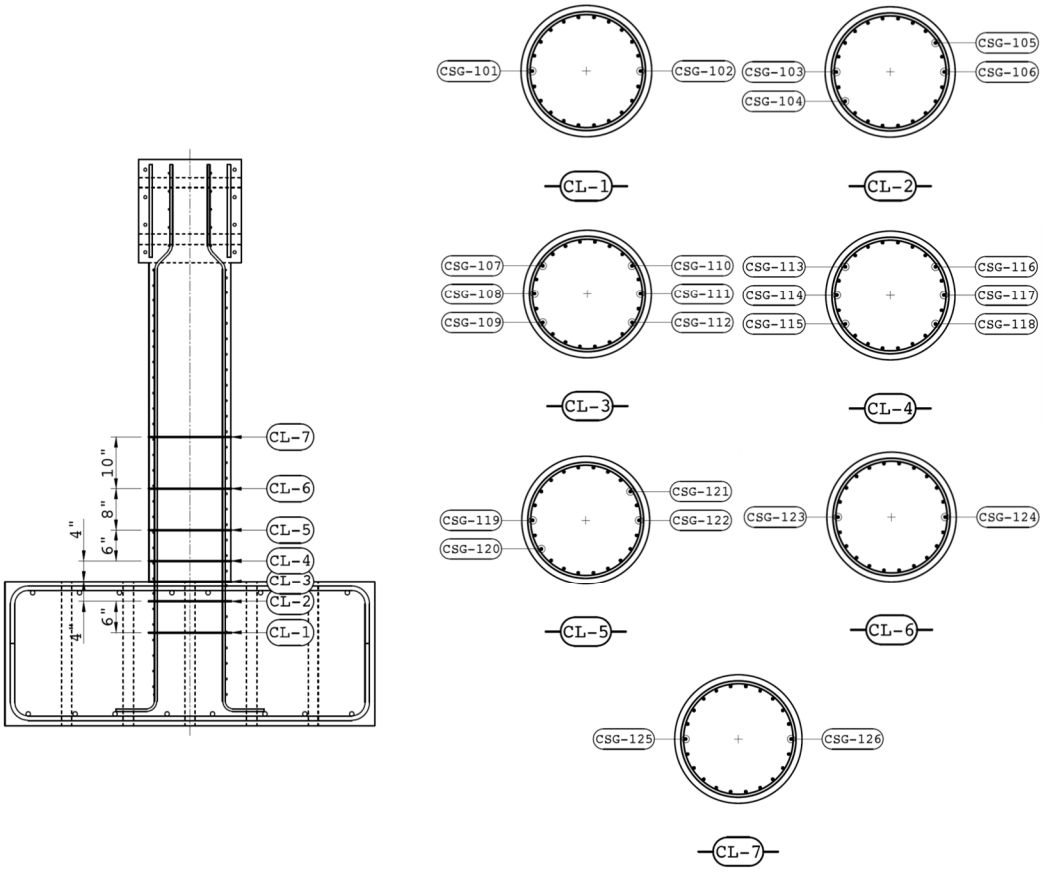

Figure 3.6 Phase I specimens: location of strain gauges on longitudinal bars.

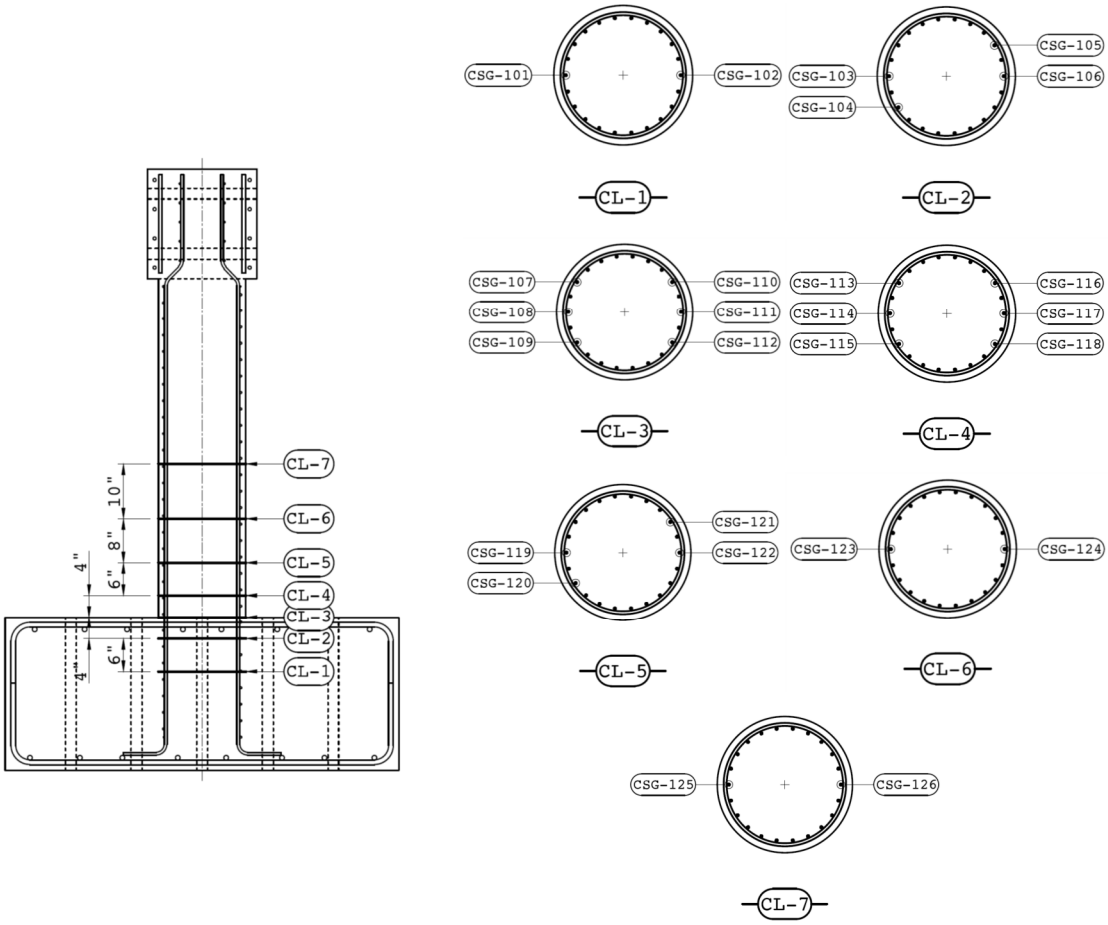

Figure 3.7 Phase II specimens: location of strain gauges on longitudinal bars.

The steps for installing the strain gauges on the longitudinal bars were per Mehrsouroush [2014] and Shoushtari et al. [2019b]. First, the ribs of the bars or threads of the threaded rods were ground using a sand belt to smoothen the gauge-bonding area. The ground surface was then sanded using a # 180 abrasive paper. Next, the bonding area was cleaned with cotton swabs soaked in a small quantity of acetone to remove any contamination. To glue the gauge, a piece of transparent tape was placed on the back of the gauge, and CN-Y adhesive was applied on the shiny face of the gauge. The strain gauge was placed in the specified location and fixed to the bar using the transparent tape. The gauge was then pressed down on the bar for approximately 60 sec until the adhesive had cured. After curing, the transparent tape was removed, and a piece of electrical tape was placed over the gauge. Then, the lead wire from each gauge wire was passed through a 1/8-in. (3.2-mm)-diameter heat shrink tube to protect it during construction. After looping the wire over the installation spot, the gauge was covered with multiple layers of electrical tape followed by a layer of mastic tape to protect the gauge against wet concrete, impact, and compacting vibrators during construction. Once all the gauges were installed, the wires were grouped using zip ties. Finally, the grouped wires were passed through a larger heat shrink tube. Figure 3.8 shows the steps of attaching strain gauges on the reinforcing bars.

Figure 3.8 Steps of attaching strain gauges on the reinforcing bars.

3.4.2 Displacement Transducers

Eight linear variable differential transformers (LVDTs), i.e., displacement transducers, were installed at four levels over the height of the columns over the north and south sides of the column body to estimate curvature and rotation along the plastic hinge. The transducers adjacent to the footing were of TR-50 series (shorter in length) and the others at higher levels were of TR-75 series (longer in length). The first transducer was placed approximately 2 in. higher than the footing surface, and the rest of transducers were spaced approximately 6 in. from centerline to centerline of the adjacent transducers; see Figure 3.9(a). Therefore, curvatures could be estimated at sections that vary from 1 in. to 17 in. above the surface of the footing. The summation of flexural and shear displacement as well as curvature could be calculated through kinematic matrix analysis using these transducers data for various points along the plastic hinge.

In addition, three string potentiometers were installed between the test model and a reference instrumentation frame to measure the absolute lateral displacements at the top of the column (center point of the loading head). The string pots were attached on the three corners of the loading head; see Figure 3.9(b). The column top relative displacement was determined by subtracting the table displacement from the absolute displacement. The table displacements were measured using internal transducers mounted onto the shake table actuators.

3.4.3 Load Cells and Accelerometers

To measure the lateral force on the column, a load cell was attached to the rigid link used to connect the column head to the mass rig, described next. Two load cells were placed on top of the spreader beam to measure the axial load on the column to help in the control of the axial load system. Three tri-axial accelerometers were placed on the footing, at the center of the loading head, and on the mass rig to measure the acceleration of the shake table and the column. The accelerometers were MEMS ADXL326 are capable of measuring–at the minimum– a full-scale range of ±16*g*.

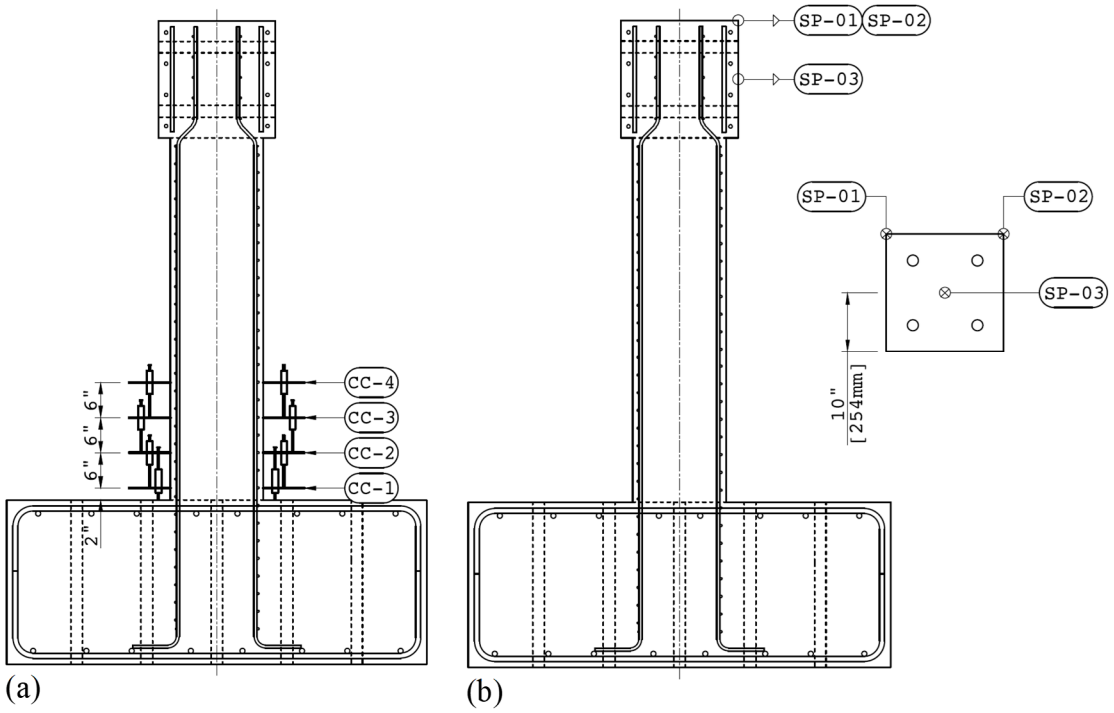

Figure 3.9 **Location of (a) displacement transducers and (b) string pots on the specimens.**

3.5 EXPERIMENTAL SETUP

The experimental setup on the shake table in both Phase I and II was identical. Figure 3.10 and Figure 3.11 show a schematic view and a photo of the actual test experimental setup from one of the specimens, respectively. The input ground motion was applied uniaxially in the north–south direction of the shake table. Columns were fixed to the footing but free at the top, as explained earlier. The footing was fixed to the shake table through 14 high-strength, 1-in.-diameter threaded rods. The column was centered and placed on the shake table, and a 1.5-in. gap between the footing and the table surface was filled by high-strength grout that was leveled out. The grout required a cure time of 48 hours before post-tensioning the high-strength rods to provide sufficient locking force between the table and the footing.

The specimen was attached laterally to a mass rig system that represented the inertia mass per Laplace et al. [1999]. The mass rig system was connected to the column head using a rigid link to apply the lateral force to the specimen. Four threaded high-strength rods were used to connect the head of the column to the rigid link. A constant axial load of 80 kips was applied on the column through a steel spreader beam, two hydraulic rams, an accumulator, and two threaded high-strength steel rods. Steel rods were connected to the hydraulic rams and extended through the PVC pipes in the footing and anchored beneath the footing. The hydraulic rams applied the axial load and the beam transferred it to the specimen in a self-equilibrating system. The accumulator was used to keep the axial load constant. Furthermore, the inertia mass was provided by three reaction blocks

weighing approximately 20 kips each in addition to the mass rig with an effective weight of 20 kips. The blocks were anchored to the mass rig using high-strength steel bars.

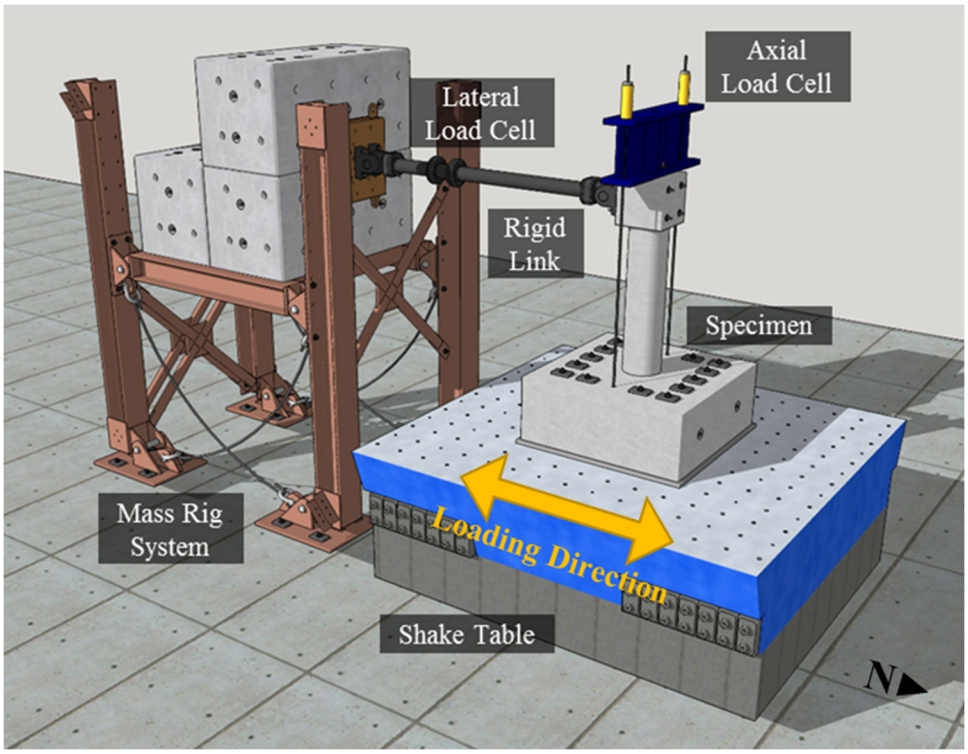

Figure 3.10 Schematic view of the experimental setup.

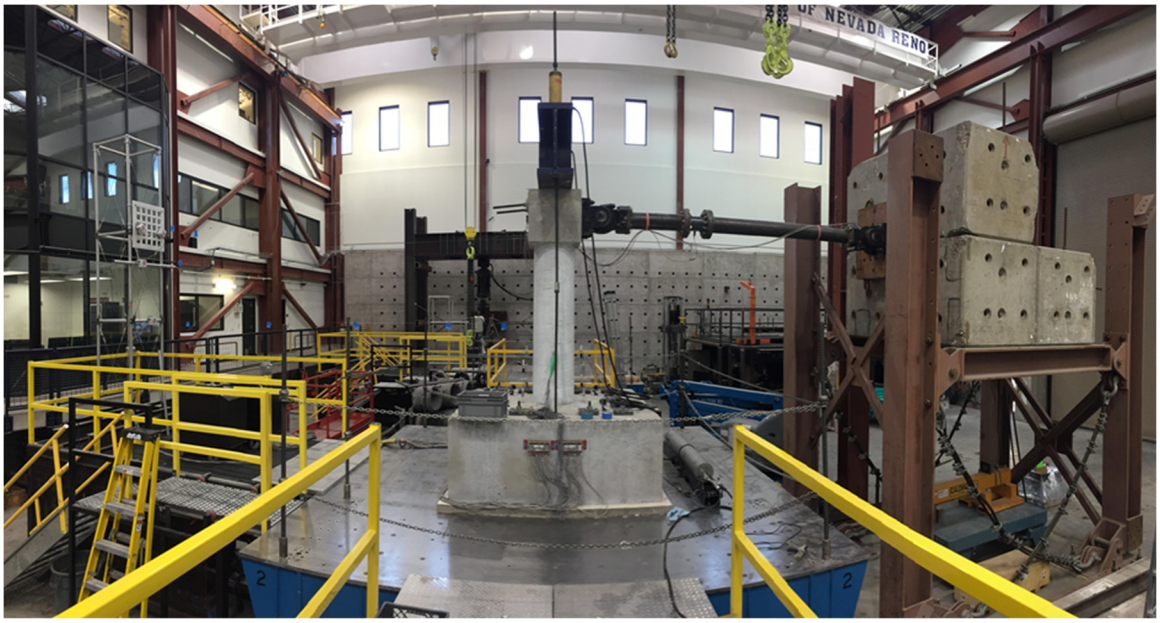

Figure 3.11 Overview of the actual experimental setup for one of the specimens.

4 Phase I: Experimental Results

4.1 OVERVIEW

The observed and measured results of the first phase of the experimental program are discussed in this chapter to analyze the response of the columns and assess their seismic performance. Phase I testing protocol included Columns LD-S3-G60, LD-S1.5-G60, and LD-S3-G60D. All three columns were tested on a shake table under the same loading protocol series based on the 2011 Tohoku long-duration earthquake. The loading protocol for all three columns began with 100% of the Tohoku mainshock earthquake followed by a 100% aftershock. The main motion was then incrementally amplified until failure occurred. The damage state of the test columns was tracked by visual observations at potentially critical locations during and after each run of earthquake motion. The data was collected using the instruments described in Chapter 3. Displacements, forces, strains, rotations, and curvatures were the key measured response factors discussed below. Several figures and tables are provided to summarize all the responses during each run for completeness.

4.2 DAMAGE OBSERVATIONS

To facilitate locating and marking cracks, the columns were painted with a thin layer of whitewash before placing the specimens on the shake table. The columns were monitored for any apparent damage due to construction, shrinkage, and temperature effects before starting the test. The initial cracks were marked with a purple crayon and labeled with number zero. Figure 4.1 through Figure 4.3 show a view of the expected columns plastic-hinge zones before starting the tests. During each run, four cameras monitored the progression of damage in the columns. The cameras were installed on the footing and were pointed toward the columns' plastic hinges. The damage was then visually inspected, and cracks were marked and labeled according to the run number after each run. Figure 4.4 through Figure 4.6 show the progression of damage in the columns after each earthquake run. Note that the photos were taken after each earthquake run. Therefore, live cracks that formed or had been active during a run that closed due to gravity loads are not available. As expected for cantilever members, extensive damage was concentrated at the columns' lower sections close to the base, i.e., plastic-hinge zone (lower north and south sides of the columns). The upper two-thirds of the columns remained damage free during the entire test sequence. Similar damage progression was observed for all three columns. The observed behavior of the individual columns

is discussed below. The footing and loading head were also examined for any damage during the test. No damage was detected except minor spalling on the footing of Column LD-S1.5-G60.

Figure 4.1 Column LD-S3-G60 before starting the test.

Figure 4.2 Column LD-S3-G60 before starting the test.

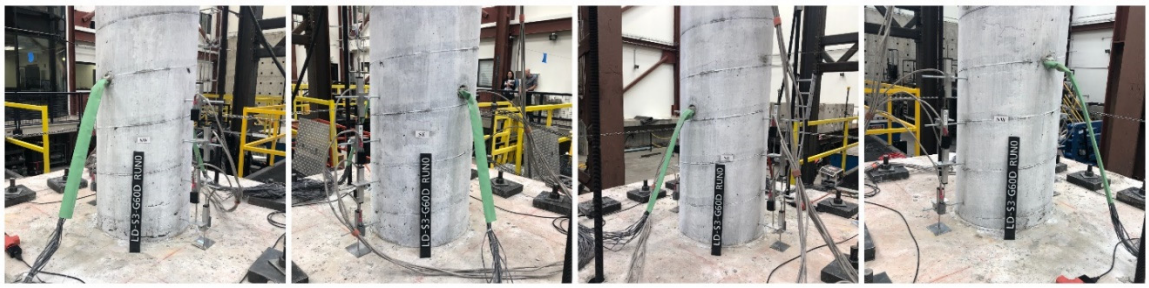

Figure 4.3 Column LD-S3-G60 before starting the test.

Figure 4.4 Column LD-S3-G60: progression of damage after each run.

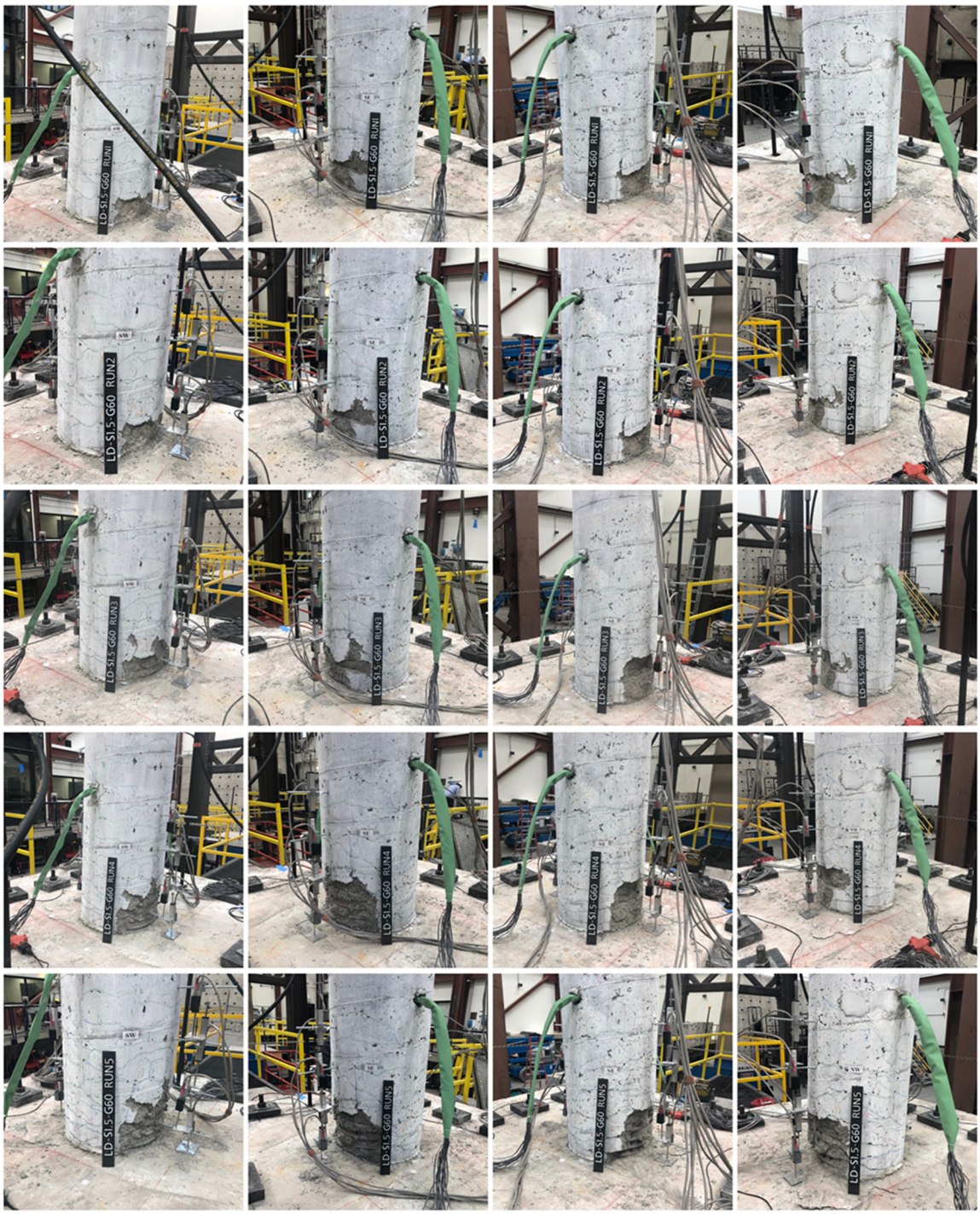

Figure 4.5 Column LD-S1.5-G60: progression of damage after each run.

Figure 4.6 Column LD-S3-G60D: progression of damage after each run.

4.2.1 Column LD-S3-G60

The damage in the Column LD-S3-G60 started with flexural cracks and yielding in the longitudinal reinforcement, followed by major spalling of the cover concrete on both south and north sides of the specimen during the first run (100% of main motion). The spirals were exposed on the north side. The height of spalling on the south and north sides was about 4 and 9.5 in., respectively. Cracks formed on the east and west sides of the column that extended to a height of approximately 25 in. No further damage was observed during the second run (aftershock). In the third run (125% of main motion), cover spalling increased to about 9 and 12 in. along the column height in the south and north sides, respectively. The core concrete damage started, the longitudinal bars were exposed on both sides, and four bars buckled on the north side. Finally, seven longitudinal bars– four bars on the north side and three bars on the south side –fractured in the fourth run (150% of main motion). At this point, the core concrete was severely damaged. Figure 4.7 presents the final damage state of Column LD-S3-G60 after the last run.

4.2.2 Column LD-S1.5-G60

Similar to the previous column, flexural cracks formed in Column LD-F1.5-G60, and longitudinal bars yielded during the first run (100% of main motion). Minor spalling of cover concrete occurred in the loading direction but was less than the spalling that occurred in the previous column. The

height of spalling on the south and north sides was about 4 and 6 in., respectively. After the aftershock (second run), no additional damage was observed in the column. During the third run (125% of main motion), spalling of the cover progressed along the plastic hinge, and a spiral was exposed. Cover spalling increased to about 6.5 and 8.5 in. along the column height on the south and north sides, respectively. After the fourth run (150% of main motion), no additional damage was sustained. Since the column had not experienced the full damage state, an additional run was performed at 160% of main motion. This fifth run caused exposure of the longitudinal bars and fracture of two bars; no buckling of the reinforcing bars was observed. Figure 4.8 presents the final damage state of Column LD-S1.5-G60 after the last run.

Figure 4.7 Column LD-S3-G60: final damage state.

Figure 4.8 Column LD-S1.5-G60: final damage state.

4.2.3 Column LD-S3-G60D

As occurred with the two previously tested columns, Column LC-S3-G60D experienced major spalling in the first and second runs (100% of main motion and aftershock). The height of spalling on the south and north sides was about 5.5 and 8 in., respectively. In the third run (125% of main motion), spalling progressed thorough the core concrete, longitudinal bars buckled, and two bars ruptured on two sides of the column. Since the bar fractures occurred after reaching the strongest

part of the motion, a fourth run @ 150% of main motion was applied. Four bars on the north side and four bars on the south side fractured in this run. Figure 4.9 presents the final damage state of Column LD-S3-G60D after the last run.

Figure 4.9 Column LD-S3-G60D: final damage state.

4.3 ACHIEVED MOTIONS

The achieved motions differed from the target ground motions, which is expected as a result of the interaction between the shake table and the specimen, as well as the closed-loop feedback used for control [Thoen and Laplace 2004]. The closed-loop control of the shake table works iteratively to correct for discrepancy between the target and feedback accelerations, but mostly for a specific range of frequencies dictated by the transfer function of the shake table. The parameters to evaluate the agreement between the target and achieved motions were the peak ground acceleration (PGA) and the spectral acceleration responses. The PGA values for the target and achieved motions for each test model and for each run are listed in Table 1.4. The parameters to compare the target and achieved motions were the ratio of the achieved to target PGA (Ach./Targ. PGA), and root mean square error of the spectral acceleration responses ($RMSE_{Sa}$); see Table 4.1. As shown in the table, the errors were higher for the first model tested. However, in the subsequent experiments, the achieved motions were closer to the target motions. Figure 4.10 through Figure 4.12 illustrate the comparisons of the response spectra of the shake table feedback accelerations for each column and in each run against the corresponding target spectra. Table 4.2 lists the target and achieved significant duration of the input motions in each run.

Table 4.1 Achieved and target motions characteristics.

Specimen	LD-S3-G60				LD-S1.5-G60					LD-S3-G60D			
Run #	1	2	3	4	1	2	3	4	5	1	2	3	4
Ach. PGA (g)	0.41	0.37	0.56	0.62	0.41	0.39	0.53	0.61	0.66	0.40	0.43	0.52	0.59
Targ. PGA	0.42	0.41	0.53	0.63	0.42	0.41	0.53	0.63	0.67	0.42	0.41	0.53	0.63
Ach./Targ.$_{PGA}$	0.98	0.90	1.06	0.99	0.98	0.95	1.01	0.97	0.98	0.95	1.05	0.99	0.94
RMSESa (g)	0.15	0.14	0.12	0.11	0.08	0.11	0.04	0.04	0.03	0.05	0.08	0.03	0.06

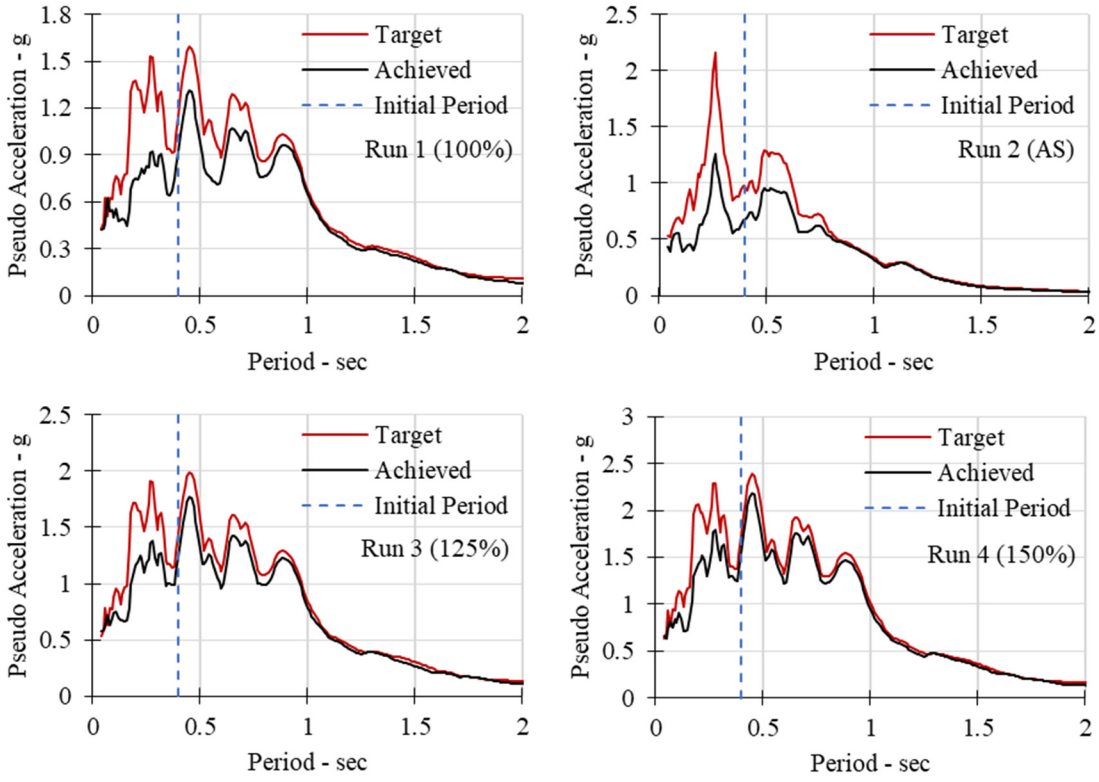

Figure 4.10 Column LD-S3-G60: achieved and target response spectra of each run.

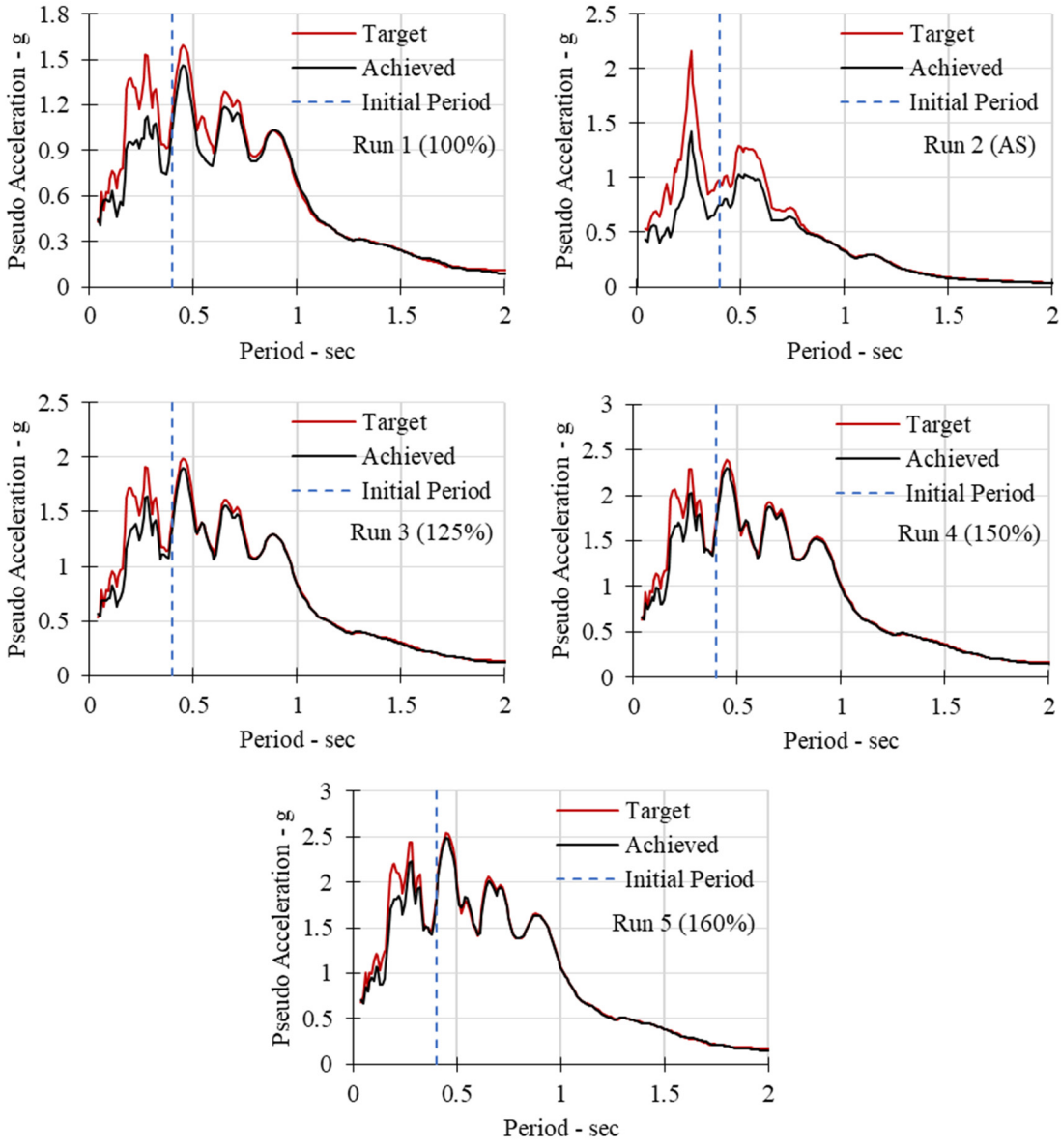

Figure 4.11 Column LD-S1.5-G60: achieved and target response spectra of each run.

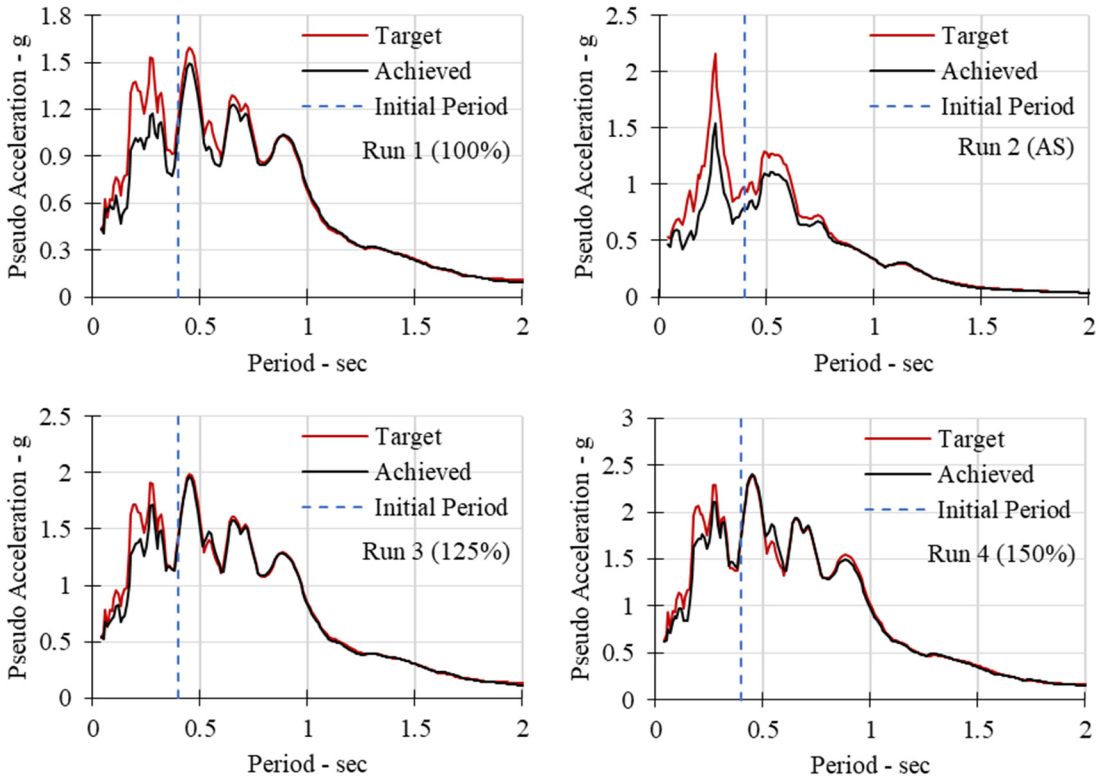

Figure 4.12 Column LD-S3-G60D: achieved and target response spectra of each run.

Table 4.2 Achieved and target significant duration of the motions.

Specimen	LD-S3-G60				LD-S1.5-G60					LD-S3-G60D			
Run #	1	2	3	4	1	2	3	4	5	1	2	3	4
Ds5-75% (sec)	35.1	4.6	33.5	33.4	33.8	4.6	33.2	33.4	33.3	33.5	4.6	33.0	32.9
Ds5-95% (sec)	67.4	13.4	66.7	63.7	65.8	11.8	63.6	63.8	62.8	65.8	10.9	62.6	61.7

Target significant durations: Main motion Ds5-75% = 32.9 sec; Ds5-95% = 61.6 sec
Aftershock Ds5-75% = 4.6 sec; Ds5-95% = 9.4 sec

4.4 DISPLACEMENT

The absolute lateral displacement of the column at the centerline of the loading head was measured using three string potentiometers attached to the corners of the loading head north face. The relative displacement—hereafter referred to as column displacement—was determined by subtracting the shake table displacement from the absolute displacement. Figure 4.13 through Figure 4.15 show the histories of the column displacement for each specimen during each run. The positive values correspond to displacement toward the south. Drift ratios were determined by the lateral displacement values divided by the column height. The peak displacements of the columns, their

respective drift ratios, and residual drift ratios in each run are listed in Table 4.3, where the peak drift ratios, i.e., drift capacity, for Columns LD-S3-G60, LD-S1.5-G60 and LD-S3-G60D are 8.94%, 13.9%, and 11.1%, respectively. The peak drift ratios in each run, as well as displacements using double axis, are also shown in Figure 4.16 for better comparison. It is evident that the second specimen with higher confinement represents the greatest displacement capacity. The third column also demonstrated higher displacement capacity compared to the first column as a result of the debonding of the longitudinal bars.

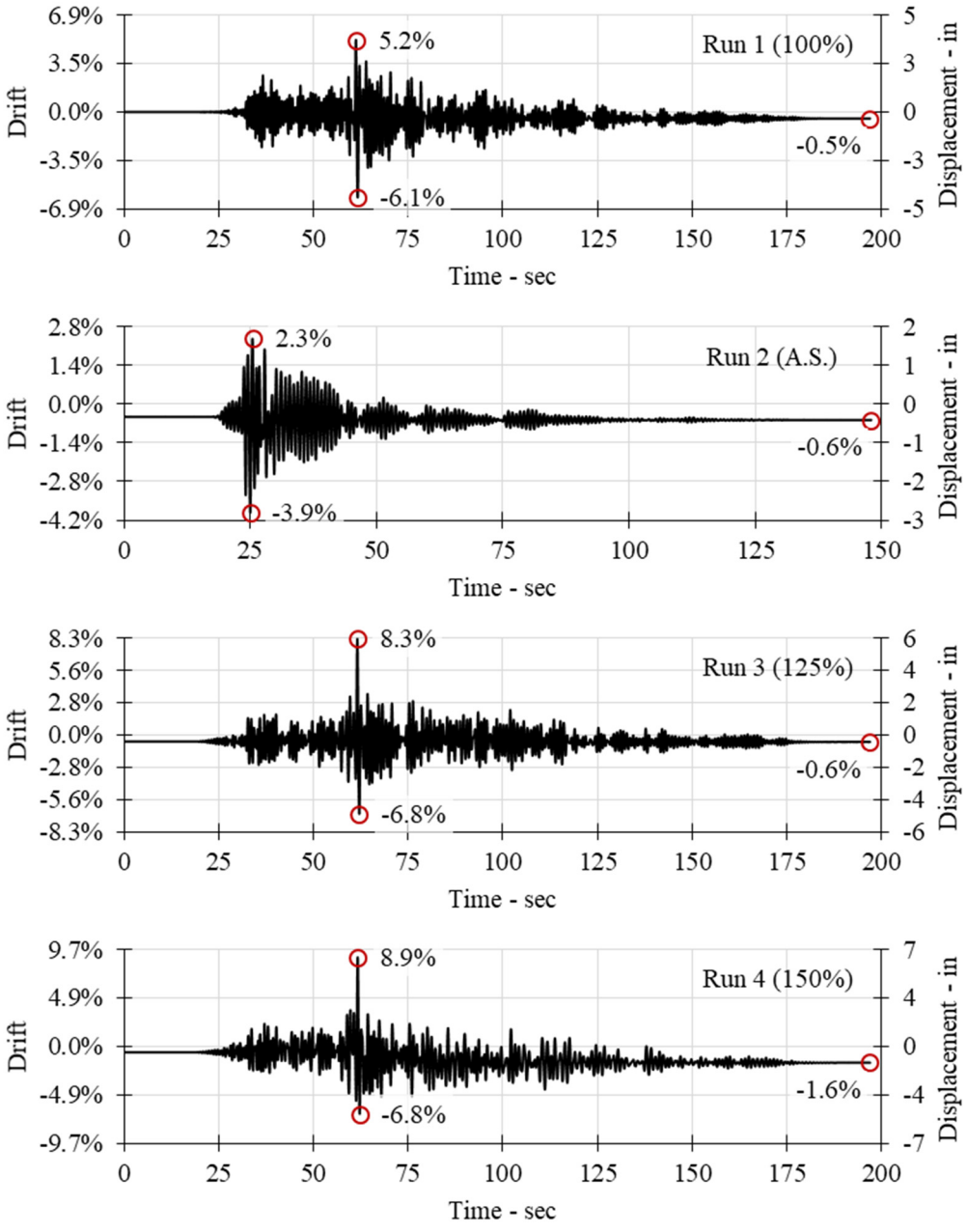

Figure 4.13 Column LD-S3-G60: displacement history in each run.

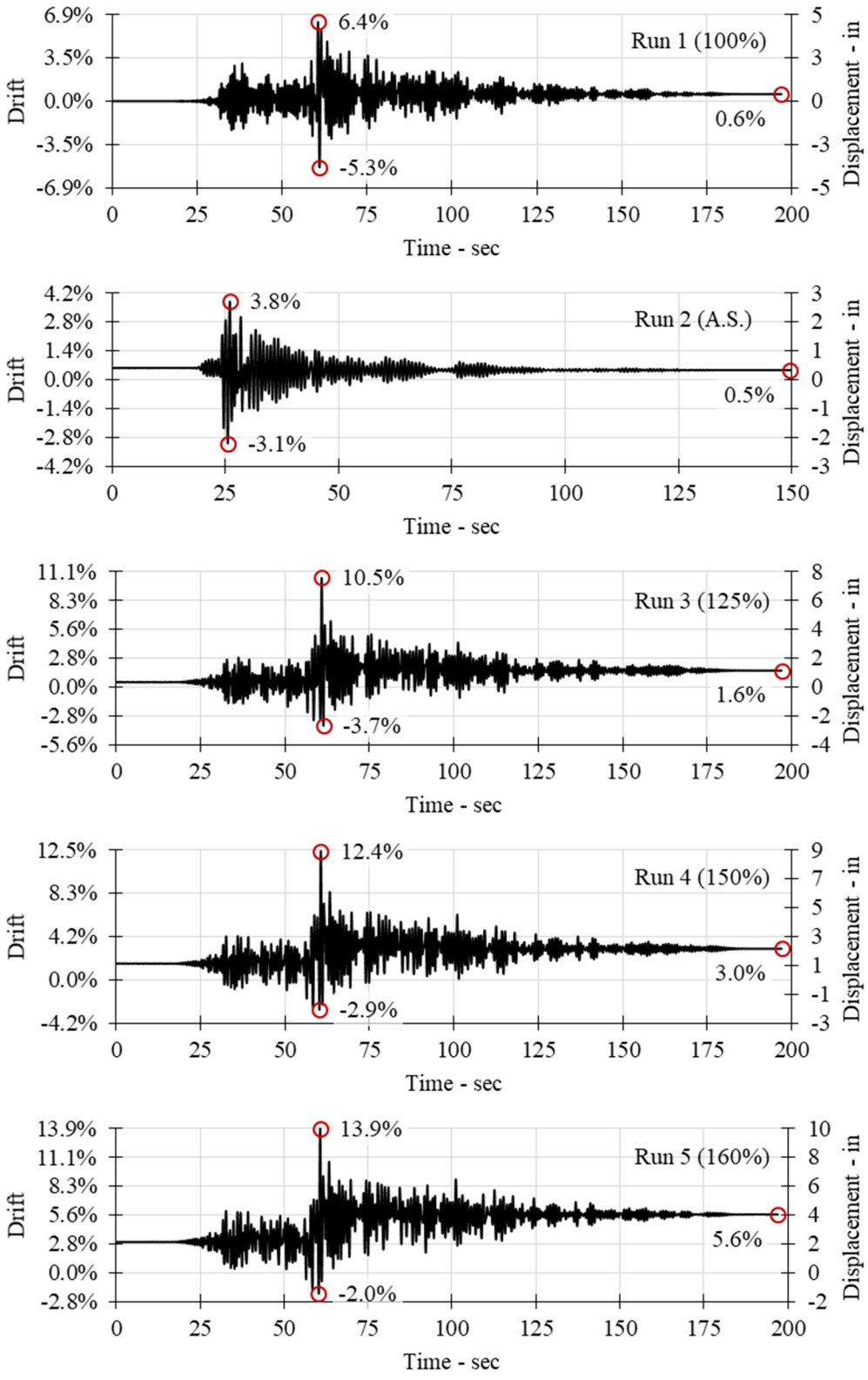

Figure 4.14 Column LD-S1.5-G60: displacement history in each run.

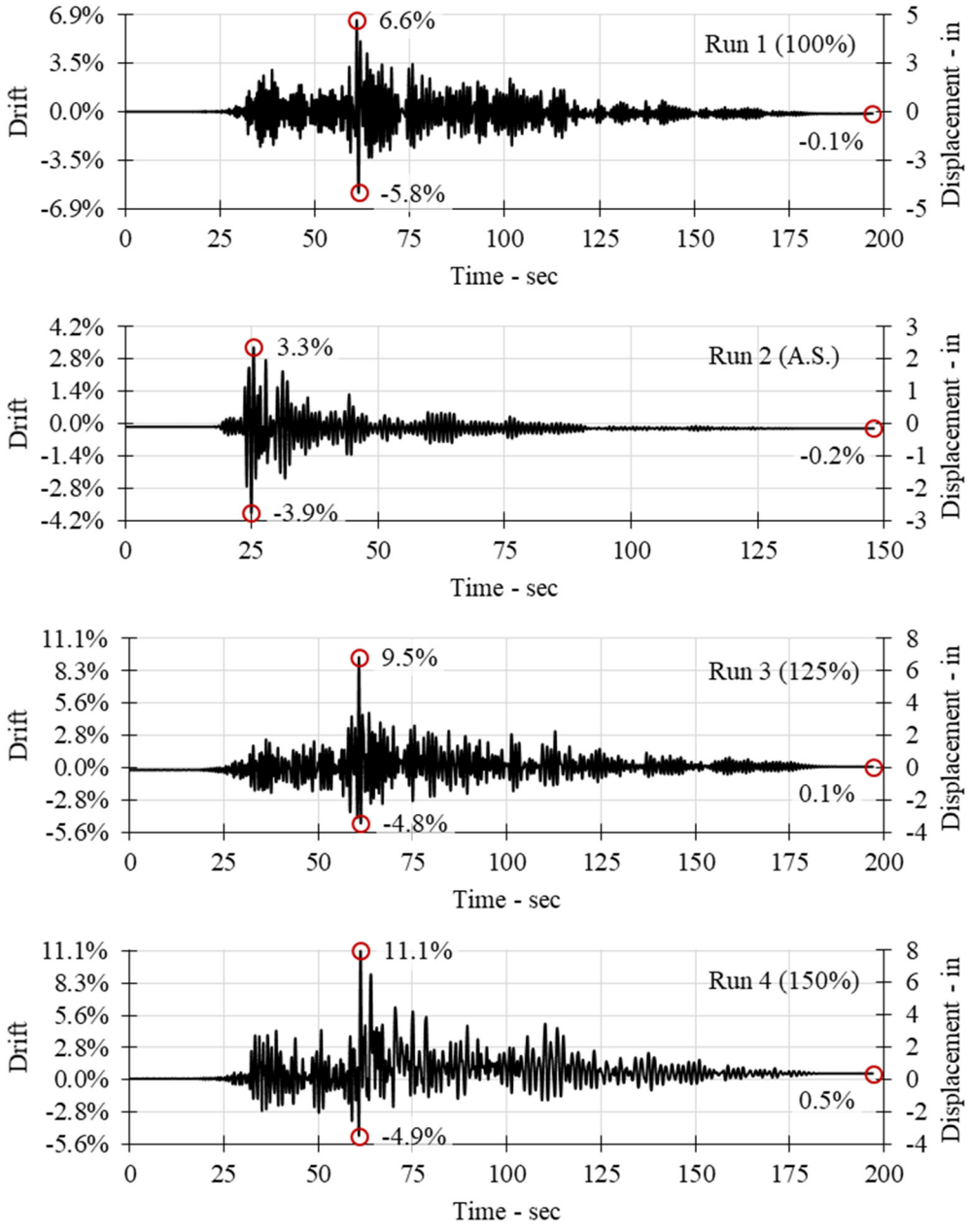

Figure 4.15 Column LD-S3-G60D: displacement history in each run.

Table 4.3 Peak responses of the columns in each run.

Specimen	LD-S3-G60				LD-S1.5-G60					LD-S3-G60D			
Run #	1	2	3	4	1	2	3	4	5	1	2	3	4
Peak disp. (in.)	4.41	2.80	5.95	6.44	4.57	2.71	7.56	8.93	10.0	4.72	2.77	6.83	7.99
Peak drift (%)	6.13	3.89	8.27	8.94	6.35	3.76	10.5	12.4	13.9	6.56	3.85	9.48	11.1
Res. drift (%)	0.47	0.57	0.59	1.18	0.57	0.46	1.58	2.99	5.60	0.14	0.22	0.07	0.53
Peak base shear (kips)	35.7	25.1	38.8	36.7	35.4	26.1	36.1	35.9	35.6	33.6	26.0	33.4	21.1
Peak bending moment (kip.ft)	214	151	233	220	212	157	217	215	214	202	156	200	127

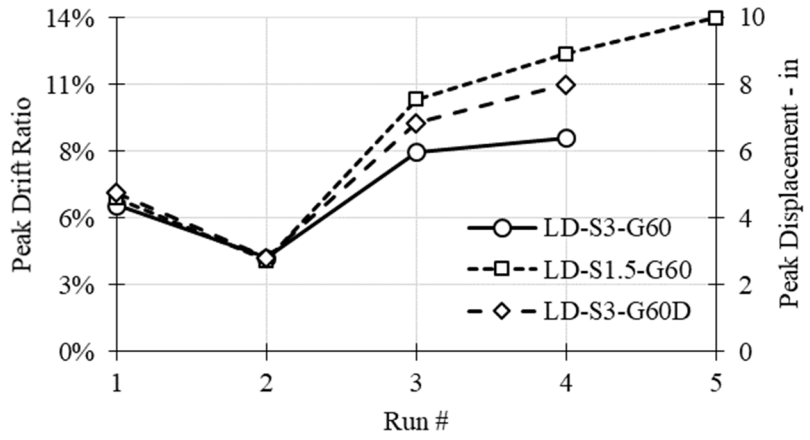

Figure 4.16 Peak drift ratios (displacements) of the columns in each run.

4.5 BASE SHEAR

Since the columns behaved like a single-degree-of-freedom structure, the base shear was measured directly from the load cell located on the mass rig link. This force was also used to calculate the column bending moment. The histories of the three columns base shear are shown in Figure 4.17 through Figure 4.19, respectively. The peak base shear and bending moment values observed for each of the columns in each run are also listed in Table 4.3 and shown in Figure 4.20 for better comparison. The maximum observed load values, i.e., force capacities, of the three columns were 38.8, 36.1, and 33.6 kips, respectively.

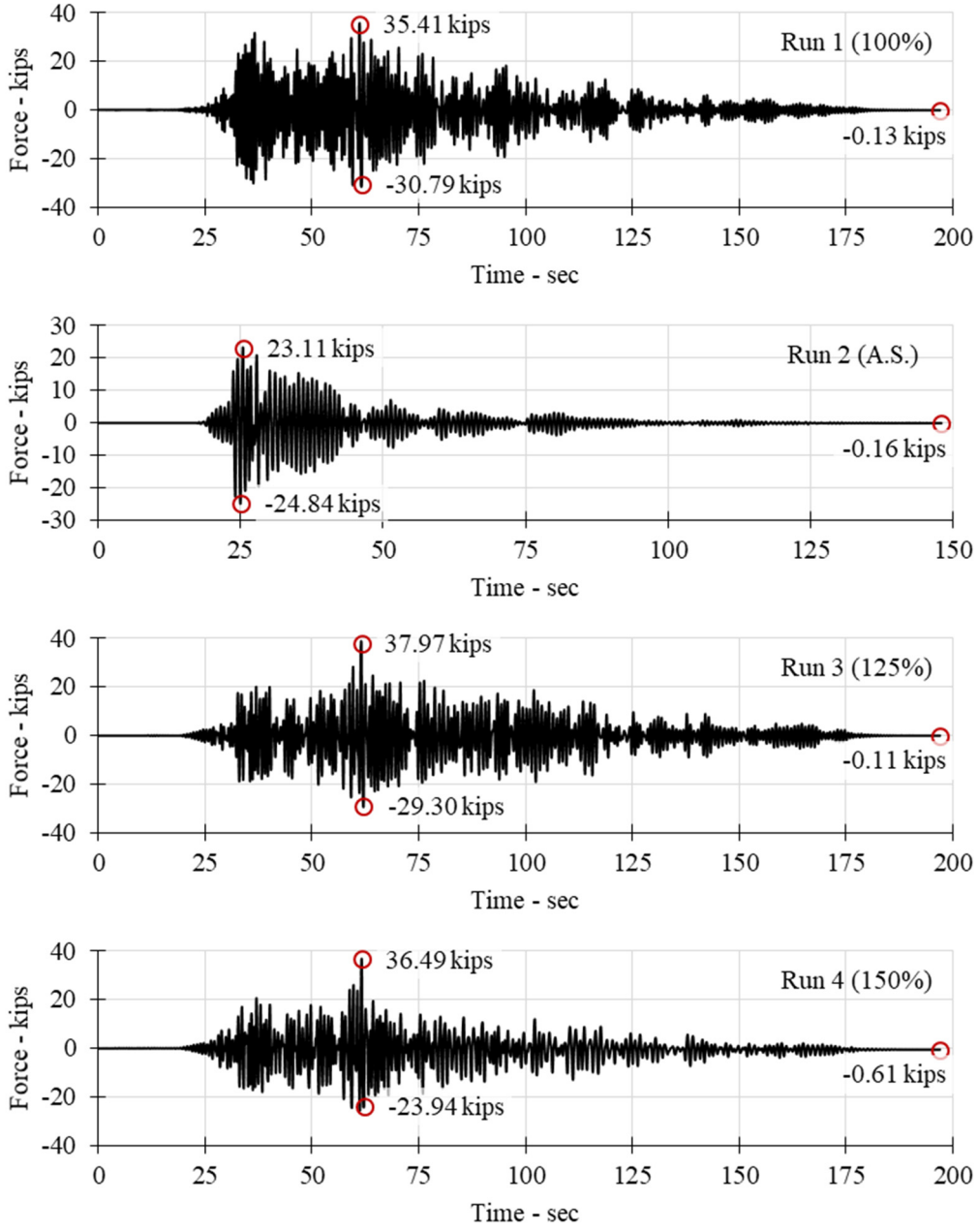

Figure 4.17 Column LD-S3-G60: base shear history in each run.

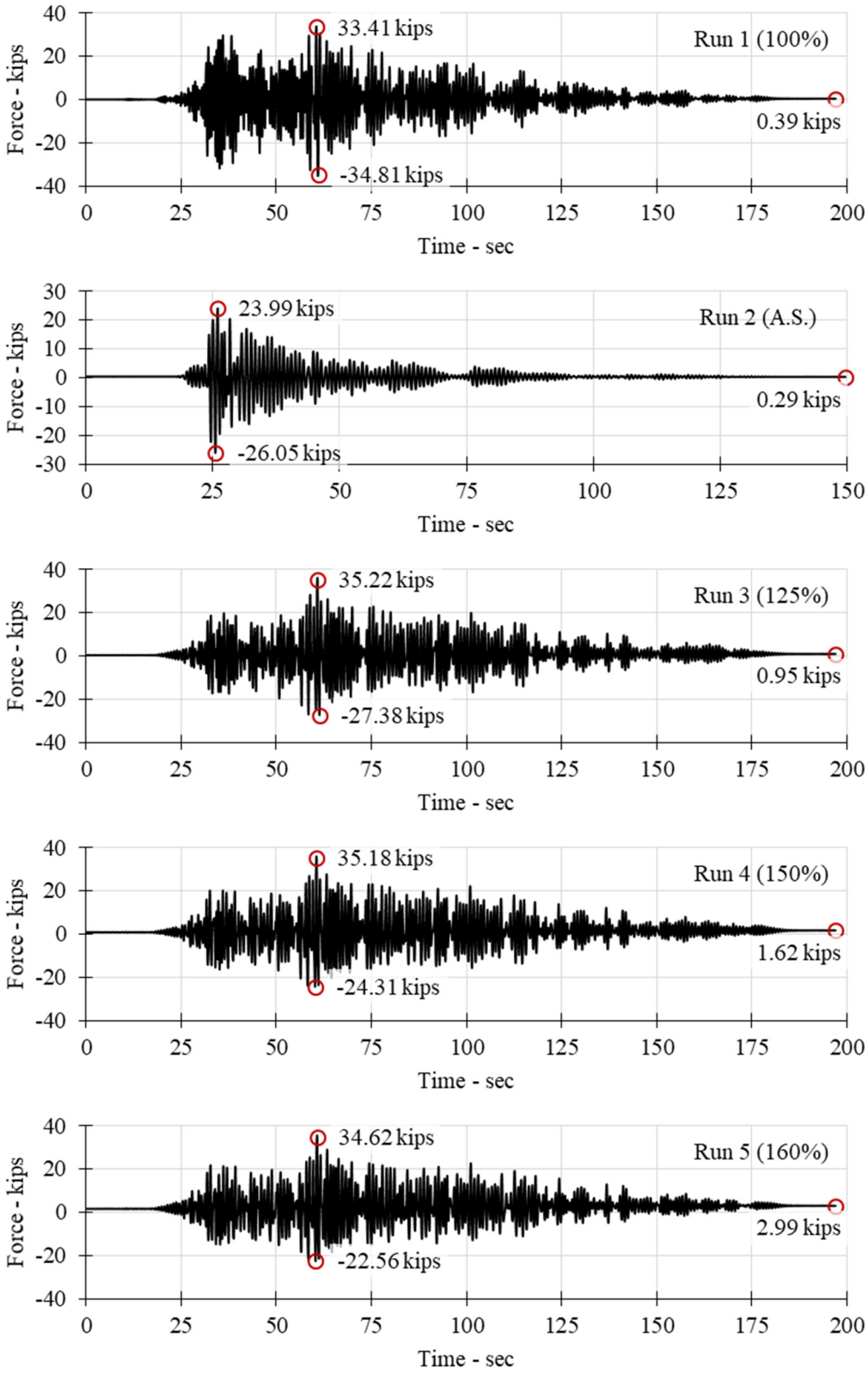

Figure 4.18 Column LD-S1.5-G60: base shear history in each run.

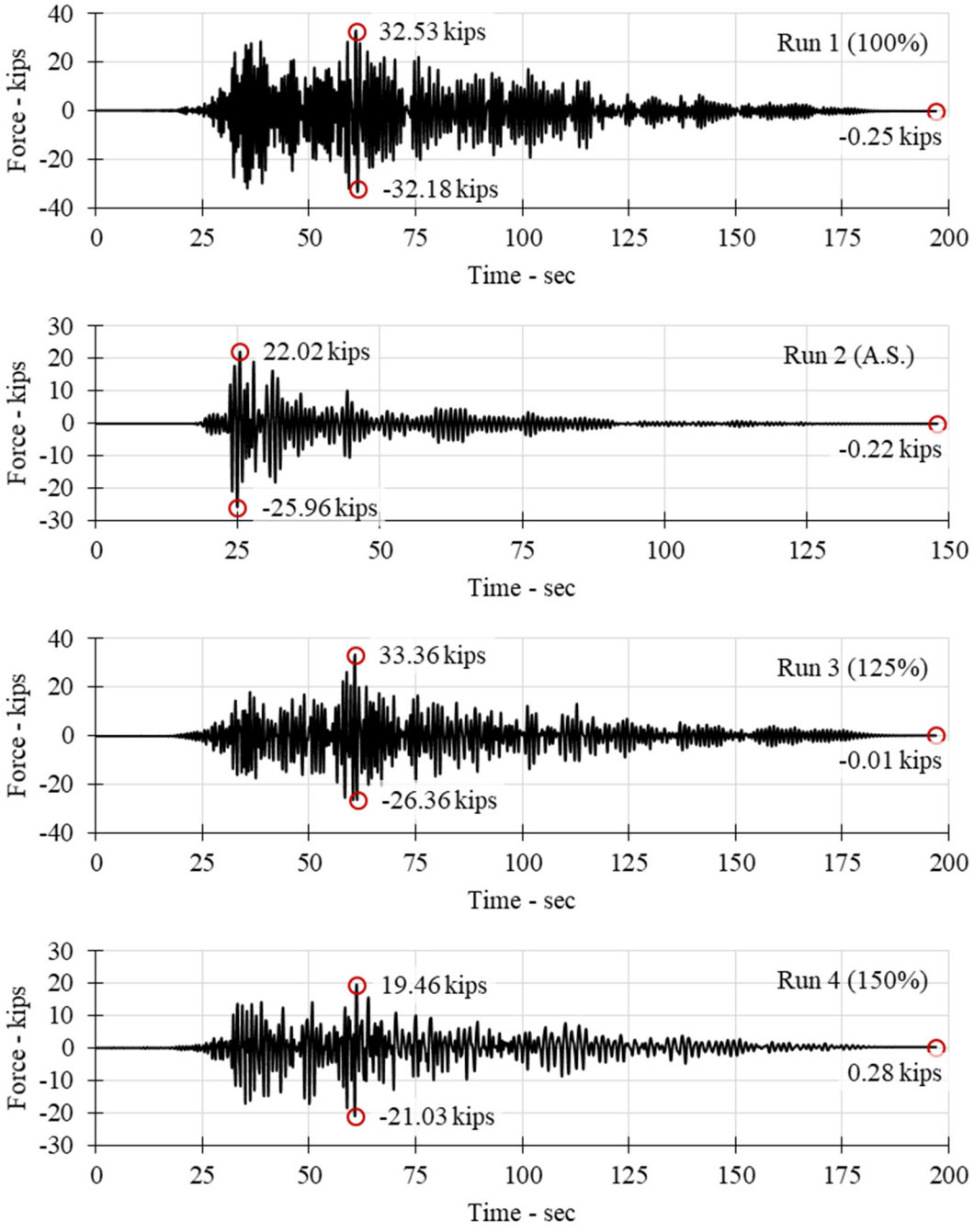

Figure 4.19 Column LD-S3-G60D: base shear history in each run.

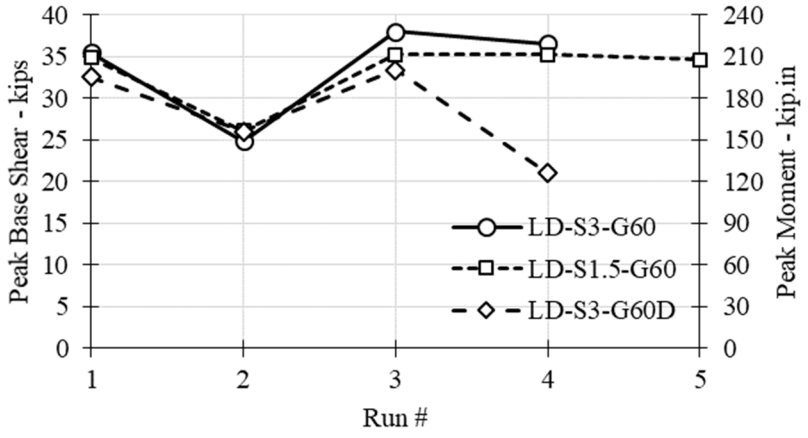

Figure 4.20 Peak base shears and bending moments of the columns in each run.

4.6 FORCE-DISPLACEMENT RELATIONSHIPS

The hysteresis relationship between the columns base shear and displacement was studied to assess the overall global and seismic behavior of the columns. Figure 4.21 through Figure 4.23 illustrate the force-displacement relationship of the three specimens from all runs. The positive values correspond to displacement toward the south. The measured envelopes of the cumulative hysteresis curves were idealized by elastoplastic curves passing through the first column longitudinal bar yielding and adjusted to preserve energy. The latter was accomplished by balancing the areas between the actual and idealized curves to preserve energy [AASHTO 2014]. Figure 4.24 represents the cumulative force-displacement relationship of the columns along with the envelopes and their respective idealized curves. The stable and wide hysteresis loops in all three columns indicate good energy dissipation and desirable ductile behavior. The accumulated dissipated energy during all runs for each column is presented in Figure 4.25. The dissipated energy was determined by calculating the area enclosed by every loop in the force-displacement relationships of the columns. The measured dissipated energy for all columns after each run is listed in Table 4.4 where the dissipated energy was similar for the three columns before the onset of the bar fracture, causing a drop-in energy.

The idealized curves were used to calculate the displacement ductility and the initial effective stiffness for further assessment. The displacement ductility was obtained by dividing the ultimate column drift ratio to the effective yield drift ratio. The first yielding of the longitudinal bars occurred at drift ratios of 1.03% for Column LD-S3-G60, 1.10% for Column LD-S1.5-G60, and 1.18% for Column LD-S3-G60D. The ultimate drift ratios determined based on the onset of the first bar fracture were 8.9%, 13.9%, and 9.6% for the three columns, respectively. The effective yield drift ratios were 1.6%, 1.7%, and 1.8%, respectively. Therefore, the displacement ductility of the three test models were estimated to be 5.60, 8.14, and 5.35, respectively. The slope of the elastic branch of the idealized curve was considered as the initial effective stiffness of the columns, resulting in 30.3, 27.2, and 24.4 kip/in. for the three columns, respectively. The results of ductility analysis of the columns are also tabulated in Table 4.5.

Table 4.4 Energy dissipation of the columns in each run.

Specimen	LD-S3-G60				LD-S1.5-G60					LD-S3-G60D			
Run #	1	2	3	4	1	2	3	4	5	1	2	3	4
Dissipated energy (kip. ft)	92	109	219	320	94	111	224	363	511	91	104	187	242

Table 4.5 Ductility capacity of the columns.

Specimen	LD-S3-G60	LD-S1.5-G60	LD-S3-G60D
Yield drift (%)	1.6	1.7	1.8
Ultimate drift (%)	8.9	13.9	9.6
Ductility	5.60	8.14	5.35

4.7 PARK AND ANG DAMAGE INDEX

The Park and Ang DI [1985] was used to quantify the seismic damage in the columns. This damage index is defined as a linear combination of the damage caused by the maximum deformation [the first term in Equation (4.1)] and by the cumulative damage resulting from the repeated cycles [the second term in Equation (4.1)].

$$\mathrm{DI} = \frac{\delta_m}{\delta_u} + \beta \frac{\int E_h}{F_y \delta_u} \tag{4.1}$$

where δ_m is the maximum displacement demand for a specific damage state; δ_u is the ultimate displacement sustained by a column from an experiment and taken as 9.8 in. [Phan et al. 2005), β is a non-negative parameter representing the effect of cyclic loading and taken as 0.15 [Fajfar 1992; Cosenza et al. 1993; Karim and Yamazaki 2001; and Hancock and Bommer 2007]; F_y is the yield force and taken as 25 kips from the current test results; and E_h is the dissipated hysteretic energy.

The DI was calculated for each specimen and after each run. The probability of damage for each column and after each run were obtained through using the calculated DI along with the experimental fragility curves; see Chapter 2. In addition, the probability of damage was compared with the actual damage that occurred in the columns. Table 4.6 lists the calculated DI, actual damage, and probability of damage from the fragility curves. Note: although the probability of damage correlated well with the actual damage in Columns LD-S3-G60 and LD-S3-G60D, the calculated DI overestimated the probability of damage for Column LD-S1.5-G60.

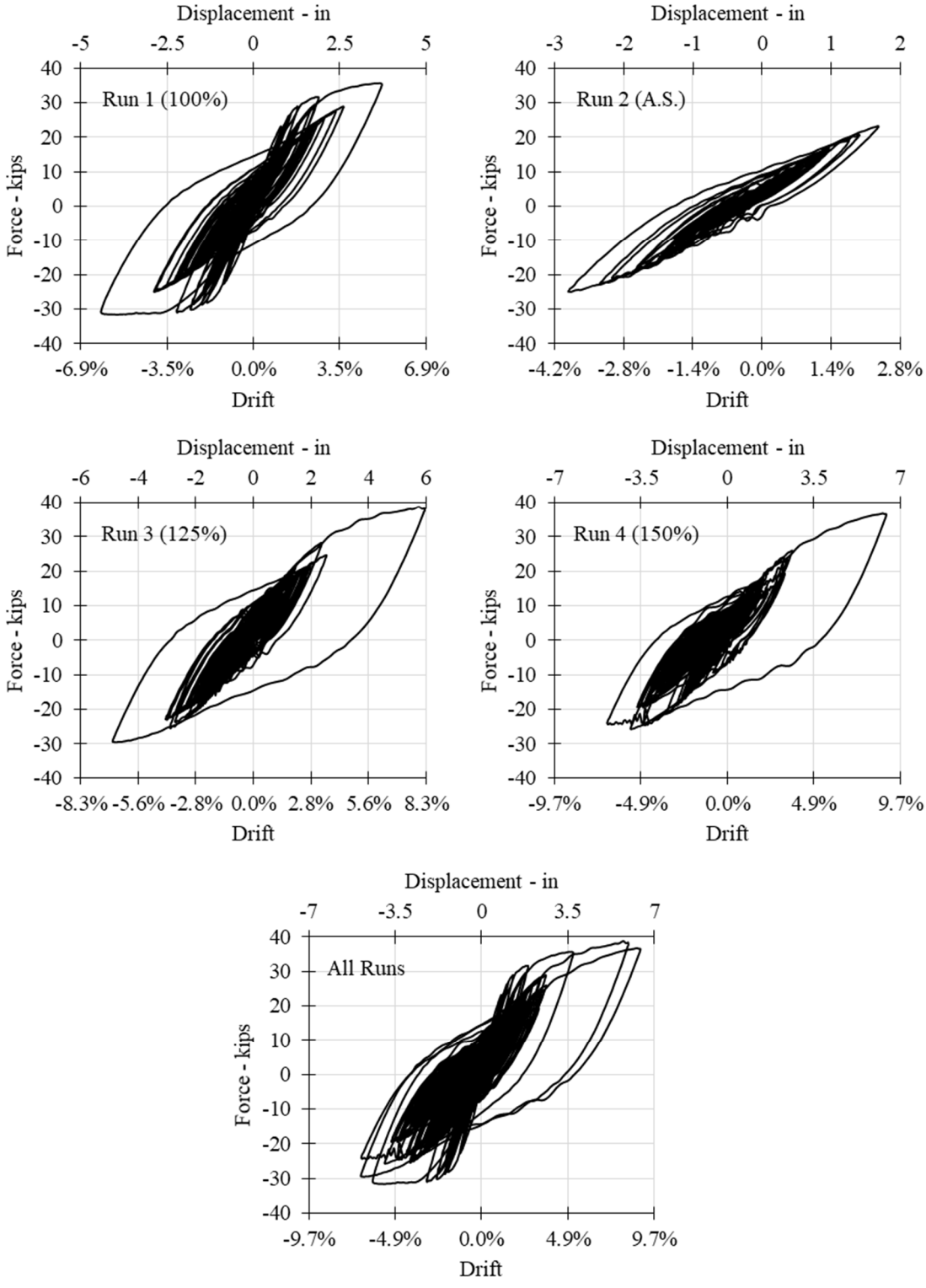

Figure 4.21 Column LD-S3-G60: force-displacement hysteresis curves for each run.

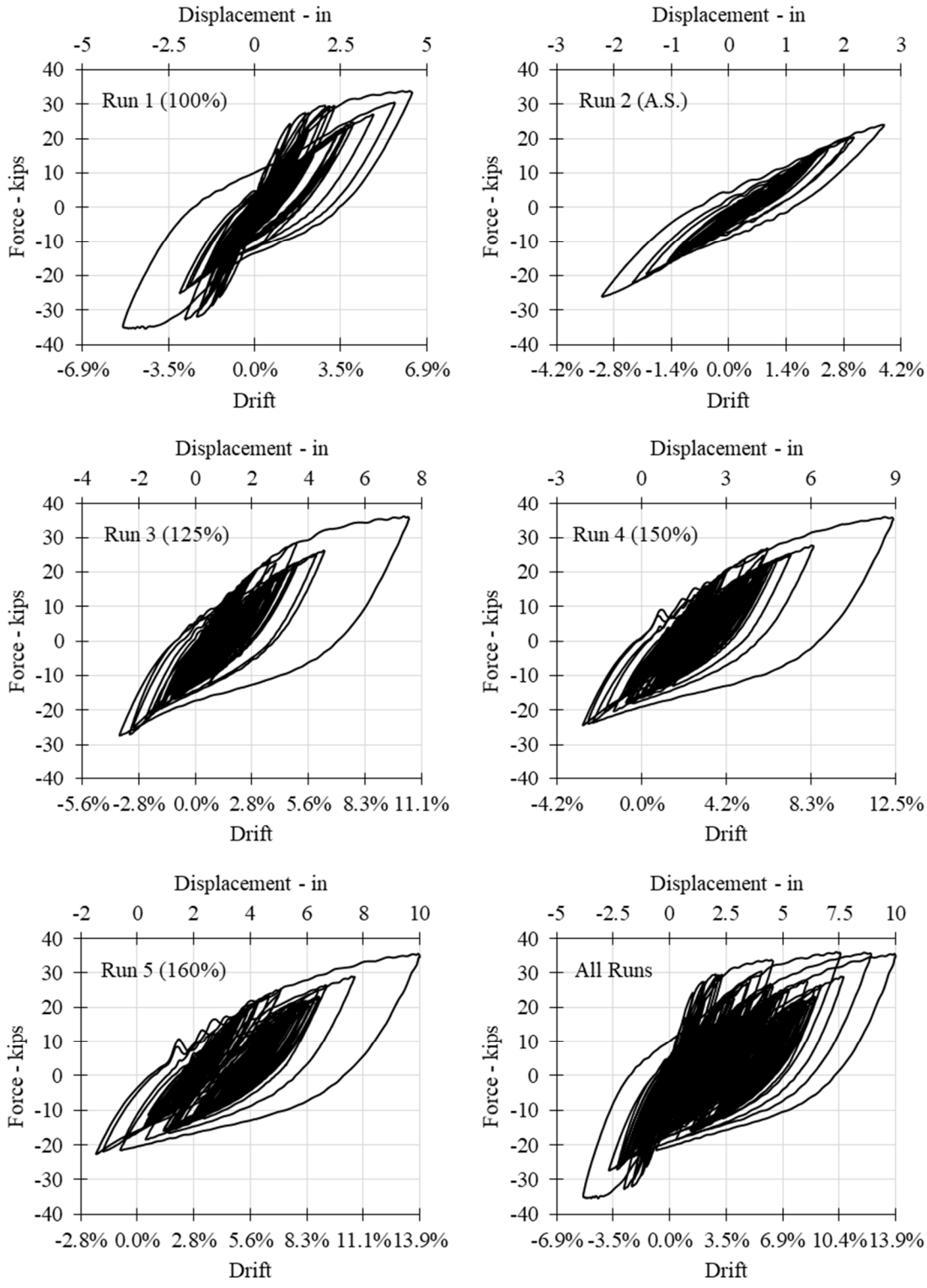

Figure 4.22 Column LD-S1.5-G60: force-displacement hysteresis curves for each run.

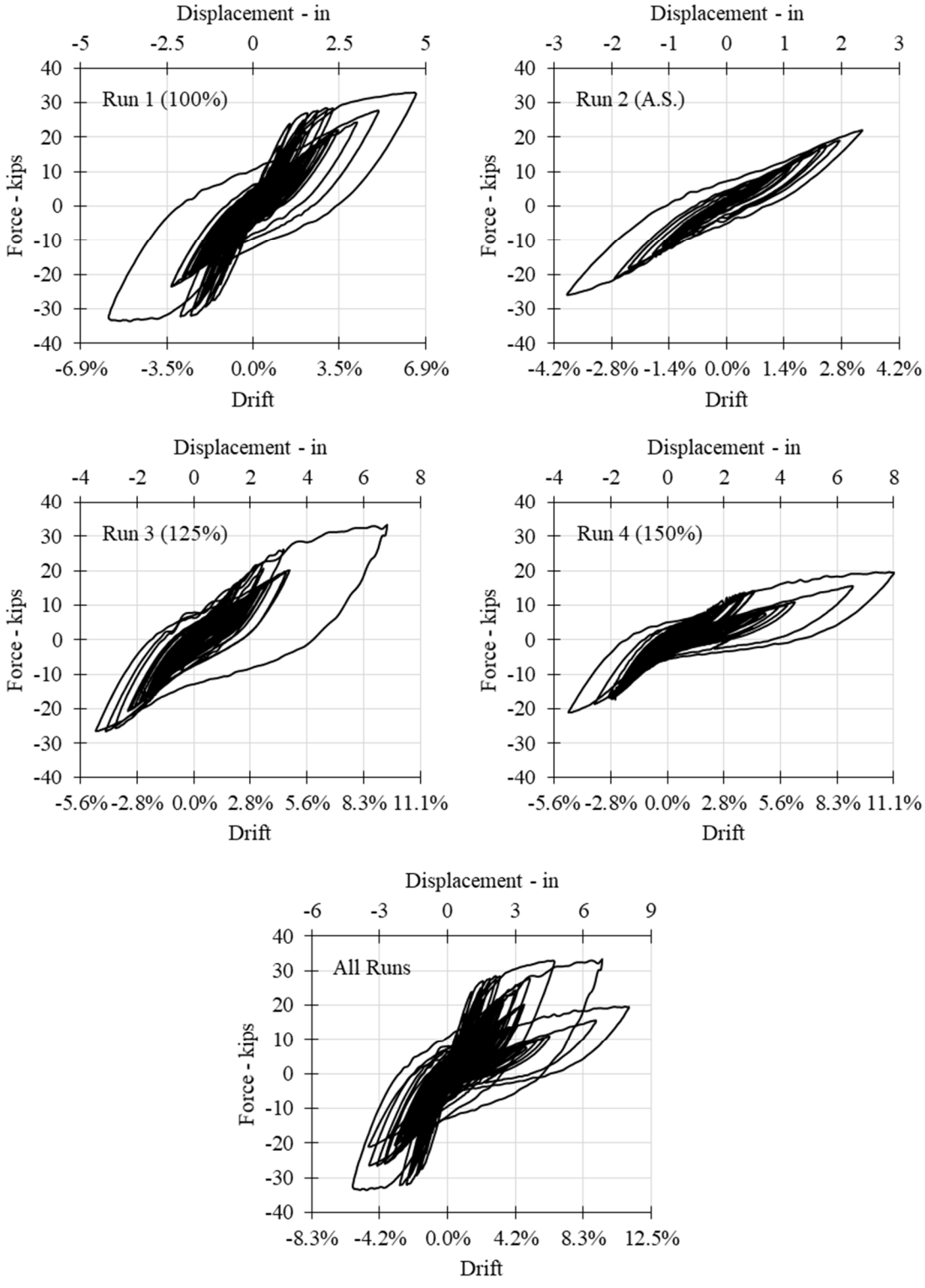

Figure 4.23 Column LD-S3-G60D: force-displacement hysteresis curves for each run.

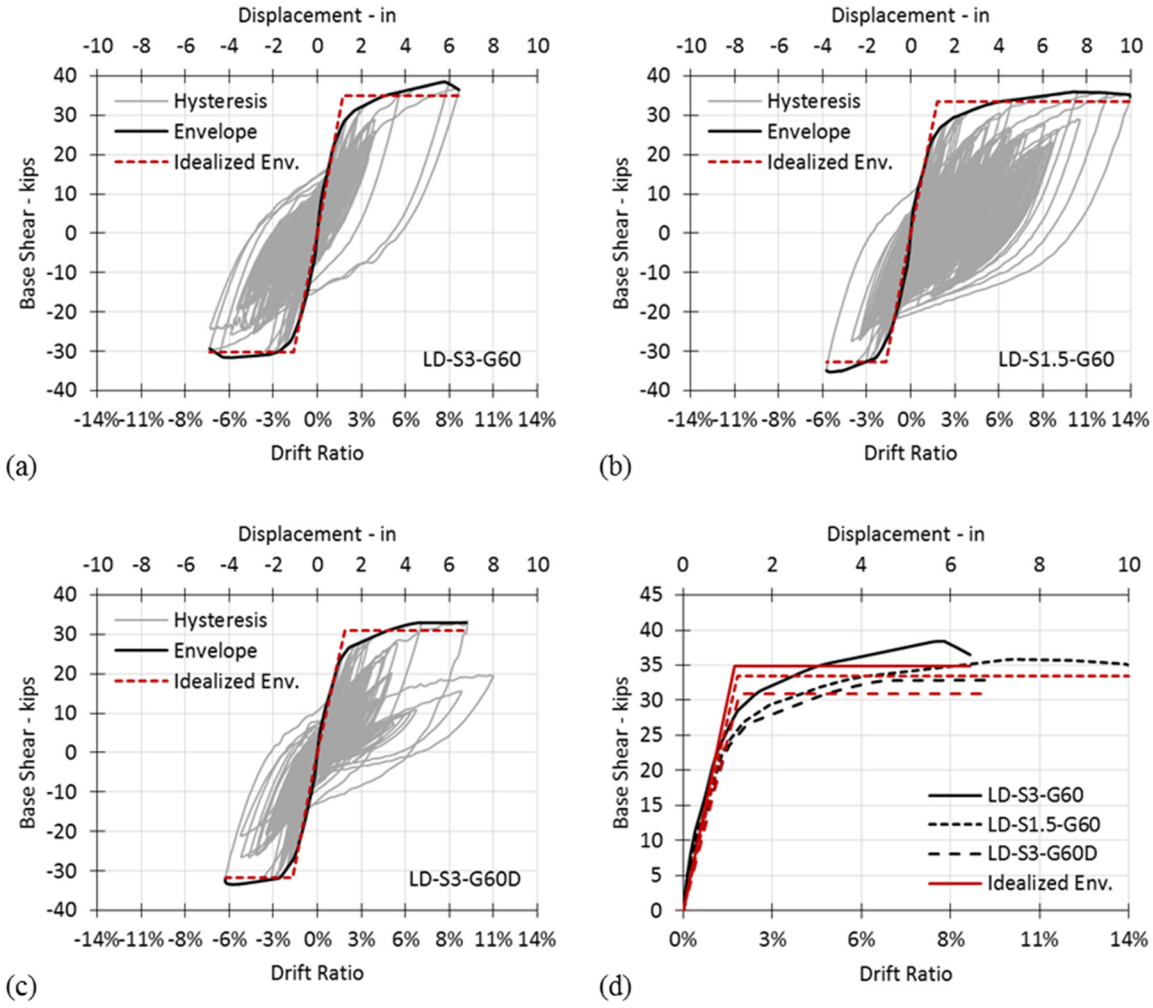

Figure 4.24 **Cumulative force-displacement relationships, envelopes, and idealized curves.**

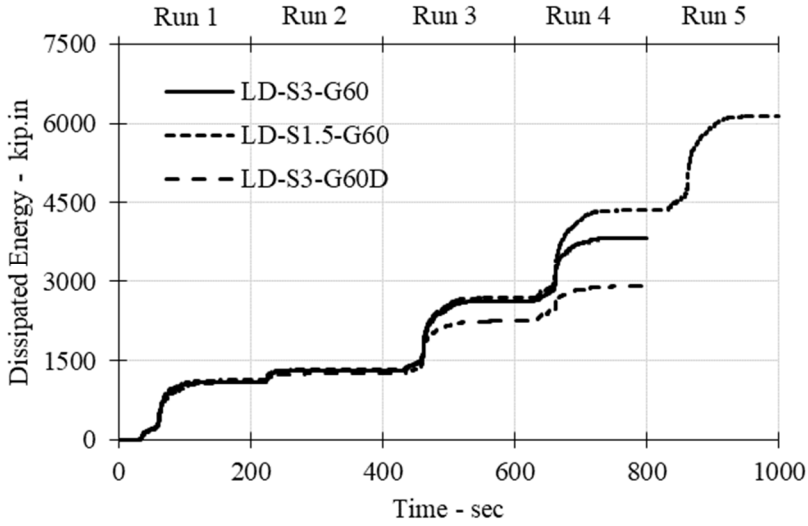

Figure 4.25 **Accumulated dissipated energy during all runs.**

Table 4.6 Park and Ang damage index of the columns in each run.

Specimen	LD-S3-G60				LD-S1.5-G60					LD-S3-G60D			
Run #	1	2	3	4	1	2	3	4	5	1	2	3	4
Disp.	0.45	0.29	0.61	0.66	0.47	0.28	0.77	0.91	1.02	0.48	0.28	0.70	0.82
Energy	0.68	0.80	1.61	2.35	0.69	0.82	1.65	2.67	3.68	0.67	0.76	1.37	1.78
DI	1.13	1.09	2.22	3.01	1.16	1.09	2.42	3.58	4.70	1.15	1.05	2.07	2.59
Predicted damage	E.R.	E.R.	B.B.	B.F.	E.R.	E.R.	B.B.	B.F.	B.F.	E.R.	B.B.	B.F.	B.F.
Actual damage	E.R.	E.R.	B.B.	B.F.	E.S.	E.S.	E.R.	E.R.	B.F.	E.R.	B.B.	B.F.	B.F.

Damage States: Minor Spalling (M.S.); Extensive Spalling (E.S.); Exposed Reinforcement (E.R.); Longitudinal Bar Buckling (B.B.); and Longitudinal Bar Fracture (B.F.)

4.8 DYNAMIC PROPERTIES

Three methods were used to obtain the natural periods (frequencies) of the columns. Table 4.7 lists the obtained periods from each method. The first method utilized the frequency response function (FRF) of the acceleration input and the measured acceleration at the top of the columns from the white noise tests. The FRF is a measure of an output of a system in response to a given input. Therefore, the relationship between the measured response acceleration of a point on structure (output) and the excitation acceleration (input) can be described as a frequency function, which can be used to describe dynamic properties of the system, such as natural period and damping. Figure 4.26 shows an example of a transfer function and the distinguishable peaks that demonstrate the fundamental frequencies of Column LD-S3-G60 from each white-noise motion. The resulting periods of the columns obtained by the aforementioned method are shown in Figure 4.27(a).

Table 4.7 Period of the columns in each run calculated using three methods.

Specimen	LD-S3-G60				LD-S1.5-G60					LD-S3-G60D			
Run #	1	2	3	4	1	2	3	4	5	1	2	3	4
White noise (sec)	0.74	0.74	0.81	1.05	0.77	0.78	0.81	0.81	0.81	0.81	0.82	0.91	1.39
Linear fit (sec)	0.83	0.83	0.93	1.21	0.86	0.86	1.08	1.16	1.44	0.88	0.91	1.09	1.58
Largest cycle (sec)	1.00	0.86	1.15	1.24	0.99	0.88	1.16	1.23	1.28	1.06	0.94	1.19	1.50

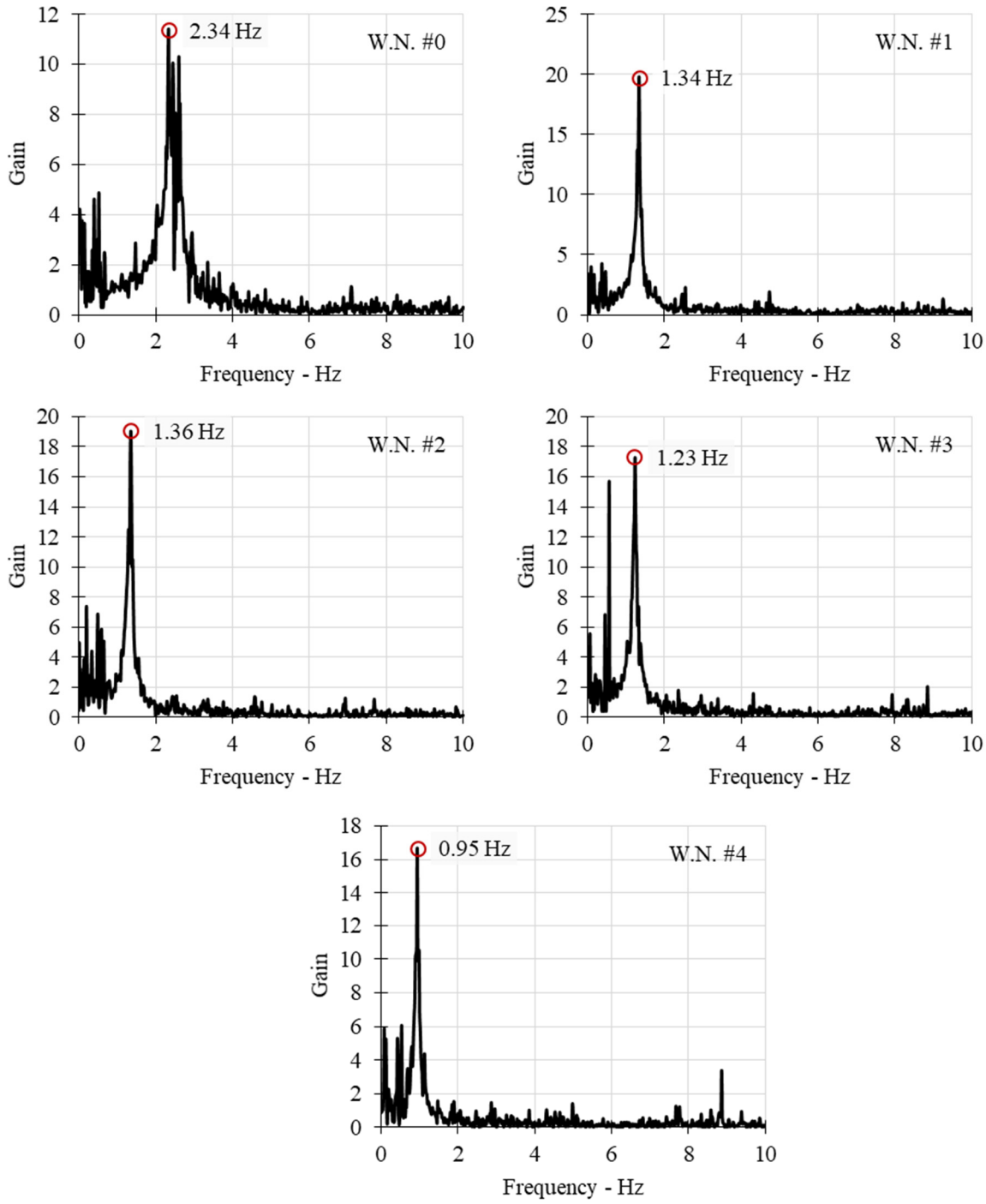

Figure 4.26 Column LD-S3-G60: frequency transfer function of each white noise run.

In the second method, periods for each run were calculated based on the slope of the linear fitting of the hysteresis force-displacement relationship and the seismic weight of the test model (i.e., 80 kip). Figure 4.28 represents the linear fitting done for each run of Column LD-S3-G60 as an example. Figure 4.27(b) shows the elongation of the periods along the runs for each column calculated through the linear fit method.

The third method used the largest displacement cycles of each run from the displacement history. The periods for each run were determined using the effective stiffnesses (k_{eff}) calculated by measuring the slope of the line connecting the maximum and minimum displacements in the largest cycle of each run on the hysteresis force-displacement relationship loops. Figure 4.27(c) and Figure 4.29 demonstrate the obtained periods for all three columns using the third method as an example of applying this method, respectively.

For Columns LD-S3-G60, LD-S1.5-G60 and LD-S3-G60D, the initial slope of the idealized force-displacement curves resulted in initial periods of 0.52, 0.55, and 0.58 sec, respectively. The calculated columns stiffnesses and the columns stiffness degradation after each run associated with each method described above are represented in Table 4.8 and Figure 4.30, respectively. All figures clearly show the elongation of the periods, which is associated with the stiffness degradation for all the test models as result of damage progression and nonlinearity spread into the column's plastic hinge. The relatively higher period of Column LD-S3-G60D is an indicator of greater damage in this column.

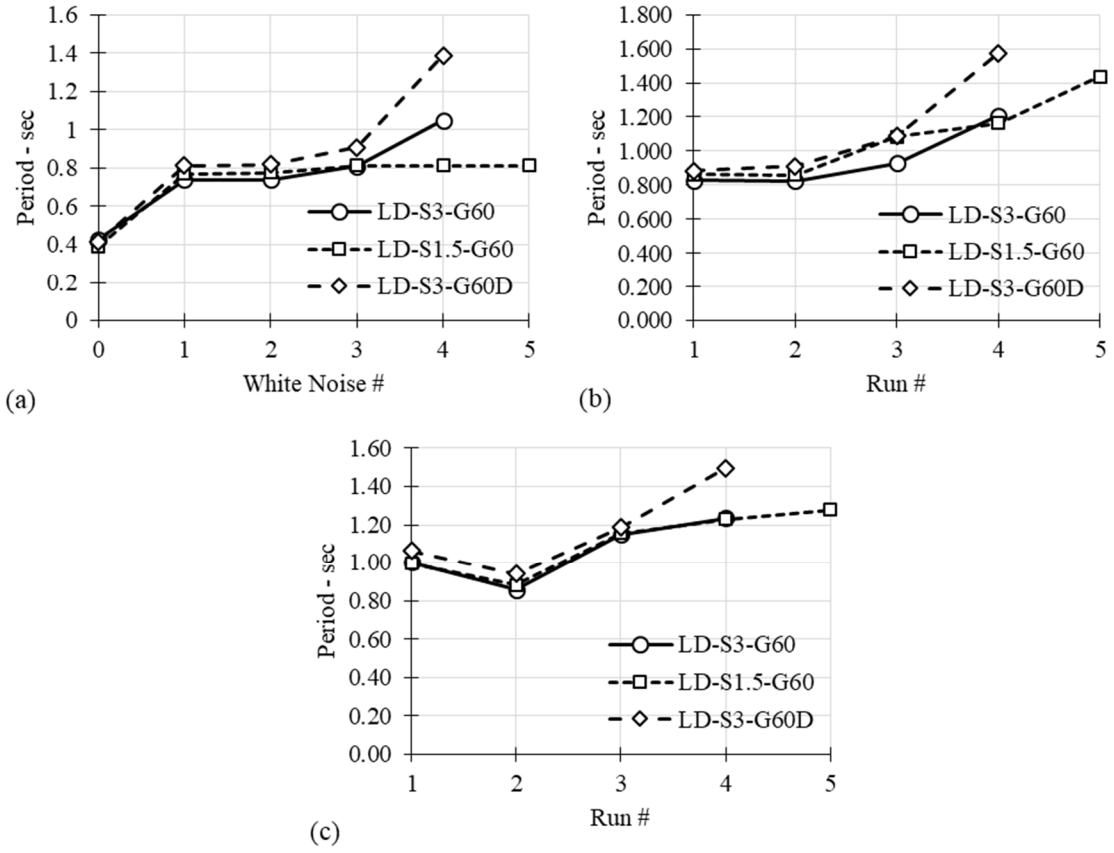

Figure 4.27 Elongation of columns periods calculated by (a) FRF (b) linear fit; and (c) largest cycle.

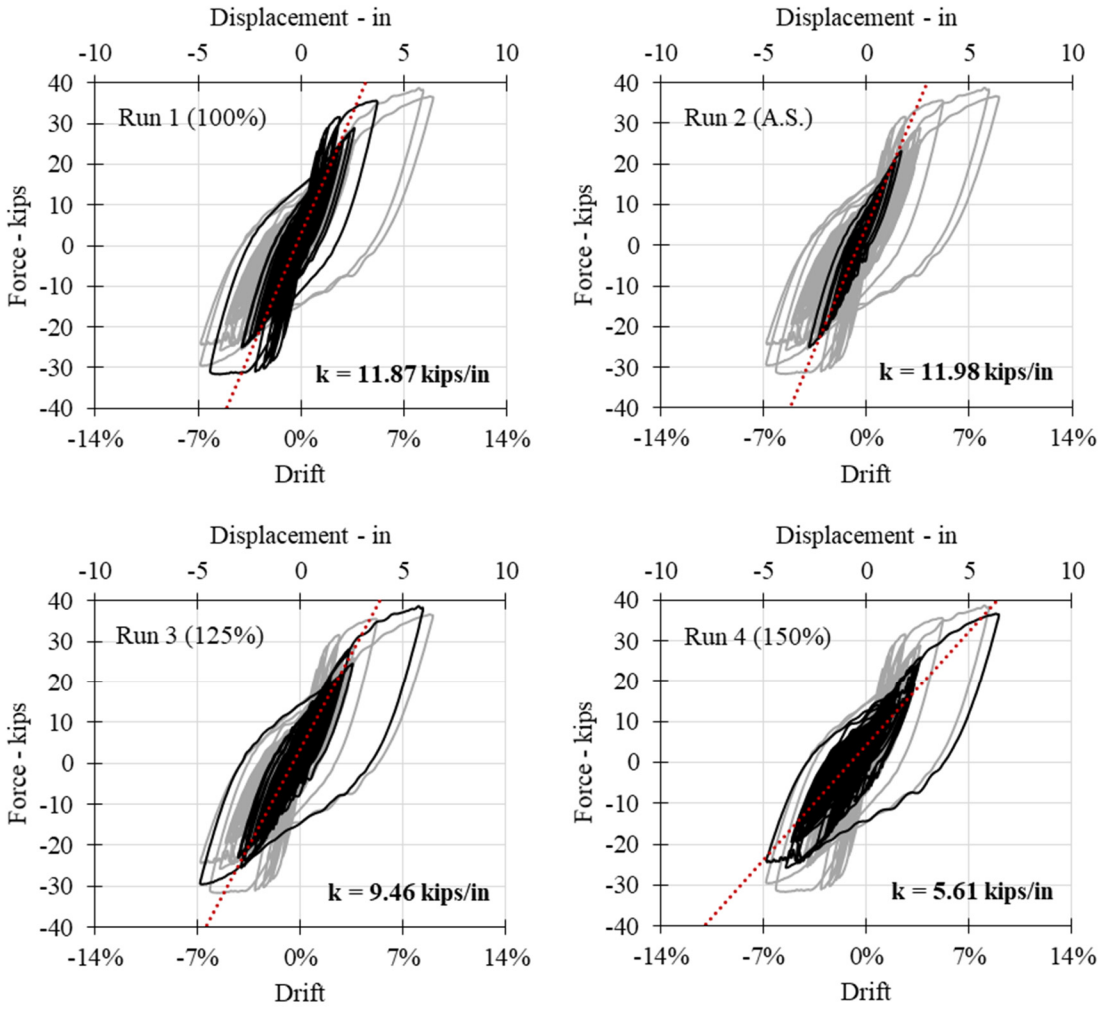

Figure 4.28 **Column LD-S3-G60: linear fit method to calculate columns stiffnesses and periods in each run.**

Table 4.8 **Stiffness of the columns in each run calculated using three methods.**

Specimen	LD-S3-G60				LD-S1.5-G60					LD-S3-G60D			
Run #	1	2	3	4	1	2	3	4	5	1	2	3	4
White noise (k/in)	14.9	14.9	12.5	7.4	13.8	13.4	12.5	12.5	12.5	12.5	12.2	9.9	4.2
Linear fit (k/in)	11.9	11.9	9.5	5.6	11.1	11.1	7.0	6.1	3.9	10.6	9.9	6.9	3.3
Largest cycle (k/in)	8.2	11.1	6.2	5.3	8.3	10.6	6.1	5.4	5.0	7.3	9.3	5.8	3.6

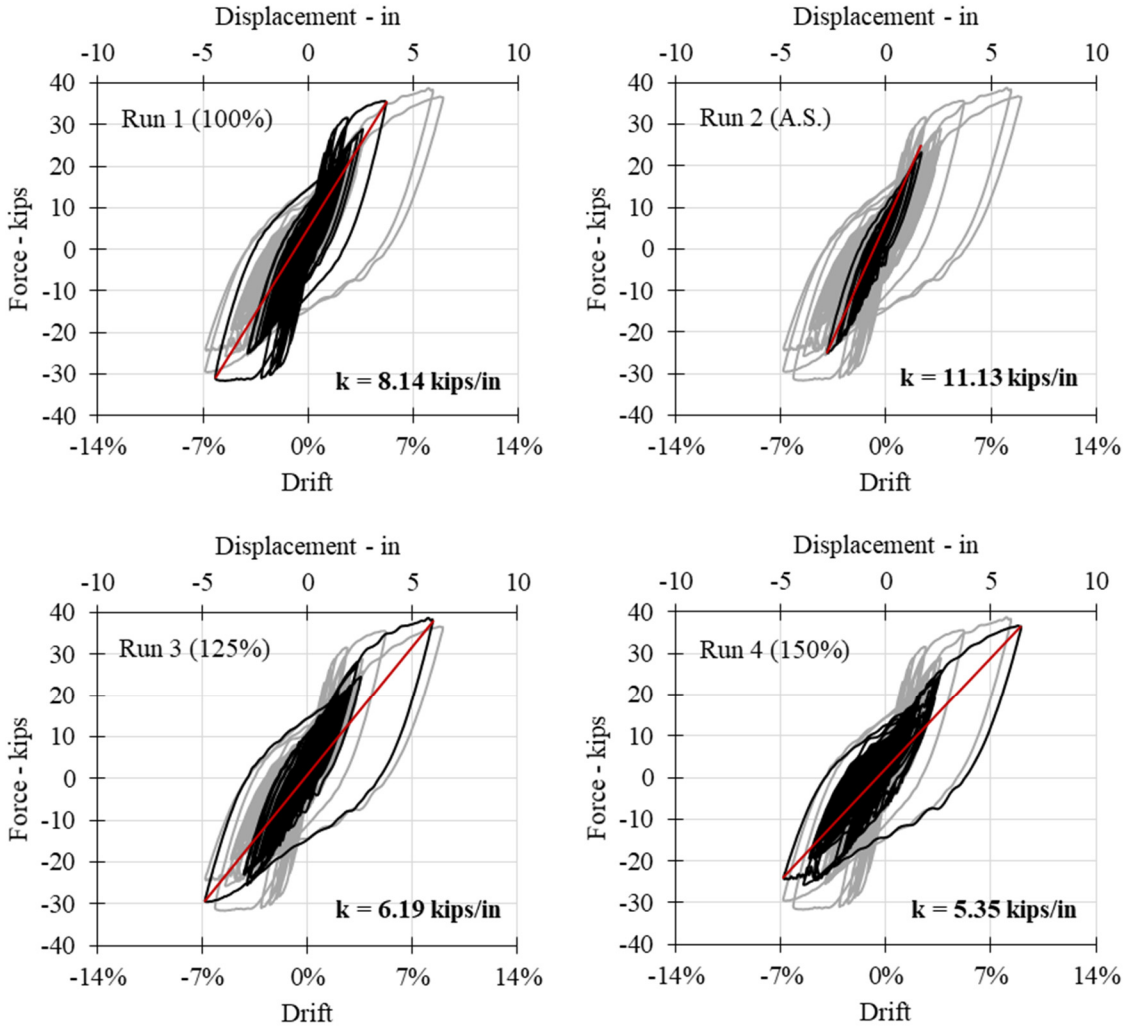

Figure 4.29 Column LD-S3-G60: largest cycle method to calculate columns effective stiffnesses and periods in each run.

The equivalent hysteretic nonlinear viscous damping ratio for the columns was calculated for each half-cycle of the force-displacement relationship curve [Varum 2003] using Equation (4.2):

$$\xi_{hys} = \frac{A_{\text{half}}}{\pi F_{\max} D_{\max}} = \frac{A_{\text{half}}}{\pi k_{\text{eff}} D_{\max}^2} \tag{4.2}$$

where A_{half} is the area enclosed by the half-loop in the force-displacement diagram corresponding to a specific cycle; $F_{\max}$ and $D_{\max}$ are the maximum force and displacement, respectively, in this half-loop; and k_{eff} is the effective stiffness. The equivalent hysteretic damping ratios calculated for the columns in each run are summarized in Table 4.9. Such additional response metrics like the equivalent hysteretic damping are provided herein for completeness, which may be used in future studies for further modeling enhancement or other applications.

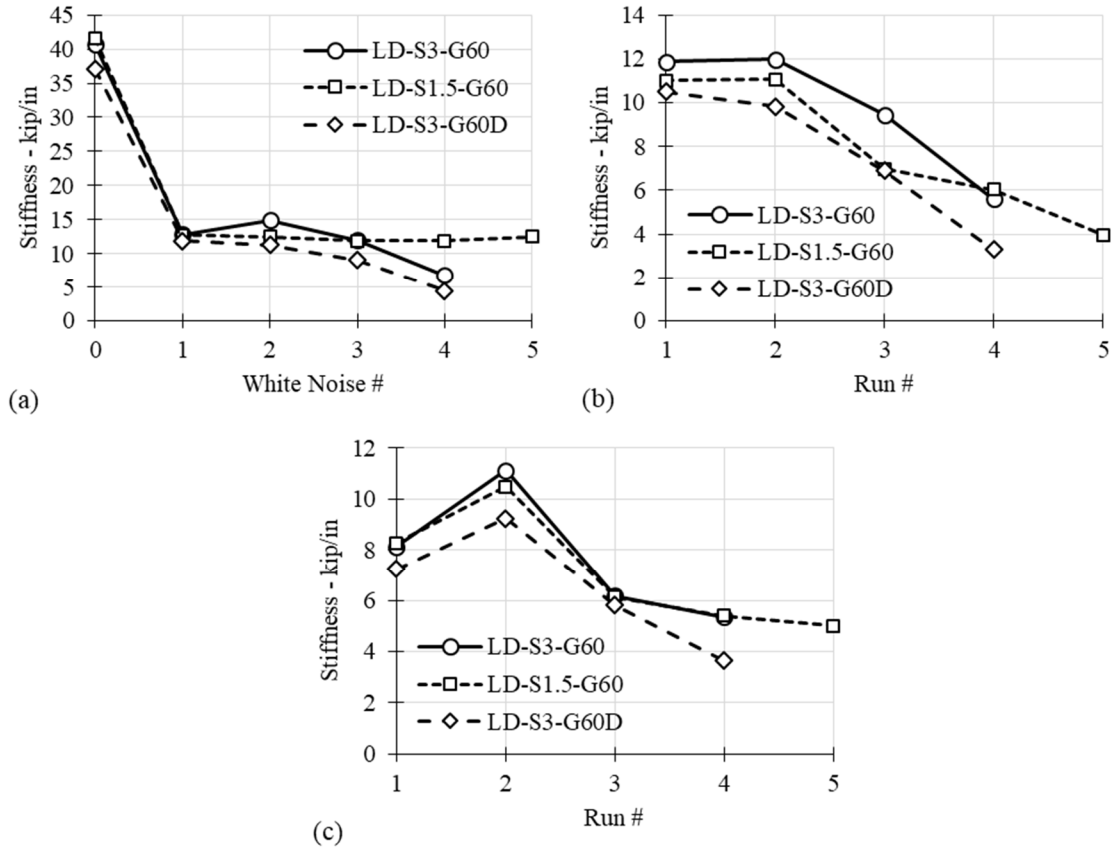

Figure 4.30 Variation of columns stiffnesses calculated by (a) FRF; (b) linear fit; and (c) and largest cycle.

Table 4.9 Equivalent hysteretic damping ratios of the columns.

Specimen	LD-S3-G60				LD-S1.5-G60					LD-S3-G60D			
Run #	1	2	3	4	1	2	3	4	5	1	2	3	4
Hysteretic damping (%)	16.3	16.9	19.2	19.7	16.8	12.2	18.6	17.3	16.5	17.0	14.1	18.5	19.1

4.9 STRAINS

Strains were measured on the longitudinal and transverse reinforcement in the columns during the tests. The strain history of the extreme northern and southern longitudinal bars at the interface of the columns are shown in Figure 4.31 through Figure 4.36. The peak strain values were used to create strain profiles, as shown in Figure 4.37 through Figure 4.39. These figures represent the peak measured strains of the extreme northern and southern longitudinal bars at each level along the columns' plastic hinges as a strain percentage and ratio of the yield strain. The gray points of the strain profiles were not recorded properly due to malfunction of the strain gauges and were

estimated based on the data obtained from other strain gauges. As expected, the figures show that the strains at or close to the column–footing interface are the greatest. Note: most of the plastic strains occurred within 30 in. from the interface for all columns. For Column LD-S1.5-G60, strains were better distributed along the length of the plastic hinge, which is attributed to the higher confinement. For the third specimen, strain concentration in the vicinity of the column–footing interface was reduced compared to the first two specimens as a result of the debonding of the longitudinal bars at the interface.

The peak strain of the longitudinal bars for each column and for each run are listed in Table 4.10 and shown in Figure 4.40 for comparison purposes. The strain values for the runs in which rupture occurred are not shown as such values were not possible to capture properly after strain gauges or their lead wires were damaged. Column LD-S1.5-G60 showed higher strain ductility compared to the other two columns, while Column LD-S3-G60D showed the lowest strain ductility. The maximum measured strain in the spirals for the three test models were 1.8, 0.8, and 1.7 times the yield strain, respectively. Spirals in the first and third columns yielded, while no yielding occurred in the second column spiral. Note: yield strain was reached during first run for the first and third columns. This occurred at almost the same time and at locations of extensive spalling.

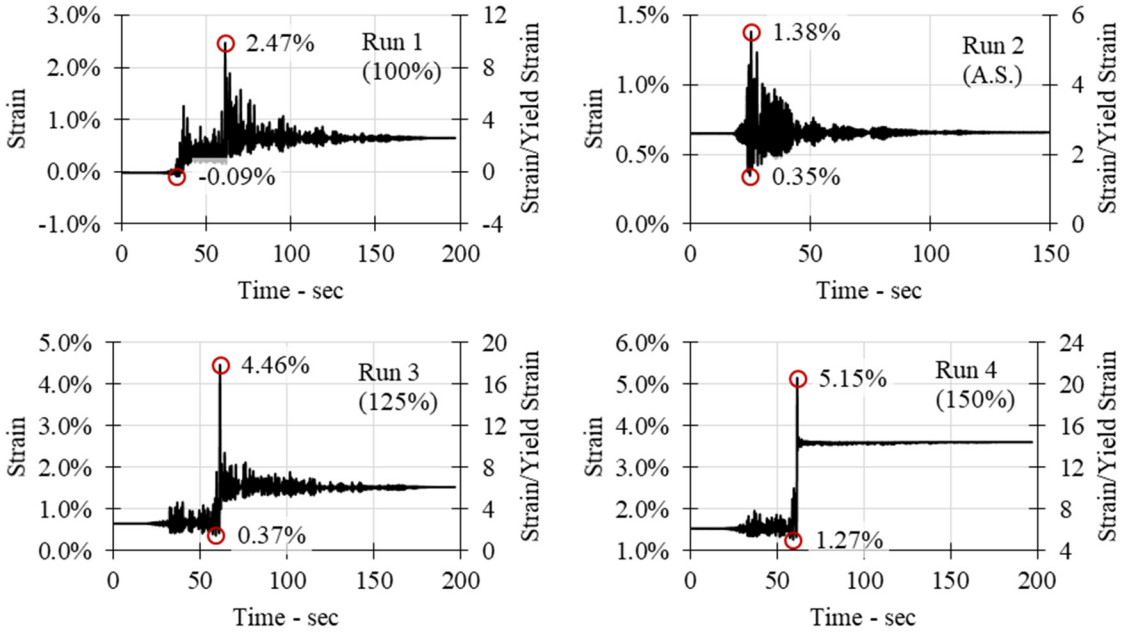

Figure 4.31 Column LD-S3-G60: strain histories of the northern longitudinal bar during each run (strain gauge 108).

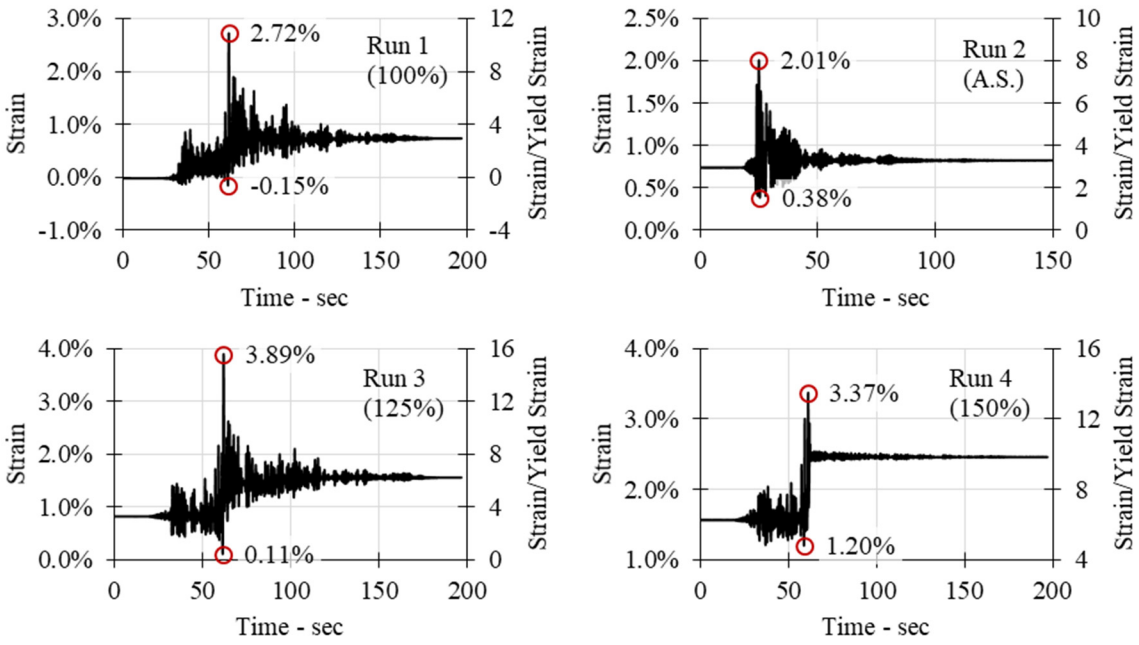

Figure 4.32 **Column LD-S3-G60: strain histories of the southern longitudinal bar during each run (strain gauge 111).**

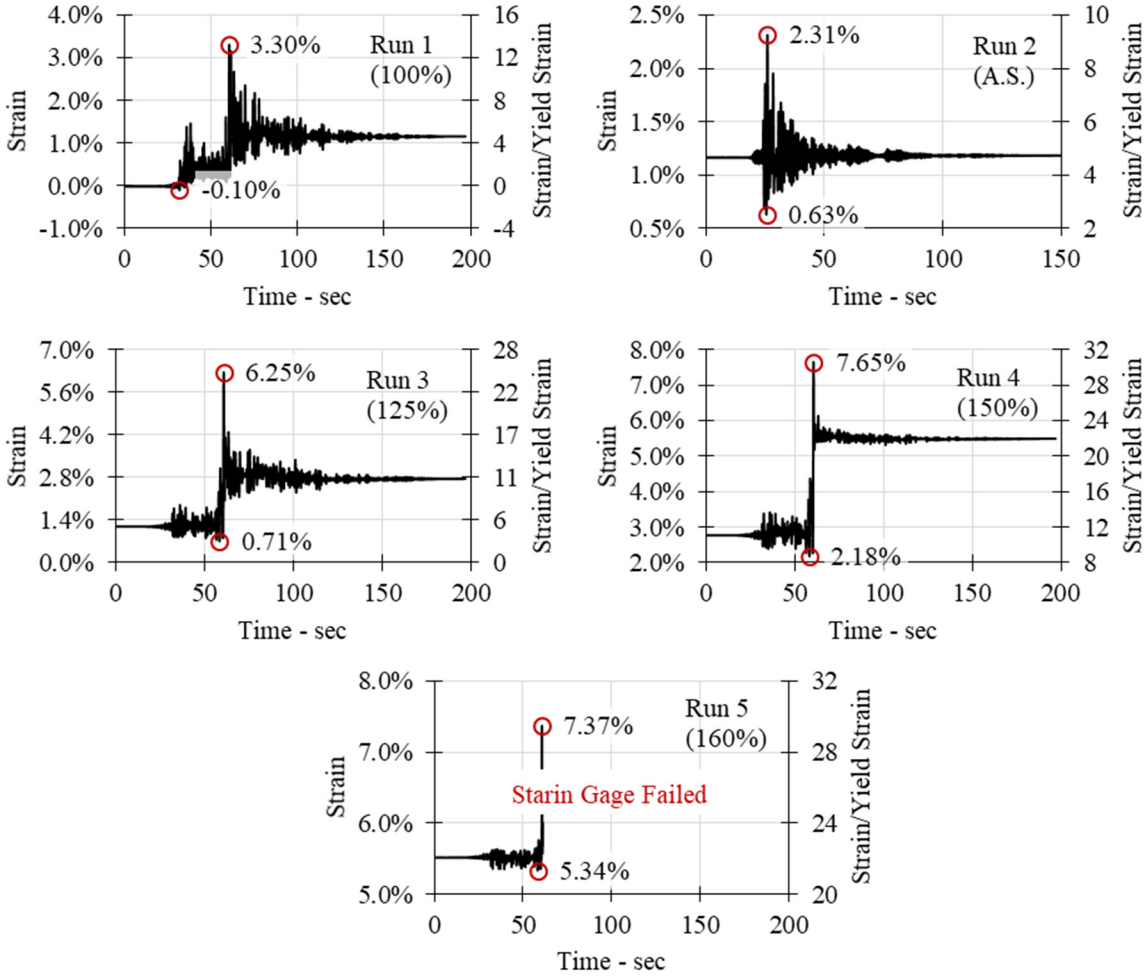

Figure 4.33 **Column LD-S1.5-G60: strain histories of the northern longitudinal bar during each run (strain gauge 108).**

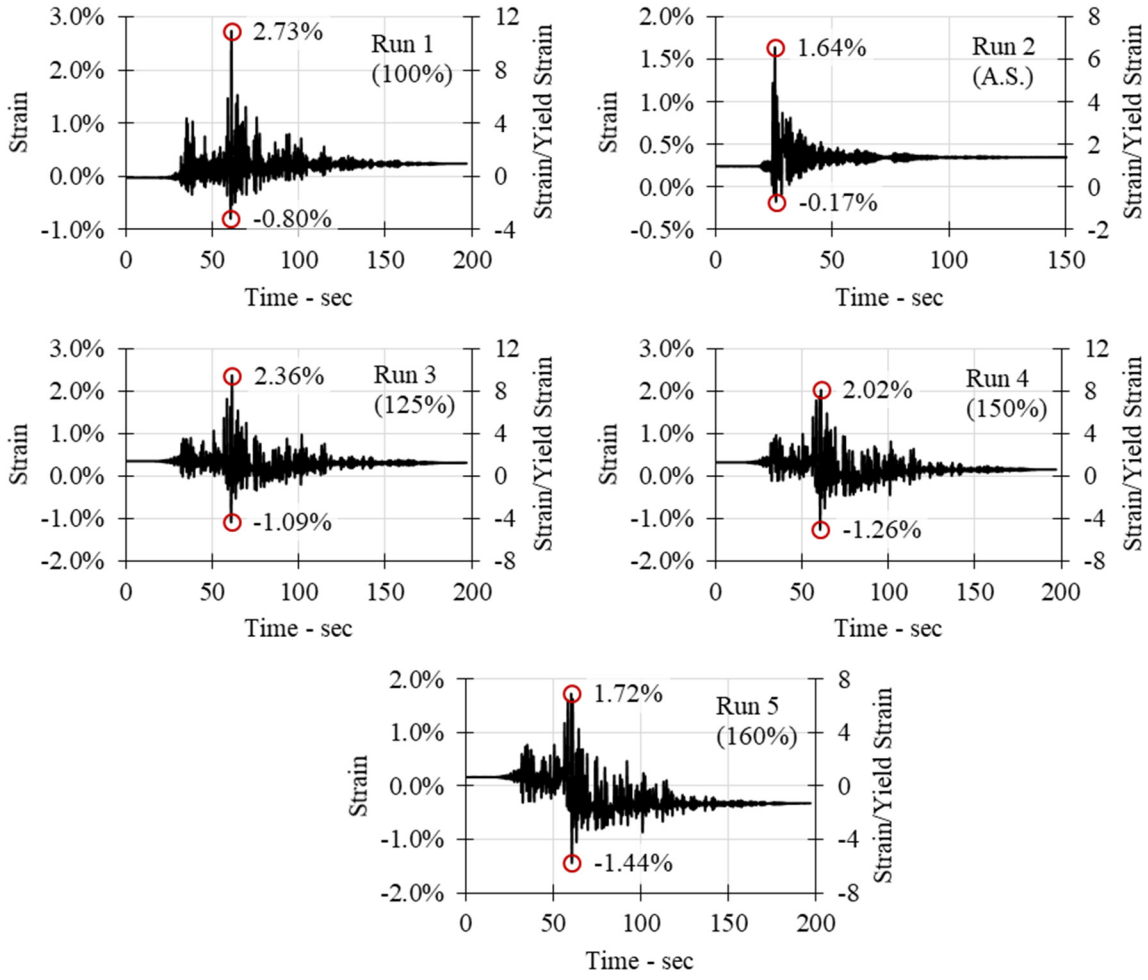

Figure 4.34 **Column LD-S1.5-G6: strain histories of the southern longitudinal bar during each run (strain gauge 111).**

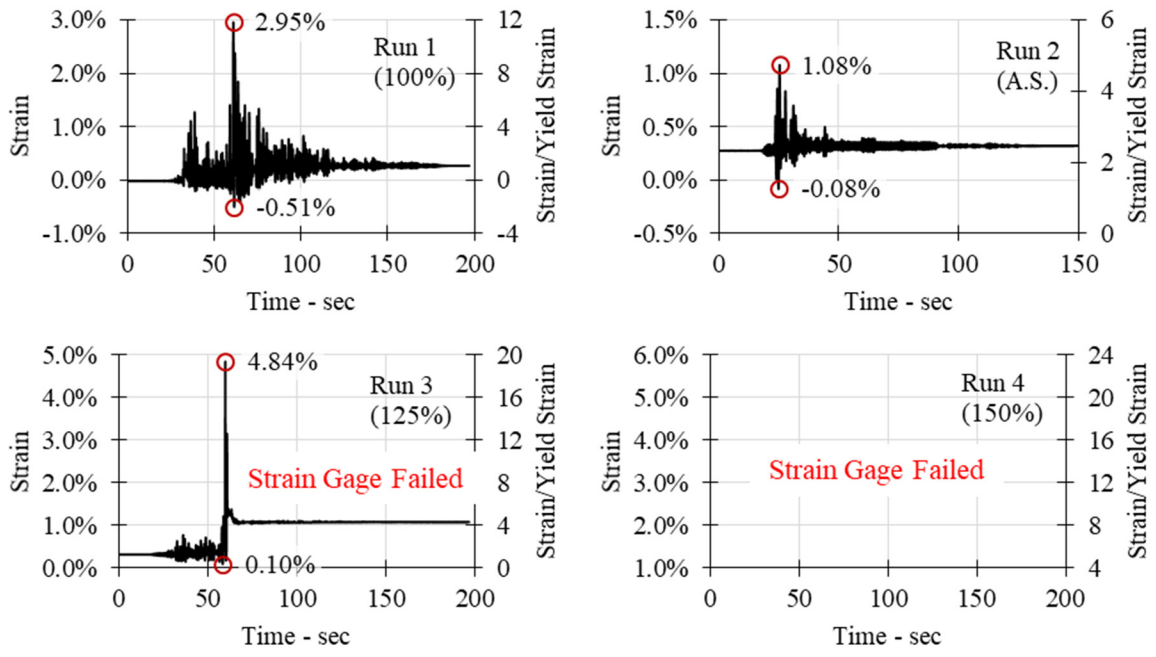

Figure 4.35 **Column LD-S3-G60D: strain histories of the northern longitudinal bar during each run (strain gauge 114).**

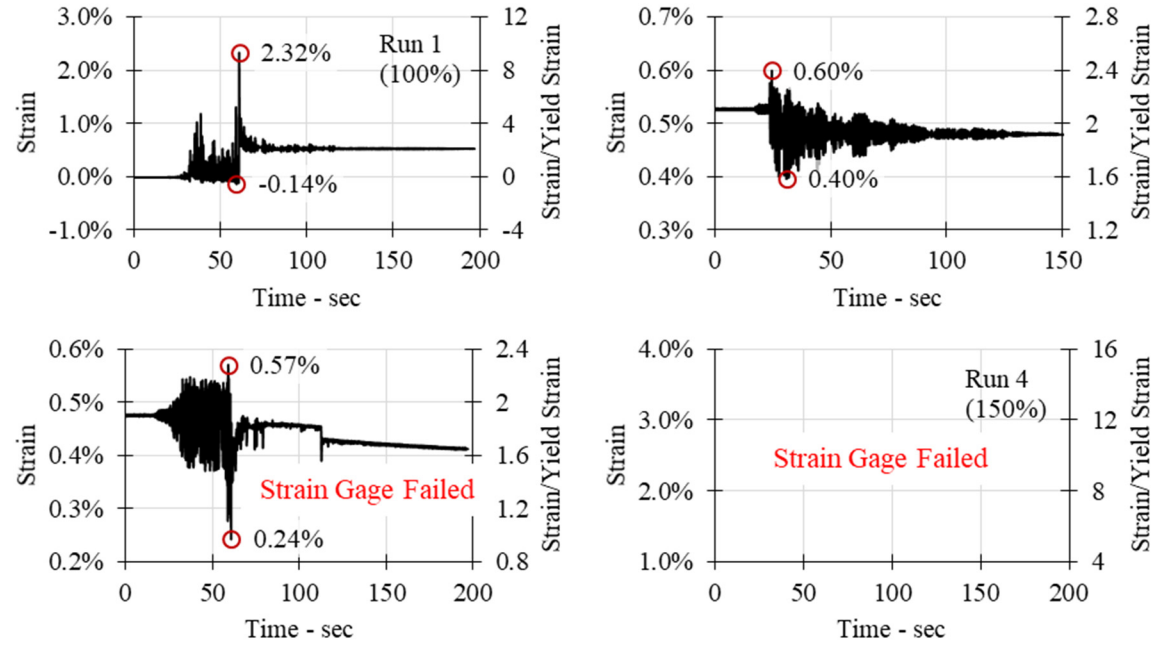

Figure 4.36 **Column LD-S3-G60D: strain histories of the southern longitudinal bar during each run (strain gauge 117).**

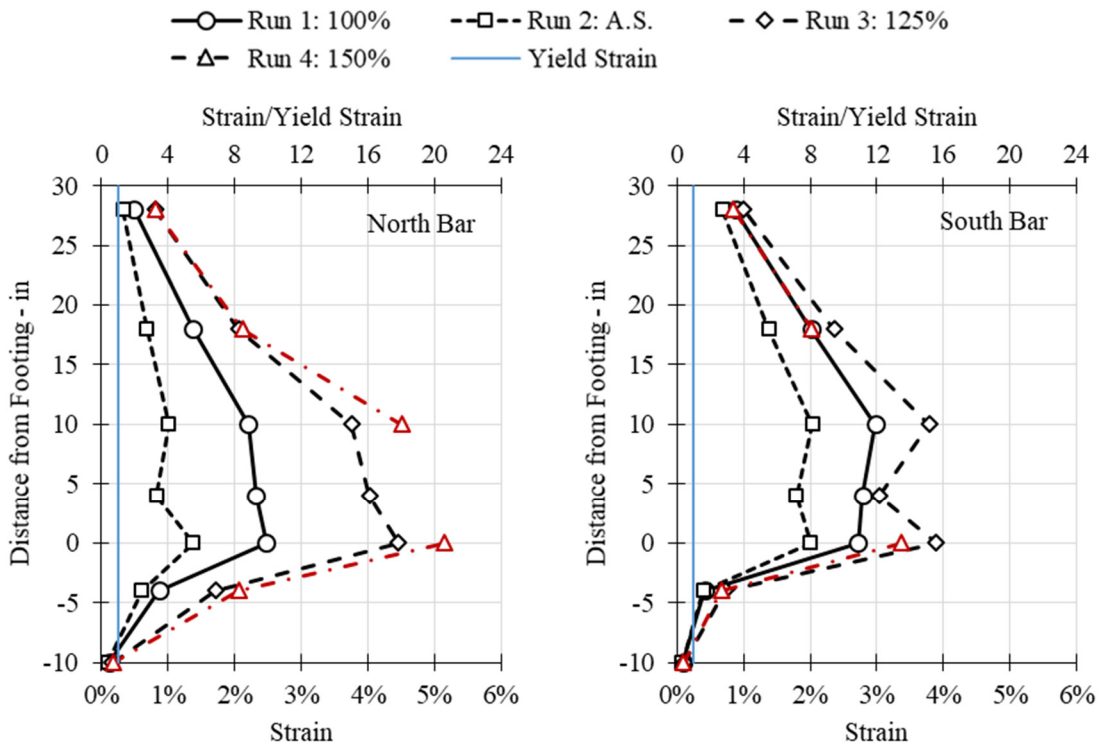

Figure 4.37 **Column LD-S3-G60: strain profile of the northern and southern longitudinal bars along the plastic hinge during each run.**

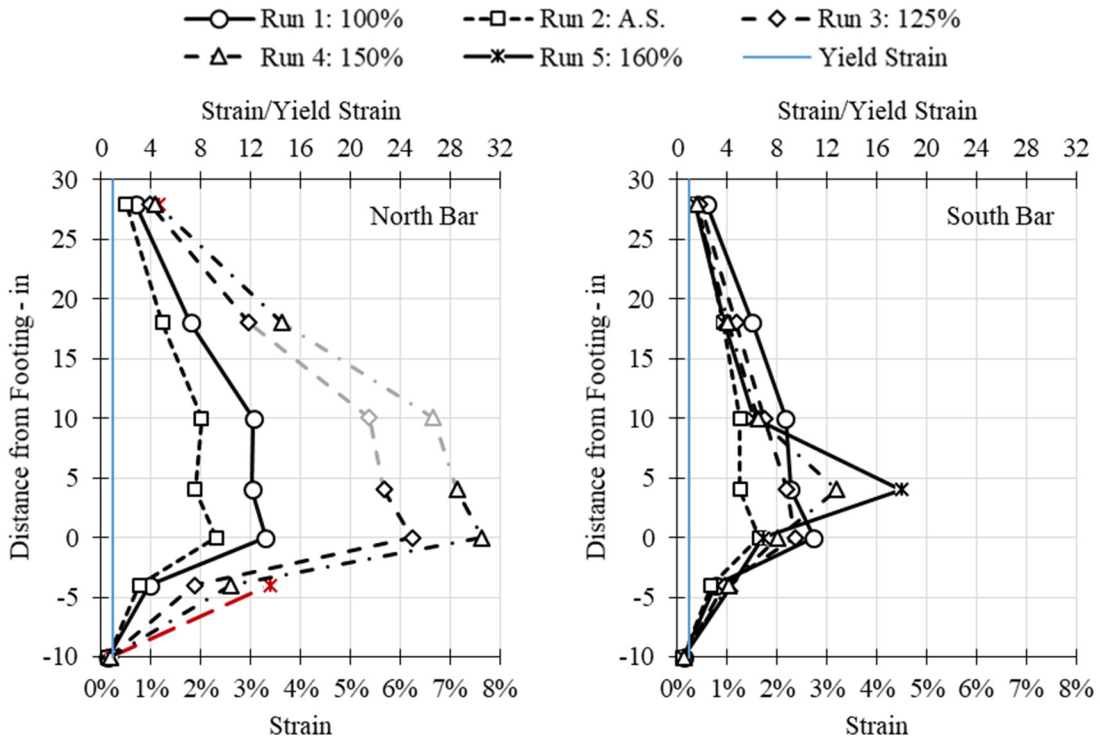

Figure 4.38 **Column LD-S1.5-G60: strain profile of the northern and southern longitudinal bars along the plastic hinge during each run.**

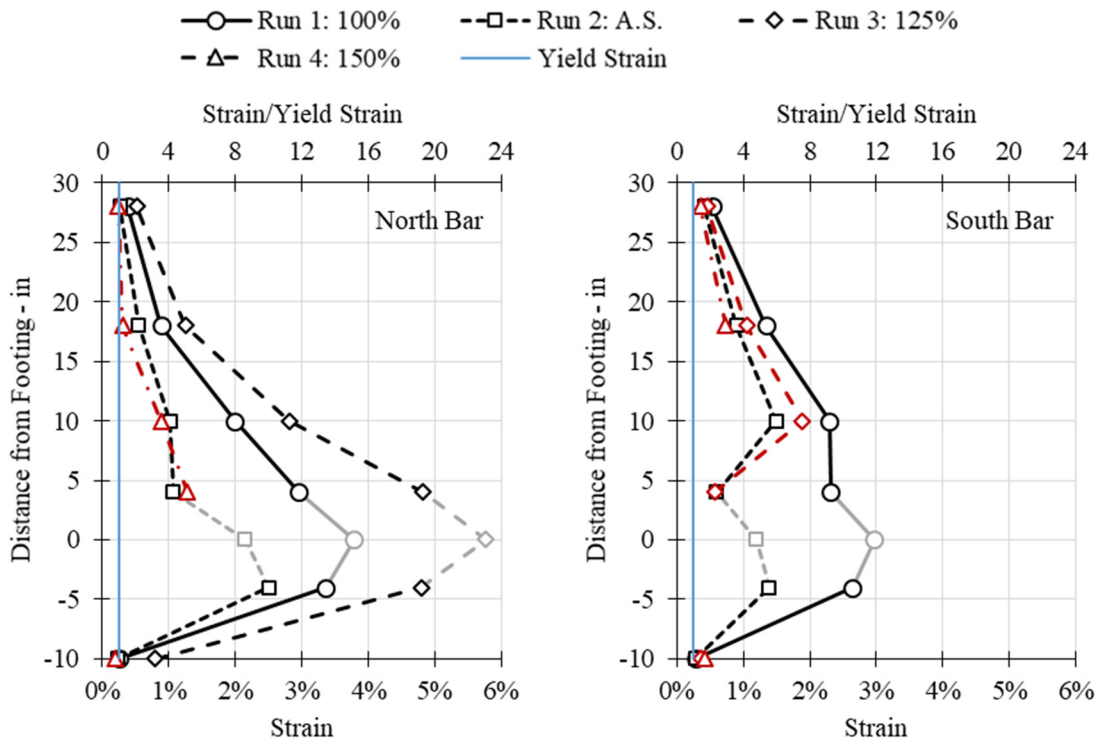

Figure 4.39 **Column LD-S3-G60D: strain profile of the northern and southern longitudinal bars along the plastic hinge during each run.**

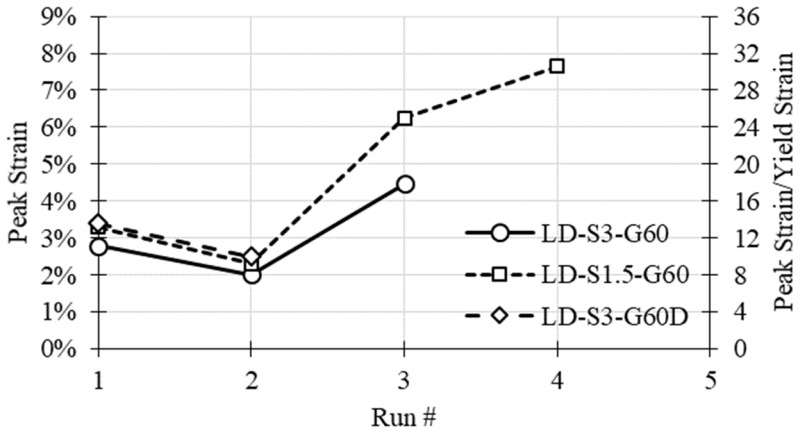

Figure 4.40 **Peak strain of the longitudinal bars of the columns in each run.**

Table 4.10 **Peak strains in longitudinal bars of the columns in each run.**

Specimen	LD-S3-G60				LD-S1.5-G60					LD-S3-G60D			
Run #	1	2	3	4	1	2	3	4	5	1	2	3	4
Strain (%)	2.8	2.0	4.5	-	3.3	2.3	6.3	7.7	-	3.4	2.5	-	-
Strain/yield	11.2	8.0	17.8	-	13.2	9.2	25.0	30.6	-	13.6	10.0	-	-

4.10 ROTATIONS AND CURVATURES

Bond-slip and flexural-related rotations and curvatures were obtained based on the measured data by Novotechnik transducers installed on the north and south faces of the columns. The nominal gauge length was 3 and 6 in. for lowest transducer and all others, respectively. The actual gauge lengths and the distance of each Novotechnik rod to the face of the columns were measured before testing and were used in the calculations. Rotation at each level was calculated by subtracting the measured vertical displacements on opposite sides of the column divided by the associated horizontal displacement. Curvatures were calculated based on the assumption that the plane sections remained plane under bending. The relative rotation at two adjacent levels was divided by the vertical distance between them to give the average curvature over the gauge length, as expressed in Equation (4.3).

$$\phi = \frac{\frac{\Delta l_2}{l_2} - \frac{\Delta l_1}{l_1}}{L} \tag{4.3}$$

where L is distance between rods of the Novotechnik pairs; l_1 and l_2 are actual gauge lengths of the north and south Novotechniks, respectively; and Δl_1 and Δl_2 are displacement measurement of the north and south Novotechniks, respectively. The $\Delta l_1/\Delta l_1$ and $\Delta l_2/\Delta l_2$ terms in Equation (4.3) represent the strain on the north and south sides of the columns, respectively.

Figure 4.41 through Figure 4.43 illustrates the columns curvature profile along the length of the plastic hinge. As shown, the curvature for all specimens was more concentrated at the column–footing interface and to some extent over the plastic-hinge length for Columns LD-S3-G60 and LD-S1.5-G60). This is attributed to the bond-slip effect and yielding. The maximum curvatures for the three columns were 0.016, 0.018, and 0.028 in.$^{-1}$, respectively, which were measured at approximately 3 in. above the footing.

The peak rotations and curvatures of the columns during each run are presented in Table 4.11 and Figure 4.44. Note that these rotations include the bond-slip effect (due to the yielding of the reinforcing bars at the column–footing interface). The diagram shows a higher rotational capacity of the last specimen due to the intentional debonding of the longitudinal bars, which confirms that debonding worked as desired. The moment-curvature relationships measured at 3 in. above the footing are also shown in Figure 4.45 through Figure 4.47.

Table 4.11 Peak rotation and curvature at the base of the columns in each run.

Specimen	LD-S3-G60				LD-S1.5-G60					LD-S3-G60D			
Run #	1	2	3	4	1	2	3	4	5	1	2	3	4
Curvature (1/in)	8.6	6.1	14.3	15.8	8.5	5.0	13.2	15.7	17.7	18.4	11.5	19.8	28.3
Rotation (rad)	36.6	27.1	46.3	48.5	25.6	14.9	40.1	47.0	53.2	55.1	34.5	59.3	84.9

All numbers / 1000.

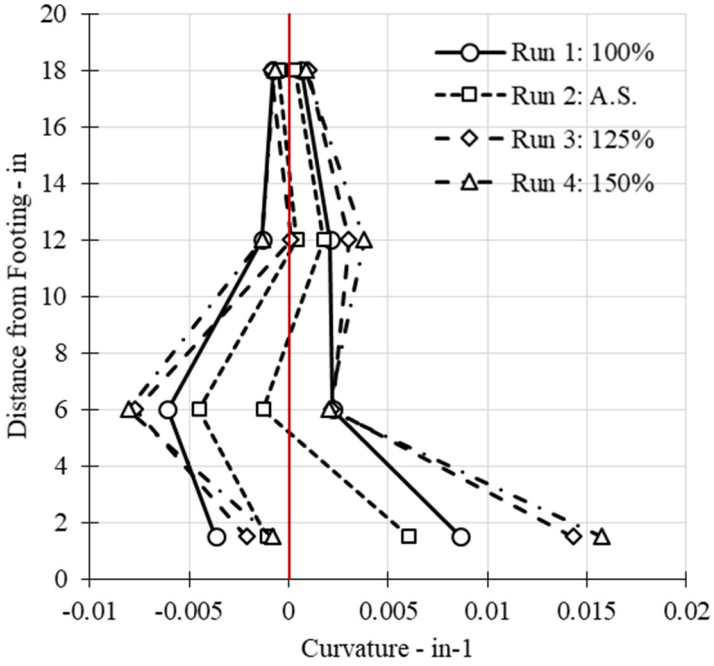

Figure 4.41 **Column LD-S3-G60: curvature profiles along the plastic hinge during each run.**

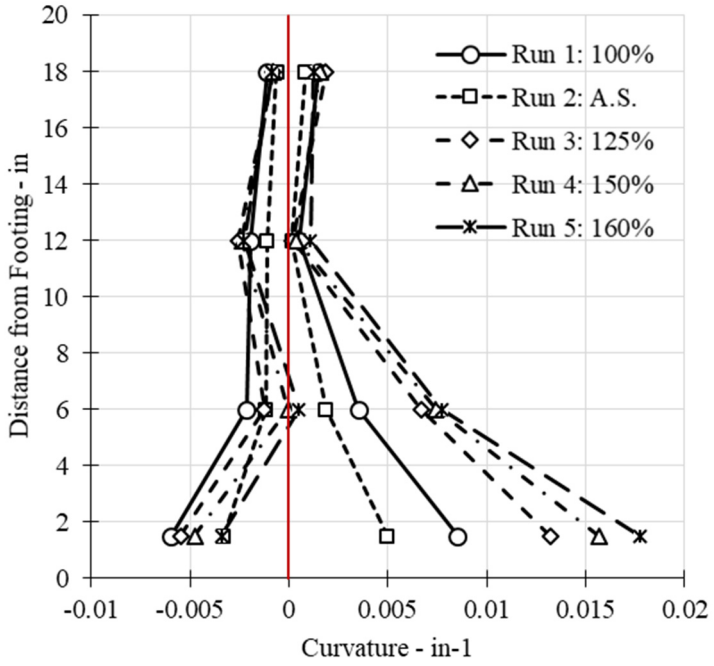

Figure 4.42 **Column LD-S1.5-G60: curvature profiles along the plastic hinge during each run.**

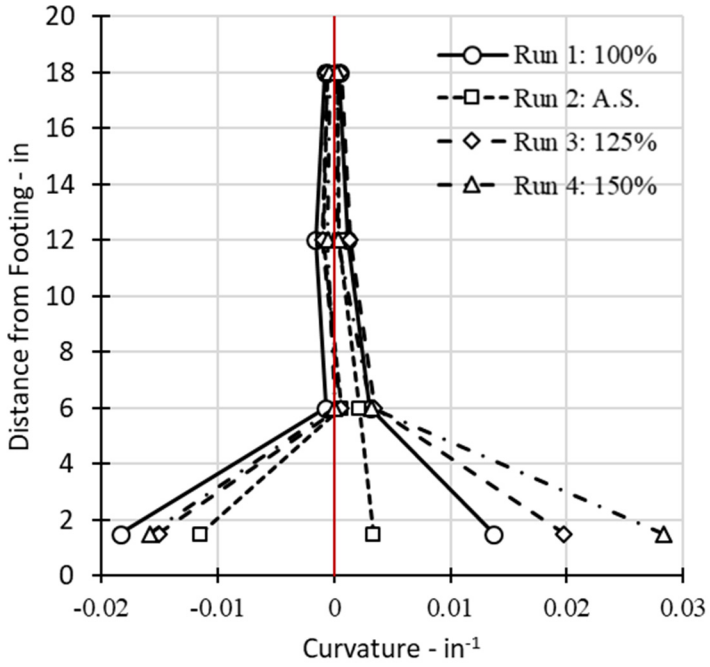

Figure 4.43 **Column LD-S3-G60; curvature profiles along the plastic hinge during each run.**

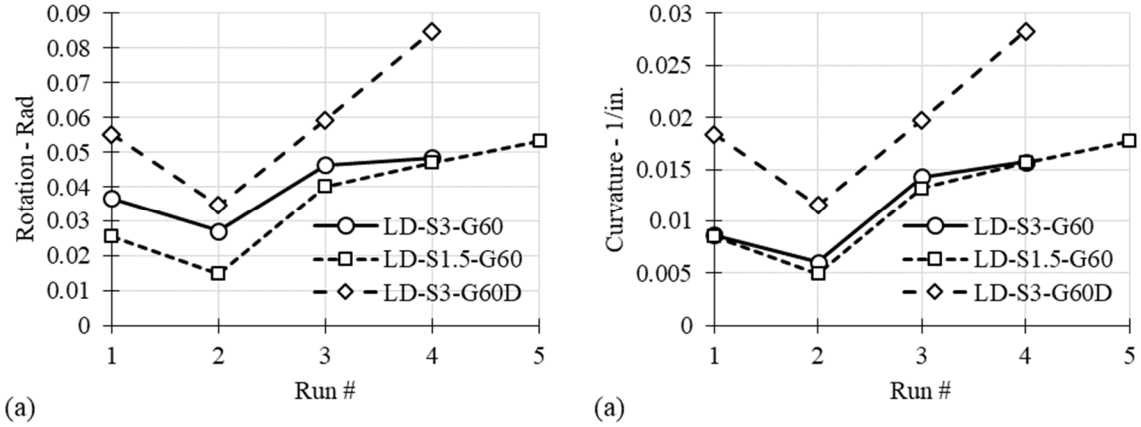

Figure 4.44 **(a) Peak rotations and (b) peak curvatures at the base of the columns in each run.**

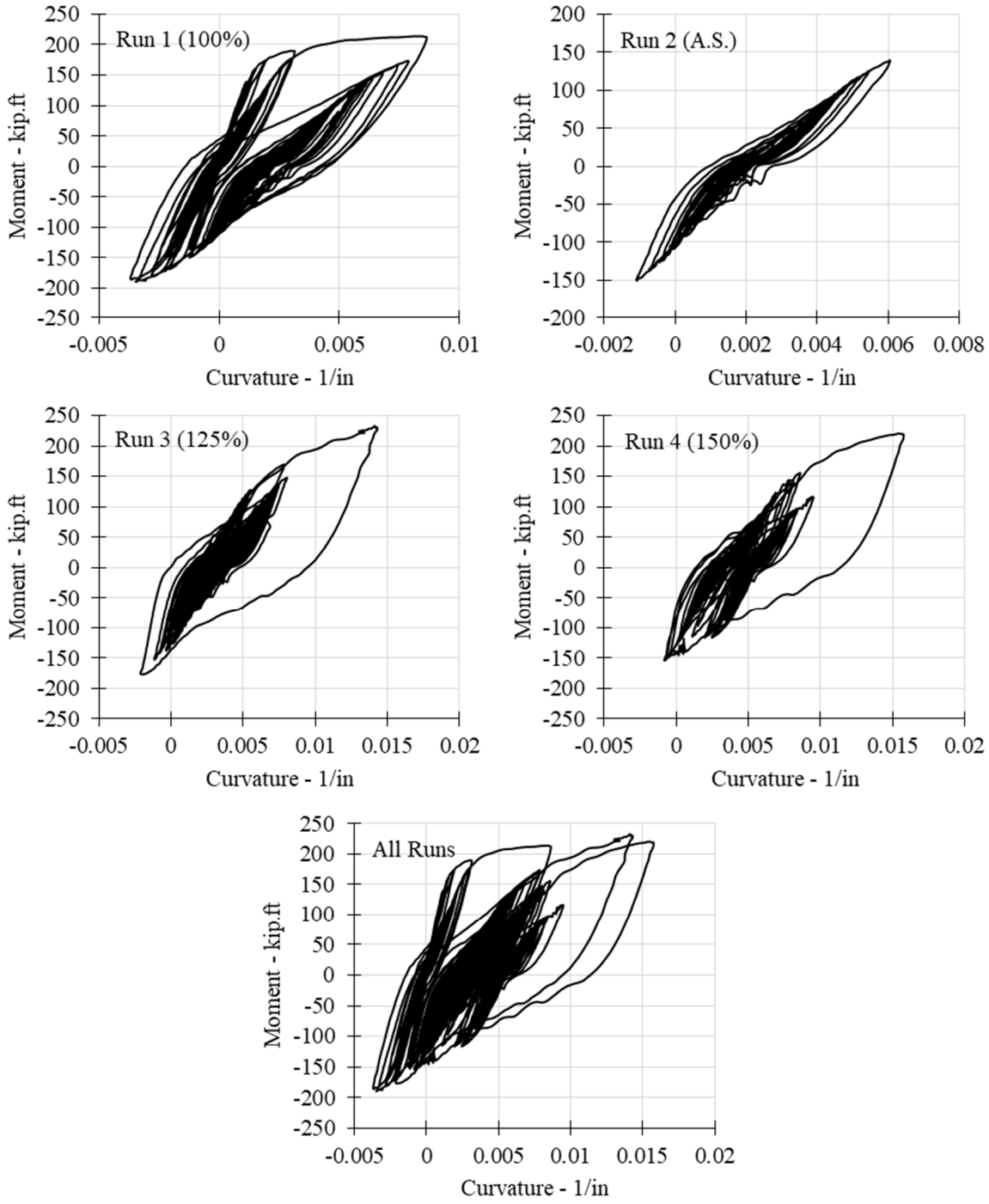

Figure 4.45 Column LD-S3-G60: moment-curvature hysteresis curves for each run.

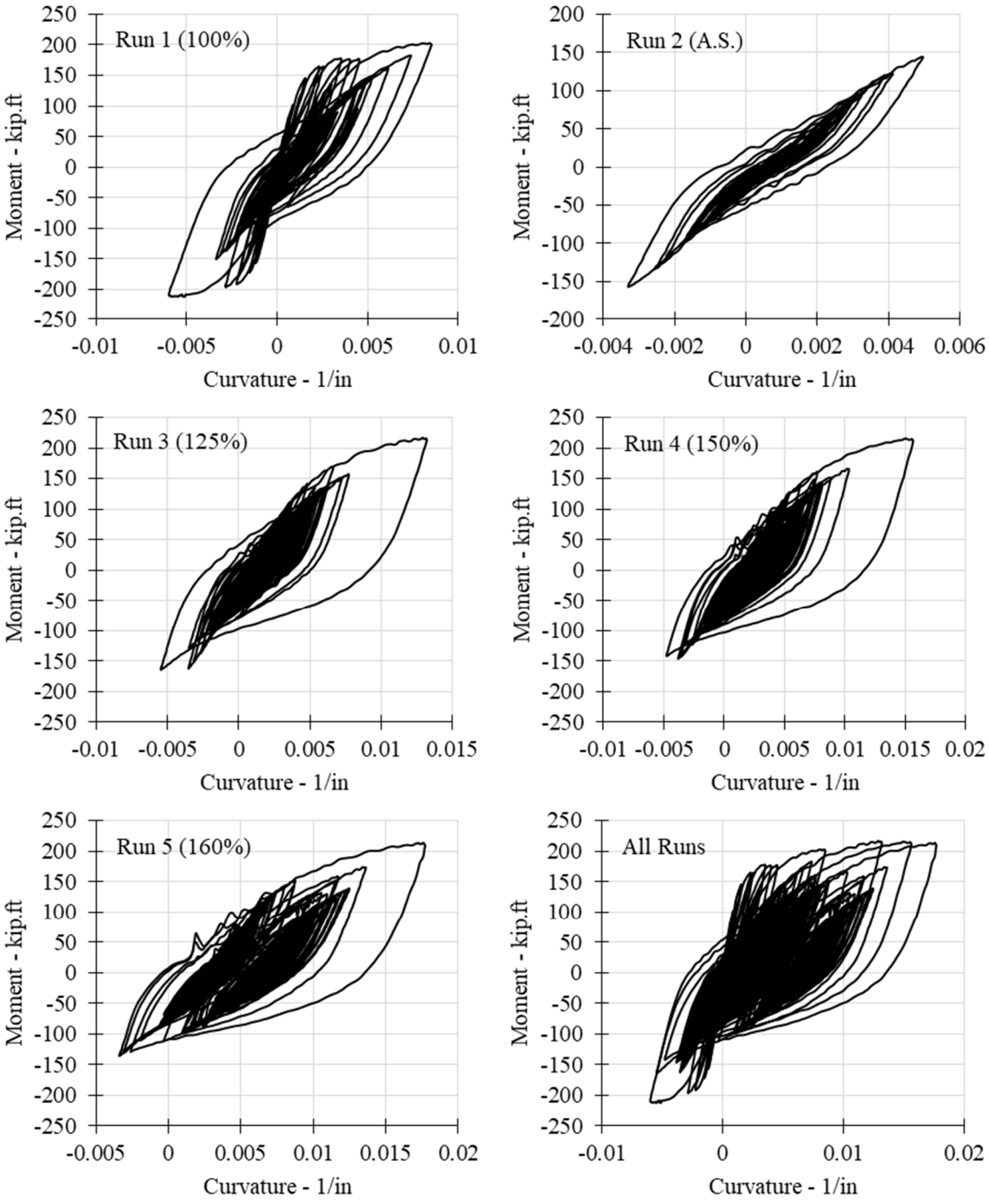

Figure 4.46 Column LD-S1.5-G60: moment-curvature hysteresis curves for each run.

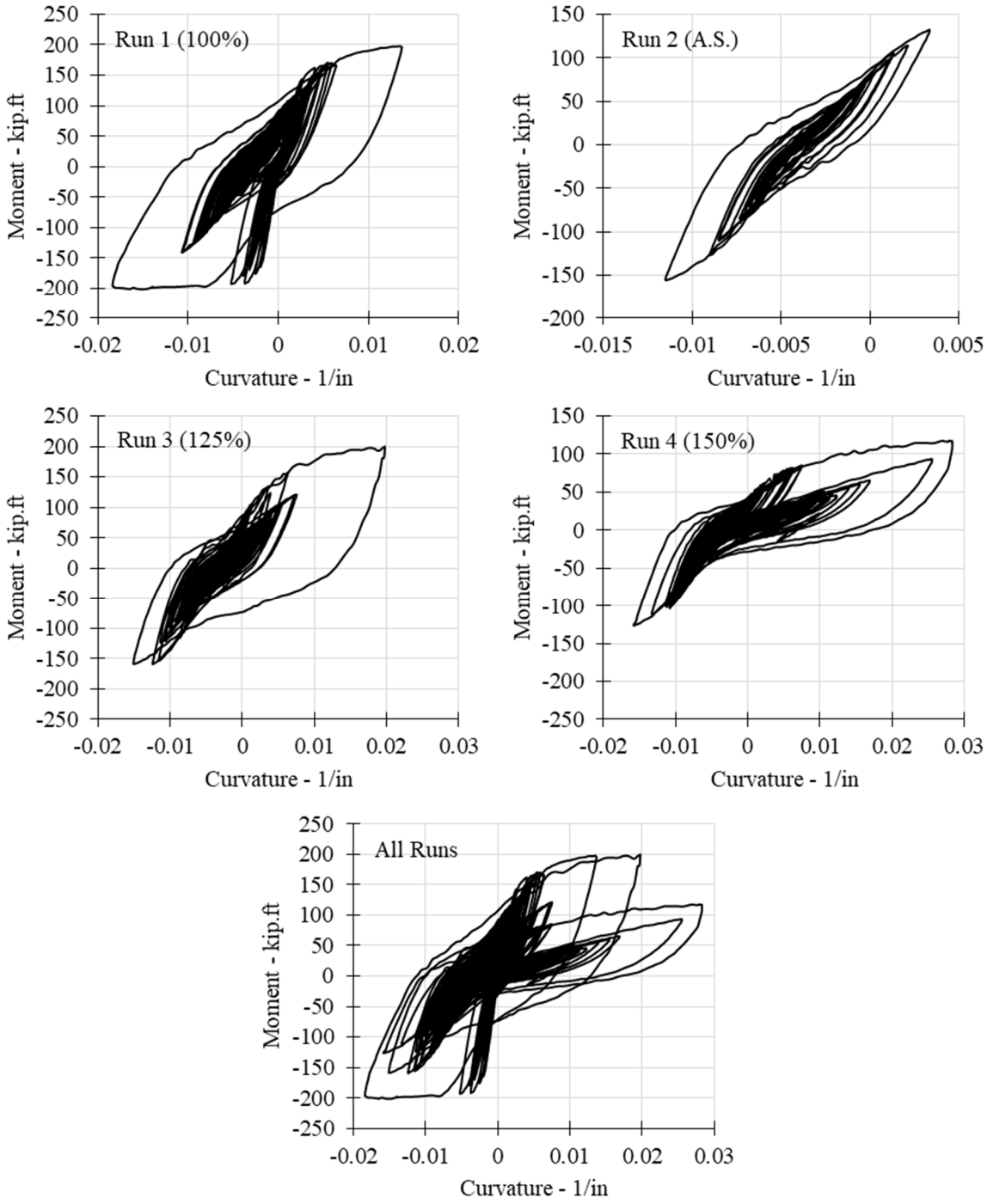

Figure 4.47 Column LD-S3-G60D: moment-curvature hysteresis curves for each run.

4.11 DISCUSSION OF TEST RESULTS

This part of the study aimed at investigating the effect of various design details on seismic response of RC bridge columns under long-duration ground motions. Three large-scale columns were designed and subjected to shake table tests under the same long-duration earthquake record. The effect of transverse steel spacing and longitudinal bar debonding in the plastic-hinge zone were of special interest.

The seismic performance of the columns was satisfactory. All columns performed in a ductile manner and underwent significant displacements. Good energy dissipation was observed based on the wide hysteresis force-displacement relationship loops. As intended, the columns had flexural-dominated behavior; damage was concentrated in the plastic hinges. The failure mode was flexural due to longitudinal bar fracture associated with low-cycle fatigue life of reinforcing bar.

Using smaller spacing for transverse reinforcement improved column performance significantly, with about 50% larger displacement capacity under long-duration ground motions. Debonding of the longitudinal bars at the column–footing interface also improved performance, but it was less effective than increased confinement, with about 20% increase in the displacement capacity attributed to the spread of yielding in the plastic-hinge zone. Note: the varied design/detailing parameters affected only the seismic performance of the columns in the nonlinear range, i.e., the initial stiffness and first yield were the same for all columns.

5 Phase II: Experimental Results

5.1 OVERVIEW

This chapter provides the results of the second phase of the experimental program including observations and measured results from the shake table tests. In Phase II, three columns were tested under long- and short-duration motions. The columns were reinforced with high-strength reinforcing bars (HSRB) and were designated as: LD-S1.5-G100; SD-S3-G100; and LD-S3-G100. The first column was tested on the shake table under 2011 Tohoku main shock. The second column was subjected to a short-duration motion from 1999 Kocaeli earthquake that was scaled by a factor of 3.68 to be spectrally close to the long-duration motion; see Chapter 2. The third column used the Tohoku ground motion but with a different loading protocol. That loading protocol for the third column began with 25% of Tohoku ground motion and then incrementally amplified until failure was obtained at 100%.

The damage state of the test columns was tracked by visual observations at potentially critical locations during and after each run of earthquake motion. The data was collected using the instruments described in Chapter 3. Displacements, forces, strains, rotations, and curvatures were the key measured response parameters, which are described in this chapter along with summary of the responses during each run presented in tables and figures.

5.2 DAMAGE OBSERVATIONS

Similar to Phase I specimens, the columns were painted with a thin layer of whitewash before placing the specimens on the shake table to facilitate locating and marking cracks. The initial cracks due to construction, shrinkage, and temperature effects were marked with a purple crayon and labeled with number zero before starting the test. Figure 5.1 through Figure 5.3 show the columns plastic hinges before starting the tests. Four cameras were installed on the footing pointed toward the column plastic hinges to monitor the progression of damage in the columns during each run. The damage was then visually inspected, and cracks were marked and labeled according to the run number after each run. Figure 5.4 through Figure 5.6 show the progression of damage in the columns after each run. As expected, extensive damage was concentrated at the columns' plastic hinges (lower north and south sides of the columns); the upper two-thirds of the columns remained damage free during the entire test sequence. The damage progression for all three columns was similar to that observed for Phase I columns. The observed behavior and measured

responses of the columns are discussed below. The footing and loading head were also examined for any damage during the test. No damage was detected.

Figure 5.1 Column LD-S1.5-G100 before starting the test.

Figure 5.2 Column SD-S3-G100 before starting the test.

Figure 5.3 Column LD-S3-G100 before starting the test.

Figure 5.4 Column LD-S3-G100: progression of damage after the first run.

Figure 5.5 Column SD-S1.5-G100: progression of damage after the first run.

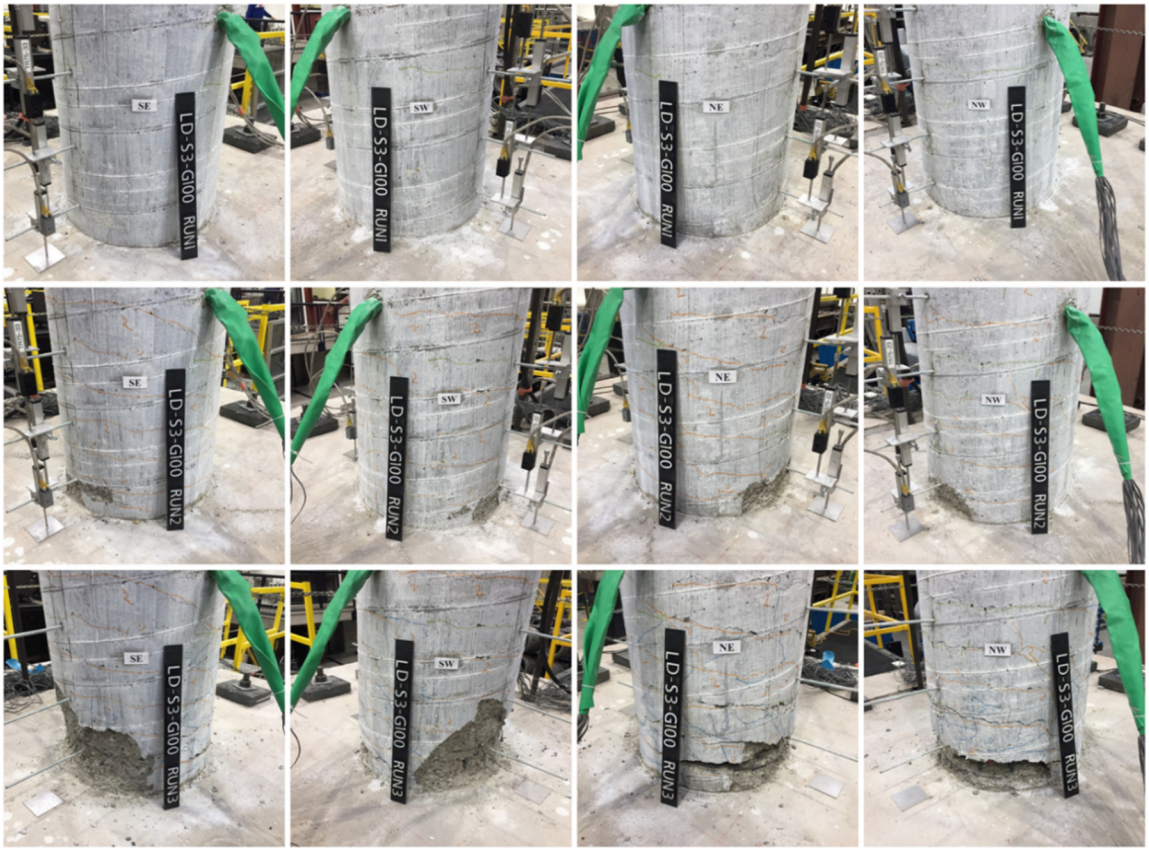

Figure 5.6 Column LD-S3-G100: progression of damage after each run.

5.2.1 Column LD-S1.5-G100

This column was tested under 100% of the 2011 Tohoku earthquake. The damage in the column started with flexural cracks and yielding in the longitudinal reinforcement. The first HSRB rupture happened at around 62 sec into the long-duration motion when the motion reached the peak acceleration; this took place on the north side of the column. Subsequently, three more HSRBs on the north side ruptured before the end of the ground-motion record. The damage on the column continued after bar rupture manifested in major spalling of the cover concrete on both south and north sides of the specimen. The spirals and longitudinal bars were exposed on the north side. The height of spalling on the south and north sides was about 4 and 5 in., respectively. Since there was

the risk of having the column or test setup becoming unstable after the many sudden bar fractures and extensive concrete damage, the shake table test was stopped a few seconds before completing the intended full ground motion. Figure 5.7 presents the final damage state of Column LD-S1.5-G100 after the shake table was stopped.

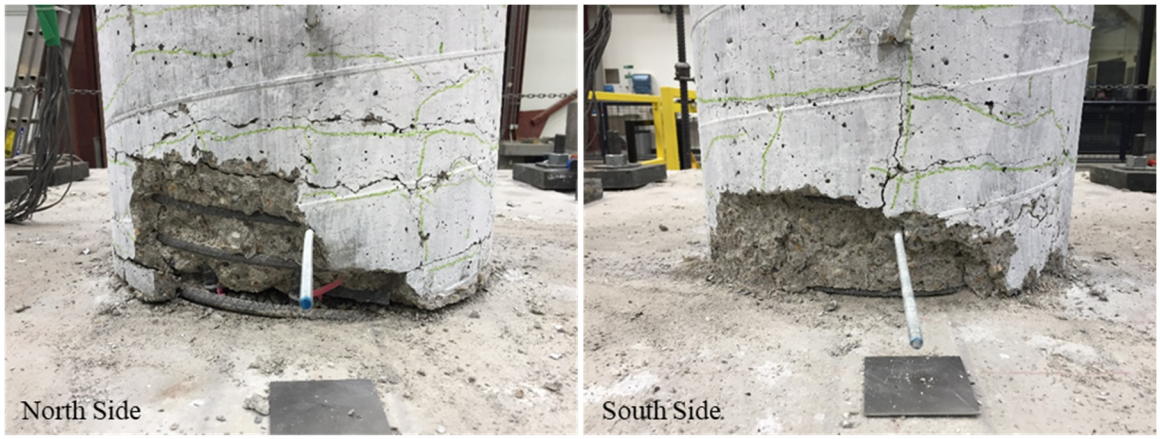

Figure 5.7 Column LD-S1.5-G100: final damage state.

5.2.2 Column SD-S3-G100

Similar to the previous column, flexural cracks formed, and the longitudinal bars yielded in the beginning of the run (the scaled 1999 Kocaeli earthquake). Some cover concrete spalling occurred in the loading direction. When the applied motion reached its PGA, one longitudinal HSRB on the north side fractured. In the following loading cycles within the same ground motion, a second HSRB fractured, and cover spalling progressed along the plastic hinge, exposing both spiral and longitudinal bars. Cover spalling increased to about 10 and 6.5 in. along the column height on the south and north sides, respectively. Three bars on the north side and two bars on the south side buckled. Figure 5.8 presents the final damage state of Column SD-S3-G100.

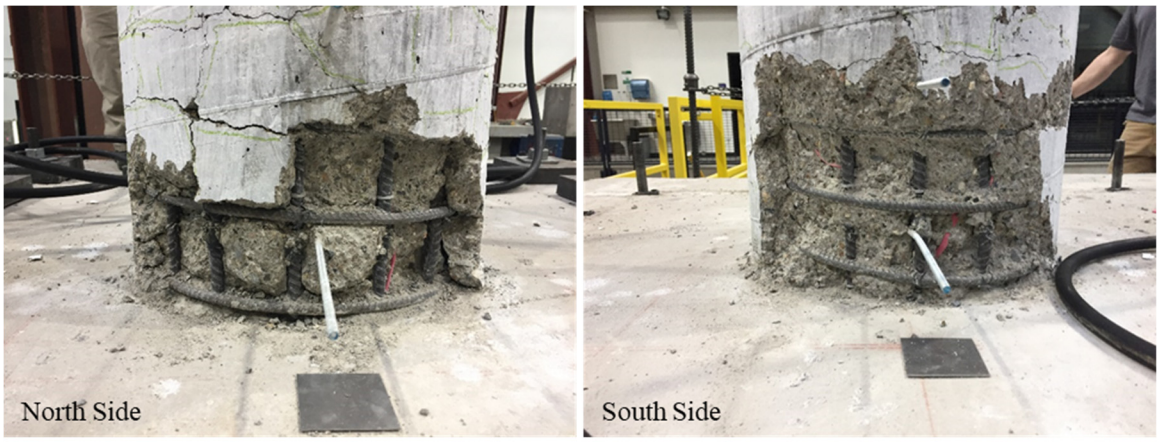

Figure 5.8 Column SD-S3-G100: final damage state.

5.2.3 Column LD-S3-G100

The loading protocol for this specimen started with 25% of 2011 Tohoku earthquake. Some flexural cracks were observed along the plastic hinge during this run. In the second run, at 50% of 2011 Tohoku earthquake, cover concrete spalling occurred without exposing the spirals. The height of the spalling was about 3 in. on both the south and north sides. The progress of damage for this column in the third run, i.e., at 100% of 2011 Tohoku earthquake, was similar to that of the first column. Four longitudinal HSRBs ruptured when the motion reached the maximum amplitude around 62 sec into the motion, which also occurred when testing the first column. All four bars were on the north side of the column and ruptured simultaneously. The damage then progressed through the core concrete and caused column instability. The applied motion was then stopped to avoid any damage to the shake table. The final height of spalling on the south and north sides was about 9 and 4.7 in., respectively. Figure 5.9 presents the final damage state of Column LD-S3-G100.

Figure 5.9 Column LD-S3-G100: final damage state.

5.3 ACHIEVED MOTIONS

As explained before, the feedback of the shake table can differ from the target input ground motions because of the interaction between the shake table and the specimen [Thoen and Laplace 2004]. Table 5.1 lists the PGA values for the target and achieved earthquake motions for each test model and for each run. The table also shows the ratio of the achieved to target PGA (Ach./Targ. PGA), and root mean square error ($RMSE_{Sa}$) of the spectral acceleration responses. It can be seen that for the first and third specimens, the achieved motion was closer to the target motions compared to the Phase I specimens; this is a result of the closed-loop iterative control that benefited from the first phase of testing. Figure 5.10 through Figure 5.12 compare the response spectra of the shake table feedback accelerations for each column and in each run with the corresponding target spectra. Table 5.2 lists the target and achieved significant duration of the input motions in each run for completeness.

Table 5.1 Achieved and target motions characteristics.

Specimen	LD-S1.5-G100	SD-S3-G100	LD-S3-G100		
Run #	1	1	1	2	3
Ach. PGA (g)	0.41	0.50	0.12	0.22	0.46
Targ. PGA (g)	0.42	0.47	0.11	0.21	0.42
Ach./Targ.$_{PGA}$	0.98	1.06	1.09	1.05	1.10
RMSESa (g)	0.11	0.12	0.03	0.03	0.03

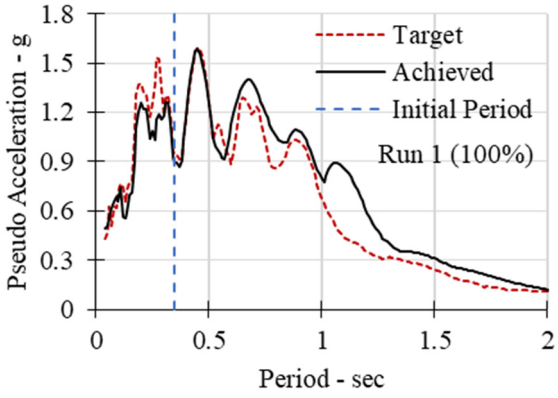

Figure 5.10 Column LD-S1.5-G100: achieved and target response spectra of the first run.

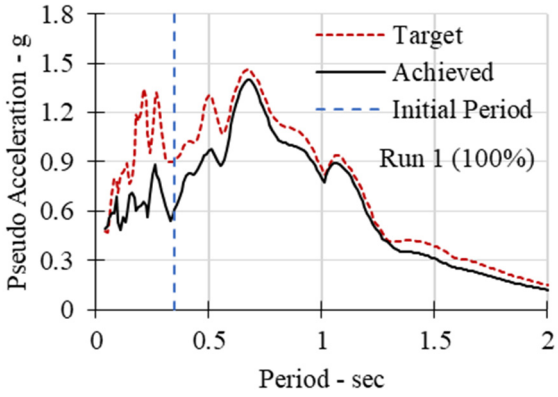

Figure 5.11 Column SD-S3-G100: achieved and target response spectra of the first run.

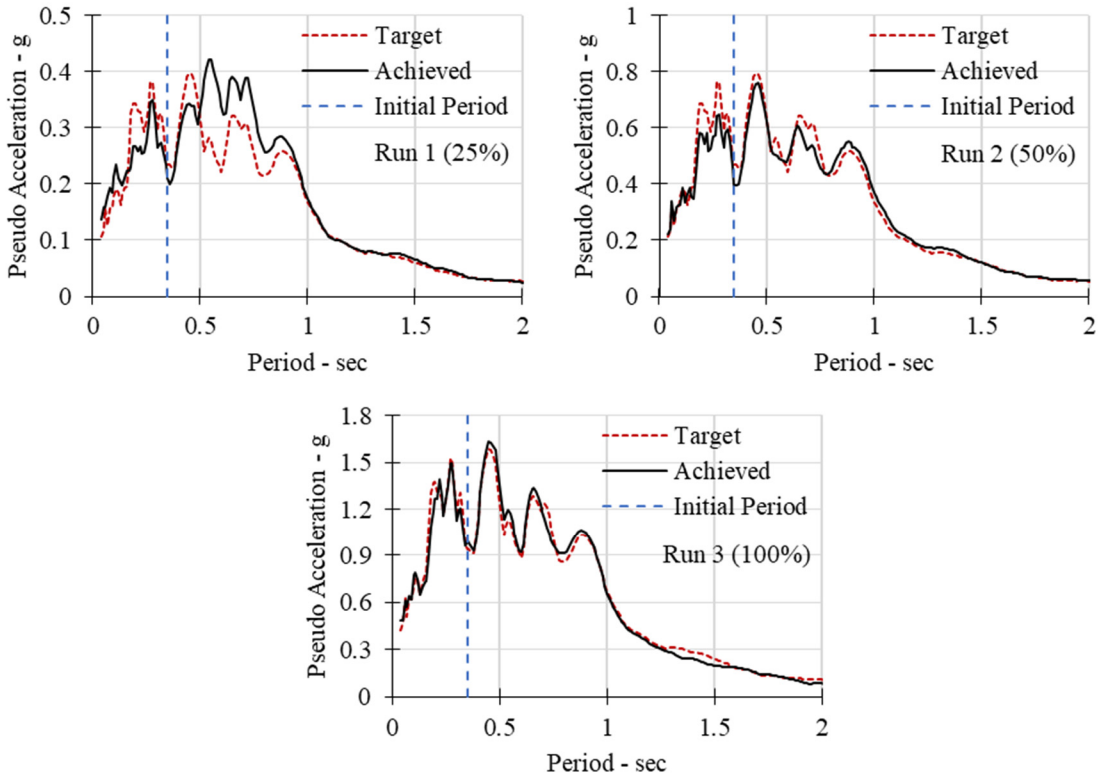

Figure 5.12 Column LD-S3-G100: achieved and target response spectra of each run.

Table 5.2 Achieved significant duration of the input motions in each run.

Specimen	LD-S1.5-G100	SD-S3-G100	LD-S3-G100		
Run #	1*	1	1	2	3*
Ds5-75% (sec)	31.1	5.8	32.8	34.0	28.2
Ds5-95% (sec)	41.5	9.3	64.4	65.9	29.6

Target significant durations: LD motion @ Ds5-75% = 32.9 sec and Ds5-95% = 61.6 sec.
Target significant durations: SD motion @ Ds5-75% = 6.2 sec and Ds5-95% = 9.9 sec.
* Run was not completed due to extensive column damage.

5.4 DISPLACEMENT

The relative displacements at the top of the columns were obtained by subtracting the table displacement from the absolute total column displacements. The histories of the column displacement for each specimen during each run are shown in Figure 5.13 through Figure 5.15. The positive values correspond to displacement toward the south. Drift ratios were determined by the lateral displacement values divided by the column height. The peak displacements of the columns, their respective drift ratios, and residual drift ratios in each run are listed in Table 5.3.

As can be seen in the table, the peak drift ratios for Columns LD-S1.5-G100, SD-S3-G100, and LD-S3-G100 were 7.42%, 9.56%, and 7.53%, respectively. Note: the columns became unstable after bar ruptures and experienced large displacements, and the shake table test was stopped to avoid collapse. The peak displacement of the columns was measured before stopping the table and was considered as the peak displacement.

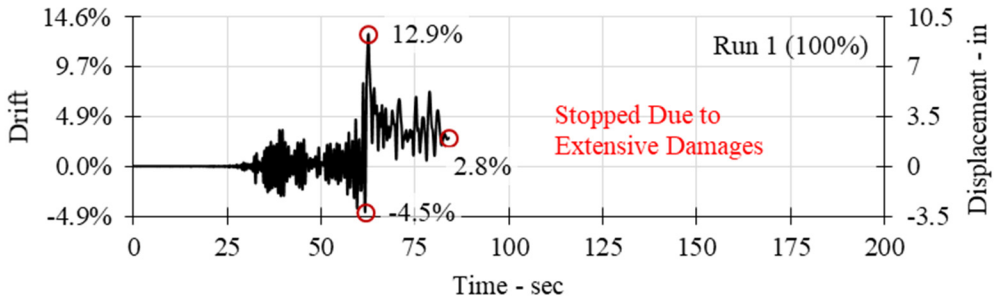

Figure 5.13 Column LD-S1.5-G100: displacement history.

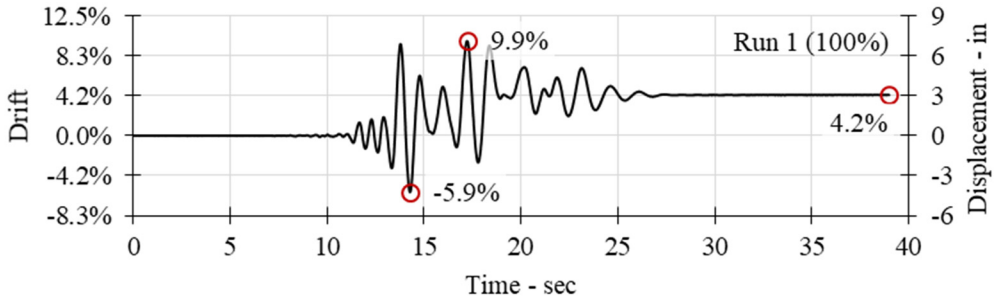

Figure 5.14 Column SD-S3-G100: displacement history.

Table 5.3 Peak responses of the columns in each run (before column collapse).

Specimen	LD-S1.5-G100	SD-S3-G100	LD-S3-G100		
Run #	1	1	1	2	3
Peak disp. (in.)	5.34	6.88	0.94	3.02	5.42
Peak drift (%)	7.42	9.56	0.13	4.2	7.53
Res. drift (%)	2.8	4.2	0.0	0.2	6.8
Peak base shear (kips)	39.4	39.6	21.3	36.6	39.2
Peak bending moment (kip.ft)	236	238	128	220	235

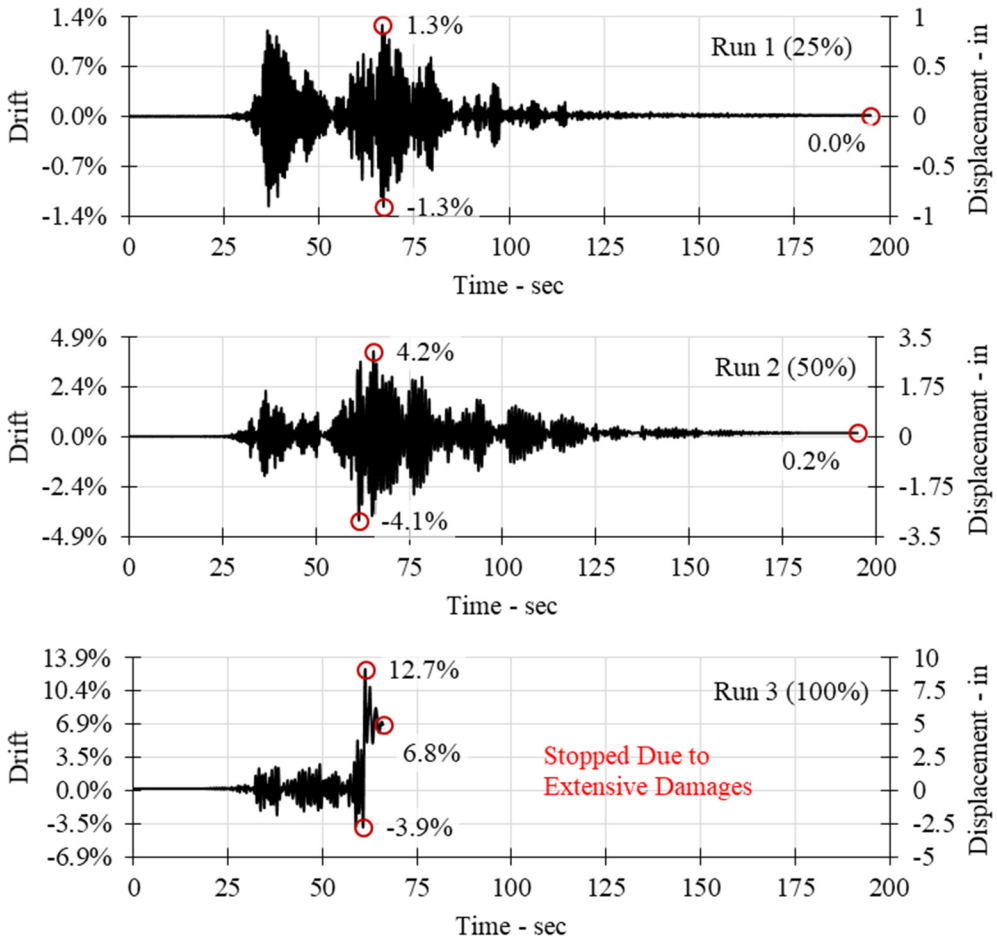

Figure 5.15 Column LD-S3-G100: displacement history.

Peak drift ratios (as well as displacements on the double axis) in each run are also shown in Figure 5.16 for a better comparison. The reader is reminded that both of the first and third columns in Phase II were tested under same long-duration earthquake but had different transverse reinforcement. The first column used tighter spiral pitch, i.e., 1.5 in. for first column versus 3 in. for the third column. Unlike what was observed in Phase I, it is evident that using smaller tie spacing for transverse reinforcement did not improve the performance of those columns with HSRBs under long-duration earthquakes. Another important observation from Phase II is that the second specimen, which was tested under the short-duration motion, showed 25% higher displacement capacity compared to the similar column tested under long-duration motion.

5.5 BASE SHEAR

As mentioned in Chapter 3, the base shear was measured from the load cell located on the mass rig link, which attached the column loading head to the mass rig system (single-degree-of-freedom equilibrium). Figure 5.17 through Figure 5.19 show the histories of the columns' base shear and bending moment. Peak values for each run are also listed in Table 5.3 and shown in Figure 5.20

for a better comparison. The maximum load capacities of the three columns were 39.4, 39.6, and 39.2 kips, respectively. As intended, the three columns had almost the same force capacity as the columns tested in Phase I that used a larger number of conventional Grade 60 bars. It is worth mentioning that the base shear in Columns LD-S1.5-G100 and LD-S3-G100 dramatically dropped after bar rupture, which demonstrates that individual HSRBs had a larger contribution to the column capacity because of their obvious higher stress capacity.

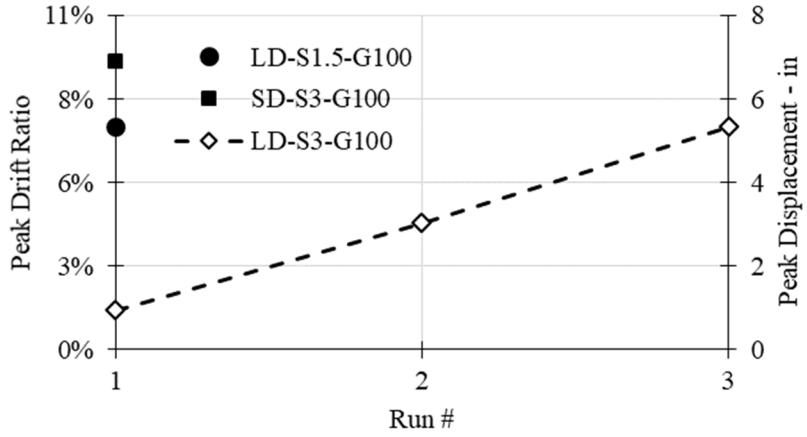

Figure 5.16 Peak drifts ratios (displacements) of the columns in each run.

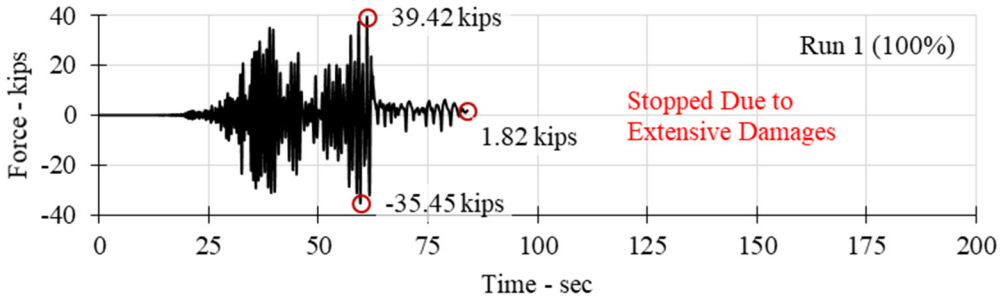

Figure 5.17 Column LD-S1.5-G100: base shear history.

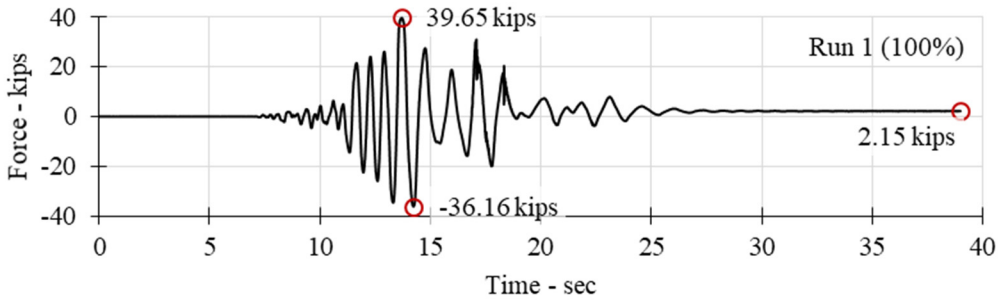

Figure 5.18 Column SD-S3-G100: base shear history.

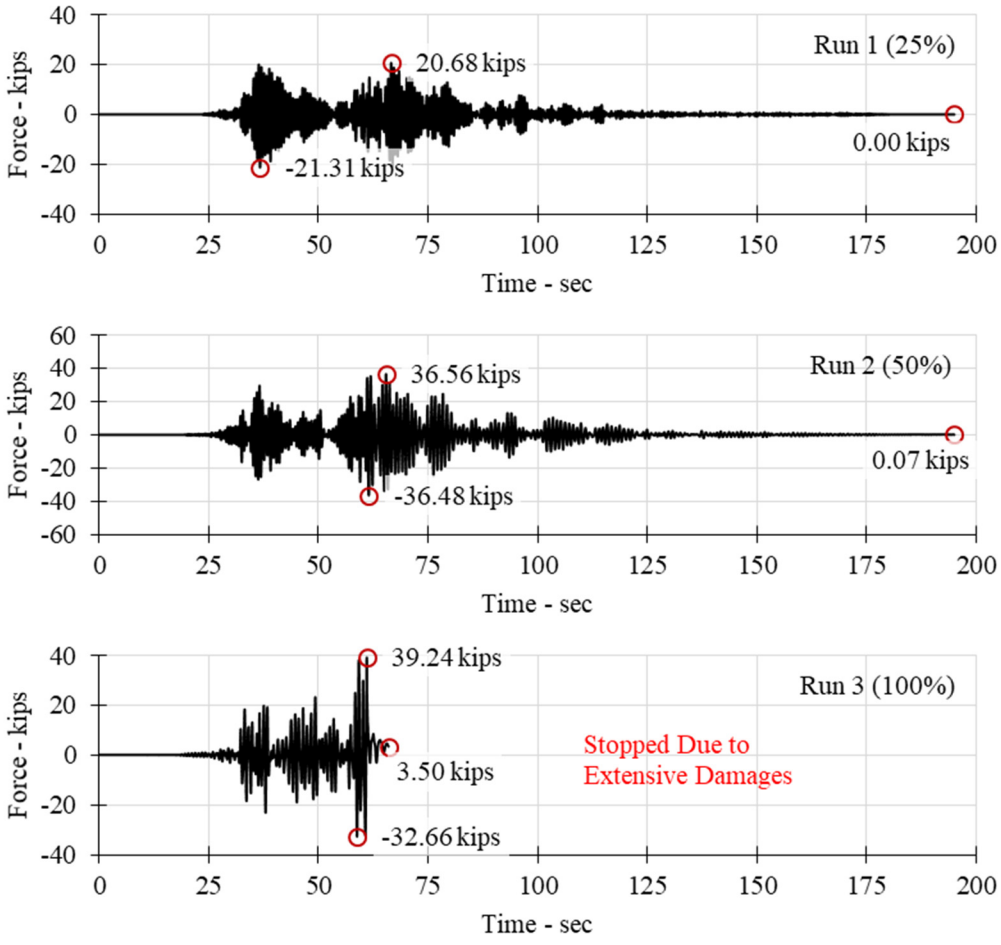

Figure 5.19 Column LD-S3-G100: base shear history.

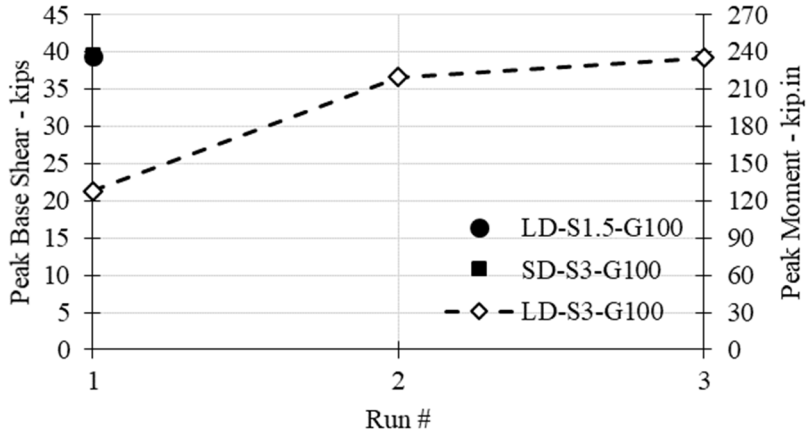

Figure 5.20 Peak base shears and bending moments of the columns in each run.

5.6 FORCE-DISPLACEMENT RELATIONSHIPS

The force-displacement relationships of the specimens during each run are illustrated in Figure 5.21 through Figure 5.23. The positive values correspond to displacement toward the south. Figure 5.24 represents the cumulative force-displacement relationship of the columns along with the envelopes and their respective idealized curves. The narrow hysteresis loops in the columns subjected to the long-duration motion when compared to the Phase I specimens (Figure 4.21 through Figure 4.23) indicate much lower energy dissipation for the columns tested in Phase II. The accumulated dissipated energy during all runs for each column is presented in Figure 5.25. The dissipated energy was determined by calculating the area enclosed by every loop in the force-displacement relationships of the columns. The measured dissipated energy of the columns after each run is listed in Table 5.4. As shown, the dissipated energy was similar for the three columns before the onset of the bar fracture, which caused the drop-in energy in the associated columns.

The idealized curve was used to calculate the displacement ductility and the initial effective stiffness. The displacement ductility was obtained by dividing the ultimate column drift ratio to the effective yield drift ratio as shown before in previous chapters. The first yielding of the longitudinal bars occurred at drift ratios of 1.03% for LD-S1.5-G100, 1.10% for SD-S3-G100, and 1.18% for LD-S3-G100. The first bar fracture for the three columns occurred at 7.42%, 9.56%, and 7.53% drift ratios, respectively, which are considered to be the ultimate drift ratios or the drift capacity. After the idealization of the force-displacement hysteresis curves, the effective yield drift ratios were calculated and found to be 2.91%, 2.84%, and 2.75% for the three columns, respectively. Therefore, the displacement ductility of the three test models were 2.55, 3.37, and 2.74, respectively. The initial effective stiffness of the columns (the slope of the elastic branch of the idealized curve) were 17.6, 18.4, and 18.6 kips/in., respectively. The discussed results of the ductility analysis of the columns are also summarized in Table 5.5 for convenience.

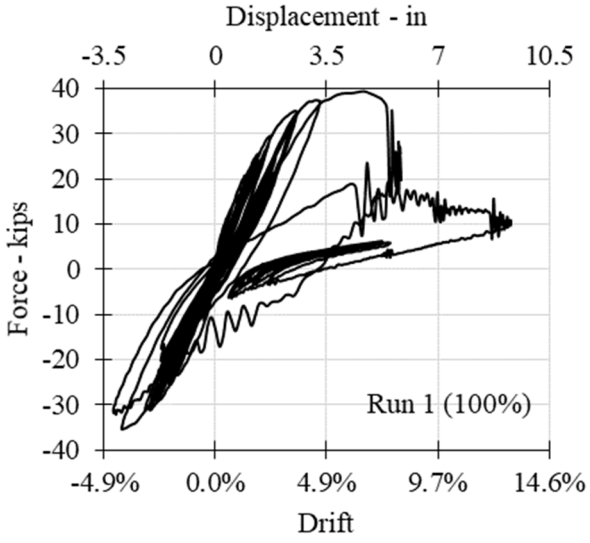

Figure 5.21 Column LD-S1.5-G100: force-displacement hysteresis curves.

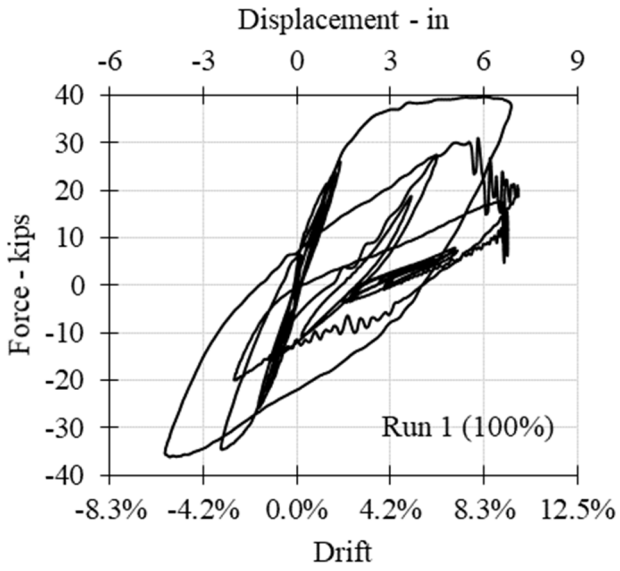

Figure 5.22 Column SD-S3-G100: force displacement hysteresis curves.

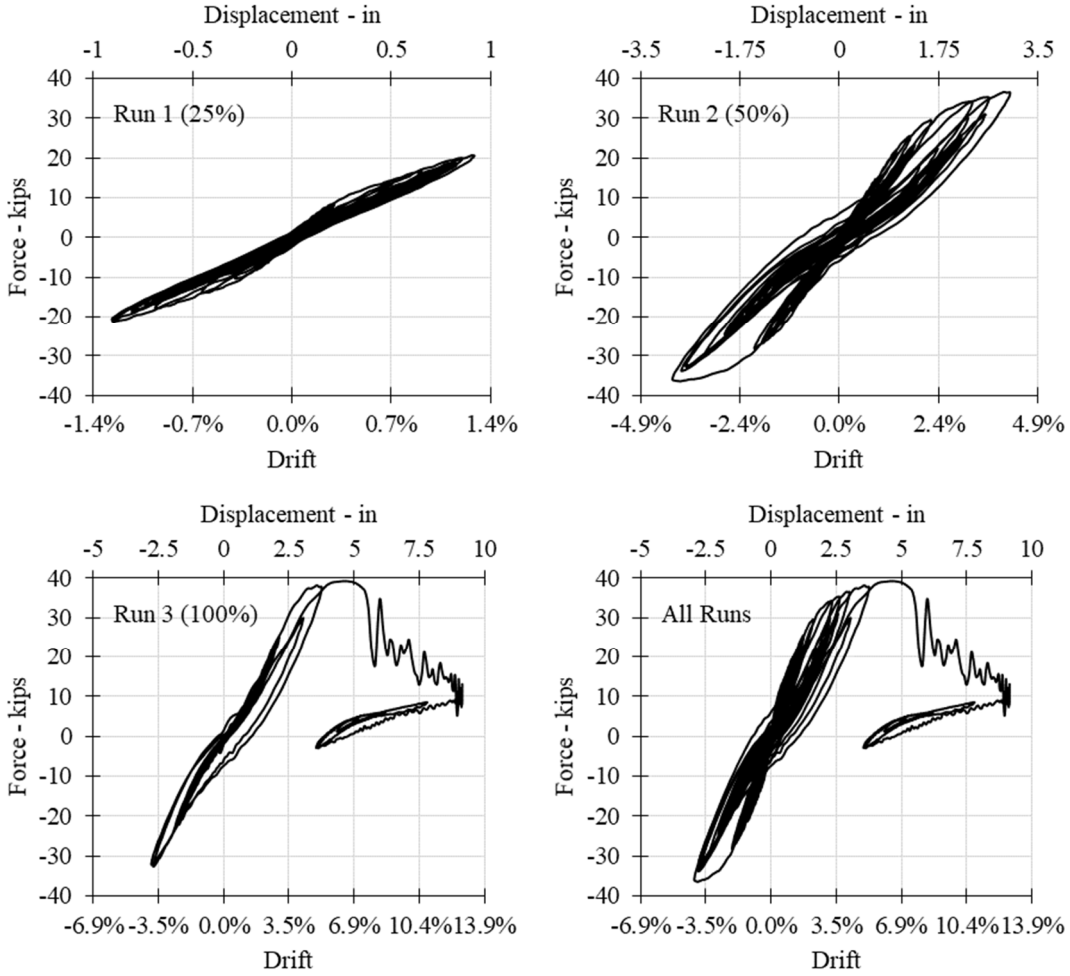

Figure 5.23 Column LD-S3-G100: force displacement hysteresis curves.

Table 5.4 Cumulative energy dissipation of the columns after each run.

Specimen	LD-S1.5-G100	SD-S3-G100	LD-S3-G100		
Run #	1	1	1	2	3
Dissipated energy (kip.ft)	52.0	53.2	9.8	48.8	79.9

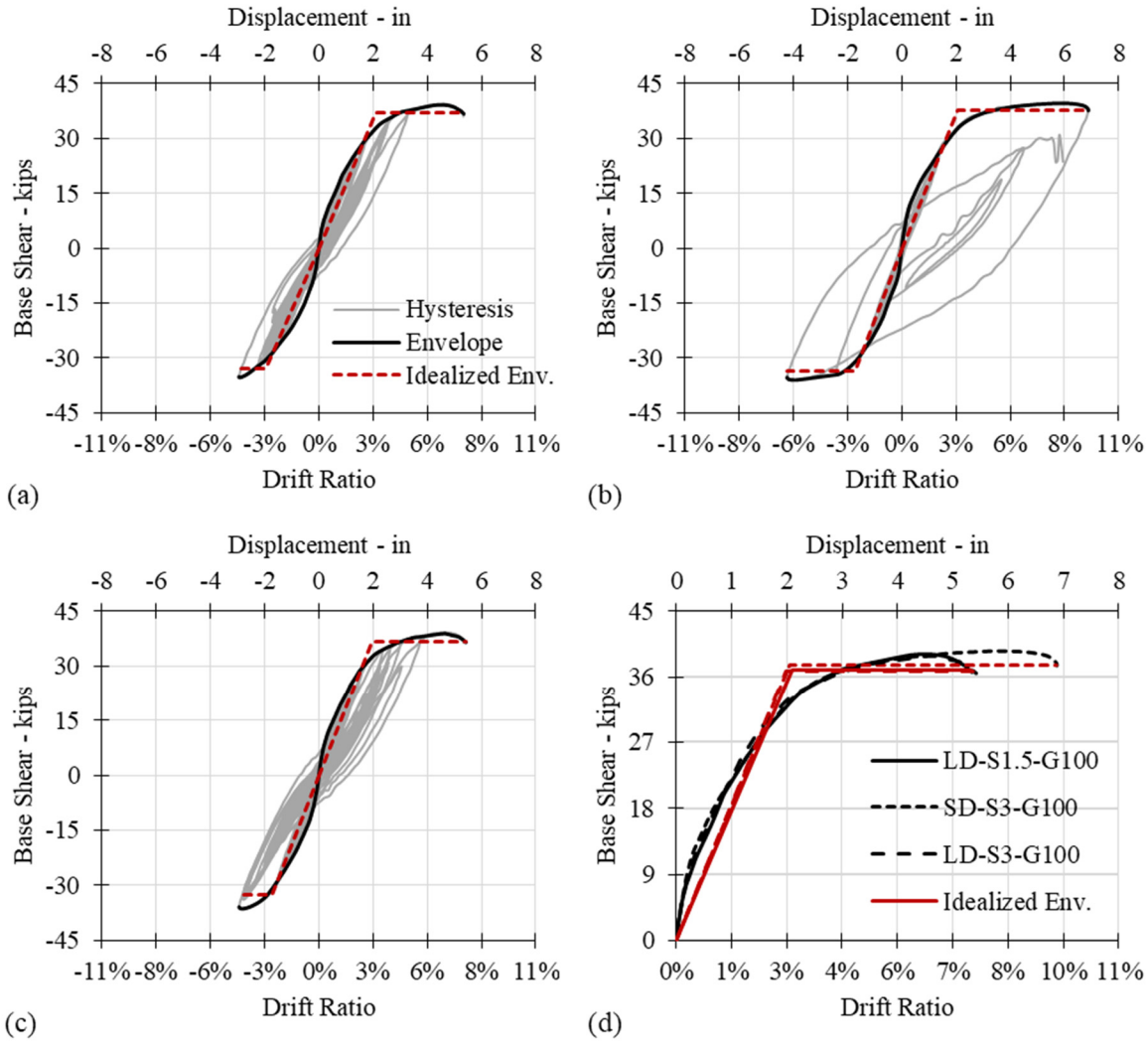

Figure 5.24 Cumulative force-displacement relationships, envelopes, and idealized envelopes.

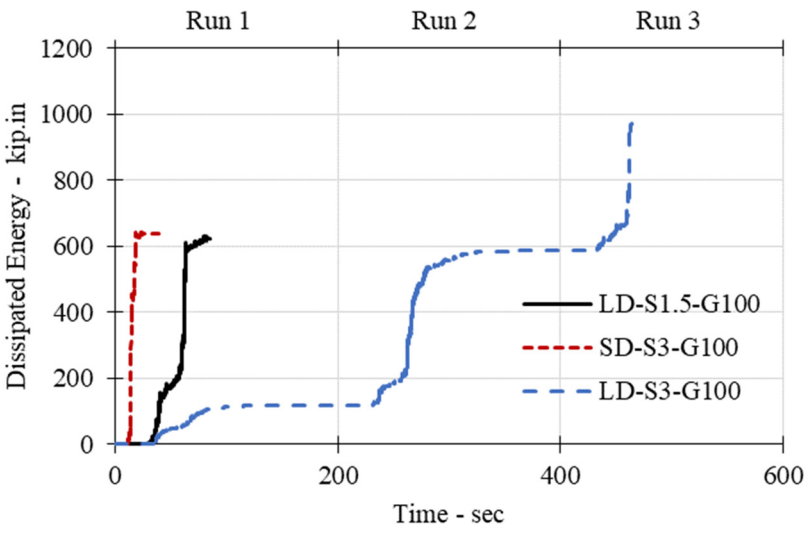

Figure 5.25 Accumulated dissipated energy during all runs.

Table 5.5 Ductility capacity of the columns.

Specimen	LD-S1.5-G100	SD-S3-G100	LD-S3-G100
Yield drift (%)	2.91	2.84	2.75
Ultimate drift (%)	7.42	9.56	7.53
Ductility	2.55	3.37	2.74

5.7 PARK AND ANG DAMAGE INDEX

Similar to Phase I of the experimental program, the Park and Ang DI [1985] and probabilities of damage were calculated for each specimen and after each run [using Equation (4.1)]. This is to quantify the seismic damage in the columns and perform a more accurate comparison between the columns. The ultimate displacement (δ_u) sustained by the reference column was determined from previous experiment and taken as 9.8 in. [Phan et al. 2005]. Since the columns experienced large displacements and lost significant force capacity after bar rupture, the maximum displacement demand (δ_m) of the columns was taken as the column's peak displacement before collapse. The yield force (F_y) was taken as 30 kips from current test results. These damage probabilities were further compared with the actual damage in the columns. Table 5.6 lists the calculated DI, actual damage, and damage probabilities obtained from the fragility curves. The predicted lower damage states (before bar fracture), corresponding to the calculated DI for all three columns, correlated well with the actual damage states. Note: the Park and Ang DI and the experimental fragility curves utilized in this study did not predict correctly the columns' bar fracture damage state; it underestimated the final damage in all three columns.

Table 5.6 Park and Ang damage index of the columns in each run.

Specimen	LD-S1.5-G100	SD-S3-G100	LD-S3-G100		
Run #	1	1	1	2	3
Disp. term	0.54	0.70	0.10	0.31	0.55
Energy term	0.32	0.33	0.06	0.30	0.49
Damage index	0.86	1.03	0.16	0.61	1.04
Predicted damage	E.R.	E.R.	-	M.S.	E.R.
Actual damage	B.F.	B.F.	-	M.S.	B.F.

Damage States: Minor Spalling (M.S.); Extensive Spalling (E.S.); Exposed Reinforcement (E.R.); Longitudinal Bar Buckling (B.B.); and Longitudinal Bar Fracture (B.F.)

5.8 DYNAMIC PROPERTIES

Per Chapter 4, three different methods were used to obtain the natural periods (frequencies) of the columns. The first method utilized the FRF, which correlated the column top's acceleration to the input from the white-noise tests. The second method used the stiffness values from linear fitting of the force-displacement hysteresis curves. The effective stiffnesses (k_{eff}) was used in the third method, obtained by measuring the slope of the line connecting the maximum and minimum displacements in the largest cycle of each run on the hysteresis force-displacement relationship loops. Table 5.7 lists the obtained periods from each method. Figure 5.26 shows the elongation of period for each specimen after the seismic damage as computed using the three methods.

The initial slope of the idealized force-displacement curves resulted in initial periods of 0.52, 0.55, and 0.58 sec for the LD-S1.5-G100, SD-S3-G60 and LD-S3-G100 test models, respectively. The calculated column stiffness and column stiffness degradation per the different methods mentioned above are shown in Table 5.8 and Figure 5.27, respectively. All figures clearly show the elongation of the periods, i.e., the stiffness degradation for all test models as nonlinearity spread in the columns' plastic hinges. The relatively higher periods of Column LD-S3-G60D are an indicator of the greater damage that occurred in this column.

The equivalent hysteretic nonlinear damping ratio for the columns was calculated for each half-cycle of the force-displacement relationship curve [Varum 2003]; see Equation (4.2). The equivalent hysteretic damping ratios calculated for the columns in each run are summarized in Table 5.9 for completeness.

Table 5.7 Period of the columns in each run calculated using three methods.

Specimen	LD-S1.5-G100	SD-S3-G100	LD-S3-G100		
Run #	1	1	1	2	3
White noise (sec)	0.78	0.78	0.4	0.75	0.78
Linear fit (sec)	0.80	1.13	0.58	0.83	0.90
Largest cycle (sec)	0.98	1.10	0.61	0.83	0.97

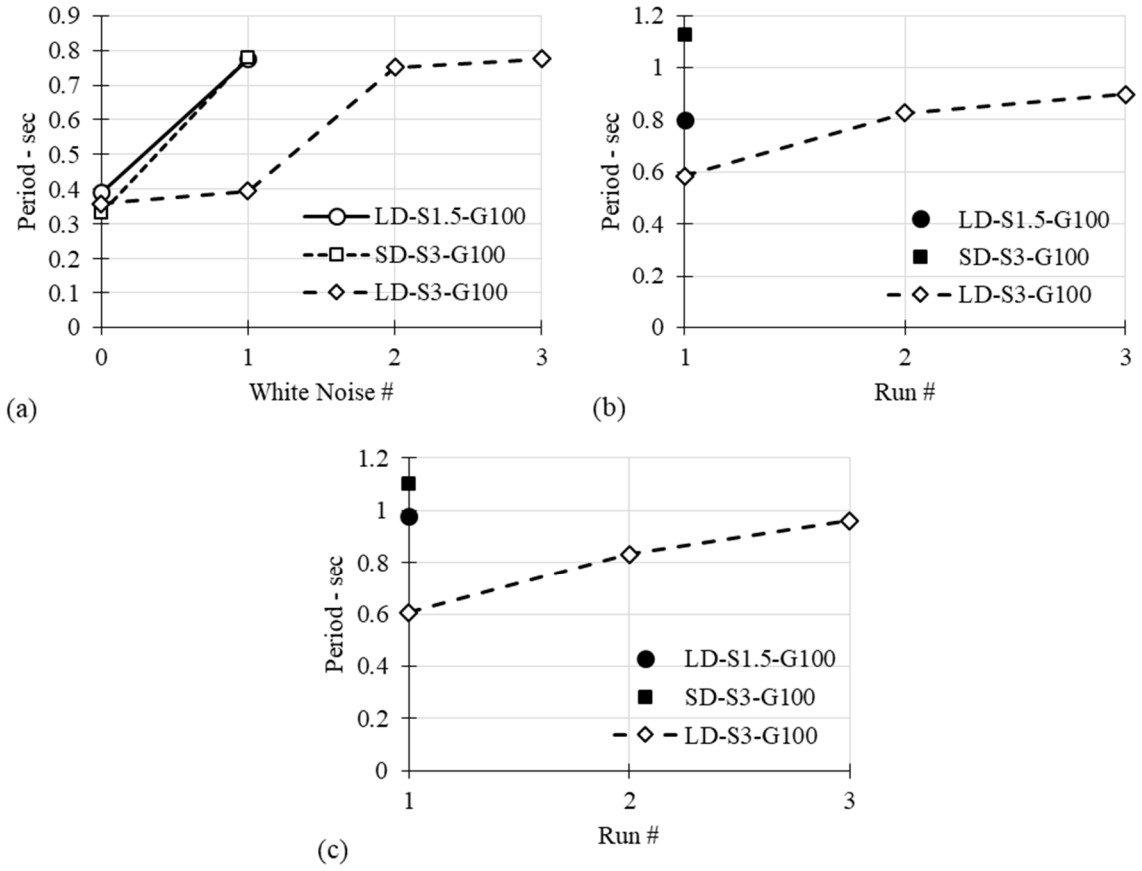

Figure 5.26 **Elongation of columns periods calculated by (a) FRF; (b) linear fit; (c) largest cycle.**

Table 5.8 **Stiffness of the columns in each run calculated using three methods.**

Specimen	LD-S1.5-G100	SD-S3-G100	LD-S3-G100		
Run #	1	1	1	2	3
White noise (k/in)	13.4	13.4	51.1	14.5	13.4
Linear fit (k/in)	12.8	6.4	24.3	11.9	10.1
Largest cycle (k/in)	8.5	6.8	22.0	11.9	8.7

Table 5.9 **Equivalent hysteretic damping ratios of the columns.**

Specimen	LD-S1.5-G100	SD-S3-G100	LD-S3-G100		
Run #	1	1	1	2	3
Hysteretic damping (%)	11.5	8.3	3.7	7.5	22.5

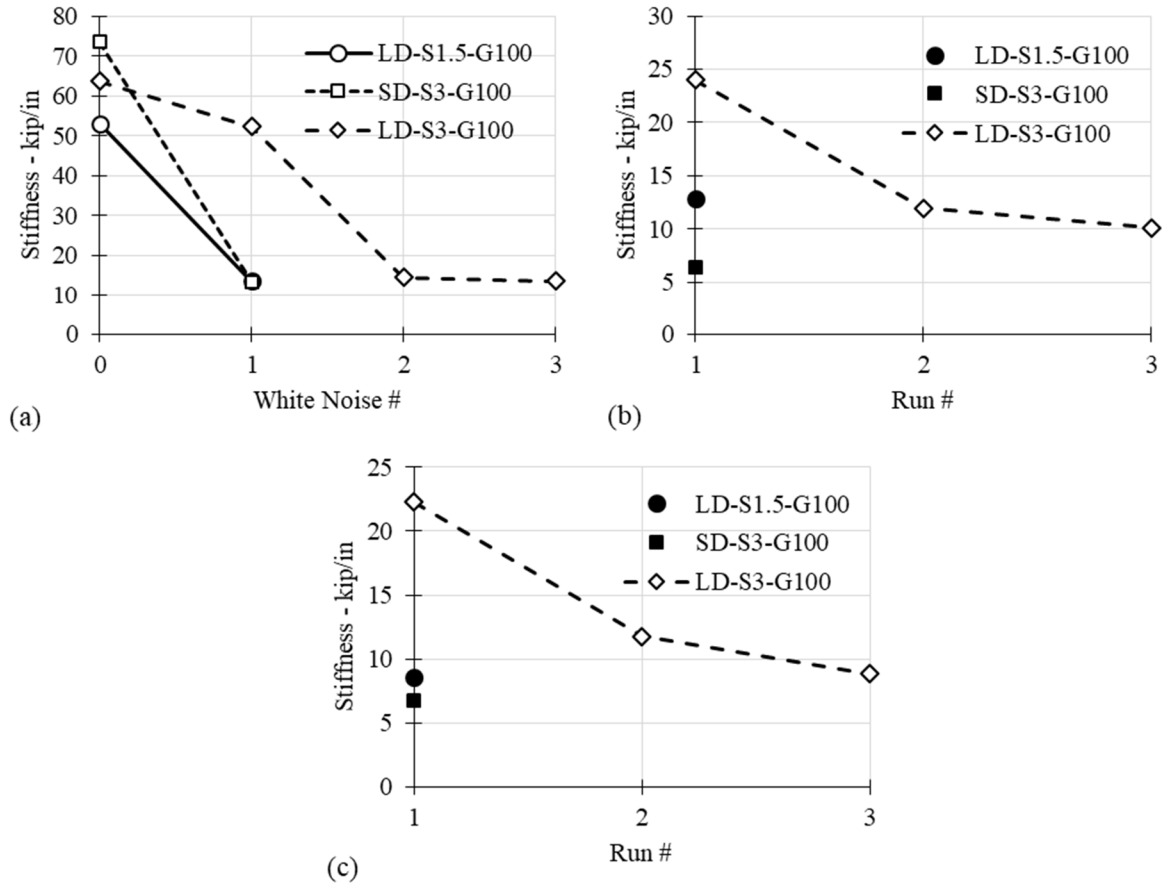

Figure 5.27 Variation of columns stiffnesses calculated by (a) FRF; (b) linear fit; and (c) largest cycle.

5.9 STRAINS

Strains were measured on the longitudinal and transverse reinforcement in the columns during the tests. The strain history of the extreme northern and southern longitudinal bars at or close to the column–footing interface is shown in Figure 5.28 through Figure 5.33. Additional figures include the strain profiles, shown in Figure 5.34 through Figure 5.36, which present the peak measured strains of the extreme northern and southern longitudinal bars at each level along the columns' plastic hinges as strain percentage and ratio of the yield strain. The gray points of the strain profiles were not recorded properly due to malfunction of the strain gauges and were estimated based on the data of the other strain gauges. Strain values for the runs in which rupture occurred are shown in red. As expected, the figures show that the interface strains are the greatest. Note: most of the plastic strains occurred within upper 30 in. from the footing face for all columns. For the first and third specimens (subjected to the long-duration motion), strains were better distributed along the length of the plastic hinge. For the second specimen (subjected to the short-duration motion), strains were mostly concentrated in the vicinity of the column–footing interface.

The peak strain of the longitudinal bars for each column and for each run before bar ruptures are listed in Table 5.10 and shown in Figure 5.37 for comparison purposes. Column SD-S3-G100 experienced higher strain ductility compared to the other two columns, which exhibited close values for strain ductility. The maximum measured strain in the spirals for the three test models was 0.2, 0.4, and 0.4 of the yield strain, respectively. Note: no yielding occurred in the columns spiral, and the HSRB rupture occurred before engaging more confinement in the core concrete.

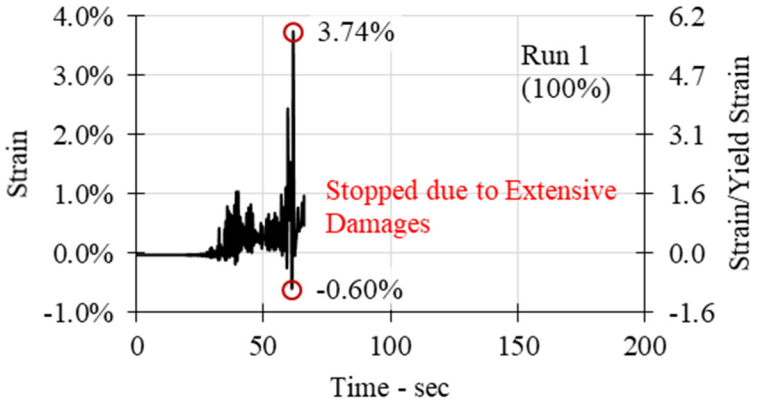

Figure 5.28 **Column LD-S1.5-G100: strain history of the northern longitudinal bar during the first test run (strain gauge 109).**

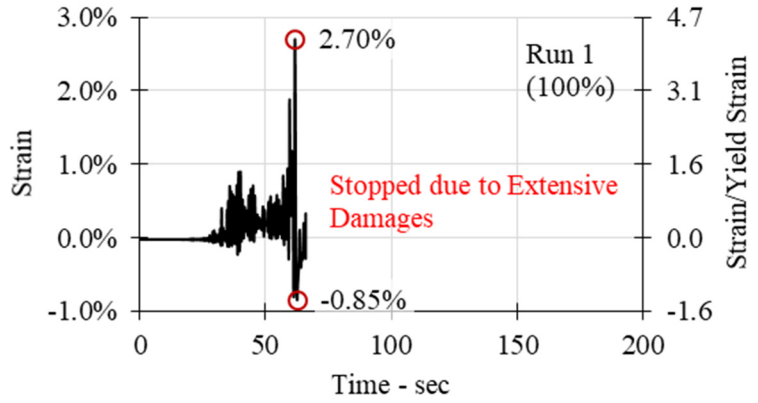

Figure 5.29 **Column LD-S1.5-G100: strain history of the southern longitudinal bar during the first test run (strain gauge 111).**

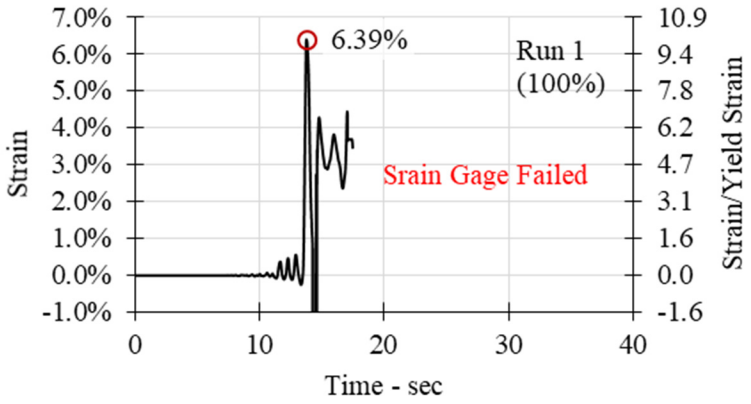

Figure 5.30 **Column SD-S3-G100: strain history of the northern longitudinal bar during the first test run (strain gauge 108).**

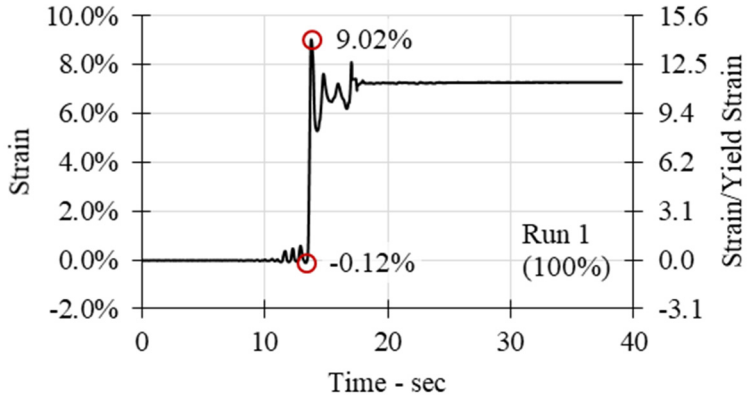

Figure 5.31 **Column SD-S3-G100: strain history of the southern longitudinal bar during the first test run (strain gauge 110).**

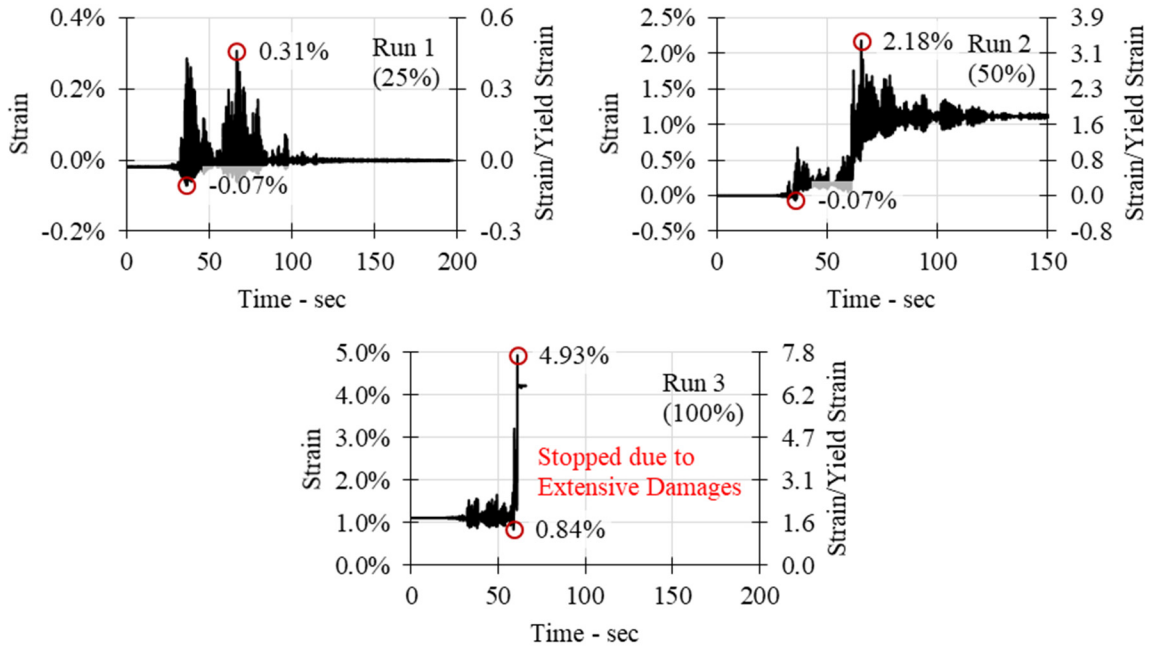

Figure 5.32 **Column LD-S3-G100: strain histories of the northern longitudinal bar during each test run (strain gauge 108).**

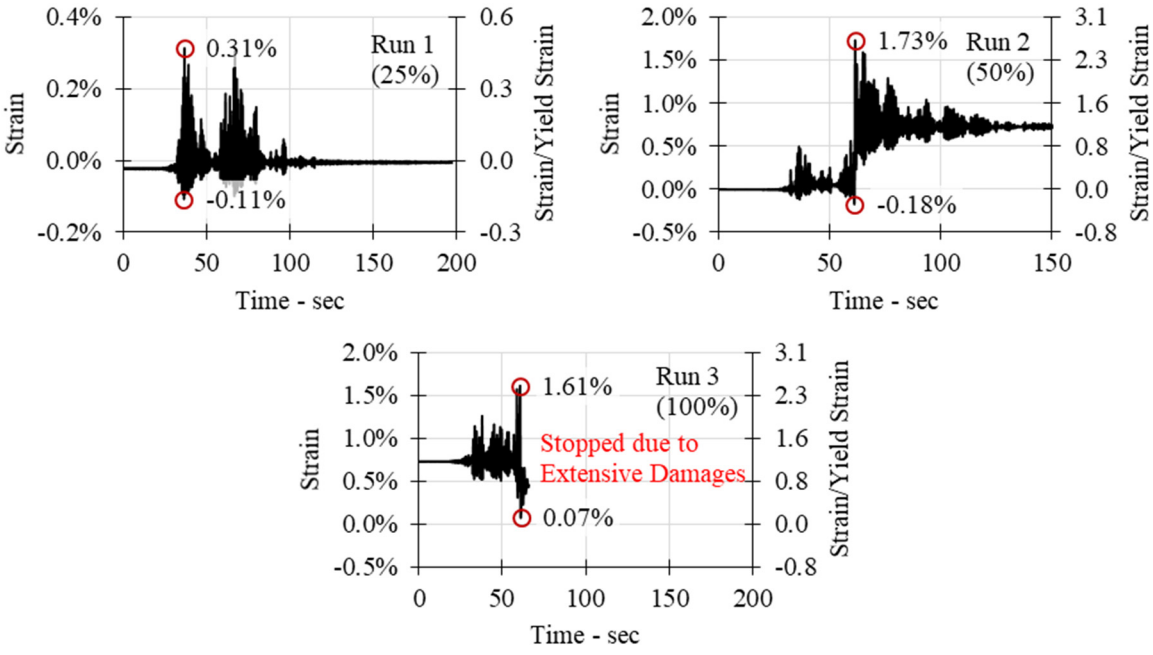

Figure 5.33 **Column LD-S3-G100: strain histories of the southern longitudinal bar during each test run (strain gauge 111).**

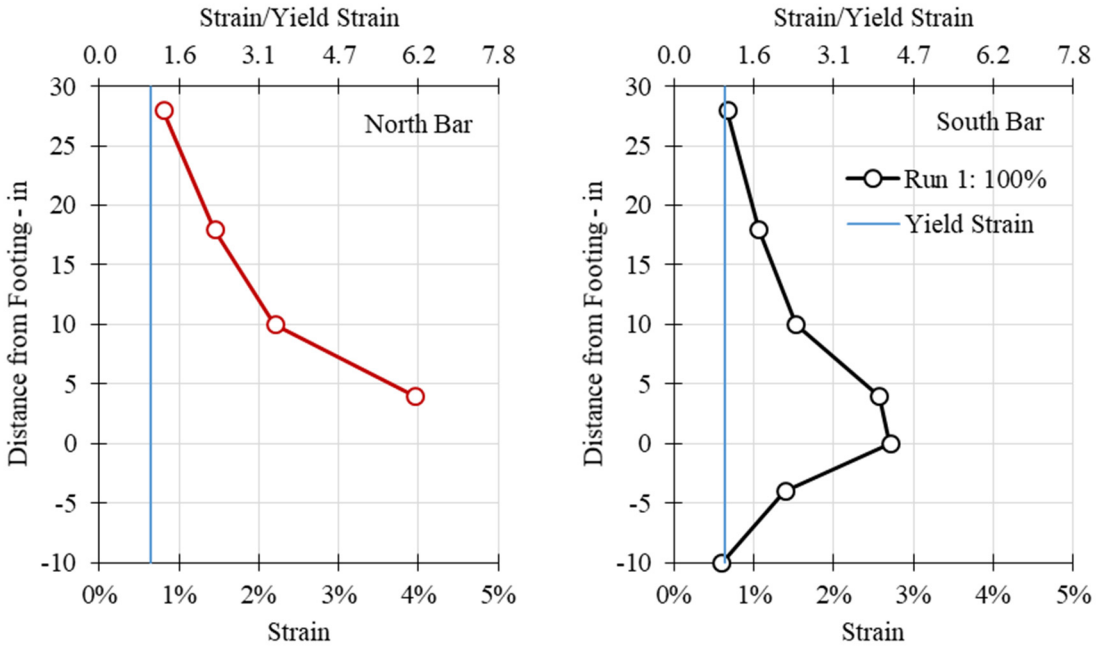

Figure 5.34 **Column LD-S1.5-G100: strain profile of the northern and southern longitudinal bars along the plastic hinge during the first test run.**

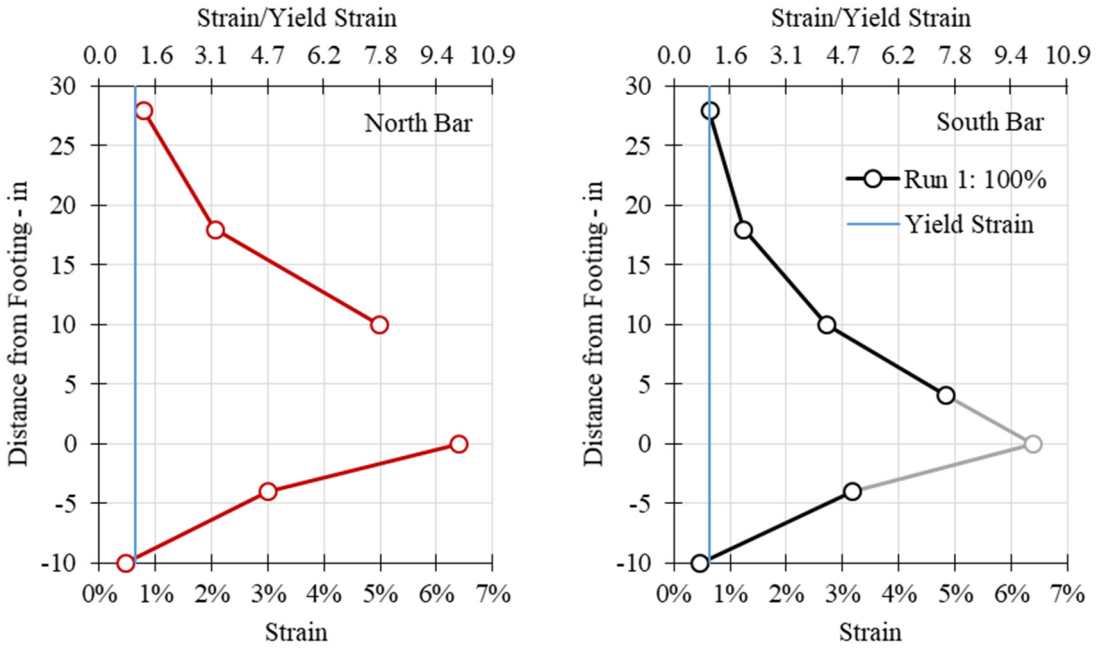

Figure 5.35 **Column SD-S3-G100: strain profile of the northern and southern longitudinal bars along the plastic hinge during the first test run.**

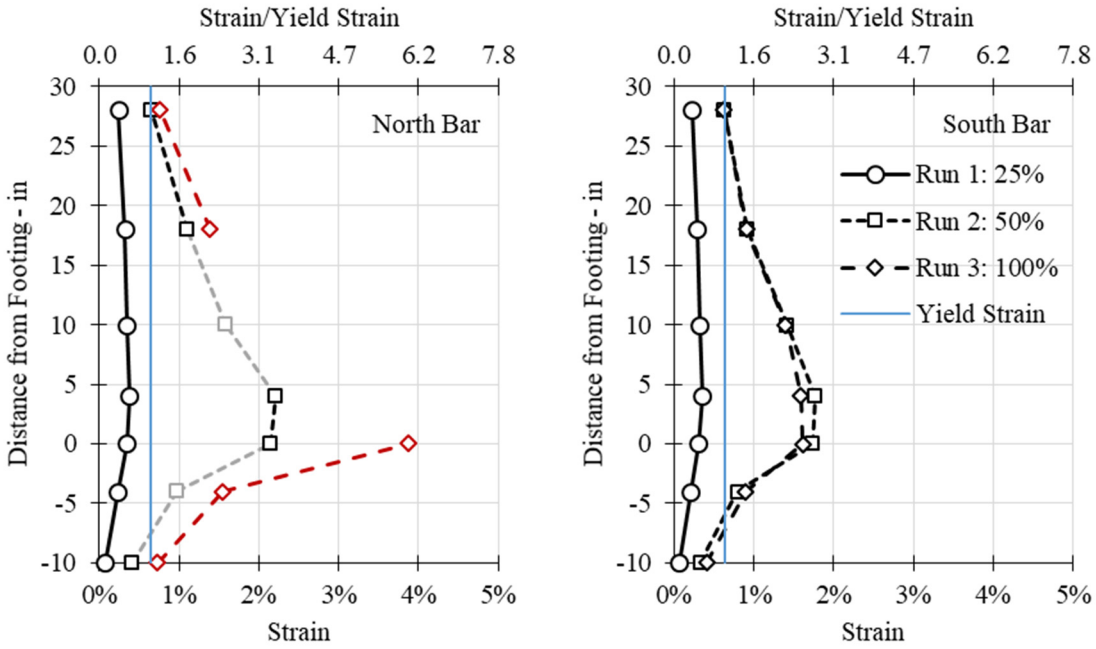

Figure 5.36 **Column LD-S3-G60D: strain profiles of the northern and southern longitudinal bars along the plastic hinge during each test run.**

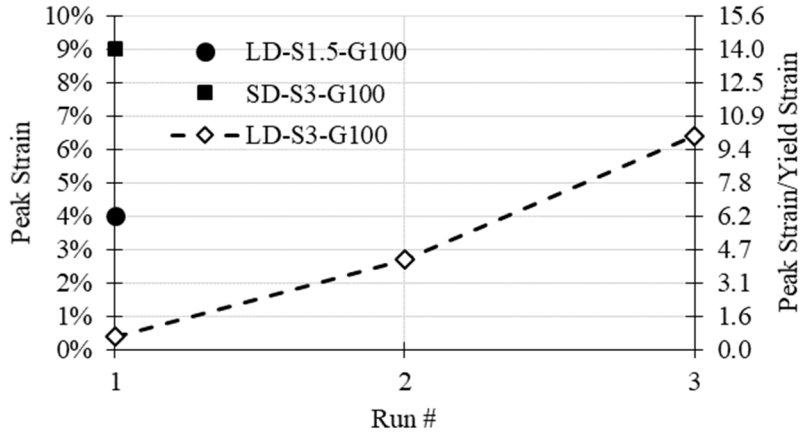

Figure 5.37 **Peak strain of the columns' longitudinal bars in each run.**

Table 5.10 **Peak strains in longitudinal bars of the columns in each run before bar rupture.**

Specimen	LD-S1.5-G100	SD-S3-G100	LD-S3-G100		
Run #	1	1	1	2	3
Strain (%)	4.0	9.0	0.4	2.7	6.4
Strain/yield	6.2	13.8	0.6	4.2	9.8

5.10 ROTATIONS AND CURVATURES

Base rotations and curvatures were calculated from the measured data by Novotechnik transducers installed on the north and south faces of the columns. The actual gauge lengths and the distance of each Novotechnik rod to the face of the columns were measured before testing and were used in the calculations. As explained in Chapter 3, rotation at each level was calculated by subtracting the measured vertical displacements on opposite sides of the column divided by the associated horizontal displacement. Curvatures were calculated based on the assumption that the plane sections remained plane under bending. The relative rotation at two adjacent levels was divided by the vertical distance between them to give the average curvature over the gauge length; see Equation (4.3).

Figure 5.38 through Figure 5.40 provide the curvature profile of the columns along the length of the plastic hinge. For all the specimens, the curvature was more concentrated at the column–footing interface and to some extent over the plastic-hinge length. This is attributed to the bond-slip effect and the yielding. The maximum curvature for the three columns were 0.013, 0.011, and 0.017 in^{-1}, respectively, which were measured at approximately 3 in. above the footing. The peak rotation and curvature values of the columns during each run are presented in Table 5.11 and Figure 5.41. Note that these rotations include the bond-slip-induced rotation (due to the yielding of the reinforcing bars at the column–footing interface). The moment-curvature relationships measured at 3 in. above the footing are also shown in Figure 5.42 through Figure 5.44.

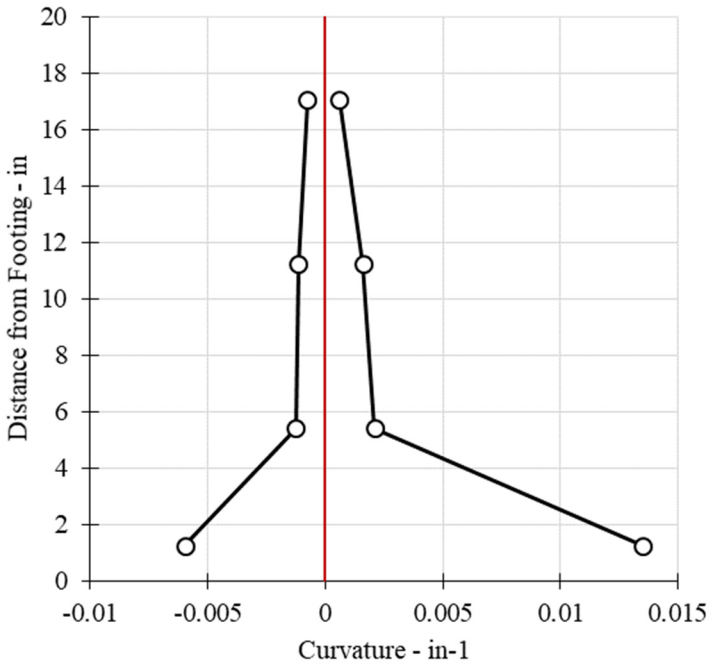

Figure 5.38 Column LD-S1.5-G100: curvature profile along the plastic hinge.

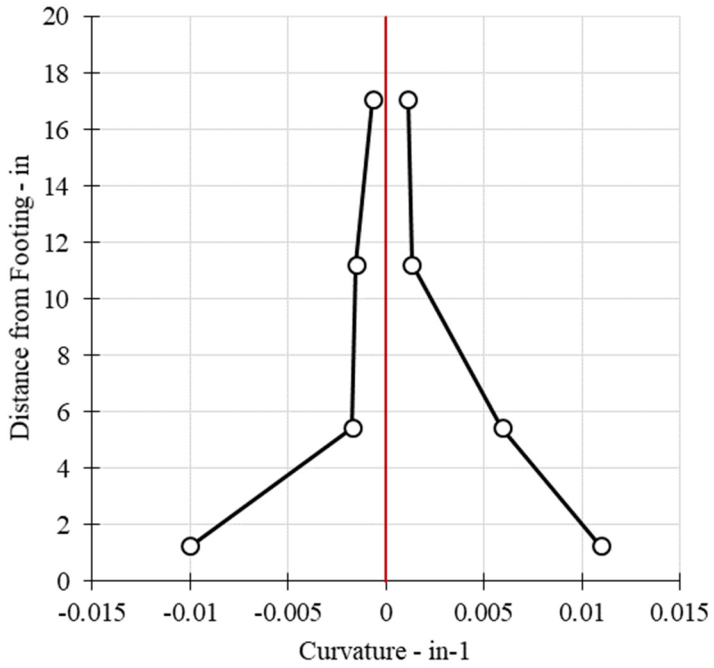

Figure 5.39 Column SD-S3-G100: curvature profile along the plastic hinge.

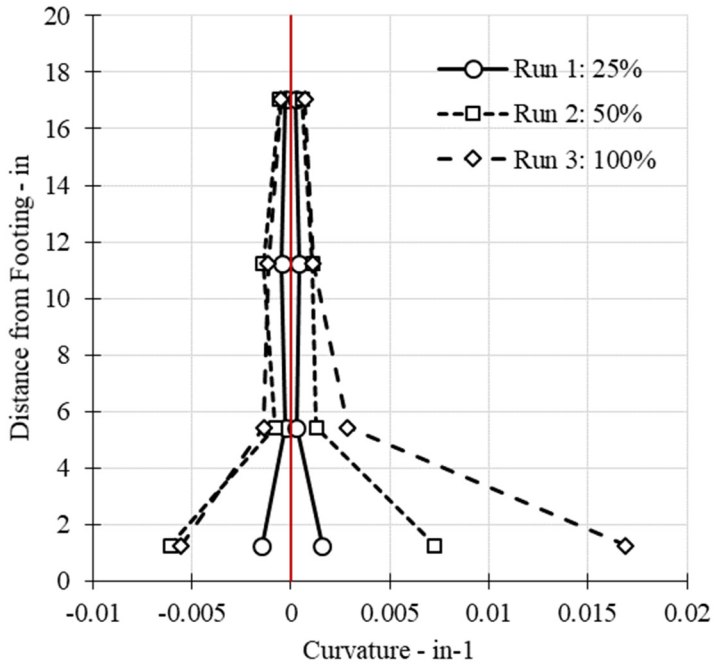

Figure 5.40 Column LD-S3-G100: curvature profile along the plastic hinge during each run.

Table 5.11 Peak rotation and curvature at the base of the columns in each run.

Specimen	LD-S1.5-G100	SD-S3-G100	LD-S3-G100		
Run #	1	1	1	2	3
Curvature (1/in)	0.013	0.011	0.002	0.007	0.017
Rotation (rad)	0.034	0.035	0.004	0.020	0.047

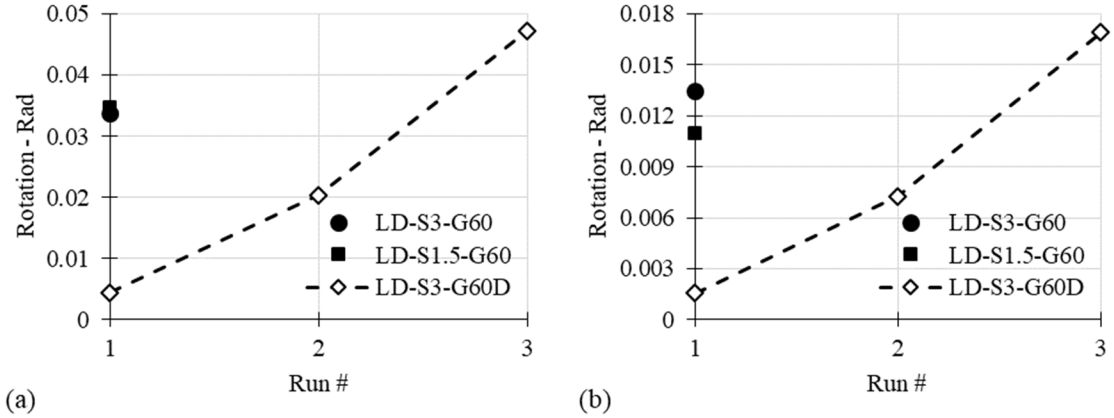

Figure 5.41 (a) Peak rotation and (b) peak curvature at the base of the columns in each run.

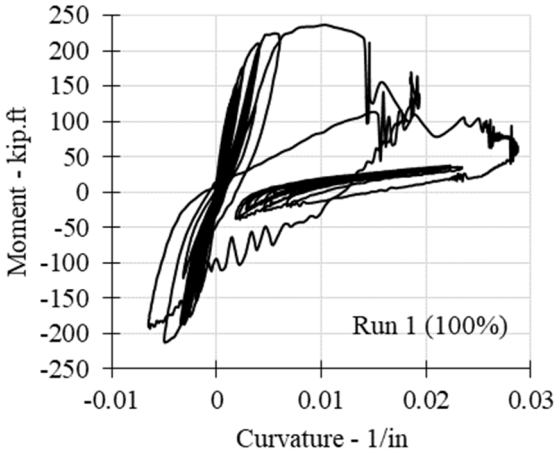

Figure 5.42 Column LD-S1.5-G100: moment curvature hysteresis curves.

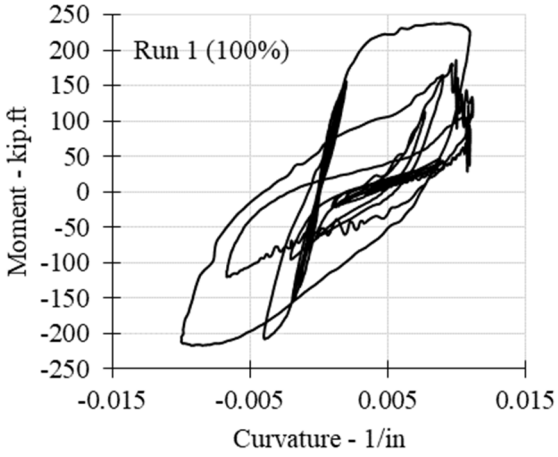

Figure 5.43 Column SD-S3-G100: moment-curvature hysteresis curves.

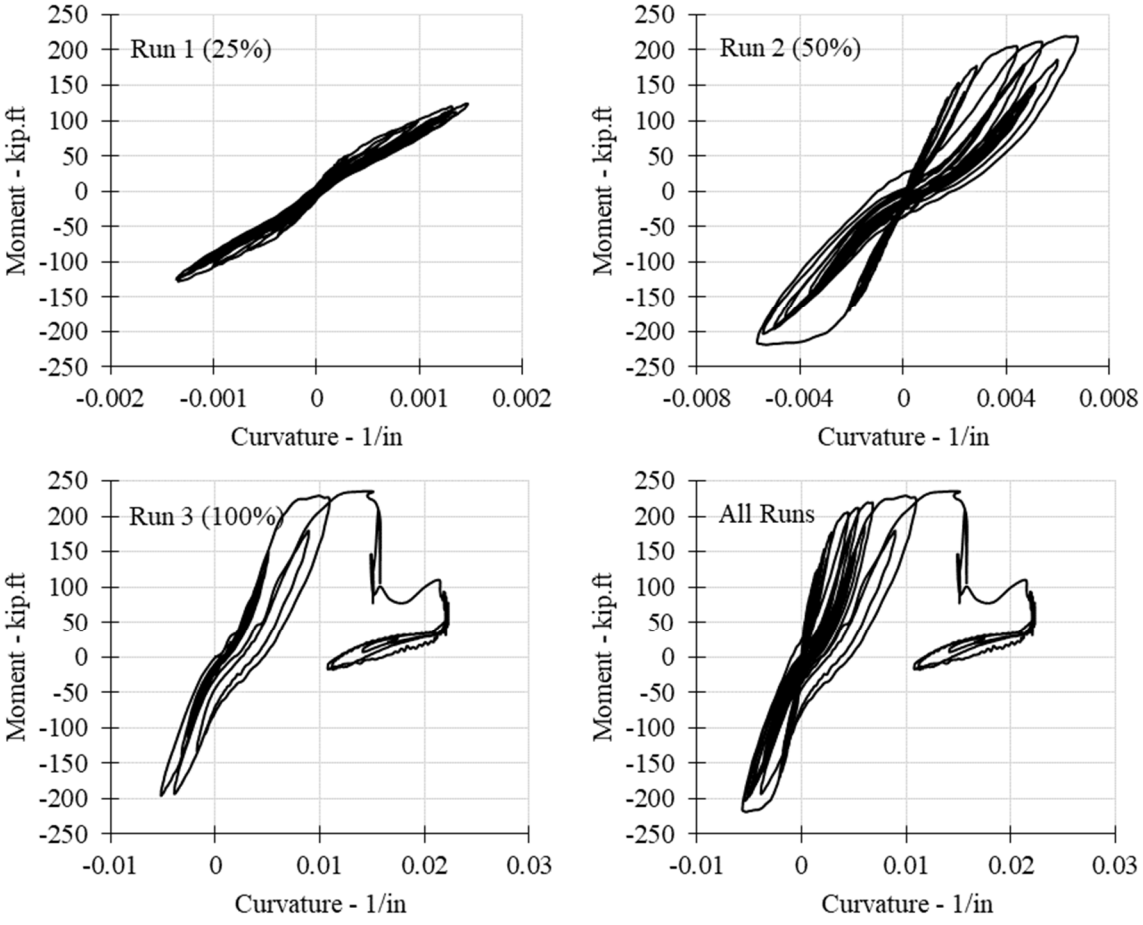

Figure 5.44 Column LD-S3-G100: moment-curvature hysteresis curves for each run.

6 Comparative Discussion of Experimental Results

6.1 OVERVIEW

The experimental program was conducted in two phases. Columns LD-S1.5-G60, LD-S3-G60, and LD-S3-G60D with varying tie spacing and debonding design details were tested in Phase I. The specimens were subjected to a series of long-duration motions from the 2011 Tohoku earthquake that comprised the full loading protocol. Phase II tested three additional columns reinforced by high-strength reinforcement. It was intended to subject Columns LD-S1.5-G100 and LD-S3-G100 in Phase II to the full loading protocol per Phase I, but the specimens failed in the 100% run. Column SD-S3-G100 in Phase II was subjected to a short-duration motion from 199 Kocaeli earthquake. This motion was linearly scaled to have a response spectrum as close as possible to the response spectrum of the Tohoku earthquake in shape and amplitude. This chapter provides a summary and comparative discussion of the shake table test results of the six column specimens in light of the differences in the design details, i.e., tie spacing, bar debonding, and grade of reinforcement.

6.2 GENERAL BEHAVIOR

The different design details of the reinforcement in each column led to the columns having different displacement/drift capacity, i.e., each column reached their capacity at different drift ratios. All columns sustained a flexural mode of degradation characterized by concrete crushing, longitudinal bar buckling, and longitudinal bar fracture: buckling in the case of the Grade 60 bars or tensile rupture in the case of the HSS bars. First, flexural cracking occurred at similar displacements for all columns, as the measured concrete compressive strength was close for all specimens. Minor diagonal cracking was also observed in all columns, indicating relatively low shear stresses. Under 100% of the LD/SD motion, the columns with higher tensile strength reinforcement (Phase II) exhibited longer and wider inclined cracks along the columns in loading direction (north–south), indicating higher shear stresses. Although major concrete spalling occurred during this run, the transverse reinforcement did not yield in any of the specimens. The columns with spirals spaced at 1.5 in. ($3d_b$), i.e., Column LD-S1.5-G60 and Column LD-S1.5-G100, appear to prevent the longitudinal bars buckling and to confine the core concrete better than

was observed in the other columns. A summary of the observed damage in the columns is listed in Table 6.1.

Table 6.1 Observed damage for each column after each run.

Run	100% LD[1]	After Shock[2]	125% LD	150% LD	160% LD
LD-S3-G60	Major cover concrete spalling	No further damage	Core concrete damage; Bar buckling	Bar fracture	-
LD-S1.5-G60			Spiral exposure	Same as previous run	Bar fracture
LD-S3-G60D			Concrete core damage; Bar buckling; Bar fracture	Bar fracture	-
LD-S1.5-G100	Major cover and core concrete Damage; Bar buckling; Bar fracture	-	-	-	-
Run	25% LD	50% LD	100% LD	-	-
LD-S3-G100	Flexural cracks	Minor cover concrete spalling	Concrete core damage; Bar buckling; Bar fracture	-	-
Run	100% SD[3]	-	-	-	-
SD-S3-G100	Major cover and core concrete damage; Bar buckling; Bar fracture	-	-	-	-

[1] LD: Long-duration motion from the 2011 Tohoku earthquake.
[2] After Shock: Motion recorded a month after the 2011 Tohoku Japan, earthquake.
[3] SD: Short-duration motion from the 1999 Kocaeli earthquake (scale factor = 3.68).

In addition, the columns reinforced with the high-strength grade 100 bars (Phase II) showed more bar buckling strength compared to the columns reinforced with conventional Grade 60 bars (Phase I) with the same tie spacing. This might be attributed to the much higher strain-hardening gradient of HSS bars (no yield plateau), which may contribute to a higher tangent axial stiffness in the inelastic strain range, leading to higher buckling strength [Sokoli et al. 2017]. Column LD-S1.5-G100 showed the least sign of bar buckling, while Column LD-G3-G60D with debonded longitudinal bars exhibited the largest buckling amplitudes. Bar buckling, strain demand, and low-cycle fatigue in combination are the main factors that cause bar fracture. The low-cycle fatigue performance varies greatly in different reinforcing bars, especially for grade 100 bars [Slavin and Ghannoum 2015]. Therefore, the results presented herein only apply to the specific HSS bar type used in this study (MMFX Chrome 9100 bars) or other types with similar fatigue performance.

6.3 PEAK DISPLACEMENTS

When sufficient confinement is provided, the deformation capacity in RC columns is often determined by the behavior of the longitudinal bars. The behavior of the longitudinal bars is also highly governed by their mechanical properties, lateral restraint, and strain demands. Phase I of the experimental study demonstrated that for the columns with conventional Grade 60 reinforcement, smaller tie spacing and debonding of the longitudinal bars increased displacement capacity by 55% and 24%, respectively. Both confinement and debonding were effective to enhance the column's performance and mitigate further adverse effects under long-duration earthquakes. Note: the efficacy of confinement was more significant than debonding.

Phase II specimens with HSS bars showed significantly lower displacement capacity by 16% and 47% less for columns with $6d_b$ and $3d_b$ tie spacing, respectively. The results also showed that higher confinement was not effective in increasing the column displacement capacity under long-duration motions. Note, it cannot be concluded that reducing tie spacing does not improve the low-cycle fatigue life of high-strength bars: the bar fractures in the columns subjected to the LD motion were mainly due to induced tensile strain demands as opposed to accumulated low-cycle fatigue. Furthermore, the column with HSS bars showed 25% higher displacement capacity when tested under the short-duration motion compared to the similar column tested under long-duration motions. The peak measured displacements (drift ratios) of the columns during each run are summarized in Table 6.2 and Figure 6.1 for convenient comparison.

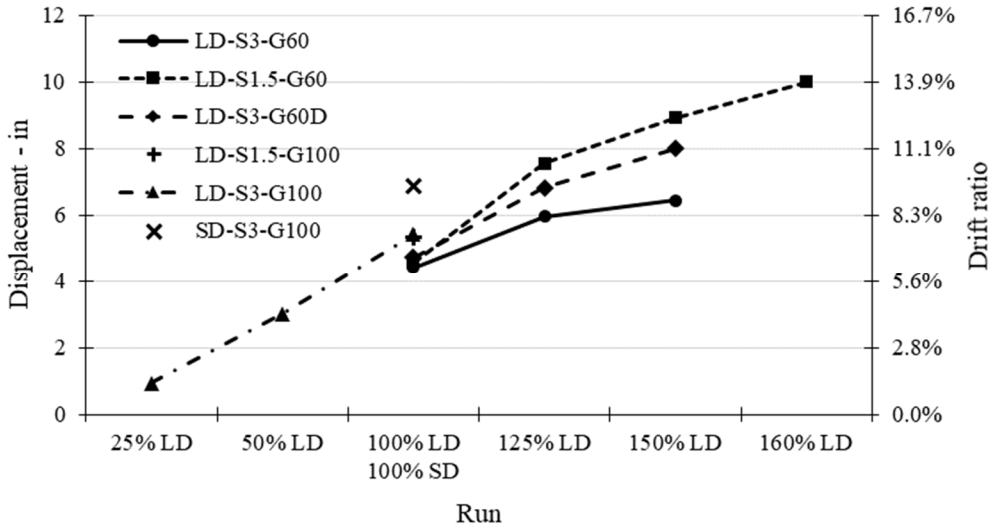

Figure 6.1 Peak measured displacements (drift ratios) for each column during each run.

Table 6.2 Peak measured displacements (drift ratios) for each column during each run.

Run	100% LD	After Shock	125% LD	150% LD	160% LD
LD-S3-G60	4.41 in. (6.13%)	2.80 in. (3.89%)	5.95 in. (8.27%)	6.44 in. (8.94%)	-
LD-S1.5-G60	4.57 in. (6.35%)	2.71 in. (3.76%)	7.56 in. (10.5%)	8.93 in. (12.4%)	10.0 in. (13.9%)
LD-S3-G60D	4.72 in. (6.56%)	2.77 in. (3.85%)	6.83 in. (9.48%)	7.99 in. (11.1%)	-
LD-S1.5-G100	5.34 in. (7.42%)	-	-	-	-
Run	25% LD	50% LD	100% LD	-	-
LD-S3-G100	0.94 in. (0.13%)	3.02 in. (4.20%)	5.42 in. (7.53%)	-	-
Run	100% SD	-	-	-	-
SD-S3-G100	6.88 in. (9.56%)	-	-	-	-

6.4 PEAK FORCES

The measured base shear as well as bending moment peak values for each column during each run are presented in Table 6.3 and Figure 6.2. As intended, all three columns tested in both Phase I and II had almost the same force capacity. Different design details of the columns did not result in major differences between the overall lateral force capacities. The response of the columns did not show significant strength degradation prior to the bar ruptures. The columns did show a lateral-strength degradation due to bar buckling, and they lost significant strength due to the fracture of longitudinal bars. It is worth mentioning that the base shear in Columns LD-S1.5-G100 and LD-S3-G100 dramatically dropped after bar rupture. Moreover, for those two columns, the tests were stopped before completing the entire ground motion to avoid any damage to the shake table or collapse of the setup. Although a similar capacity as Phase I columns was targeted in design, the columns with HSS bars still exhibited higher base shear (bending moment) capacity due to the higher yield force and the strain hardening behavior of Grade 100 ASTM A1035 bars.

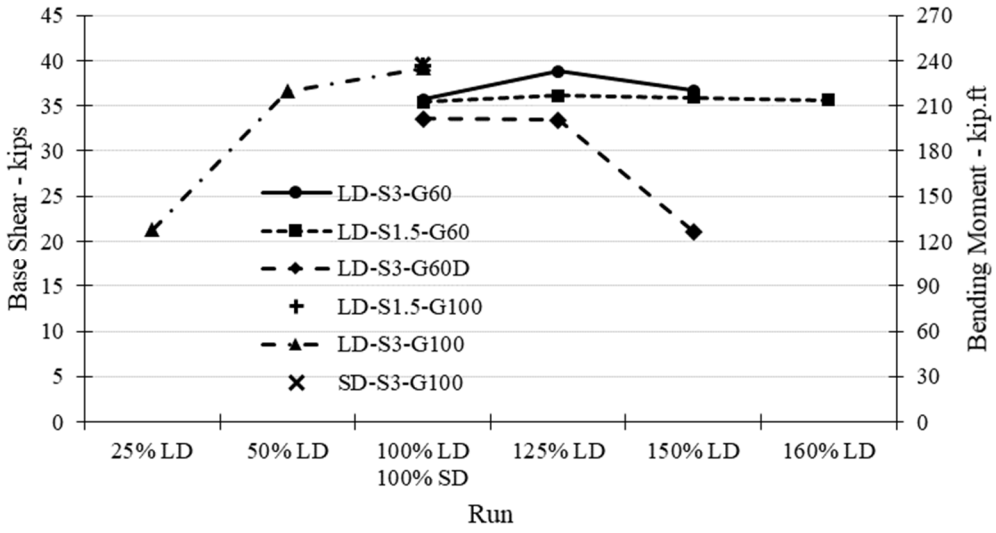

Figure 6.2 **Peak measured base shear (bending moment) for each column during each run.**

Table 6.3 **Peak measured base shear (bending moment) for each column during each run.**

Run	100% LD	After Shock	125% LD	150% LD	160% LD
LD-S3-G60	35.7 kip (214 kip.ft)	25.1 kip (151 kip.ft)	38.8 kip (233 kip.ft)	36.7 kip (220 kip.ft)	-
LD-S1.5-G60	35.4 kip (212 kip.ft)	26.1 kip (157 kip.ft)	36.1 kip (217 kip.ft)	35.9 kip (215 kip.ft)	35.6 kip (214 kip.ft)
LD-S3-G60D	33.6 kip (202 kip.ft)	26 kip (156 kip.ft)	33.4 kip (200 kip.ft)	21.1 kip (127 kip.ft)	-
LD-S1.5-G100	39.4 kip (236 kip.ft)	-	-	-	-
Run	25% LD	50% LD	100% LD	-	-
LD-S3-G100	21.3 kip (128 kip.ft)	36.6 kip (220 kip.ft)	39.2 kip (235 kip.ft)	-	-
Run	100% SD	-	-	-	-
SD-S3-G100	39.6 kip (238 kip.ft)	-	-	-	-

6.5 FORCE-DISPLACEMENT RELATIONSHIPS

6.5.1 Hysteretic Behavior

All the columns exhibited a typical lateral force versus displacement hysteretic response. The hysteretic force-displacement loops were observed to be essentially linear in loading and unloading prior to the yielding of longitudinal bars. This indicates limited slippage of the longitudinal bars in the surrounding concrete at the flexural cracks. When the longitudinal bars yielded in tension

and were pushed back to zero stresses, the significant plastic tensile strains in the reinforcing bar did not allow the flexural cracks to close in unloading. To zero the strains and close the cracks at this stage, sufficient compressive stresses must be applied. Thus, since the cracks were still open in re-loading, the section stiffness was mainly determined by the longitudinal bars. Therefore, the stiffness of this branch of the hysteresis loops was less until the strain in longitudinal bars reached zero. Although this behavior was observed in all the columns, the columns reinforced by HSS bars (Phase II) showed a much stiffer crack closing phase, which may be due to the higher strength of the Grade 100 bars, requiring a larger force to close the cracks.

6.5.2 Envelope Response

The envelopes of the base shear versus displacement as well as bending moment versus drift ratios are shown for all columns using double axis; see Figure 6.3. Figure 6.4 demonstrates the envelopes normalized with their nominal moment strength. Column LD-S3-G60 exhibited unequal or asymmetric strength in positive and negative directions that may attributed to a construction error as the concrete cover on the north and south sides of the column was uneven. Differences in transverse reinforcement spacing and debonding details showed little influence on the column's strength. The columns with Grade 100 bars (Phase II) showed different envelope curves than the columns in Phase I. These columns showed more hardening or strength gains after the yielding of the longitudinal bars. It appears that the hardening behavior (no plateau) of the ASTM A1035 bars contributed to this overall global hardening behavior. The strength degradation in all columns was initiated when bar buckling happened, although buckling was much less pronounced in the HSS columns.

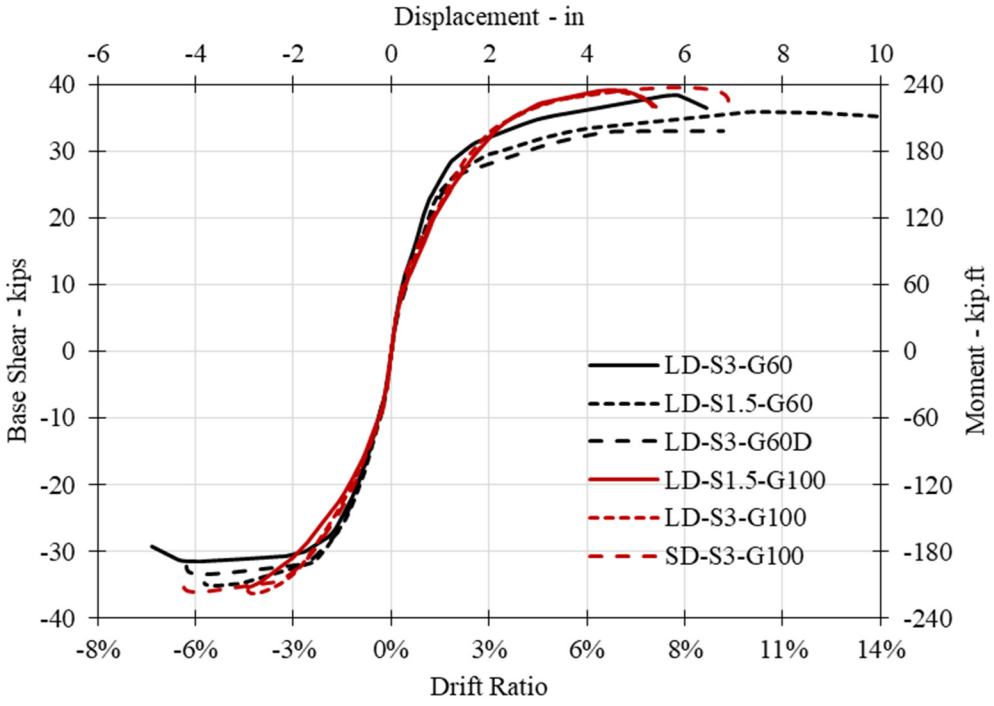

Figure 6.3 Force-displacement envelope curves for each column.

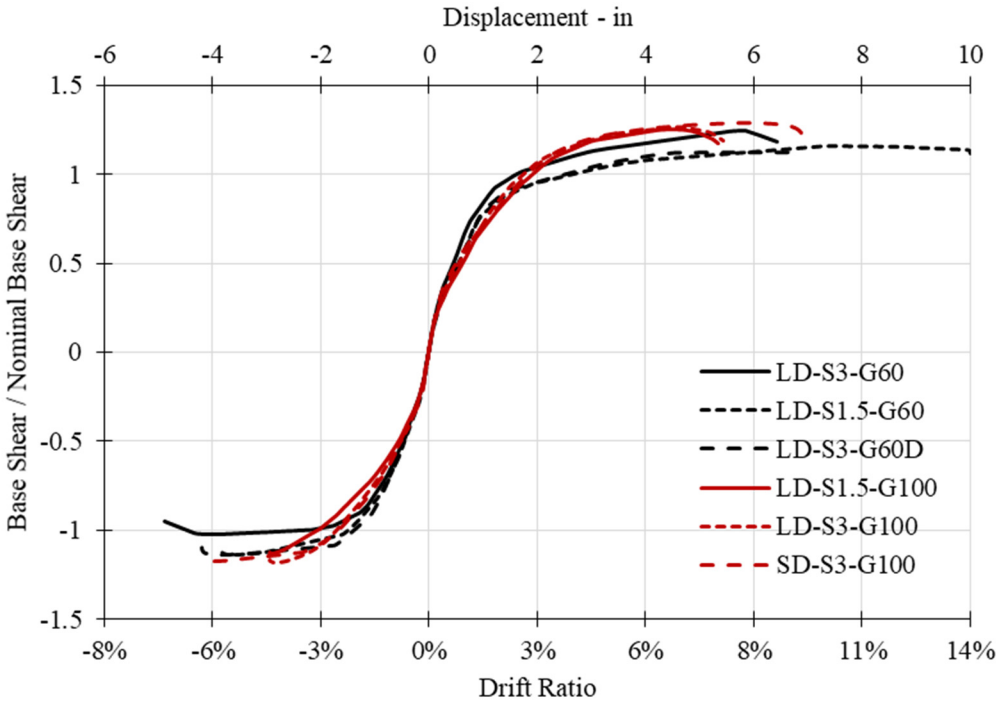

Figure 6.4 Normalized force-displacement envelope curves for each column.

6.5.3 Ductility Capacity

To calculate displacement ductility, the envelope curves were idealized according to AASHTO provisions. The results of ductility analysis of the columns are summarized in Table 6.4. The higher concrete confinement in Column LD-S1.5-G60, whereby the tie spacing was reduced, significantly improved the column's ductility capacity by 45% compared to Column LD-S3-G60. The columns with HSS reinforcing bars had higher effective yield displacements, as dictated by the reinforcement behavior as well as lower ultimate displacements. Hence, they exhibited smaller displacement ductility compared with the columns with conventional reinforcement. This observation was found to be consistent with recent studies that considered HSS for ultra-high-performance concrete (UHPC) columns [Naeimi and Moustafa 2020; Aboukifa et al. 2020]. In general, this may be attributed to the higher yield strain and less ductile behavior of the HSS alloys and Grade 100 ASTM A1035 bars. Displacement ductility of Columns LD-S3-G60 and LD-S1.5-G60 were 2.0 and 3.2 times larger than those of the similar columns with HSS, respectively. In addition, smaller transverse reinforcement spacing in these columns did not show any sign of increasing the displacement ductility. Furthermore, the column with HSS, when tested under short-duration motion, demonstrated 23% higher displacement ductility compared to the similar column tested under the long-duration motion.

Table 6.4 Idealized yield, ultimate drift ratio, and ductility capacity of each column.

Specimen	Yield drift (%)	Ultimate drift (%)	Ductility
LD-S3-G60	1.60	8.94	5.60
LD-S1.5-G60	1.70	13.9	8.14
LD-S3-G60D	1.76	9.41	5.35
LD-S1.5-G100	2.91	7.42	2.55
LD-S3-G100	2.75	7.53	2.74
SD-S3-G100	2.84	9.56	3.37

6.5.4 Energy Dissipation

Cumulative dissipated energy for each column after each run is listed in Table 6.5 and shown in Figure 6.5. Such cumulative energy was computed as the cumulative area enclosed within or under the force-displacement relationship curves. The absolute dissipated energy in each run can be calculated by subtracting the value from the previous run from the cumulative energy of that run. Column LD-S1.5-G60 showed highest cumulative energy dissipation, while the amount of total dissipated energy for the three columns in Phase I before the onset of bar fracture was similar. Also, the results indicate that the columns with HSS bars, when tested under long-duration motions, demonstrated narrower hysteresis loops compared to those with regular reinforcement, indicating lower energy dissipation. For instance, Column LD-S3-G60 dissipated more than three times of the energy compared to Column LD-S3-G100 under the 100% LD earthquake level. This lower energy dissipation and narrower hysteretic loops for columns with HSS bars are mainly attributed to the following: (1) the higher effective yield force (i.e., higher effective yield displacement); (2) lack of a well-defined yield plateau; (3) the lower *T/Y* ratio for the high-strength steel bars; and (4) the differences in the stiffness of the re-loading branch in the columns hysteretic behavior explained in Section 6.5.1 above. A yield plateau and higher *T/Y* ratio produce wider and larger hysteresis loops, leading to higher energy dissipation. The equivalent hysteretic nonlinear damping ratio was also calculated for each half-cycle of the force-displacement relationship curve. The results are summarized in Table 6.6.

Table 6.5 Cumulative dissipated energy for each column after each run.

Run	100% LD	After Shock	125% LD	150% LD	160% LD
LD-S3-G60	92 kip.ft	109 kip.ft	219 kip.ft	320 kip.ft	-
LD-S1.5-G60	94 kip.ft	111 kip.ft	224 kip.ft	363 kip.ft	511 kip.ft
LD-S3-G60D	91 kip.ft	104 kip.ft	187 kip.ft	242 kip.ft	-
LD-S1.5-G100	52 kip.ft*	-	-	-	-
Run	25% LD	50% LD	100% LD	-	-
LD-S3-G100	10 kip.ft	49 kip.ft	80 kip.ft*	-	-
Run	100% SD	-	-	-	-
SD-S3-G100	53 kip.ft	-	-	-	-

* Run was not completed due to extensive column damage.

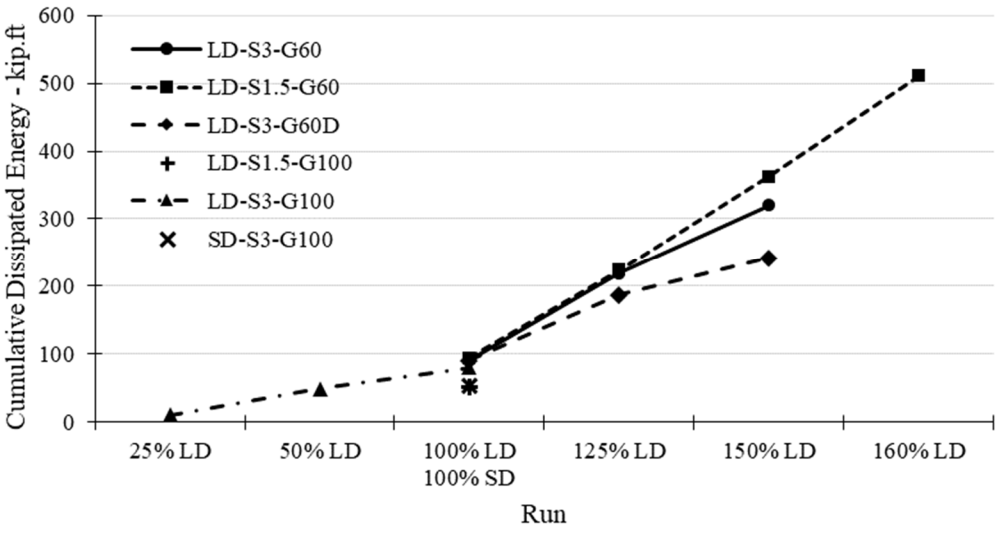

Figure 6.5 Cumulative dissipated energy for each column after each run.

Table 6.6 Hysteretic damping computed in each run for each column.

Run	100% LD	After Shock	125% LD	150% LD	160% LD
LD-S3-G60	16.3%	16.9%	19.2%	19.7%	-
LD-S1.5-G60	16.8%	12.2%	18.6%	17.3%	16.5%
LD-S3-G60D	17.0%	14.1%	18.5%	19.1%	-
LD-S1.5-G100	11.5%*	-	-	-	-
Run	25% LD	50% LD	100% LD	-	-
LD-S3-G100	3.7%	7.5%	22.5%*	-	-
Run	100% SD	-	-	-	-
SD-S3-G100	8.3%	-	-	-	-

* Run was not completed due to extensive column damage.

6.6 DYNAMIC PROPERTIES

The initial effective stiffness for each column was obtained from the idealized curves. Column LD-S3-G60D with debonded bars showed lowest initial effective stiffness among the Phase I specimens. Higher effective yield displacements in the columns with HSS bars caused lower initial effective stiffness for these columns. The columns stiffnesses and periods were obtained using the FRF method from the white noise tests and summarized for all columns in Table 6.7 For such FRF estimates, the shake table acceleration feedback was used as input, and the measured acceleration at the top of the columns was used as the output correlated in the function. The results demonstrate that the periods elongated as damage progressed in the columns. All the columns had similar periods, i.e., similar stiffness, under 100% of the long-or short-duration motion. Figure 6.6 and Figure 6.7 show the natural period and stiffness of the columns prior to starting the test and after each run, respectively.

Table 6.7 **Stiffness (period) of each column computed before test and after each run using FRF.**

Run	W.N. 0	W.N. 1	W.N. 2	W.N. 3	W.N. 4	W.N. 5
LD-S3-G60	44.2 kip/in (0.43 sec)	14.9 kip/in (0.74 sec)	14.9 kip/in (0.74 sec)	12.5 kip/in (0.81 sec)	7.4 kip/in (1.05 sec)	-
LD-S1.5-G60	53.2 kip/in (0.39 sec)	13.8 kip/in (0.77 sec)	13.4 kip/in (0.78 sec)	12.5 kip/in (0.81 sec)	12.5 kip/in (0.81 sec)	12.5 kip/in (0.81 sec)
LD-S3-G60D	47.1 kip/in (0.42 sec)	12.5 kip/in (0.81 sec)	12.2 kip/in (0.82 sec)	9.9 kip/in (0.91 sec)	4.2 kip/in (1.39 sec)	-
LD-S1.5-G100	53.2 kip/in (0.39 sec)	13.4 kip/in (0.78 sec)	-	-	-	-
LD-S3-G100	63.6 kip/in (0.36 sec)	51.1 kip/in (0.4 sec)	14.5 kip/in (0.75 sec)	13.4 kip/in (0.78 sec)	-	-
SD-S3-G100	73.6 kip/in (0.33 sec)	13.4 kip/in (0.78 sec)	-	-	-	-

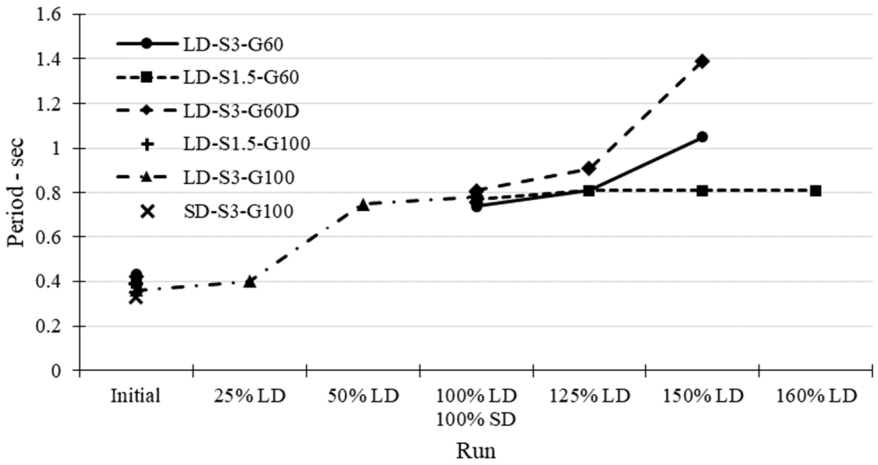

Figure 6.6 **Period of each column computed before test and after each run using FRF.**

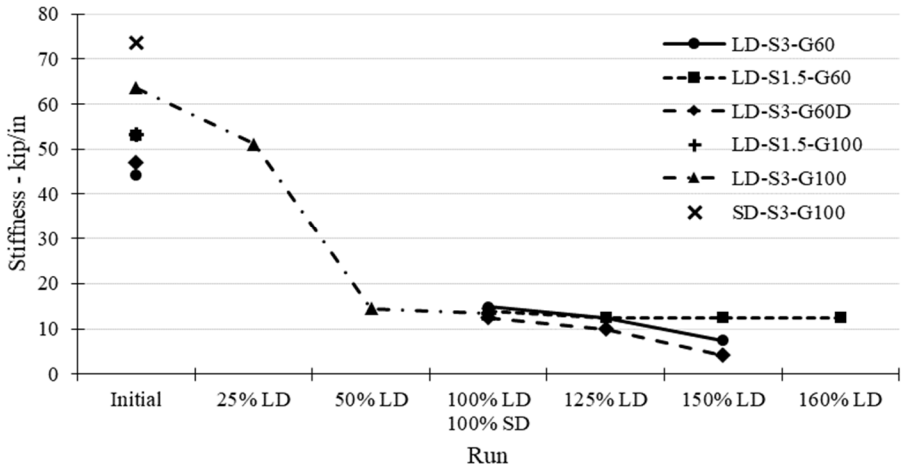

Figure 6.7 Stiffness of each column computed before test and after each run using FRF.

6.7 PEAK STRAINS AND CURVATURES

The first yield in the columns was determined when the first longitudinal bar reached the yield strain. The assumed yield strain for high-strength bars was based on the 0.2% strain offset method. As mentioned earlier, the first yield in the columns with high-strength bars occurred at higher strength and higher displacement due to higher yield strain.

Strain profiles of the columns in Phases I and II show that, for columns reinforced with regular-strength reinforcement, smaller tie spacing resulted in a better strain distribution along the length of the plastic hinge. Also, debonding of the longitudinal bars at the column–footing interface reduced the strain concentration in the vicinity of the interface. The measured strains in the debonded bars showed that although the yielding spread along the debonded length, it did not reduce the peak strains. The columns reinforced with HSS, showed more strain concentration. Note: a better strain distribution and higher strain ductility was observed in these columns when tested under long-duration motion compared to when tested under short-duration motions. In the columns reinforced with Grade 60 bars, spirals in both columns with 3-in. tie spacing yielded under 150% LD. In the column with 1.5-in. tie spacing, no yielding occurred in the spirals even at 160% LD. Maximum strain in the spiral in the columns reinforced with HSS did not exceed 40% of the yield strain, i.e., evidence of much less engaged core concrete confinement. The peak recorded strains of longitudinal bars in the columns during each run are shown in Table 6.8 for completeness.

The peak measured curvature of the columns during each run are listed in Table 6.9. The column with debonded bars exhibited the highest curvatures compared with the other columns. In addition, the columns in the second phase with high-strength bars showed higher curvatures, which was due to rapid extensive ruptures that occurred in these columns.

Table 6.8 Peak measured strain in longitudinal bars for each column during each run.

Run	100% LD	After Shock	125% LD	150% LD
LD-S3-G60	2.8% (11.2ε_y)	2.0% (8.0ε_y)	4.5% (17.8ε_y)	5.2% (20.6ε_y)
LD-S1.5-G60	3.3% (13.2ε_y)	2.3% (9.2ε_y)	6.3% (25.0ε_y)	7.7% (30.6ε_y)
LD-S3-G60D	3.4% (13.6ε_y)	2.5% (10.0ε_y)	4.8% (19.4ε_y)	-
LD-S1.5-G100	4.0% (6.2ε_y)	-	-	-
Run	25% LD	50% LD	100% LD	-
LD-S3-G100	0.4% (0.6ε_y)	2.7% (4.2ε_y)	6.4% (9.8ε_y)	-
Run	100% SD	-	-	-
SD-S3-G100	9.0% (13.8ε_y)	-	-	-

Gray values indicate the peak strains measured before bar rupture or strain gauge failure.

Table 6.9 Peak measured curvature at the base of each column during each run.

Run	100% LD	After Shock	125% LD	150% LD	160% LD
LD-S3-G60	0.009 in^{-1}	0.006 in^{-1}	0.014 in^{-1}	0.016 in^{-1}	-
LD-S1.5-G60	0.009 in^{-1}	0.005 in^{-1}	0.013 in^{-1}	0.016 in^{-1}	0.018 in^{-1}
LD-S3-G60D	0.018 in^{-1}	0.012 in^{-1}	0.020 in^{-1}	0.028 in^{-1}	-
LD-S1.5-G100	0.013 in^{-1}	-	-	-	-
Run	25% LD	50% LD	100% LD	-	-
LD-S3-G100	0.002 in^{-1}	0.007 in^{-1}	0.017 in^{-1}	-	-
Run	100% SD	-	-	-	-
SD-S3-G100	0.011 in^{-1}	-	-	-	-

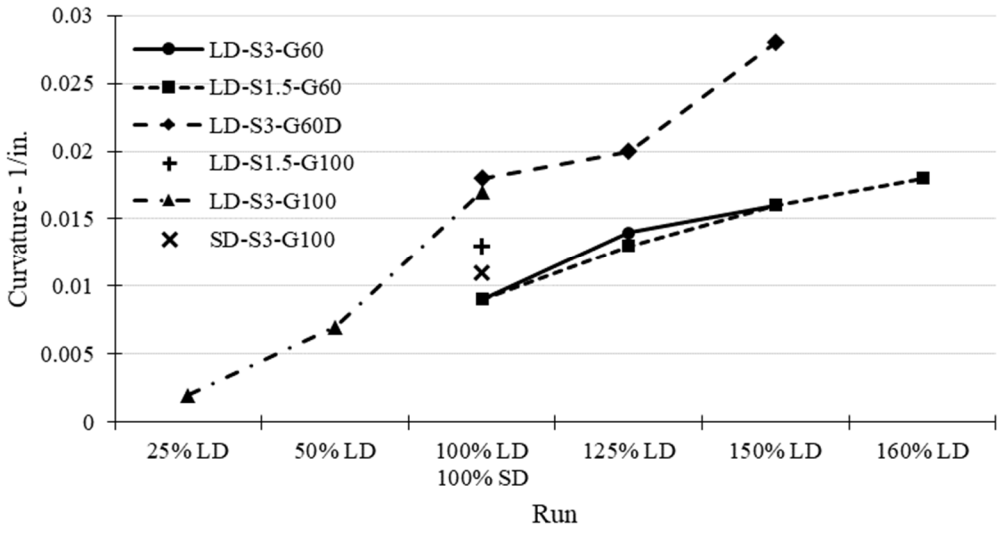

Figure 6.8 Peak measured curvature at the base of each column during each run.

7 Post-Test Analysis

7.1 OVERVIEW

The objective of this part of the study is to further assess and validate the modeling assumptions presented in Chapter 2, based on the correlation between the calculated and measured responses from the experiments. Thus, all six tested columns were analyzed subsequent to the shake table tests using OpenSees [McKenna 2011] as discussed below. The measured results were first compared to the predicted results from the pre-test models to identify any issues with the model. Further refinements were then made to improve agreement between the measured and calculated responses. The modifications included updating the input excitation, boundary conditions, and material properties, especially the low-cycle fatigue model. The actual shake table feedback acceleration was used as the input motion in the OpenSees model. The concrete and steel properties measured on test days were used to update the materials in the models.

The correlation between the measured and calculated results were assessed by comparing various seismic responses including column top displacement, base shear, base rotation, and strains in the longitudinal bars. The error between the measured and calculated results was then determined. A positive error indicates that the model overestimated the measured response. The modeling assumptions and the correlation between the calculated and measured responses are described next.

7.2 PREDICTED VERSUS MEASURED RESPONSES

The measured results were first compared to the predicted global and local seismic responses, including column displacement, base shear, dissipated energy, and strains in the longitudinal bars. The responses were compared up to onset of the first bar fracture. Figure 7.1 through Figure 7.5 compare the measured and predicted cumulative force-displacement relationships for all six columns. The peak displacements (and associated drift ratios) and base shears (and associated bending moments) for each column during each run are compared in Table 7.1 and Table 7.2, respectively.

As seen in the figures and tables, the differences in the displacements and base shears were consistently higher for the Phase II columns with high-strength steel (HSS) bars. The cause of this discrepancy was mainly attributed to the steel material used for HSS bars in the pre-test model (*Steel02*). In addition, it was shown that the low-cycle fatigue model utilized in the pre-test model

underestimated the fatigue life of the conventional Grade 60 bars but overestimated that of HSS (Grade 100 MMFX) bars. Possible reasons for this different behavior of Grade 100 bars are discussed in Chapter 6. Figure 7.3 and Figure 7.4 show the measured and predicted columns displacement histories. The correlation between the measured and predicted displacement histories was somewhat closer in the Phase I columns; the model did not predict the residual displacements that occurred during the tests.

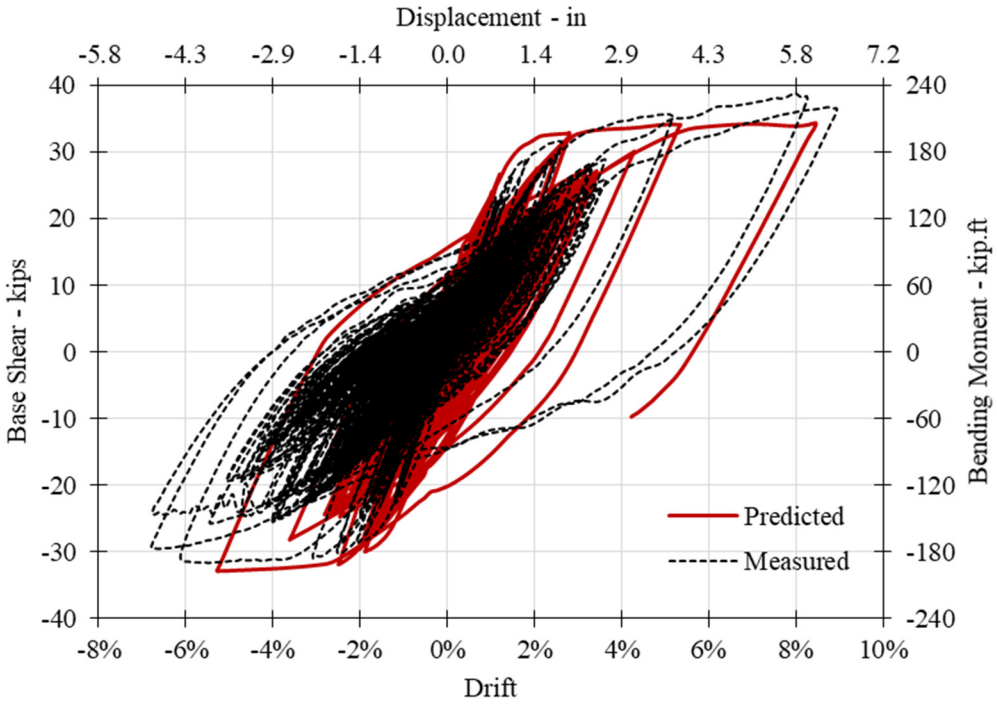

Figure 7.1 **Measured versus predicted force-displacement relationship for Column LD-S3-G60.**

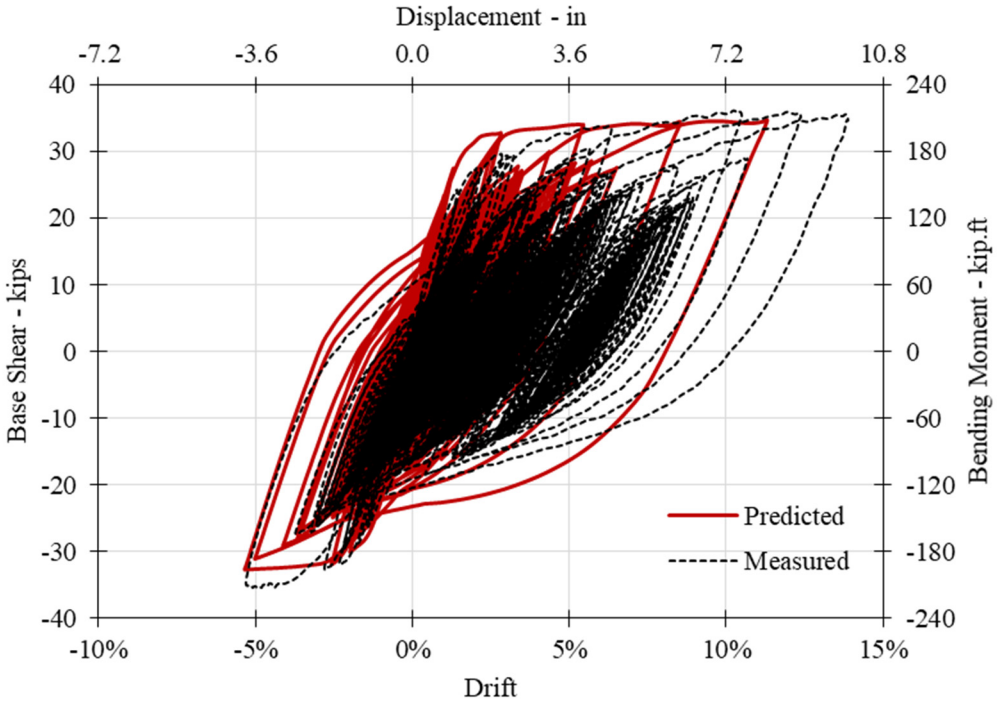

Figure 7.2 **Measured versus predicted force-displacement relationship for Column LD-S1.5-G60.**

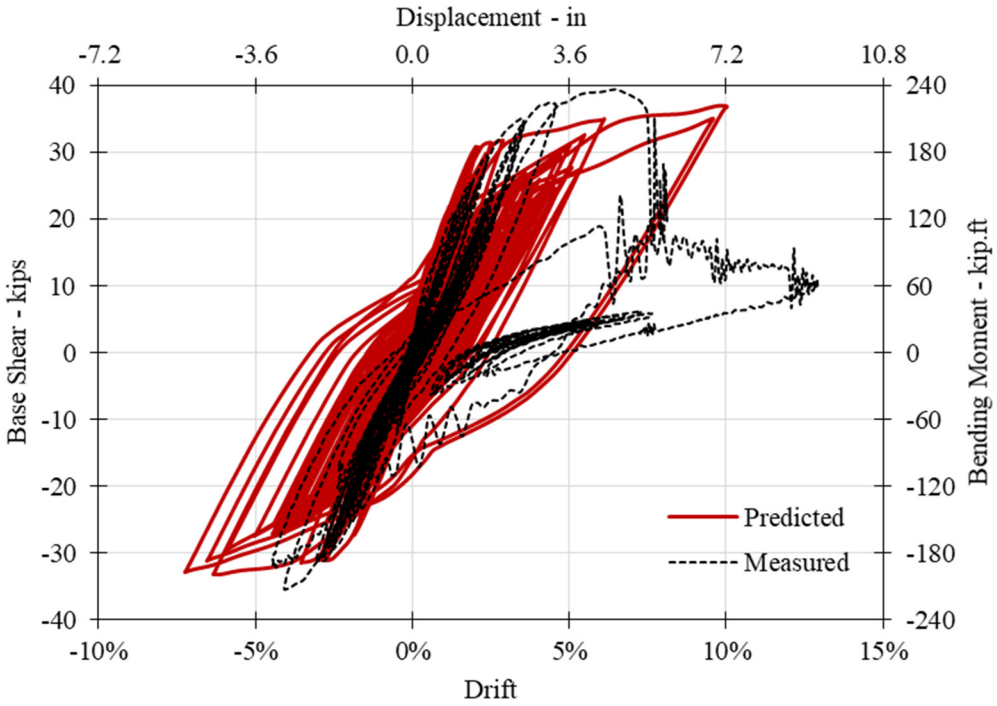

Figure 7.3 **Measured versus predicted force-displacement relationship for Column LD-S1.5-G100.**

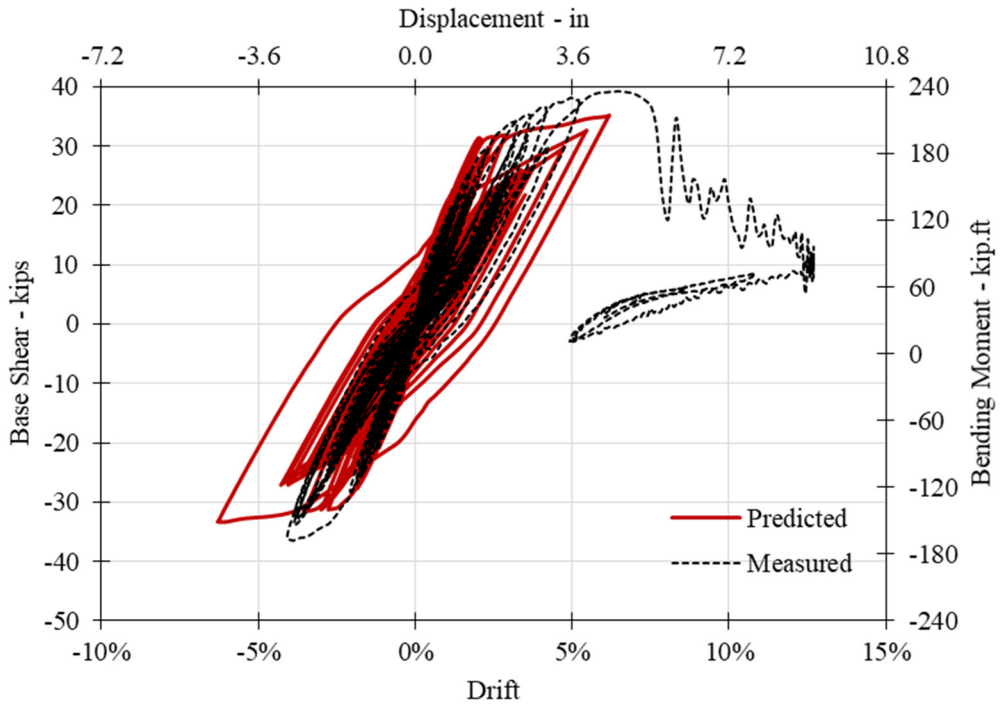

Figure 7.4 **Measured versus predicted force-displacement relationship for Column LD-S3-G100.**

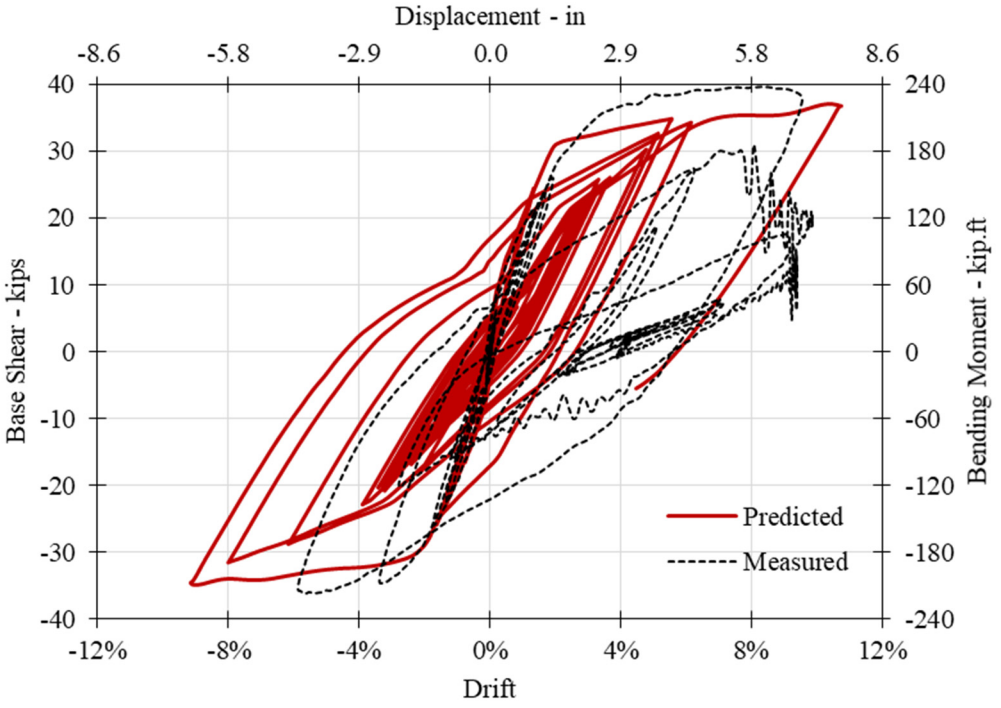

Figure 7.5 **Measured versus predicted force-displacement relationship for Column SD-S3-G100.**

Table 7.1 Peak predicted and measured displacements (drift ratios) for each column during each run.

Run		100% LD[1]	After Shock[2]	125% LD	150% LD	160% LD
LD-S3-G60	Predicted	3.85 in. (5.35%)	2.18 in. (3.03%)	6.09 in. (8.46%)	-	-
	Measured	4.41 in. (6.13%)	2.80 in. (3.89%)	5.95 in. (8.27%)	6.44 in. (8.94%)	-
LD-S1.5-G60	Predicted	3.92 in. (5.44%)	2.11 in. (2.93%)	6.14 in. (8.53%)	8.14 in. (11.3%)	-
	Measured	4.57 in. (6.35%)	2.71 in. (3.76%)	7.56 in. (10.5%)	8.93 in. (12.4%)	10.0 in. (13.9%)
LD-S3-G60D	Predicted	4.21 in. (5.85%)	2.03 in. (2.82%)	5.98 in. (8.31%)	6.76 in. (8.82%)	-
	Measured	4.72 in. (6.56%)	2.77 in. (3.85%)	6.83 in. (9.48%)	7.99 in. (11.1%)	-
LD-S1.5-G100	Predicted	4.57 in. (6.35%)	3.21 in. (4.46%)	7.23 in. (10.0%)	6.90 in. (9.58%)	-
	Measured	5.34 in. (7.42%)	-	-	-	-
Run		**25% LD**	**50% LD**	**100% LD**	**-**	**-**
LD-S3-G100	Predicted	-	-	4.53 in. (6.29%)	-	-
	Measured	0.94 in. (1.31%)	3.02 in. (4.20%)	5.42 in. (7.53%)	-	-
Run		**100% SD[3]**	**125% SD**	**-**	**-**	**-**
SD-S3-G100	Predicted	6.59 in. (9.15%)	7.74 in. (10.8%)	-	-	-
	Measured	6.88 in. (9.56%)	-	-	-	-

[1] LD: Long-duration motion from the 2011 Tohoku earthquake.
[2] After Shock: Motion recorded a month after the 2011 Tohoku earthquake.
[3] SD: Short-duration motion from the 1999 Kocaeli earthquake (scale factor= 3.68).

Table 7.2 Peak predicted and measured base shear (bending moment) for each column during each run.

Run		100% LD[1]	After Shock[2]	125% LD	150% LD	160% LD
LD-S3-G60	Predicted	34.1 kip (205 kip.ft)	25.3 kip (152 kip.ft)	34.4 kip (206 kip.ft)	-	-
	Measured	35.7 kip (214 kip.ft)	25.1 kip (151 kip.ft)	38.8 kip (233 kip.ft)	36.7 kip (220 kip.ft)	-
LD-S1.5-G60	Predicted	34.0 kip (204 kip.ft)	25.0 kip (150 kip.ft)	34.5 kip (207 kip.ft)	34.7 kip (208 kip.ft)	-
	Measured	35.4 kip (212 kip.ft)	26.1 kip (157 kip.ft)	36.1 kip (217 kip.ft)	35.9 kip (215 kip.ft)	35.6 kip (214 kip.ft)
LD-S3-G60D	Predicted	32.1 kip (193 kip.ft)	24.2 kip (145 kip.ft)	32.2 kip (193 kip.ft)	31.3 kip (188 kip.ft)	-
	Measured	33.6 kip (202 kip.ft)	26 kip (156 kip.ft)	33.4 kip (200 kip.ft)	21.1 kip (127 kip.ft)	-
LD-S1.5-G100	Predicted	35.0 kip (210 kip.ft)	27.1 kip (163 kip.ft)	37.0 kip (222 kip.ft)	35.1 kip (211 kip.ft)	
	Measured	39.4 kip (236 kip.ft)	-	-	-	-
Run		**25% LD**	**50% LD**	**100% LD**	**-**	**-**
LD-S3-G100	Predicted	-	-	35.2 kip (211 kip.ft)	-	-
	Measured	21.3 kip (128 kip.ft)	36.6 kip (220 kip.ft)	39.2 kip (235 kip.ft)	-	-
Run		**100% SD[3]**	**125% SD**	**-**	**-**	**-**
SD-S3-G100	Predicted	34.8 kip (209 kip.ft)	37.1 kip (223 kip.ft)	-	-	-
	Measured	39.6 kip (238 kip.ft)	-	-	-	-

[1] LD: Long-duration motion from the 2011 Tohoku earthquake.
[2] After Shock: Motion recorded a month after the 2011 Tohoku earthquake.
[3] SD: Short-duration motion from the 1999 Kocaeli earthquake (scale factor= 3.68).

7.3 REFINEMENT OF THE PRE-TEST MODELS

As discussed in the previous section, the differences between the measured and the predicted results indicated that additional refinements were necessary, and some modeling assumptions revised. The modifications included four categories: (1) the input earthquake records, (2) the material models and properties, (3) the low-cycle fatigue model, and (4) the bond-slip model at the base.

7.3.1 Earthquake Loading

Instead of the target motions, the shake table acceleration feedback from the different tests were used as the input excitations in the post-test analyses in the OpenSees model. The achieved shake

table accelerations were baseline-corrected and processed using a band-pass filter of order 10 with cut-in and cut-out frequencies of 0.1 Hz and 20 Hz, respectively. A *UniformExcitation* load pattern was used to apply the motions at the base node of the column. The time step in the analyses was selected to be 0.003906 sec, which corresponded to the reciprocal of 256 Hz (the data acquisition sampling frequency as well as controller rate of the shake table).

7.3.2 Materials Models and Properties

7.3.2.1 Concrete

The *Concrete02* uniaxial material was utilized to model the cover and core concrete fibers in the nonlinear beam–column element that represented the column. The concrete properties were updated based on the measured test-day properties. Three concrete models—including *Concrete02*, *Concrete01withSTIC*, and *Concrete04*—are commonly used in OpensSees models. A parametric study conducted by Mehraein [2016] and an analytical study on bridge modeling by Shoushtari et al. [2020] showed that the *Concrete02* model resulted in fewer convergence issues compared to the other two models. It was also shown that the effect of different hysteretic behavior of each concrete model on the global response of member is negligible. The modeling parameters for the cover and core concrete are listed in Table 7.3. The properties of confined core concrete were determined using the Mander's model [Mander et al. 1988]. The concrete tensile strength in *Cocnrete02* was ignored.

Table 7.3 Parameters used to define *Concrete02* material for concrete core and cover in the post-test model.

Parameter		f_c' (ksi)	ε_{c0}	f_{cu}' (ksi)	ε_{cu}	λ
Phase I	Cover	7.5	0.002	0.0	0.005	0.4
	Core (6db)	9.71	0.0049	7.99	0.0168	0.4
	Core (3db)	11.54	0.0074	9.98	0.0255	0.4
Phase II	Cover	5.5	0.002	0.0	0.005	0.4
	Core (6db)	7.64	0.0059	6.43	0.0202	0.4
	Core (3db)	9.32	0.0089	8.20	0.0306	0.4

7.3.2.2 Reinforcing Steel

Two different material models were used for the column longitudinal bars in the fiber section: *ReinforcingSteel* for conventional Grade 60 A706 bars; and *RambergOsgoodSteel* for high-strength Grade 100 A1035 bars. The *ReinforcingSteel* uniaxial material is based on the model proposed by Chang and Mander [1994] and includes the yield plateau and strain hardening regions in the stress–strain relationship. The softening region, which is a localization effect due to necking, is ignored in this material. This geometric effect is a function of the measurement gauge length and is due to the reduction in area of the bar in tension. Note: the envelope curve of the material model *Steel02* differed from the measured curve obtained in the tensile coupon tests for Grade 100

bars; therefore, the post-test analyses were performed using the *RambergOsgoodSteel* uniaxial material for HSS longitudinal bars in the column fiber section. The Ramberg–Osgood model describes the nonlinear stress–strain relationship in steel material near its yield point with a smooth elastic-plastic transition [Equation (7.1)]. In this material, the elastic strain portion of the stress–strain curve is modeled with a line, while the plastic portion is modeled by the Ramberg and Osgood's power law [1943]:

$$\varepsilon = \frac{\sigma}{E} + \alpha \left(\frac{\sigma}{f_y} \right)^n \tag{7.1}$$

where ε and σ are the strain and stress; E is the Young's modulus of elasticity; f_y is the yield strength obtained from offset method; α is the yield offset (taken as 0.002); and n is the parameter that controls the transition from elastic to plastic branches (taken as 30).

The effect of the high loading rate on the steel was also considered in the post-test analyses as discussed next. Table 7.4 and Table. 7.5 present the input modeling parameters for Grade 60 and Grade 100 steel materials, respectively, after modifying the strain rate effect.

Table 7.4 Parameters used to define *ReinforcingSteel* material for Grade 60 bars in the post-test model.

Parameter	f_y (ksi)	f_u (ksi)	E_s (ksi)	E_{sh} (ksi)	ε_{sh}	ε_u
Value	74.5	117.7	29000	1160	0.0045	0.092

Table 7.5 Parameters used to define *RambergOsgoodSteel* material for Grade 60 bars in the post-test model.

Parameter	f_y (ksi)	E_s (ksi)	α	n
Value	148.8	28000	0.002	30

7.3.3 Strain Rate Effects

Earthquake loading typically involves high strain rates that are likely to affect rate-dependent materials, e.g., such as polymers or physical phenomena like viscosity or friction in base isolators or dampers. Although concrete and steel tests to determine their properties are generally conducted at very low loading rates, relatively high loading rates are experienced during the shake table tests, which tend to increase concrete and steel strengths. Different formulations have been proposed [Kulkarni and Shah 1998; Zadeh and Saiidi 2007; and Zhang et al. 2018] to modify the concrete compressive strength and the yield and ultimate stress of the steel as a function of the strain rate. Kulkarni and Shah [1998] formulations were utilized in this study to determine the modified material properties for Grade 60 steel used in the analytical model. No similar comprehensive studies have been conducted on HSS rebars, especially the Grade 100 MMFX bars used in this

study. Thus, a set of material tests were conducted to investigate the effect of high strain rate on Grade 100 MMFX bars steel bars. The stress–strain relationship of the bars was determined by conducting monotonic tensile tests under six different loading rates of 0.05, 0.5, 5, 10, 15, and 20 in./min on at least three samples. The corresponding resulted strain rates prior to yielding were approximately 45, 450, 3500, 6500, 8000, and 10,000 $\mu\varepsilon$/sec, respectively.

The obtained stress–strain relationship curves for each strain rate are plotted in Figure 7.6 for comparison purposes. The strain-rate effect on the yield strength, tensile strength, tensile-to-yield strength (*T/Y*) ratio, and fracture strain were examined. The axial strains were measured using a high-resolution optical extensometer. Figure 7.7 through Figure 7.10 show the effect of strain rate on the steel characteristics for Grade 100 bars. The results indicate that the strain rate becomes more significant in ranges higher than 4000 $\mu\varepsilon$/sec; however, the tensile strength is independent of the strain rate and remained constant under different loading rates. Accordingly, higher yield strength produces a lower *T/Y* ratio that, in turn, significantly reduces the low-cycle fatigue life of steel bars. This might be one of the causes that leads to the early bar rupture observed in Phase II columns.

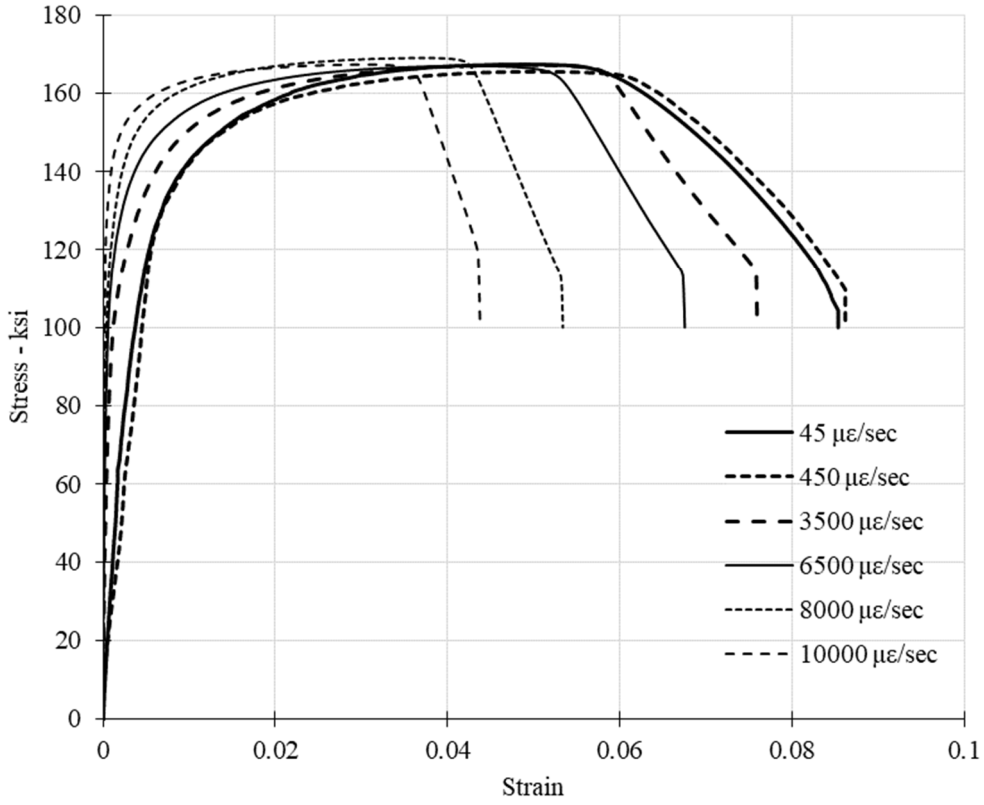

Figure 7.6 Effect of strain rate on the stress–strain relationship of high-strength steel.

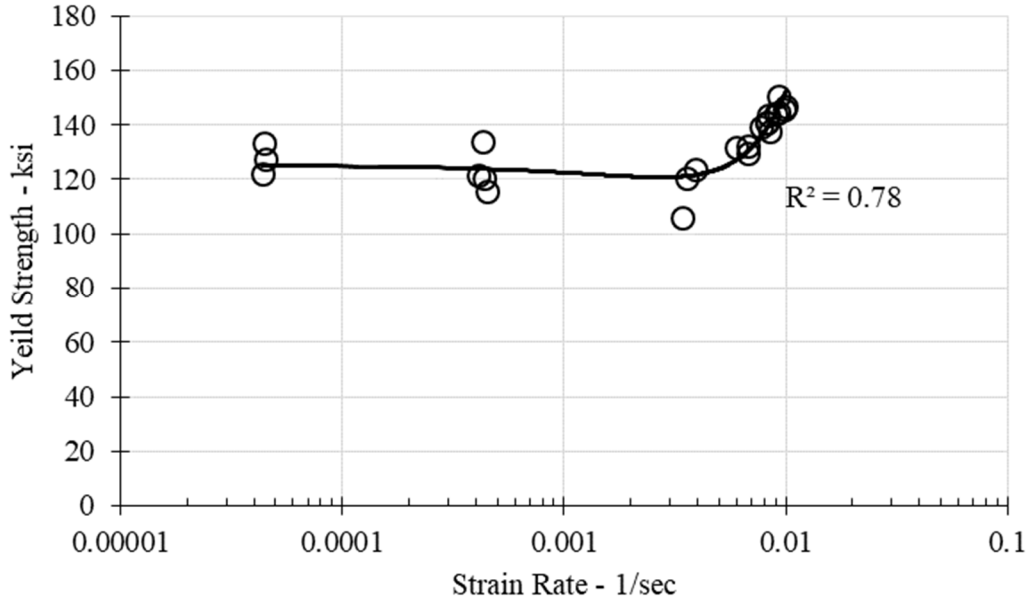

Figure 7.7 **Effect of strain rate on the yield strength for high-strength steel.**

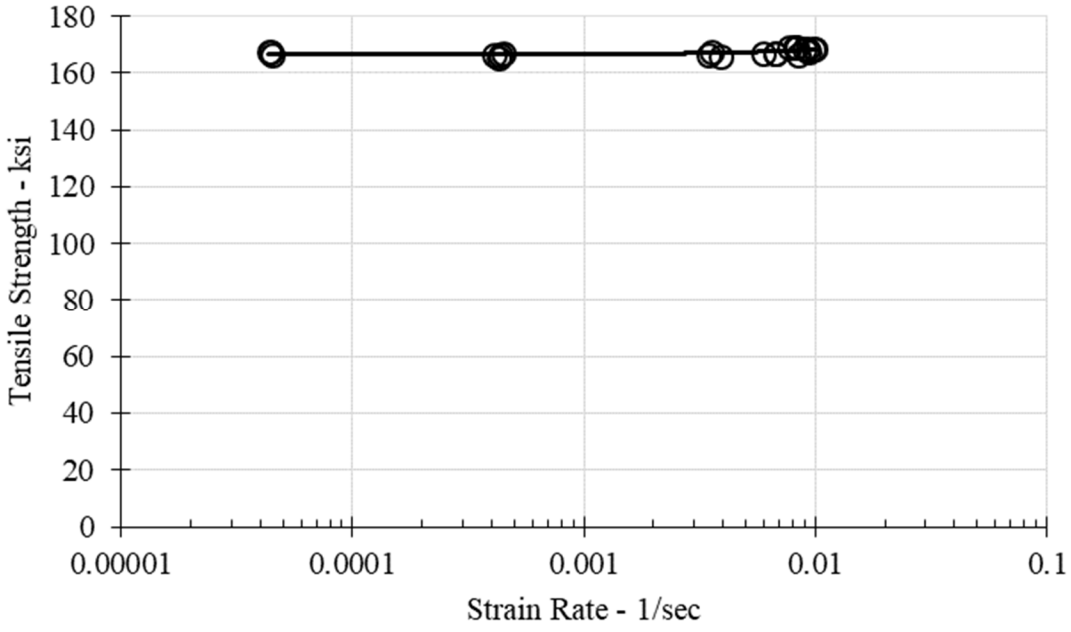

Figure 7.8 **Effect of strain rate on the tensile strength for high-strength steel.**

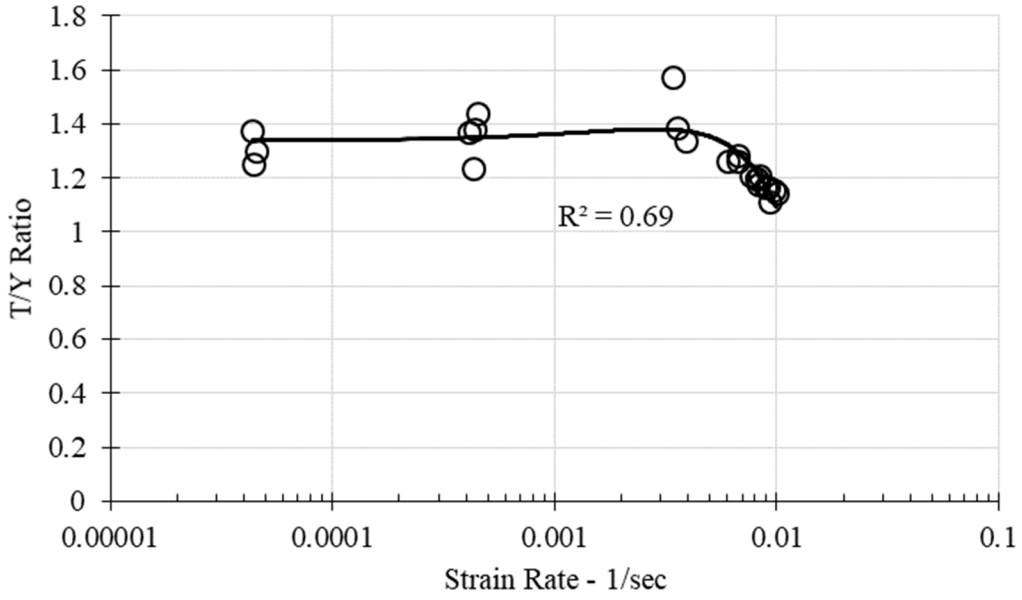

Figure 7.9 Effect of strain rate on the *T/Y* ratio for high-strength steel.

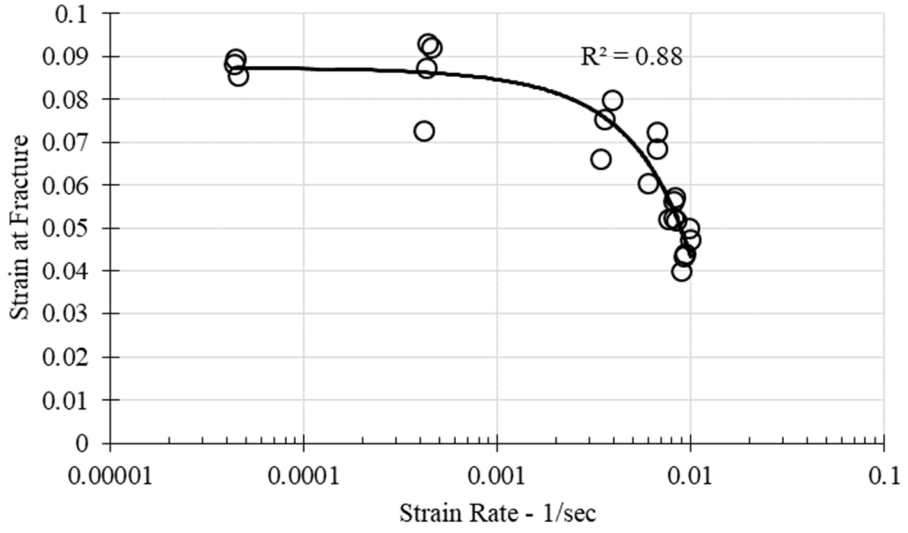

Figure 7.10 Effect of strain rate on the fracture strain for high-strength steel.

Because the measured dynamic strain rates on the steel reinforcement varied during the shake table tests, an average tensile strain rate of 18,000 $\mu\varepsilon$/sec was used in the model prior to first yielding of each bar. The concrete strains were not recorded during the compressive tests, and an average strength from the compression tests of the concrete cylinders at test dates were utilized as the concrete compressive strength in the model. Because such strain data was unnecessary—as the effect of loading rate on the concrete strength is known to be insignificant—it was neglected in this study.

The yield and ultimate stress of the Grade 60 steel were amplified by the strain-rate factor SRF_S determined by Equations (7.2) through (7.4) [Kulkarni and Shah 1998]. The static strain rate (ε_{st}) was assumed as 250 $\mu\varepsilon$/sec, which is the approximate rate applied during the tensile tests. Thus, the strain-rate factor for the steel reinforcement was equal to 1.03. This factor was applied (through multiplication) to the measured yield stress (72.3 ksi) and ultimate stress (113.3 ksi), which resulted in 74.3 and 116.4 ksi, respectively.

$$\mathrm{SRF}_S = \mathrm{SRF}_{45} + \frac{\mathrm{SRF}_{75} - \mathrm{SRF}_{45}}{30}\left(f_y - 45\right) \tag{7.2}$$

$$\mathrm{SRF}_{45} = 0.0328 \ln\left(\frac{\dot{\varepsilon}}{\dot{\varepsilon}_{\mathrm{st}}}\right) + 0.9873 \tag{7.3}$$

$$\mathrm{SRF}_{75} = 0.0124 \ln\left(\frac{\dot{\varepsilon}}{\dot{\varepsilon}_{\mathrm{st}}}\right) + 0.9632 \tag{7.4}$$

where f_y is measured yield stress of bars in ksi; SRF_S is the strain-rate factor for steel with yield stress f_y; SRF_{45} and SRF_{75} are strain-rate factors for steel with yield stress of 45 ksi and 75 ksi, respectively; and $\dot{\varepsilon}$ and $\dot{\varepsilon}_{\mathrm{st}}$ are dynamic and static strain rates, respectively ($\mu\varepsilon$/sec).

Based on the test results, a new equation was developed to account for the strain-rate effect on Grade 100 MMFX bars. For this purpose, the strain rates were normalized by 4000 $\mu\varepsilon$/sec as the threshold of the effective strain rate, and the yield strength was normalized by the yield stress measured in the static test (124 ksi). A linear regression analysis was then done in a log–linear space; see Figure 7.11. The developed equation [Equation (7.5)] was used to obtain the strain rate factor $\mathrm{SRF}_{100\mathrm{MMFX}}$ to amplify the yield stress of the Grade 100 bars

$$\mathrm{SRF}_{100\mathrm{MMFX}} = 0.134 \ln\left(\frac{\dot{\varepsilon}}{4000}\right) + 1.0 \tag{7.5a}$$

$$\mathrm{SRF}_{100\mathrm{MMFX}} = 0.134 \ln(\dot{\varepsilon}) - 0.111 \tag{7.5b}$$

where $\mathrm{SRF}_{100\mathrm{MMFX}}$ is the strain-rate factor for the MMFX reinforcing bar with nominal yield stress of 100 ksi; and $\dot{\varepsilon}$ is dynamic strain rate ($\mu\varepsilon$/sec). The strain-rate factor for the HHS bars equal to 1.20 was used. The yield strength was amplified from 124 ksi to 149 ksi. This value was used to perform sectional analysis and to determine the low-cycle fatigue parameters. For the first time, the above procedure was used exclusively for modeling HSS reinforcing bars in seismic columns. Thus, validating this modeling approach for HSS against the shake table tests is expected to augment further future research studies in this area.

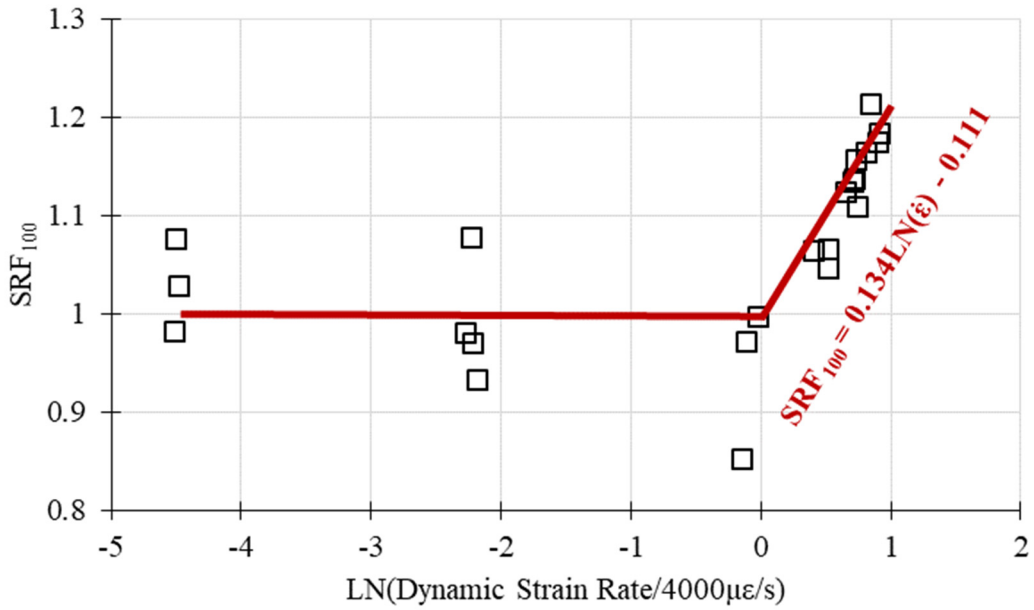

Figure 7.11 Strain-rate modification factor for high-strength steel.

7.3.4 Bond-Slip Model

The bond-slip effect was added to the model in terms of a moment-rotation (M-θ) curve assigned to a *zeroLength* element at the base of the column (rotational spring) based on the bond-slip model proposed by Wehbe et al. [1997]. The modeling parameters for the bond-slip model were calculated from the results of the sectional analysis performed in OpenSees using the Wehbe model's equations listed below:

$$\theta = \frac{\delta l}{d - c} \tag{7.6}$$

$$\delta l = \begin{cases} \dfrac{d_b f_s^2}{8 E_s u} & \text{Elastic Range } (f_y < f_y) \quad (7.7a) \\ \dfrac{\varepsilon_y l_2}{2} + \dfrac{(\varepsilon_s + \varepsilon_y) l_1}{2} & \text{Nonlinear Range } (f_s \geq f_y) \quad (7.7b) \end{cases}$$

$$u = \frac{9.5\sqrt{f_c'}}{d_b} \leq 800 \text{ psi} \quad \#11 \text{ or smaller bars} \tag{7.8}$$

$$l_1 = \frac{(f_s - f_y) d_b}{4u} \qquad l_2 = \frac{f_y d_b}{4u} \tag{7.9}$$

where θ is bond-slip rotation; δl is additional extension of the longitudinal outermost bar; d is effective depth of the column section; c is distance from the extreme compression fiber to the neutral axis; d_b is the longitudinal bar diameter; f_s and ε_s are steel stress and corresponding strain,

respectively; E_s is steel modulus of elasticity; f_y and ε_y are steel yield stress and corresponding yield strain, respectively; u is basic bond strength of tension bars; and f_c' is concrete compressive strength.

Based on the calibration results for the bond-slip model used in this study, it is recommended to develop the moment-rotation backbone curve using three points: one point in the elastic range and two points in the nonlinear range as follows:

$$\text{Point 1: } M_1 = 0.2 \sim 0.3M_u \qquad \theta_1 \text{ from Equations (7.6) and (7.7a)} \tag{7.7}$$

$$\text{Point 2: } M_2 = 0.75 \sim 0.85M_u \qquad \theta_2 \text{ from Equations (7.6) and (7.7b)} \tag{7.8}$$

$$\text{Point 3: } M_3 = M_u \qquad \theta_3 \text{ from Equations (7.6) and (7.7b)} \tag{7.9}$$

where M and θ M are section bending moments and the corresponding section bond-slip rotations, respectively; and M_u is the ultimate moment capacity of the section as the steel stress reaches the tensile strength. The modeling parameters for the bond-slip model calculated for each column are listed in Table 7.6.

In Column LD-S3-G60D, debonding of the longitudinal bars helped to improve the column displacement capacity due to spread of yielding and subsequent larger bond-slip rotation at the base of the column. For simplicity's sake, the effect of bar debonding in this column was simulated by modifying the bond-slip model.

Table 7.6 Bond-slip model parameters in positive (and negative) direction used in the post-test model.

Parameter	M_1 (kip.in.)	θ_1 (rad)	M_2 (kip.in.)	θ_2 (rad)	M_3 (kip.in.)	θ_3 (rad)
LD-S3-G60	1200 (-1200)	0.001 (-0.001)	2200 (-2350)	0.007 (-0.008)	3300 (-2535)	0.03 (-0.03)
LD-S1.5-G60	1200 (-1100)	0.0015 (-0.0015)	2100 (-2400)	0.009 (-0.008)	2600 (-3500)	0.03 (-0.03)
LD-S3-G60D	1200 (-1200)	0.002 (-0.002)	2100 (-2500)	0.012 (-0.01)	2450 (-2800)	0.03 (-0.03)
LD-S1.5-G100	1400 (-1400)	0.0025 (-0.0025)	2900 (-3100)	0.017 (-0.017)	3055 (-3220)	0.03 (-0.03)
LD-S3-G100	1000 (-1000)	0.003 (-0.003)	2800 (-2800)	0.01 (-0.009)	3050 (-3170)	0.03 (-0.03)
SD-S3-G100	1400 (-1400)	0.0025 (-0.0023)	2800 (-2600)	0.015 (-0.009)	2975 (-3110)	0.03 (-0.03)

7.3.5 Low-Cycle Fatigue Model

The steel material assigned to the reinforcing bars was wrapped by the *Fatigue* material in OpenSees to account for the low-cycle fatigue induced failure/rupture of reinforcing bars. The low-cycle fatigue modeling parameters were determined using the fatigue-fracture model developed by Zhong and Deierlein [2019], which is the modified version of the one used in the

pre-test analysis. Note that at the time of the pre-test analysis, just the preliminary equations were available. For the post-test analysis, the final versions [Equations (7.13) to (7.16)] were used in the OpenSees model. The same equations were utilized for both Grade 60 and Grade 100 steel considering amplified yield stresses due to the strain rate effect.

$$\varepsilon_p = C_f \left(2N_f\right)^{-\alpha_f} \tag{7.10}$$

$$\alpha_f 0.080 - 0.045\left(f_y/60\text{ ksi}\right) + 0.027\left(s/d_b\right) - 0.129(T/Y) \tag{7.11}$$

$$C_f = 0.5^{\alpha_f}\left(\varepsilon_f - f_y/E\right) \tag{7.12}$$

$$\varepsilon_f = f_y/E_s - 0.043\left(f_y/60\text{ ksi}\right) + 0.128(T/Y) + 0.018(d_b/1\text{ in.}) \tag{7.13}$$

where ε_p is plastic strain amplitude; $2N_f$ is number of half cycles; C_f and α_f are material properties; f_y is steel yield strength; s is clear spacing of reinforcing bar; d_b is nominal size of reinforcing bar; T/Y is steel ultimate strength to yield strength ratio; ε_f is fracture strain amplitude; and E_s is modulus of elasticity. The modified yield stress due to strain rate effect was used to determine the low-cycle fatigue parameters. The modeling parameters for the fatigue material calculated for each column are listed in Table 7.7.

Table 7.7 Fatigue material parameters used in the post-test model.

Parameter	C_f	α_f
LD-S3-G60	0.12	-0.39
LD-S1.5-G60	0.127	-0.31
LD-S3-G60D	0.12	-0.39
LD-S1.5-G100	0.04	-0.20
LD-S3-G100	0.04	-0.28
SD-S3-G100	0.04	-0.28

7.4 POST-TEST ANALYTICAL RESULTS VERSUS MEASURED DATA

To assess the correlation between the analytical model with the measured results, responses were compared in terms of the peak values and response histories during each run. Table 7.8 lists the peak measured and calculated displacements (drift ratios) for each column during each run. As suggested by the results, there is a good agreement between the measured and calculated peak displacements. The differences in the peak base shears for each column during each run are presented in Figure 7.12 through Figure 7.27, which show the force-displacement hysteresis curves during each run, the cumulative force-displacement hysteresis curves, and displacement history for each of the columns tested. Based on the various figures, the agreement between the measured and calculated force-displacement hysteresis, among other responses, was found to be reasonable, and the final calibrated/modified modeling inputs are deemed adequate for all models.

Table 7.8 Peak measured and calculated displacements (drift ratios) for each column during each run.

Run		100% LD	After Shock	125% LD	150% LD	160% LD
LD-S3-G60	Calculated	4.29 in. (5.97%)	3.12 in. (4.34%)	5.88 in. (8.17%)	6.69 in. (9.30%)	-
	Measured	4.41 in. (6.13%)	2.80 in. (3.89%)	5.95 in. (8.27%)	6.44 in. (8.94%)	-
LD-S1.5-G60	Calculated	4.53 in. (6.29%)	2.63 in. (3.65%)	7.18 in. (9.97%)	8.91 in. (12.4%)	9.85 in. (13.7%)
	Measured	4.57 in. (6.35%)	2.71 in. (3.76%)	7.56 in. (10.5%)	8.93 in. (12.4%)	10.0 in. (13.9%)
LD-S3-G60D	Calculated	4.54 in. (6.30%)	3.17 in. (4.40%)	7.33 in. (10.2%)	-	-
	Measured	4.72 in. (6.56%)	2.77 in. (3.85%)	6.83 in. (9.48%)	-	-
LD-S1.5-G100	Calculated	5.58 in. (7.74%)	-	-	-	-
	Measured	5.34 in. (7.42%)	-	-	-	-
Run		25% LD	50% LD	100% LD	-	-
LD-S3-G100	Calculated	0.79 in. (1.10%)	3.63 in. (5.04%)	4.44 in. (6.17%)	-	-
	Measured	0.94 in. (1.31%)	3.02 in. (4.20%)	5.42 in. (7.53%)	-	-
Run		100% SD	-	-	-	-
SD-S3-G100	Calculated	6.79 in. (9.43%)	-	-	-	-
	Measured	6.88 in. (9.56%)	-	-	-	-

Table 7.9 Peak measured and calculated base shear (bending moment) for each column during each run.

Run		100% LD[1]	After Shock[2]	125% LD	150% LD	160% LD
LD-S3-G60	Calculated	36.5 kip (219 kip.ft)	27.8 kip (167 kip.ft)	37.2 kip (223 kip.ft)	37.1 kip (223 kip.ft)	-
	Measured	35.7 kip (214 kip.ft)	25.1 kip (151 kip.ft)	38.8 kip (233 kip.ft)	36.7 kip (220 kip.ft)	-
LD-S1.5-G60	Calculated	34.4 kip (207 kip.ft)	27.7 kip (166 kip.ft)	35.0 kip (210 kip.ft)	35.5 kip (213 kip.ft)	35.6 kip (214 kip.ft)
	Measured	35.4 kip (212 kip.ft)	26.1 kip (157 kip.ft)	36.1 kip (217 kip.ft)	35.9 kip (215 kip.ft)	35.6 kip (214 kip.ft)
LD-S3-G60D	Calculated	33.7 kip (202 kip.ft)	29.6 kip (178 kip.ft)	33.9 kip (203 kip.ft)	-	-
	Measured	33.6 kip (202 kip.ft)	26.0 kip (156 kip.ft)	33.4 kip (200 kip.ft)	21.1 kip (127 kip.ft)	-
LD-S1.5-G100	Calculated	35.0 kip (210 kip.ft)	27.1 kip (163 kip.ft)	37.0 kip (222 kip.ft)	35.1 kip (211 kip.ft)	
	Measured	39.4 kip (236 kip.ft)	-	-	-	-
Run		25% LD	50% LD	100% LD	-	-
LD-S3-G100	Calculated	20.5 kip (123 kip.ft)	37.0 kip (222 kip.ft)	38.7 kip (232 kip.ft)	-	-
	Measured	21.3 kip (128 kip.ft)	36.6 kip (220 kip.ft)	39.2 kip (235 kip.ft)	-	-
Run		100% SD[3]	-	-	-	-
SD-S3-G100	Calculated	39.7 kip (238 kip.ft)	-	-	-	-
	Measured	39.6 kip (238 kip.ft)	-	-	-	-

[1] LD: Long-duration motion from the 2011 Tohoku earthquake.
[2] After Shock: Motion recorded a month after the 2011 Tohoku earthquake.
[3] SD: Short-duration motion from the 1999 Kocaeli earthquake (scale factor= 3.68).

According to Table 7.8 and Table 7.9, the differences between the measured and calculated dominant peak responses ranged from 1.5% to 8%. The measured hysteretic responses were reasonably captured by the model during the first runs prior to the extensive core damage or bar fracture with a reasonable estimation of the column stiffness. Although the models were not able to capture residual displacements properly in the runs when core damage or bar fractures occurred, the pattern of the curve and the peak forces and displacements in the dominant direction (i.e., positive direction) matched to a reasonable degree. The same can be seen in the displacement histories. In the dominant direction, the correlation of data is better estimated compared to the non-dominant direction. The analytical model for Phase II columns with HSS bars also captured the peak values with good accuracy. The model closely captured the loading stiffness but was less

accurate for unloading and reloading branches. This can be attributed to the *RambergOsgood* material model used in the OpenSees model for the HSS. Accounting for Bauschinger effect in reloading behavior of the steel material may address this issue [To 2017]. Thus, further studies are needed to develop a more accurate material model for the Grade 100 MMFX steel bar.

The reasonable accuracy in the calculated column stiffnesses and displacement histories demonstrate that the bond-slip model was able to realistically simulate base rotations due to bond slip. In addition, the predicted instance of the first bar fracture for all columns was adequately close enough to that observed in the experiments. This indicates that the fatigue fracture model and modified steel materials based on the high strain-rate effect helped significantly in accurately capturing the low-cycle fatigue life of longitudinal reinforcing bars. A set of the recommended modeling assumptions are summarized and presented in Chapter 9.

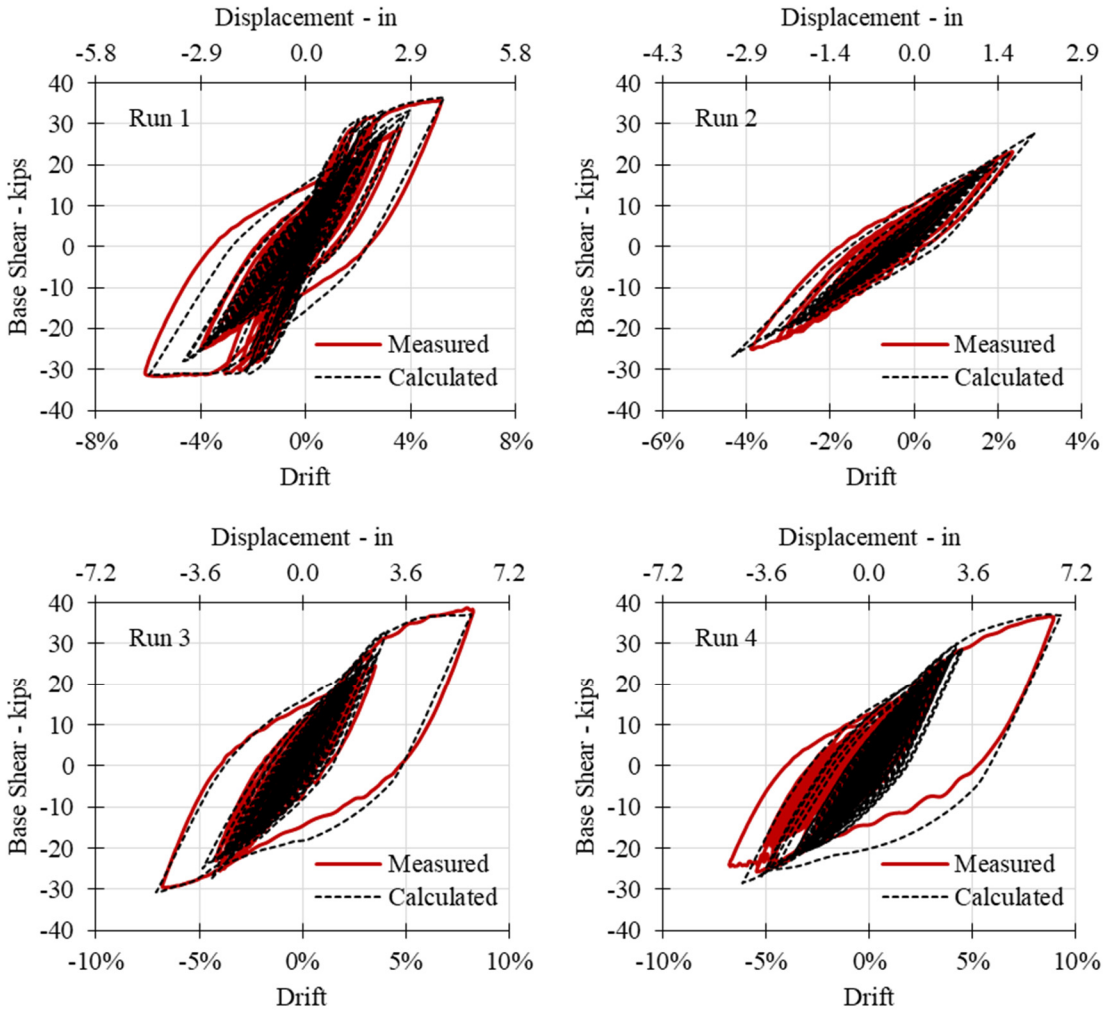

Figure 7.12 Measured versus calculated force-displacement relationships for Column LD-S3-G60 for each run.

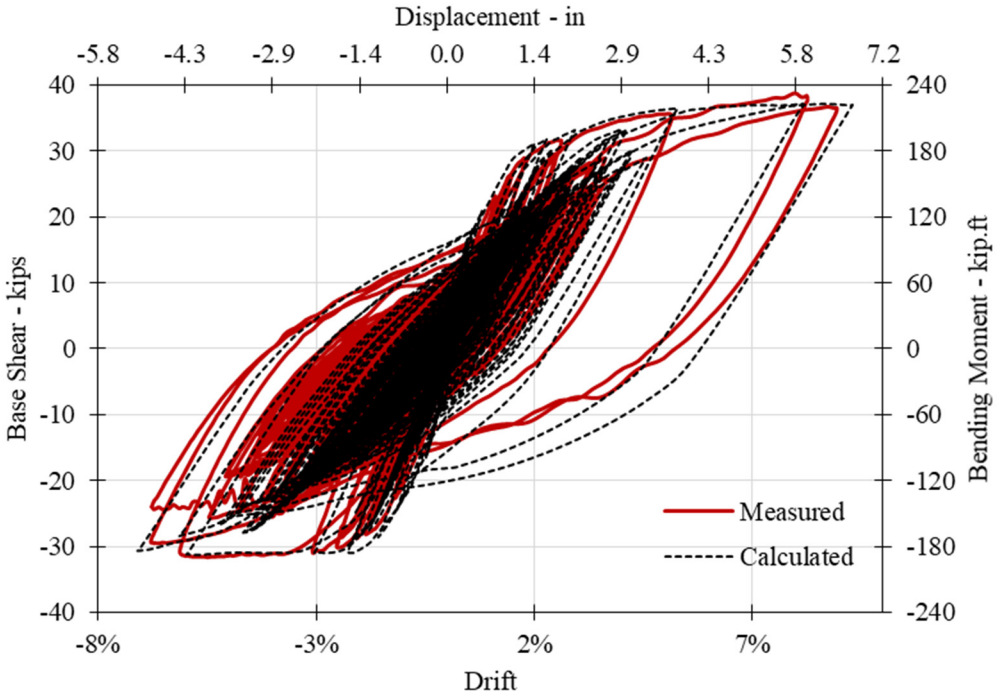

Figure 7.13 **Measured versus calculated cumulative force-displacement relationships for Column LD-S3-G60.**

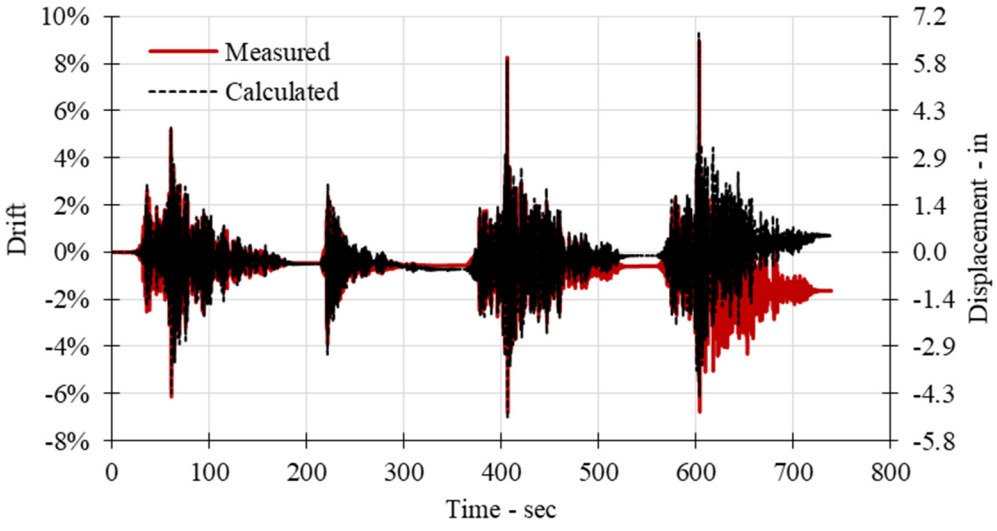

Figure 7.14 **Measured versus calculated displacement history for Column LD-S3-G60.**

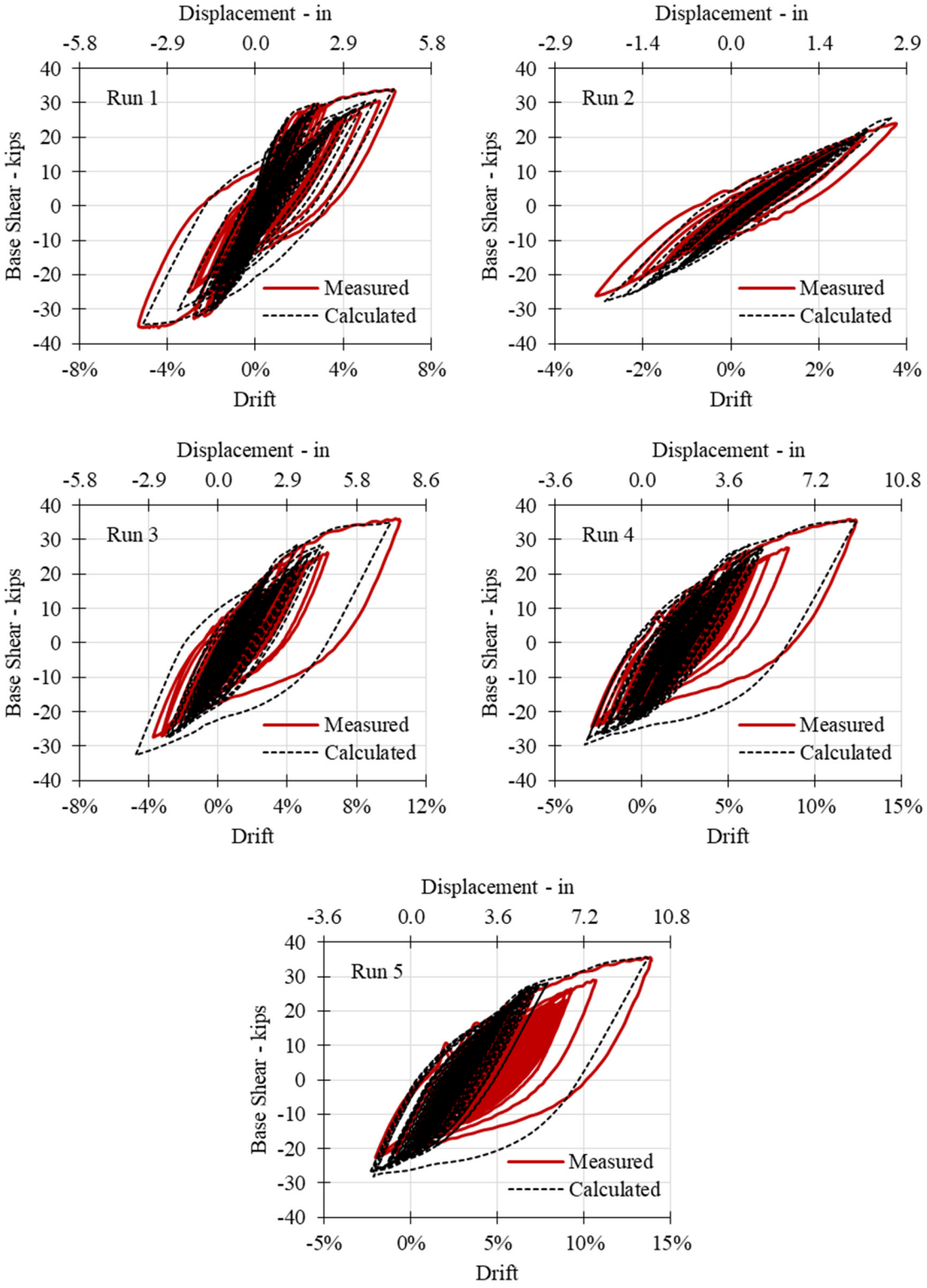

Figure 7.15 **Measured vs calculated force-displacement relationships for Column LD-S1.5-G60.**

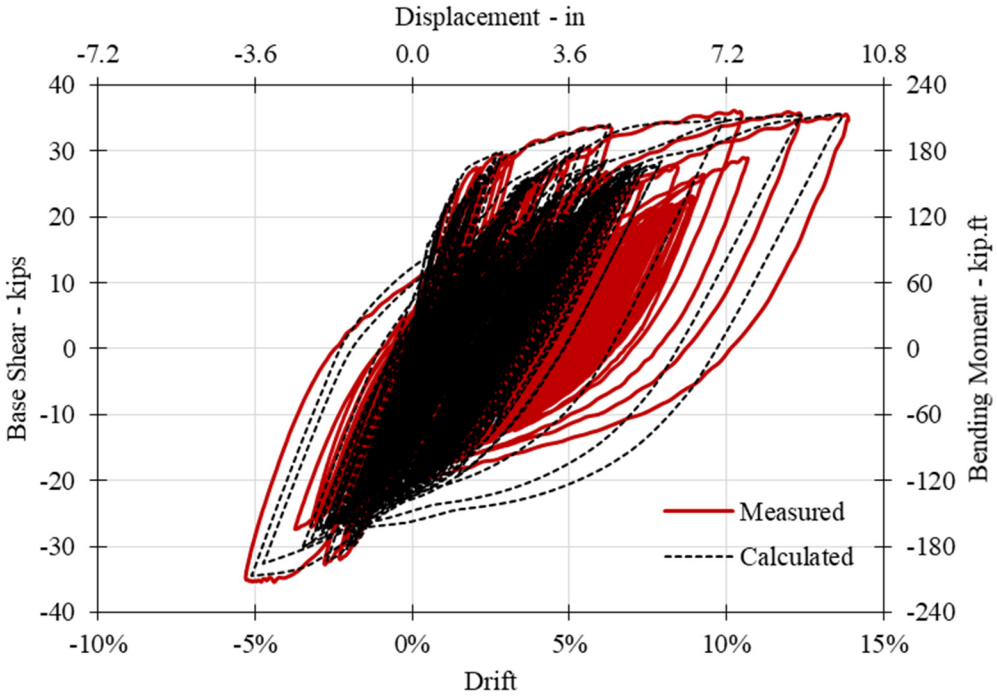

Figure 7.16 **Measured versus calculated cumulative force-displacement relationships for Column LD-S1.5-G60.**

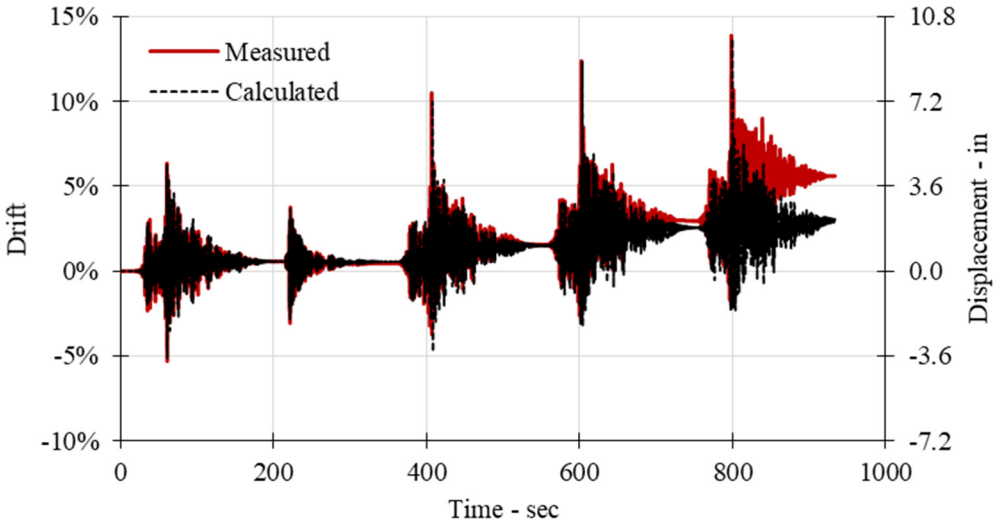

Figure 7.17 **Measured versus calculated displacement history for Column LD-S1.5-G60.**

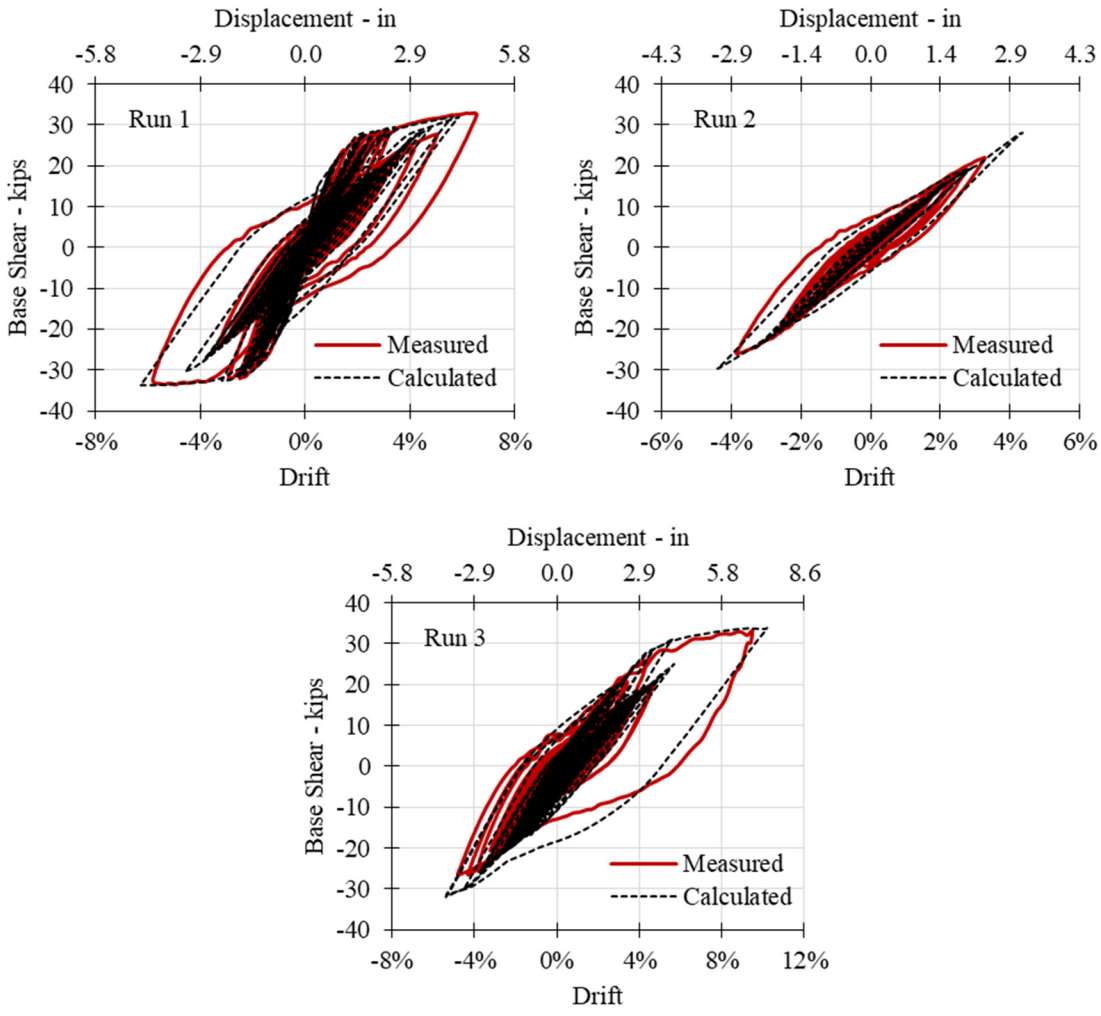

Figure 7.18 **Measured vs calculated force-displacement relationships for Column LD-S1.5-G60 for each run.**

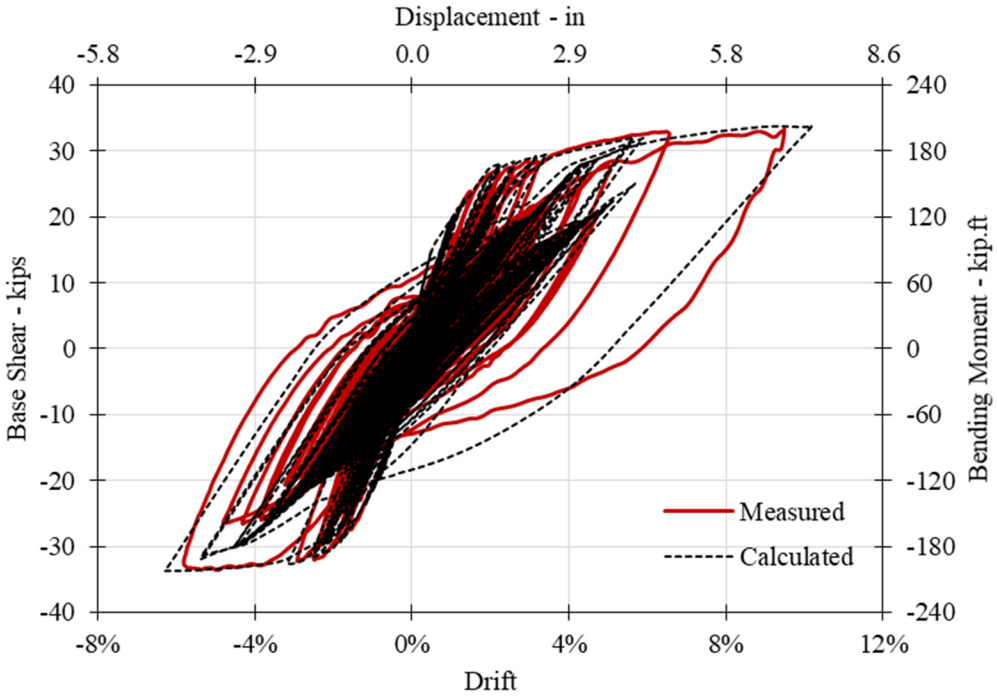

Figure 7.19 **Measured versus calculated cumulative force-displacement relationships for Column LD-S1.5-G60.**

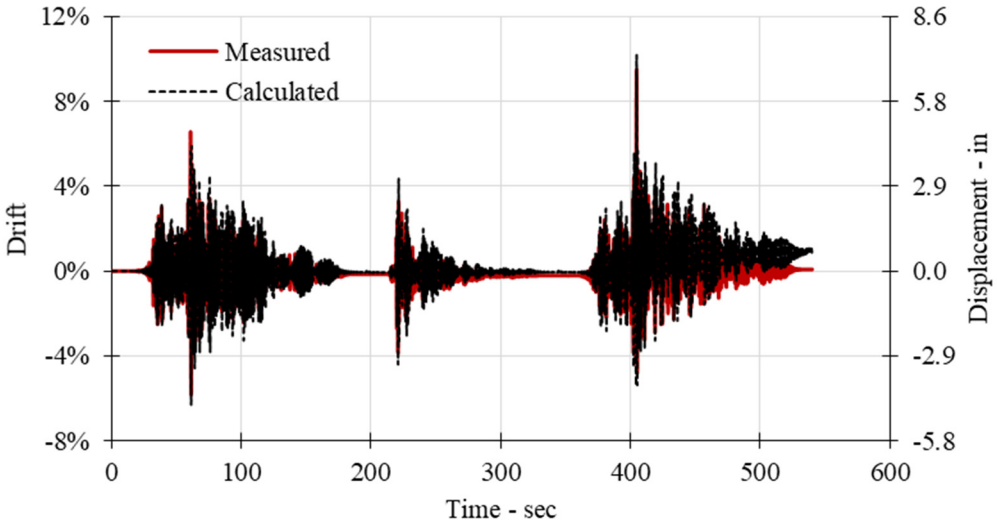

Figure 7.20 **Measured versus calculated displacement history for Column LD-S1.5-G60.**

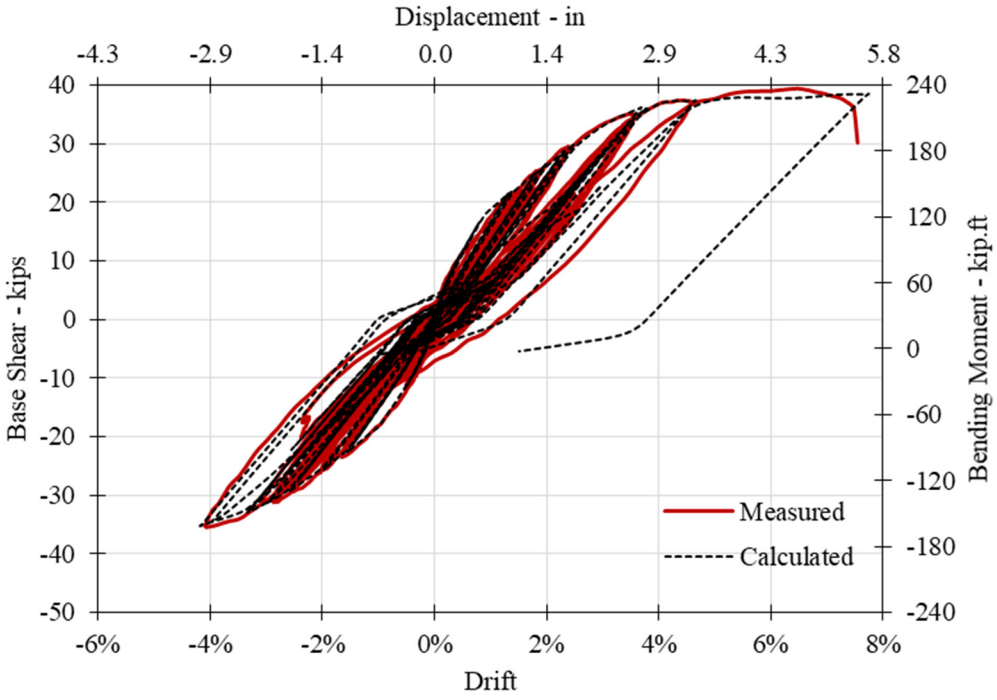

Figure 7.21 **Measured versus calculated force-displacement relationships for Column LD-S1.5-G100.**

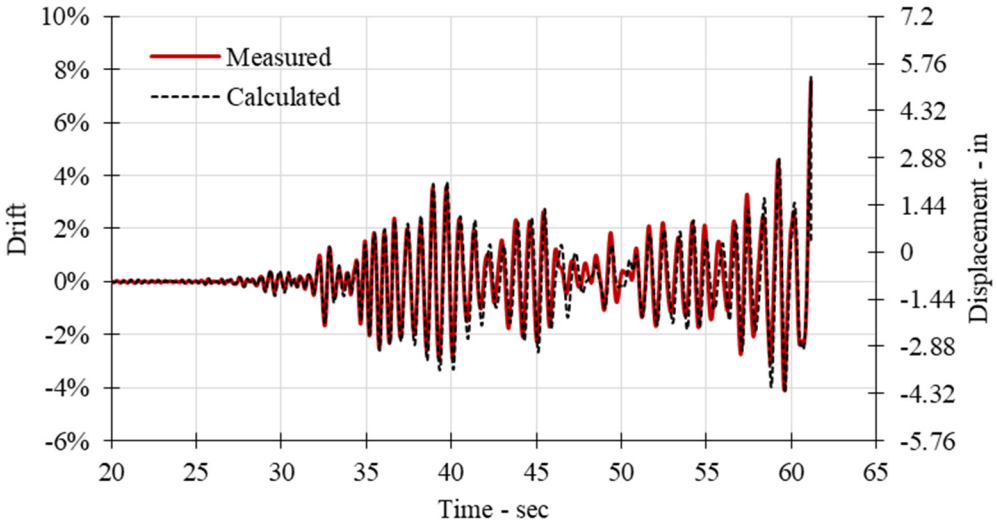

Figure 7.22 **Measured versus calculated displacement history for Column LD-S1.5-G100.**

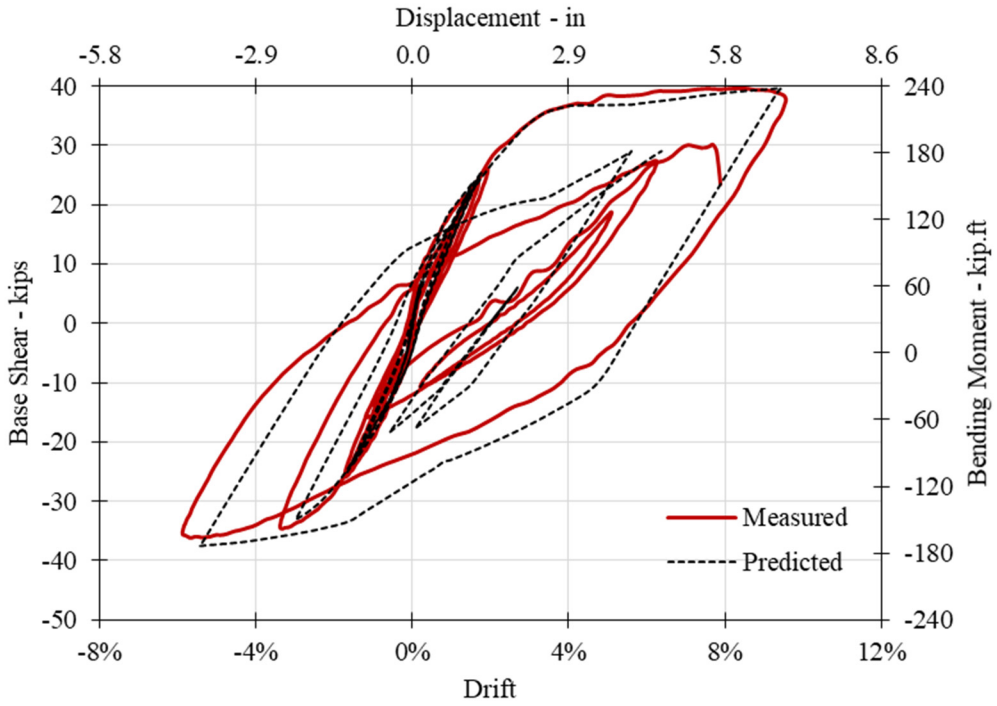

Figure 7.23 **Measured versus calculated force-displacement relationships for Column SD-S3-G100.**

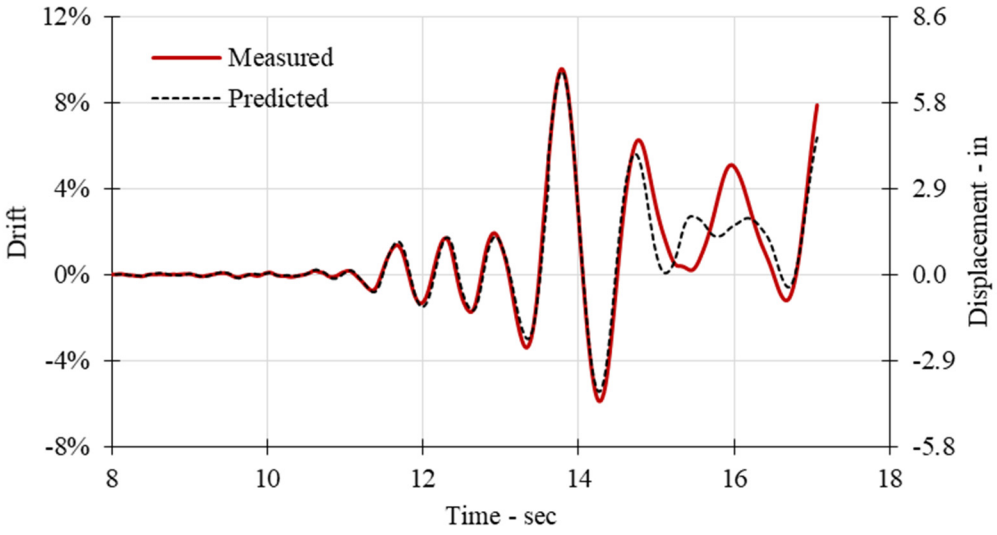

Figure 7.24 **Measured versus calculated displacement history for Column SD-S3-G100.**

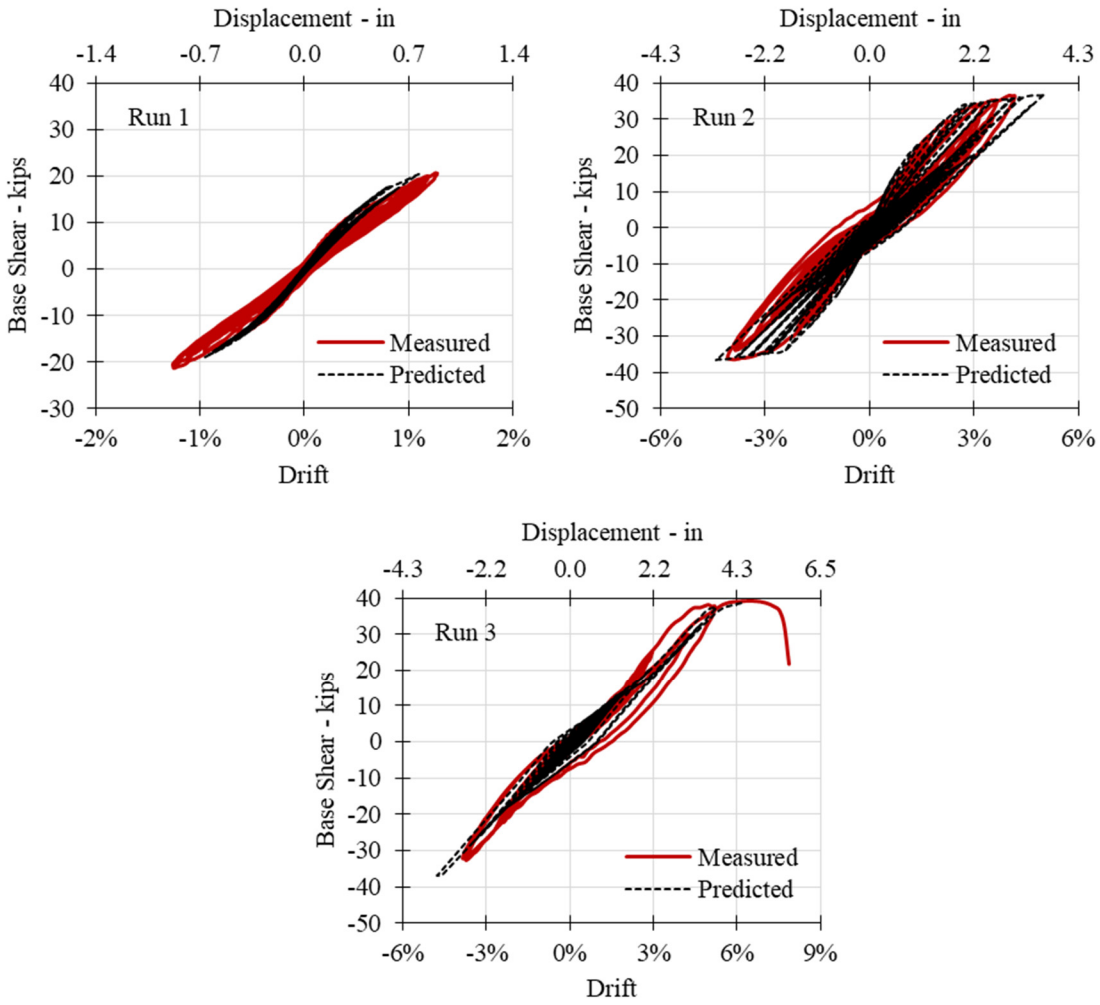

Figure 7.25 **Measured versus calculated force-displacement relationships for Column LD-S3-G100 for each run.**

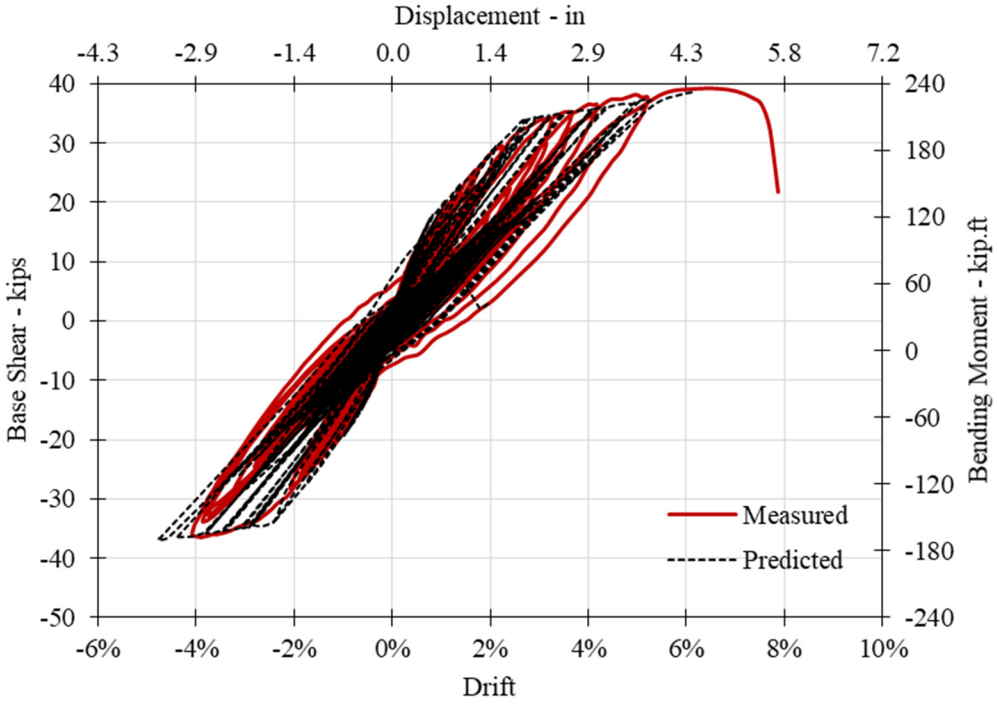

Figure 7.26 **Measured versus calculated cumulative force-displacement relationships for Column LD-S3-G60.**

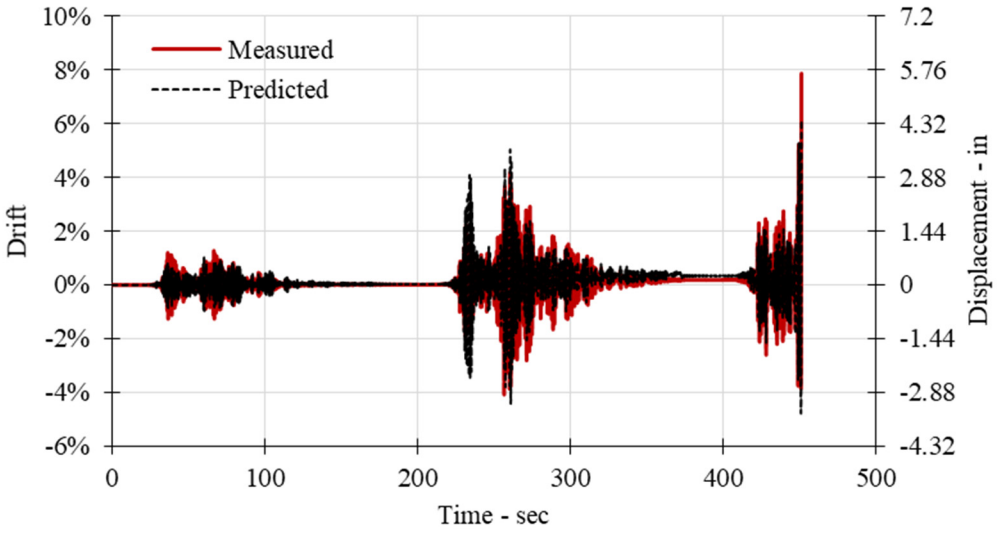

Figure 7.27 **Measured versus calculated displacement history for Column LD-S3-G100.**

8 Prototype Bridge Study

8.1 OVERVIEW

The objective of this chapter is to present recommendations that could be incorporated into seismic design provisions to consider the duration effect in the design of bridges located at sites with potential occurrence of large-magnitude and long-duration earthquakes. Therefore, an analytical study on a typical representative prototype bridge is conducted and discussed here. For this purpose, several versions of two-span two-column bent archetype bridges were considered to develop hazard-consistent fragility models by post-processing the results of a comprehensive IDA. The seismic performance of the archetype bridges was evaluated using the nested ground-motion set via the site-specific hazard adjustment framework for IDA, i.e., SHAF-IDA [Zhong 2020]. The column design ductility demand and confinement spacing ratios were used as the IMs in the fragility analysis. Safety design domains that consider duration effects were calibrated through the development of surrogate models for different bridge performance levels. Then, the recommended site-specific design strategies are discussed.

8.2 CURRENT DESIGN PRACTICE

The current bridge design standards and guidelines usually define the expected performance targets of bridges by classifying them into three different categories: Ordinary, Recovery, and Important [Caltrans 2019; AASHTO 2014]. The ordinary bridges are typically expected to experience major post-earthquake damage. Although, the replacement of the bridge is likely, they are designed for the life safety seismic hazard level (Safety Evaluation Earthquake) and have a minimal probability of collapse. The design philosophy for ordinary bridges to achieve this performance target is to design based on “strong beam—weak column” proportioning principle known as capacity design. In this design philosophy, the seismic critical members (SCM) are intentionally designed for energy dissipation/damping while the capacity protected members are designed to remain essentially elastic when the design seismic hazards (DSH) occur. Formation of flexural plastic hinges in critical members (columns) and failure of sacrificial elements such as shear keys and abutment backwalls are the main components of energy dissipation in a bridge system, according to current design philosophies and adopted codes.

For the ordinary bridges, the DSH is typically characterized by the design spectrum (DS) which is taken as a spectrum based on a 5% probability of exceedance in 50 years (or 975-year

return period). The displacement ductility demand (μ_D) of a SCM is a common parameter that has been widely adopted by design codes to quantify the bridge displacement demand under the DS as expressed in the following equations:

$$\mu_D \frac{\Delta_D}{\Delta_y} \tag{8.1}$$

$$\Delta_D \frac{WS_a}{K} \quad \text{from equivalent static analysis} \tag{8.2}$$

where Δ_D is displacement demand of the bent; Δ_y is displacement of the bent at the instant a plastic hinge forms; W is tributary weight of the structure; Sa is the design spectral acceleration coefficient at the structure period; and K is effective stiffness of the bent. According to Caltrans' *Seismic Design Criteria* [2019] for standard ordinary bridges, the maximum displacement ductility demand shall not exceed 5 for the single-column-bent bridges and 4 for the multi-column-bent bridges.

The codes design criteria such as the maximum displacement ductility, minimum transverse reinforcement, and maximum transverse reinforcement spacing are mainly based on the seismic hazard with the short and moderate ground-motion duration. However, the recent experimental and analytical studies [Mohammed 2016; Alian et al. 2019] have revealed that earthquake duration can have a significant impact on bridge columns performance by decreasing the displacement capacity on the order of 25% and increasing the risk of structural collapse.

Under long-duration ground motions, bar fracture failures occur at lower intensity levels and at smaller displacement demands. This observation is discussed further in this chapter. Therefore, overlooking the duration effect in designing bridges in or around subduction zones would result in an insufficient or inappropriate design. This chapter focuses on providing the computational tools that can help mitigate potential adverse duration effects for the design of bridge columns.

8.3 METHODOLOGY

As mentioned above, the current standards and guidelines of structural design and assessment (for bridges as well as other structures) do not typically account for the effect of earthquake duration. Structures are mainly designed based on the equivalent linear methods based on code-defined design spectrum. In those rare cases where nonlinear response history analysis is conducted, there is no requirement in the code to select ground motions of longer durations. The same is true for performance-based earthquake engineering (PBEE) of structures. The FEMA P695 methodology [Kircher et al. 2010] incorporates cumulative damage measures in collapse analysis; however, earthquake duration is not explicitly considered in its algorithm of quantifying damage measures. Therefore, the higher risk of reinforcement fatigue and fracture under long-duration earthquakes is not considered in current design codes or PBEE guidelines.

Incremental dynamic analysis (IDA) is an increasingly popular method among the engineering community that involves nonlinear dynamic analyses to perform a comprehensive assessment of the seismic behavior of structures [Vamvatsikos and Cornell 2002]. The major

limitation of IDA is that the real hazard of a unique site is not reflected in the analysis. The site-specific motions can be more important when long-duration earthquakes are expected to occur. Furthermore, large record-to-record variability is inevitable in IDA and is closely related to the IM used in the analysis. By selecting efficient IMs, the dispersion of the results reduces; therefore, fewer records are required to obtain the same confidence level in the results.

Several research studies have been conducted to address the above-mentioned issues. Vamvatsikos and Cornell [2002] demonstrated that using a single optimal spectral value or vector and scalar combinations of them can significantly reduce the dispersion in results. Also, they concluded that the ordinates of the elastic spectrum and the spectral shape of each individual record can provide promising candidates for highly efficient IMs. Baker [2007] suggested that in order to investigate the effectiveness of a potential vector IM, an effective approach is to scale records to the primary IM parameter and then use regression analysis to measure the effect of the additional IM parameters. An adaptive IDA (AIDA) procedure was proposed by Lin and Baker [2013] to adaptively change the ground-motion suites at different ground-motion intensity levels to match hazard-consistent properties for structural response assessment. This approach specifies a bin size to limit the applicable intensity range of individual ground motion in IDA based on its causal parameters such as magnitudes.

Raghunandan and Liel [2013] recommended considering the duration of the ground motion in addition to its intensity and frequency content in design and seismic risk assessment of structures. Marafi et al. [2016] proposed an IM to account for the combined effects of spectral acceleration, ground-motion duration, and response spectrum shape. Chandramohan [2016] developed a structural reliability framework, computing non-parametric and hazard-consistent collapse fragility curves by expanding the FEMA P695 far-field set by including 44 long-duration records and adjusting raw collapse fragility functions based on two metrics. The first metric, the Sa_{Ratio} [Baker and Cornell 2006; Eads et al. 2015], was intended to control the effect of spectral shape. The second metric used in the study was the 5–75% significant duration, Ds_{5-75} [Bommer and Martinez-Pereira 1999]. The Sa_{Ratio} [expressed in Equation (8.3) below] is a scalable metric that quantifies the average *Sa* value at a range of periods that typically influences the post-yield and higher-mode structural responses.

$$Sa_{\text{Ratio}}(T_a T_1 T_b) = \frac{Sa(T_1)}{\left[\prod_{i=1}^{N} Sa(T_1)\right]^{1/N}} \qquad T_i \in \left[T_a : 0.01T_1 : T_b\right] \tag{8.3}$$

where T_1 is fundamental period of the structure; *Sa* is spectral acceleration; and T_a and T_b are the period range of interest, which are taken as $0.27T_1$ and $3T_1$, respectively, as suggested by Eads et al. [2015].

Zhong [2020] extended the other studies [Baker and Cornell 2006; Kircher et al. 2010; and Chandramohan 2016] to develop the site-specific hazard adjustment framework for IDA (SHAF-IDA), which provides a rigorous method for systematically assessing site-specific structural performance. It consists of a pre-processing algorithm for sampling a record set for the IDA with desired combination of supplementary IMs, i.e., a nested ground-motion set. In addition, with SHAF-IDA's hazard adjustment procedure for post-processing raw IDA results, it is possible to

develop the surrogate models using closed-form solutions of structural performance metrics as a function of ground-motion IMs, and then integrating it with the site-specific hazard information to assess the probabilistic distribution of the structural performance metrics of interest (e.g., peak curvature ductility, reinforcing bar damage state, and structural collapse). This framework was used in this study to select the ground-motion set and develop surrogate models for different bridge performance levels at the specific sites. The surrogate models were then used to develop the site-specific design strategies to consider duration and spectral shape effects. More details are provided in Sections 8.7 and 8.8.

8.4 NESTED GROUND-MOTION SET

Incremental dynamic analysis requires a series of nonlinear dynamic response history analyses for an ensemble of ground motions of increasing intensity to attain an accurate indication of the nonlinear dynamic response of the structure due to strong ground motion. The number of ground motions should be sufficient to cover the full range of responses that could be expected considering the inherent randomness of the earthquake records. The selected ground motions should have relatively large magnitudes so that smaller scale factors are needed. Furthermore, the selected records should be suitable for a range of periods.

The records used in this study were obtained from the PEER strong-motion databases [Kishida et al. 2018]. Two IMs of interest were ground-motion duration measure ($D_{S5–75}$) and spectral shape measure (Sa_{Ratio}). Twenty-five ground-motion pairs were adopted from Zhong [2020] for this part of the study. The hand-picked set covers a wide range of both Sa_{Ratio} (from 0.8 to 2.8) and D_{S5-75} (from 3 to 90 sec). Each pair included two components that were applied to the bridge models bidirectionally in two perpendicular directions. Table 8.1 lists the selected ground-motion pairs and the corresponding Sa_{Ratio} and $D_{S5–75}$. An orthogonal grid of the suite of records in Sa_{Ratio}–D_{S5-75} domain is illustrated in Figure 8.1. This method for selecting ground motions prohibited a strong correlation among the IMs (known as collinearity), which potentially complicates distinguishing their effects on the corresponding coefficients in the response prediction model. The conditional period range for the Sa_{Ratio} was taken as 0.2 to 3.0 sec based on the fundamental periods of the prototype bridges, ranging from 0.6 to 1.5 sec; see Table 8.2. Among the 25 ground-motion pairs, 10 pairs had $D_{S5–75}$ longer than 25 sec, which are categorized as long-duration ground motions. Zhong [2020] also demonstrated that a set of 25 nested records could provide similar structural response estimations as a set of 100 records. Thus, the number of nested records in the generic set is flexible.

Table 8.1 Nested ground-motion set.

#	RSN[1]	Earthquake	Record components		$D_{S5\text{-}75}$ (sec)	Sa_{Ratio}
			Longitudinal[2]	Transverse[3]		
1	171	Imperial Valley	EMO000	H-EMO270	2.2	0.93
2	230	Mammoth Lakes	CVK090	CVK180	6.9	0.99
3	1526	Chi-Chi, Taiwan	TCU098-E	TCU098-N	17.7	0.92
4	6001809	Maule, Chile	CONC-L	CONC-T	33.7	0.73
5	4000789	Tohoku, Japan	FKS005EW	FKS005NS	66.0	1.01
6	2655	Chi-Chi, Taiwan	TCU122E	TCU122N	2.8	1.10
7	159	Imperial Valley	AGR003	AGR273	6.7	1.07
8	1519	Chi-Chi, Taiwan	TCU087-E	TCU087-N	15.5	1.16
9	1343	Chi-Chi, Taiwan	ILA056-N	ILA056-W	39.4	1.07
10	4000369	Tohoku, Japan	FKSH16W2	FKSH16S2	76.9	1.35
11	825	Cape Mendocino	CPM000	CPM090	2.7	1.42
12	1042	Northridge	CWC180	CWC270	6.5	1.49
13	3001964	Michoacan, Mexico	UNION00E	UNION90E	15.7	1.45
14	6001815	Maule, Chile	CURI-NS	CURI-EW	36.4	1.61
15	4001102	Tohoku, Japan	NIG012EW	NIG012NS	83.3	1.56
16	3474	Chi-Chi, Taiwan	TCU079E	TCU079N	2.8	2.02
17	5001478	Gisborne, New Zealand	N46W	S44W	6.9	2.02
18	6001143	Tarapaca, Chile	CEMEN--L	CEMEN--T	16.1	2.05
19	6001799	Maule, Chile	CCSP007	CCSP097	34.0	1.97
20	4000101	Tohoku, Japan	8AD-EW	8AD-NS	75.1	2.08
21	639	Whittier Narrows	OBR270	OBR360	2.8	2.62
22	608	Whittier Narrows	WAT180	WAT270	7.1	2.64
23	1104	Kobe, Japan	FKS000	FKS090	16.0	2.57
24	6005357	Illapel, Chile	C01OHNE	C01OHNN	31.1	2.26
25	4000124	Tohoku, Japan	90F-EW	90F-NS	84.9	3.53

[1] Record Sequence Number in PEER NGA-West2 or NGA-Sub databases.
[2] The motion component applied in the longitudinal direction of the bridge.
[3] The motion component applied in the transverse direction of the bridge.

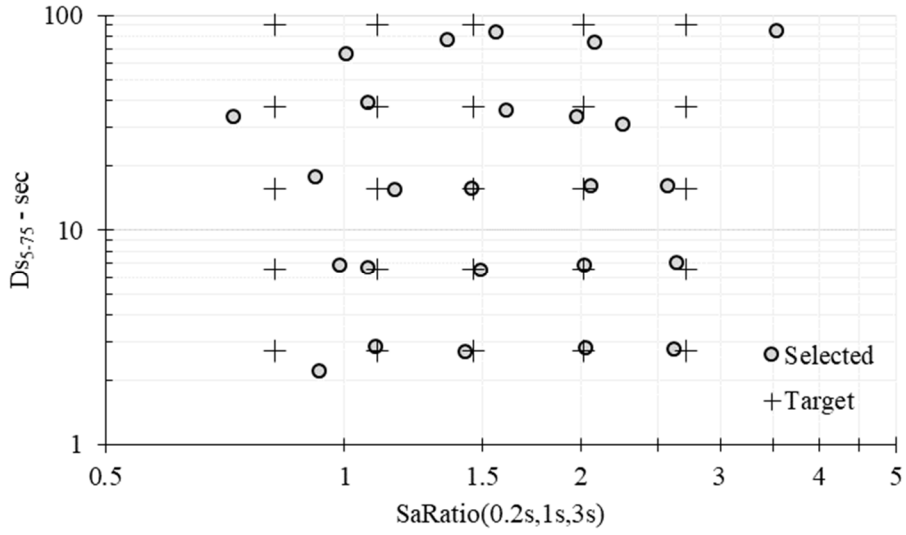

Figure 8.1 Sa_{Ratio}-$Ds_{5–75}$ **domain of the nested ground-motion set.**

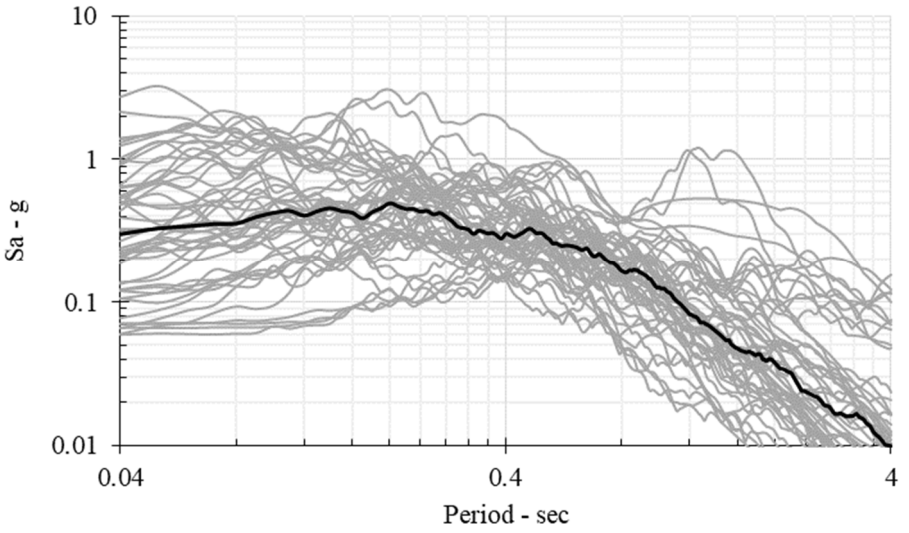

Figure 8.2 **Response spectra of the nested ground-motion set.**

8.5 PROTOTYPE BRIDGES DESCRIPTION

Twenty-four hypothetical prototype bridges with box girder superstructure were designed and modeled in OpenSees platform to perform IDAs. The bridges were meant to resemble typical multi-span bridges in seismic zones such as California. The general configuration of the bridges is shown in Figure 8.3. The prototype bridges comprised three equal spans of 100 ft, and two bents

with two columns in each bent with integral bent cap beams. The width of the prototype superstructure section was 45 ft, allowing for three 12-ft wide lanes and two shoulders. The clear height of the columns was 24 ft, and the spacing between the two columns within the bent was 25 ft.

The superstructure type and the main dimensions resemble typical bridges located in seismic regions. Accordingly, data for the hypothetical prototype bridge were selected based on average values from the California Highway Bridges Inventory[1]. The prototype geometry, including the barrier rails and wearing surface, resulted in approximately 1400 kips of dead load over each bent. The different bridge columns designs were selected based on two different design strategies: (1) decrease the deformation demand by increasing reinforcement ratio, thereby reducing the design ductility demand (μ_D), which is equivalent to increasing the design strength; and (2) increase the cyclic deformation capacity by reducing the tie spacing thereby increasing the post-buckle bar fracture resistance.

The combination of two different longitudinal reinforcement ratios of approximately 1% and 2%, five column section diameters of 36 in., 42 in., 48 in., 54 in., and 60 in., and three different tie spacing of $2d_b$, $4d_b$, and $6d_b$, which produced 24 archetype bridges or different design cases. The reinforcing bar sizes were maintained the same for all 24 designs to minimize the differences from potential bond-slip effects. The concrete cover depth for all specimens was 2 in. The axial load index (ALI) for the columns, defined as the dead load divided by the product of the nominal concrete compressive strength (4 ksi) and the gross cross-sectional area of each column $\text{ALI} = (\text{ALI} = P_{\text{dead}} / f_c' A_g)$, was maintained between 0.07 and 0.18, which is within the typical range for actual bridges. The design properties of the different prototype bridges are summarized in Table 8.2.

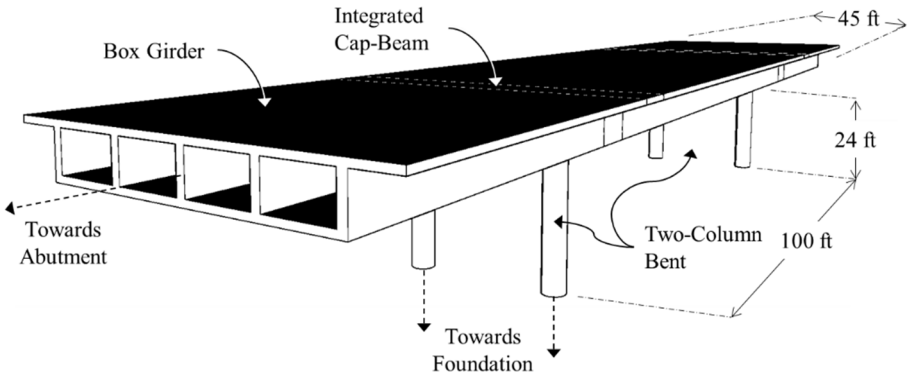

Figure 8.3 Configuration of the prototype bridges.

[1] https://gisdata-caltrans.opendata.arcgis.com/

Table 8.2 Design properties of the prototype bridges.

Bridge ID	D_c (in.)	ρ_l	s/d_b	T (sec)	Δ_y (in.)	μ_D^*	ϕ_Y (in.$^{-1}$)
D60-6db-R1.99	60	1.99	6	0.58	2.56	1.87	0.000097
D60-4db-R1.99	60	1.99	4	0.58	2.61	1.85	0.000099
D60-2db-R1.99	60	1.99	2	0.59	2.72	1.78	0.000103
D60-6db-R1.10	60	0.99	6	0.64	2.00	2.78	0.000086
D60-4db-R1.10	60	0.99	4	0.64	2.03	2.75	0.000088
D60-2db-R1.10	60	0.99	2	0.65	2.11	2.66	0.000091
D54-6db-R1.91	54	1.91	6	0.70	2.57	2.42	0.000106
D54-4db-R1.91	54	1.91	4	0.70	2.62	2.38	0.000110
D54-2db-R1.91	54	1.91	2	0.70	2.74	2.29	0.000115
D48-6db-R2.07	48	2.07	6	0.84	2.75	2.95	0.000122
D48-4db-R2.07	48	2.07	4	0.84	2.81	2.89	0.000125
D48-2db-R2.07	48	2.07	2	0.84	2.93	2.78	0.000133
D48-6db-R1.04	48	1.04	6	0.95	2.12	4.50	0.000105
D48-4db-R1.04	48	1.04	4	0.95	2.16	4.42	0.000109
D48-2db-R1.04	48	1.04	2	0.94	2.21	4.29	0.000114
D42-6db-R2.25	42	2.25	6	1.05	2.98	3.71	0.000140
D42-4db-R2.25	42	2.25	4	1.05	3.03	3.64	0.000144
D42-2db-R2.25	42	2.25	2	1.05	3.17	3.47	0.000154
D36-6db-R2.45	36	2.45	6	1.40	3.27	5.05	0.000165
D36-4db-R2.45	36	2.45	4	1.39	3.31	4.94	0.000174
D36-2db-R2.45	36	2.45	2	1.38	3.42	4.73	0.000185
D36-6db-R1.84	36	1.84	6	1.49	2.92	6.10	0.000155
D36-4db-R1.84	36	1.84	4	1.47	2.94	5.95	0.000163
D36-2db-R1.84	36	1.84	2	1.45	3.00	5.76	0.000176

* Calculated for San Francisco

8.6 NUMERICAL MODEL

The prototype bridge was modeled in OpenSees. The box girders were modeled by the elastic beam–column elements with distributed translational and rotational masses for simplicity. Note: this assumption is considered valid as previous studies have demonstrated that superstructure elements can be still modeled using linear elastic elements even if the reinforcement inside the box-girders or bent caps yield [Moustafa and Mosalam 2015]. Elastomeric pads at the supports were modeled using the *Elastomeric Bearing* element [Roeder et al. 1987]. The response of the shear keys was simulated using the *Hysteretic* material [Megally et al. 2001]. Backfill soil behind the abutment wall was modeled using the *HyperbolicGap* material according to Aviram et al. [2008]. Columns were modeled using the *nonlinearBeamColumn* elements with distributed plasticity. Columns were connected to the above girder using *rigidLink* elements. The *Zero-Length Section* elements were used at both ends of the columns to consider bond-slip rotations. *Bond SP01* material was used to account for the bond-slip effects [Zhao and Sritharan 2007]. The soil–foundation springs were used beneath the columns to simulate laterally loaded pile foundation according to the approach developed by McGann et al. [2011]. The various modeling assumptions stated above for the different bridge components have also been verified and implemented recently

to model California-specific multi-frame bridges [Abbasi and Moustafa 2019; Shoushtari 2019(a); and Shoushtari et al. 2019c], which provided confidence in extending these assumption in this study.

Concrete response was modeled using the *Concrete02* material. The *ReinforcingSteel* material was used to simulate reinforcement responses. To simulate the constitutive and failure laws of steel reinforcement, the *ReinforcingSteel* material was wrapped to the *DuctileFracture* material developed by Zhong [2020]. Modeling parameters for the *DuctileFracture* material consist of three groups: void-growth and cyclic deterioration coefficients (c_{mono} and c_{cycl}), necking amplification model coefficients (k_1 and k_2), and buckling adjustment model parameters (b_1 and b_2). These parameters were determined based on the following equations proposed by Zhong [2020]:

$$\ln\left(c_{\text{mono}}\right) = -3.96 - 1.85\ln(\varepsilon_{su}) + 0.2\ln(d_b) \tag{8.4}$$

$$\ln\left(c_{\text{cycl}}\right) = 5.9 + 1.53\ln(f_y/60\text{ ksi}) + 2.32\ln(\varepsilon_{su}) + 1.11\ln(d_b) \tag{8.5}$$

$$\ln\left(k_1\right) = 2.21 - 0.32\ln(T/Y) - 0.66\ln(d_b) \tag{8.6}$$

$$\ln\left(k_2\right) = 1.29 - 0.64\ln(f_y/60\text{ ksi}) - 0.46\ln(d_b) \tag{8.7}$$

$$\ln\left(b_1\right) = -2.53 - 1.9\ln(T/Y) - 1.36\ln(d_b) \tag{8.8}$$

$$\ln\left(b_2\right) = -3.29 - 0.49\ln(\varepsilon_{su}) - 0.7\ln(\psi s/d_b) \tag{8.9}$$

where ε_{su} is ultimate strain of the steel; d_b is diameter of the longitudinal bar; f_y is yield stress of the steel; T/Y is steel tensile strength to yield strength ratio; s is transverse steel spacing; and ψ is equivalent slenderness factors of the longitudinal bar that can be obtain by Equation (8.10):

$$\ln\left(\psi\right) = 0.65 - 0.09\ln(k_c/k_b) - 1.67\ln(c/d_b) \tag{8.10}$$

$$k_b = \frac{\pi E_{\text{eff}} I}{s^3}, k_c = \frac{n_t E_t A_t}{n_{sl} l_e} = \frac{4\alpha E_t A_t}{3(D - 2c - d_{bt})} \text{ for circular hoops or spirals} \tag{8.11}$$

where k_b is bending stiffness of the longitudinal bar; k_c is constraining stiffness of the transverse reinforcement; c is concrete cover; E_{eff} is effective hardening modulus; I is moment of inertia of the section; n_t is number of lateral tie/hoop legs; E_t is elastic modulus of the transverse reinforcement; A_t is average area of a single transverse tie; n_{sl} is number of longitudinal bars subjected to constraints; l_e is length of one lateral tie/loop leg; α is radius angle between two neighboring longitudinal bars; D is section diameter; and d_{bt} is transverse reinforcement diameter.

A concentrated soil–foundation spring with condensed response based on simulated laterally loaded pile foundation was used beneath the column element following the approach developed by McGann et al. [2011]. Pushover analysis and section analysis were conducted to determine the yield displacements and fundamental periods of the bridges as well as yield curvature of the sections; see Table 8.2.

8.7 IDA RESULTS AND SURROGATE MODELS DEVELOPMENT

A comprehensive SHAF-IDA was conducted on the 24 bridge prototypes. Column curvatures were recorded during the analyses as they are typically used in defining component damage threshold (CDT) of the bridge columns [Ramanathan 2012; Mangalathu 2017]. Per Mangalathu [2017], four CDT damage states were defined in this study: (1) CDT-0 corresponding to the first yield of reinforcement; (2) CDT-1 corresponding to the minor cracking in concrete cover; (3) CDT-2 corresponding to the large shear cracking, major spalling, or confinement yield; and (4) CDT-3 corresponding to longitudinal bar buckling or rupture, concrete core compressive failure, or confinement rupture.

The median value of the curvature ductility (μ_ϕ) limit for each CDT were 1.0, 5.0, 11.0, and 17.5 for CDT0 to CDT3, respectively. Table 8.3 lists the corresponding curvature limits for each of the above-mentioned CDTs. For each CDT, the *Sa* values under which the bridge column curvature exceeds the corresponding limit were determined. A curvature limit of 0.005 1/in. was defined as the collapse intensity (Sa_{col}) for each ground motion. The selection of this curvature limit was based on engineering judgment and experience as noticeable strength and stiffness degradation is usually experienced by bridge columns at this curvature value. The onset of the first bar fracture was also tracked in the analyses through the fracture index (FI) simulations to determine the corresponding Sa_{FF}.

Figure 8.4 shows the fragility curves of all CDTs as well as these two damage states against the CDT-3 for three bridges with a 60-in.-diameter column and 1.99% steel ratio but different tie spacing (D60-R1.99). As seen for these bridges, the first bar fracture fragility curves are very close to their CDT-3 damage state. This matches with the defined CDT-3 damage state. It is clear from the fragility curves that reducing the tie spacing results in the ascending trend of the median *Sa* for the first bar fracture and collapse damage states. The bridge typically would not fail directly after the first bar fracture, and the median Sa_{col} is found about 30% higher than the median Sa_{FF}. The first bar fracture was the critical damage state most sensitive to the earthquake duration and is capable of causing severe global collapse.

Figure 8.5 through Figure 8.8 demonstrate the main observations from the IDA results of the bridge archetypes. The two factors that clearly affected Sa_{FF} and Sa_{col} were Sa_{Ratio} and $Ds_{5–75}$. The figures also feature two threshold values (dashed lines) for these two factors to help identify the overall ascending or descending trend. For Sa_{Ratio} greater than 1.8, the sensitivity of the median *Sa* to the spectral shape is decreased. In the same manner, the effect of $Ds_{5–75}$ is more significant when it is greater than 10 sec. Based on these two observations, San Francisco (a 975-year expected conditional $Ds_{5\text{-}75}$ of 10 sec and an Sa_{Ratio} of 1.65) was selected as the reference site. This selection is discussed further in the next section.

The first bar fracture *Sa* value was mainly affected by the displacement ductility demand factor (μ_D) and the confinement spacing ratio (s/d_b). The same was observed for CDT-2, CDT-3, and collapse. To quantitatively describe these trends, the least squares regression was conducted to develop surrogate models for the median *Sa* of different bridge damage states. Equations (8.11) through (8.14) summarize the surrogate models developed for the San Francisco reference site to quantify the bridge median fragility:

$$\ln(Sa_{CDT2}) = 0.70 + 0.17\ln(SA_{\text{Ratio}}) - 0.036\ln(Ds_{5-75}) - 0.23\ln(\mu_D) - 0.02\ln(s/d_b) \quad (8.11)$$

$$\ln(Sa_{CDT3}) = 1.20 + 0.20\ln(SA_{\text{Ratio}}) - 0.105\ln(Ds_{5-75}) - 0.22\ln(\mu_D) - 0.10\ln(s/d_b) \quad (8.12)$$

$$\ln(Sa_{FF}) = 1.50 + 0.17\ln(SA_{\text{Ratio}}) - 0.193\ln(Ds_{5-75}) - 0.17\ln(\mu_D) - 0.15\ln(s/d_b) \quad (8.13)$$

$$\ln(Sa_{col}) = 1.53 + 0.33\ln(SA_{\text{Ratio}}) - 0.142\ln(Ds_{5-75}) - 0.20\ln(\mu_D) - 0.14\ln(s/d_b) \quad (8.14)$$

Table 8.3 Corresponding curvature limits for each CDT.

Bridge ID	φ_{CDT0} (in.$^{-1}$)	φ_{CDT1} (in.$^{-1}$)	φ_{CDT2} (in.$^{-1}$)	φ_{CDT3} (in.$^{-1}$)
D60-6db-R1.99	0.000097	0.000483	0.001064	0.001692
D60-4db-R1.99	0.000099	0.000495	0.001089	0.001733
D60-2db-R1.99	0.000103	0.000515	0.001132	0.001801
D60-6db-R1.10	0.000086	0.000432	0.000951	0.001513
D60-4db-R1.10	0.000088	0.000440	0.000968	0.001540
D60-2db-R1.10	0.000091	0.000453	0.000996	0.001585
D54-6db-R1.91	0.000106	0.000528	0.001161	0.001847
D54-4db-R1.91	0.000110	0.000549	0.001207	0.001921
D54-2db-R1.91	0.000115	0.000573	0.001260	0.002005
D48-6db-R2.07	0.000122	0.000609	0.001339	0.002131
D48-4db-R2.07	0.000125	0.000627	0.001379	0.002194
D48-2db-R2.07	0.000133	0.000663	0.001458	0.002320
D48-6db-R1.04	0.000105	0.000525	0.001154	0.001836
D48-4db-R1.04	0.000109	0.000547	0.001203	0.001913
D48-2db-R1.04	0.000114	0.000569	0.001251	0.001990
D42-6db-R2.25	0.000140	0.000700	0.001539	0.002449
D42-4db-R2.25	0.000144	0.000722	0.001589	0.002528
D42-2db-R2.25	0.000154	0.000772	0.001698	0.002702
D36-6db-R2.45	0.000165	0.000827	0.001820	0.002895
D36-4db-R2.45	0.000174	0.000868	0.001909	0.003037
D36-2db-R2.45	0.000185	0.000927	0.002039	0.003244
D36-6db-R1.84	0.000155	0.000774	0.001703	0.002709
D36-4db-R1.84	0.000163	0.000817	0.001798	0.002860
D36-2db-R1.84	0.000176	0.000882	0.001941	0.003088

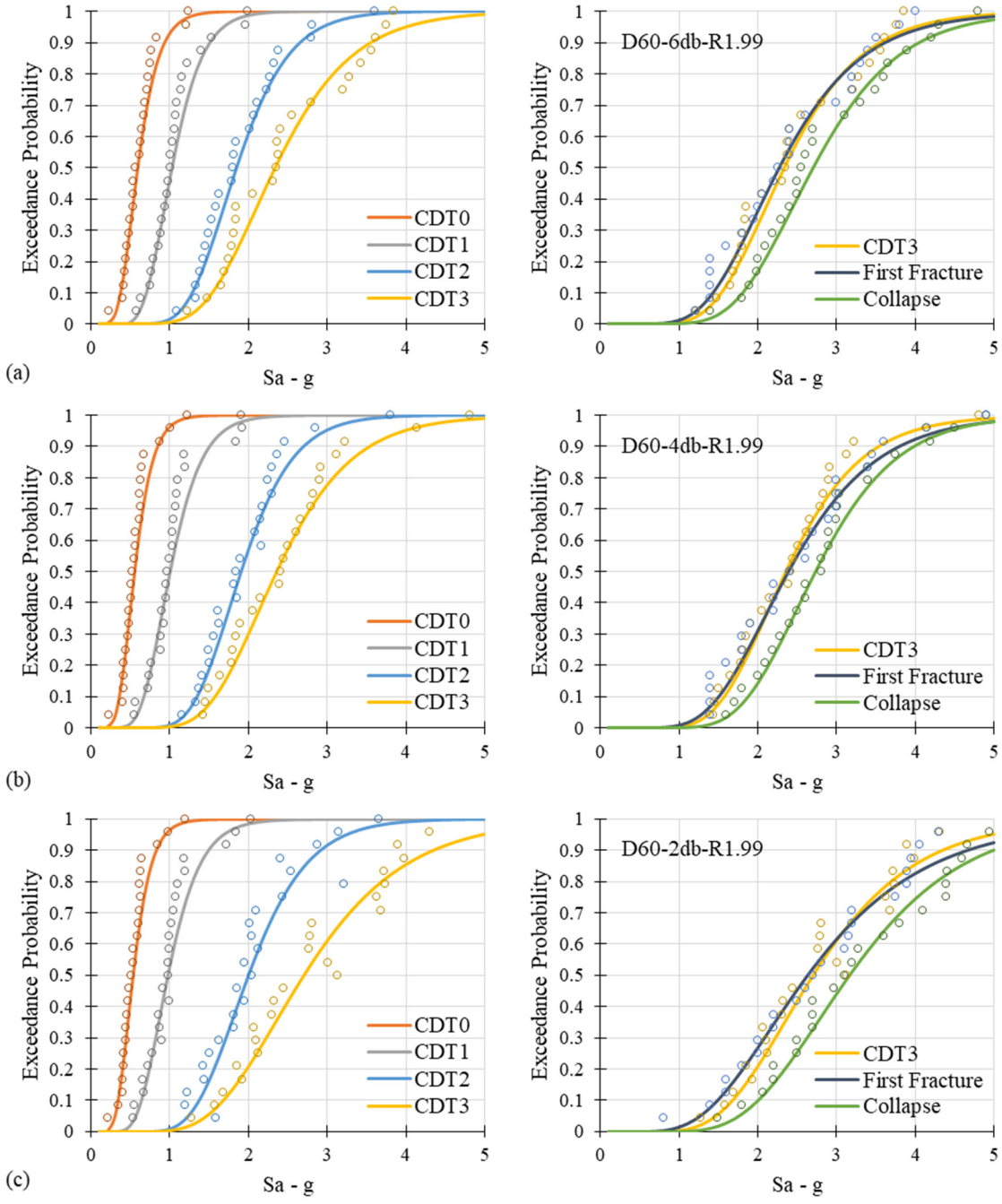

Figure 8.4 **Analytical fragility curves: (a) bridge D60-S6-R1.99; (b) bridge D60-S4-R1.99; and (c) bridge D60-S2-R1.99.**

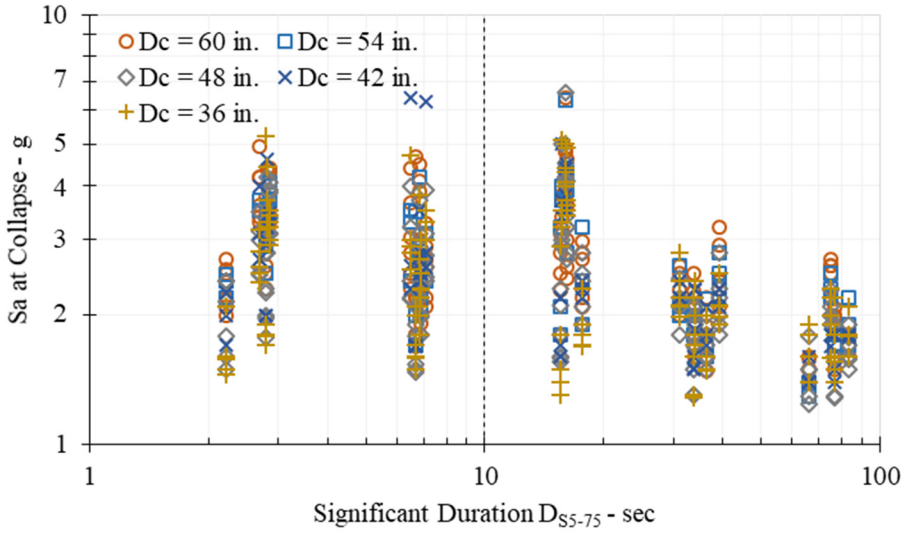

Figure 8.5 Significant duration effect on the collapse *Sa* of all bridges.

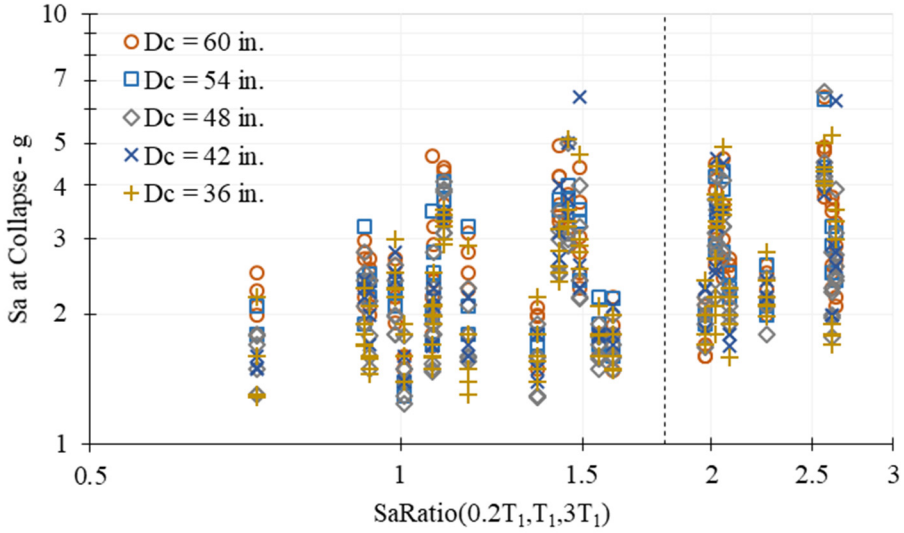

Figure 8.6 Sa_{Ratio} effect on the collapse *Sa* of all bridges.

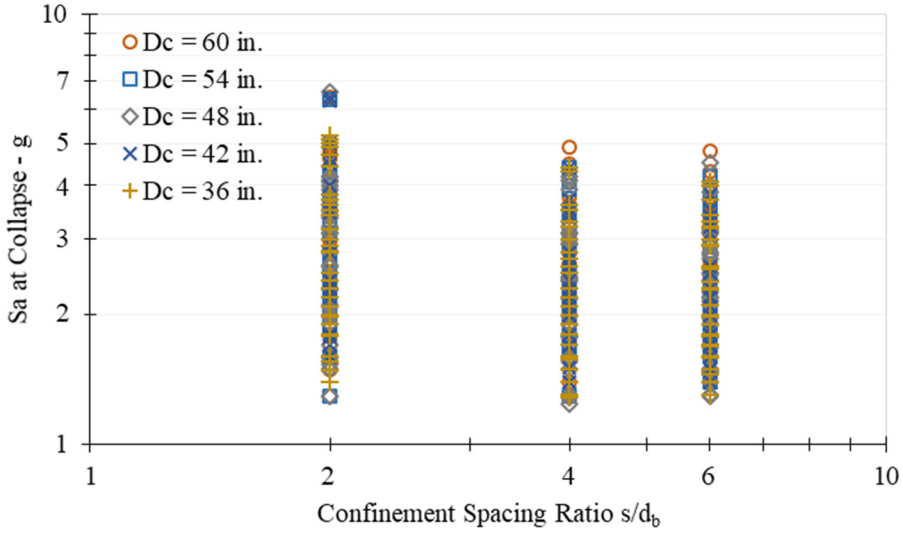

Figure 8.7 Confinement spacing ratio effect on the collapse *Sa* of all bridges.

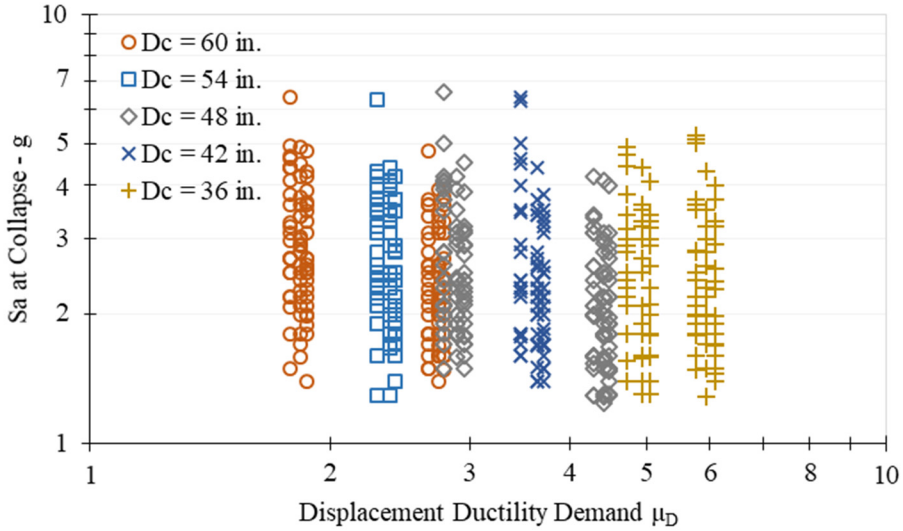

Figure 8.8 Displacement ductility demand effect on the collapse *Sa* of all bridges.

8.8 SITE SPECIFIC DESIGN STRATEGIES

Since the median $Ds_{5–75}$ and Sa_{Ratio} target for San Francisco (975-year Sa = 1.05g, expected conditional Sa_{Ratio} = 1.64 and $Ds_{5–75}$ = 10 sec) is close to the duration and Sa_{Ratio} threshold in Figure 8.5 and Figure 8.6, it was selected as the reference site. Zhong [2020] investigated 109 sites in the U.S. Pacific Northwest region and Alaska, which are shown in Figure 8.9. Red triangles show that 18 sites have higher 975-year Sa intensities compared to San Francisco. Zhong [2020] developed the generalized conditional IM (GCIM) targets, i.e., Sa, Sa_{Ratio}, and Ds_{5-75} conditioning on the Sa for the sites with 975-year Sa intensities greater than 0.3g, for six return periods, i.e. 224, 475, 975, 2475, 4975, and 9950 years. Figure 8.10 shows the computed median values of the GCIM targets for the 975-year return period.

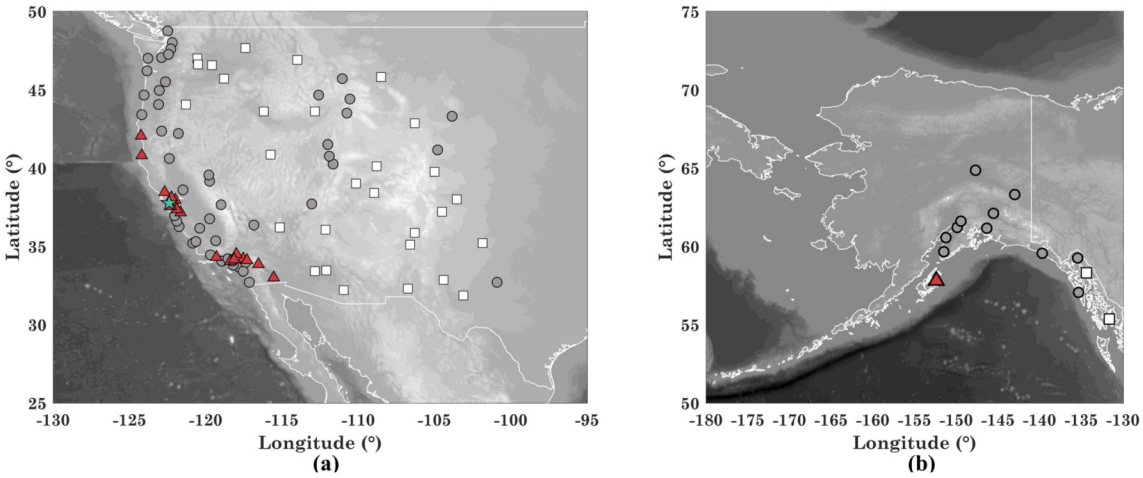

Figure 8.9 **Studied sites: (a) western U.S. sites and (b) representative Alaskan sites. The star mark corresponds to San Francisco *Sa* = 1.05*g*, the triangular sites have *Sa* > 1.05*g*, the round sites have 0.3*g* ≤ *Sa* < 1.05*g*, and the square sites have *Sa* < 0.3*g*. (this figure is courtesy of Zhong [2020]).**

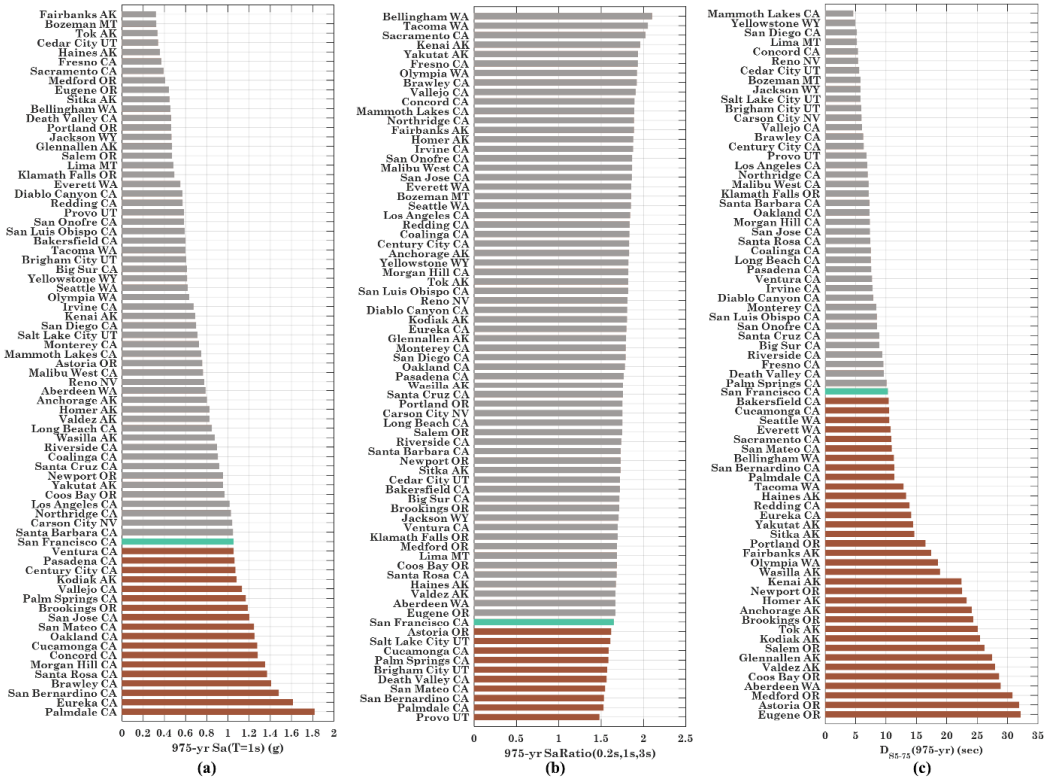

Figure 8.10 **Seismic hazard and GCIM of sites with *Sa* > 0.3*g*: (a) 975-year *Sa*(*g*); (b) 975-year Sa_{Ratio}; and (c) 975-year $Ds_{5\text{-}75}$ (sec) (figure courtesy of Zhong [2020]).**

As discussed earlier, decreasing the design displacement ductility demand factor (μ_D) and/or the confinement spacing ratio (s/d_b) would be considered as reasonable mitigation design strategies. The current standards or design philosophy does not consider the effect of earthquake duration and are mainly based on the universal seismic hazard. They limit these design variables to $\mu_D = 5$ and $s/d_b = 6$ for a bridge system with multi-column bents. These limiting values were used as the reference design. San Francisco, which is used as the reference site hazard, is assumed to be representative of the universal seismic hazard.

Zhong [2020] developed the following procedure to improve the design domain of μ_D and s/d_b for each site, which was adopted and expanded in this study:

1. Obtain the seismic hazard deaggregation results for the given site and compute the median GCIM target values developed for 975-year return period (Sa_{Ratio} and Ds_{5-75}).
2. Develop the surrogate model for the interested damage state and given site:

$$\ln(Sa) = c_0 + c_1 \ln(Sa_{\text{Ratio}}) + c_2 \ln\left(Ds_{5-75}\right) + c_3 \ln\left(\mu_D\right) + c_4 \ln\left(s/d_b\right) \tag{8.15}$$

3. Substitute the current minimum design properties [see the starred parameters in Equation (8.16)] under the reference site hazard into the surrogate model and obtain the reference performance plane. Designs on or above this plane correspond to equal or higher median capacity compared to the reference performance and are considered desirable:

$$\ln(Sa^*) = c_0 + c_1 \ln(Sa^*_{\text{Ratio}}) + c_2 \ln\left(Ds^*_{5-75}\right) + c_3 \ln\left(\mu^*_D\right) + c_4 \ln\left(s/d^*_b\right) \tag{8.16}$$

4. Find the intersection curve between the surrogate model surface and the reference performance plane, which can be projected on the design domain of μ_D and s/d_b:

$$\ln(Sa) \geq \ln(Sa^*) \tag{8.17}$$

$$c_1 \ln\left(\frac{Sa_{\text{Ratio}}}{Sa^*_{\text{Ratio}}}\right) + c_2 \ln\left(\frac{Ds_{5-75}}{Ds^*_{5-75}}\right) \geq c_3 \ln\left(\frac{\mu^*_D}{\mu_D}\right) + c_4 \ln\left(\frac{s/d^*_b}{s/d_b}\right) \tag{8.18}$$

$$c_1 \ln\left(\frac{Sa_{\text{Ratio}}}{1.65}\right) + c_2 \ln\left(\frac{Ds_{5-75}}{10.25\,\text{sec}}\right) \geq c_3 \ln\left(\frac{5}{\mu_D}\right) + c_4 \ln\left(\frac{6\,\text{in.}}{s/d_b}\right) \tag{8.19}$$

5. Find the domain from the current design domain but enveloped by the projected limit curve. This domain would be the new design criteria that accounts for duration and spectral shape effects:

$$\ln(\mu_D) \leq -\ln\left(Sa^{c_1/c_3}_{\text{Ratio}}\right) - \ln\left(Ds^{c_2/c_3}_{5-75}\right) - \ln\left(s/d_b{}^{c_4/c_3}\right) + C \tag{8.20}$$

$$\mu_D \leq \frac{e^C}{\left(Sa_{\text{Ratio}}\right)^{c_1/c_3} \cdot \left(Ds_{5-75}\right)^{c_2/c_3} \cdot \left(s/d_b\right)^{c_4/c_3}} \tag{8.21}$$

$$C = \frac{0.5c_1 + 2.33c_2 + 1.8c_4}{c_3} + 1.61 \tag{8.22}$$

An individual design domain can be obtained for all damage states of interest following the above procedure. The new design criteria are specified by the joint combination of the ductility demand and confinement space ratio. For an arbitrary site, engineers may use these new design domains to check the design using the current design procedure. For instance, Equations (8.23) and (8.24) are the design domains developed for Portland (Sa = 0.46, Sa_{Ratio} = 1.69, Ds_{5-75} = 16 sec) for single-column [Zhong 2020] and multi-column bents:

$$\left(\mu_D\right)_{FF} = \frac{104\left(Sa_{\text{Ratio}}\right)^{0.78}}{\left(Ds_{5-75}\right)^{0.97} \cdot \left(s/d_b\right)^{0.65}} = \frac{10.6}{\left(s/d_b\right)^{0.65}} \quad \text{for multi-column bent} \tag{8.23}$$

$$\left(\mu_D\right)_{FF} = \frac{15\left(Sa_{\text{Ratio}}\right)^{1.11}}{\left(Ds_{5-75}\right)^{0.52} \cdot \left(s/d_b\right)^{0.37}} = \frac{3.8}{\left(s/d_b\right)^{0.37}} \quad \text{for single-column bent} \tag{8.24}$$

The procedure presented above is used to determine the design domains (μ_D and s/d_b) to achieve the target performances of different damage states. Developing the surrogate models and then designing domains for a specific site following the proposed procedure requires the engineer to repeat the regression analysis for the intended site using the existing IDA data for single- or multi-column bridges. To simplify the use of these new design domains, the boundary values of the allowable ductility demand and confinement spacing ratio, i.e., $\mu_D(s/d_b = 6)$ and $s/d_b(\mu_D = 5)$, were computed for multi-column bent bridges for the studied sites with $Sa > 0.3g$; see Table 8.4. Similar design limits for single-column bent bridges were provided by Zhong [2020]. These new maximum allowable limits can be used to check the design.

Figure 8.11 shows the design domains and the corresponding boundary limits (circular points in figures) for four sites: Los Angeles, Eugene, Portland, and Anchorage with different Sa_{Ratio} and Ds_{5-75} targets. According to Table 8.4 most of the sites in Oregon and Alaska—and some sites in Washington—need more restrictive design criteria for multi-column bent bridges. The limited μ_D values for these sites range from 1.6 to 4.8, and the limited s/d_b range from 1.0 to 5.6. Table 8.4 may be utilized by engineers to check the design of any multi-span multi-column straight bridges in the U.S. Pacific Northwest region and Alaska. Other bridges with different alignments (e.g., skewed bridges or curved bridges) require developing new analytical models and conducting a new IDA.

Figure 8.12 compares the design domain for the single- and multi-column bent bridges at the same sites. The design domain for multi-column bent bridges—especially in the case of the maximum allowable μ_D—is seen to be more sensitive to the duration effect compared to that for single-column bent bridges. Based on these results, it is suggested that more restrictive design criteria for multi-column bent bridges be considered at sites with significant long-duration shaking (longer that 30 sec); see Table 8.4 for sites in Oregon.

Table 8.4 Multi-column bent bridge design criteria for the sites with *Sa* > 0.3*g*.

Site	975yr Sa_{Ratio}	975yr $Ds_{5\text{-}75}$ (sec)	$\mu_D(s/d_b = 6)$	$s/d_b(\mu_D = 5)$
Grand Canyon Village AZ	1.82	6.72	5.00	6.00
Palo Verde AZ	1.87	15.12	**3.97**	**3.90**
Phoenix AZ	1.85	9.76	5.00	6.00
Tucson AZ	2.15	7.73	5.00	6.00
Bakersfield CA	1.72	10.39	5.00	6.00
Big Sur CA	1.71	8.85	5.00	6.00
Brawley CA	1.92	6.19	5.00	6.00
Century City CA	1.83	6.28	5.00	6.00
Coalinga CA	1.83	7.43	5.00	6.00
Concord CA	1.89	5.33	5.00	6.00
Cucamonga CA	1.58	10.47	**4.74**	**5.50**
Death Valley CA	1.56	9.59	5.00	6.00
Diablo Canyon CA	1.80	7.81	5.00	6.00
Eureka CA	1.79	14.10	**3.89**	**4.10**
Fresno CA	1.93	9.53	5.00	6.00
Irvine CA	1.87	7.76	5.00	6.00
Long Beach CA	1.75	7.43	5.00	6.00
Los Angeles CA	1.84	6.85	5.00	6.00
Malibu West CA	1.86	7.08	5.00	6.00
Mammoth Lakes CA	1.89	4.58	5.00	6.00
Monterey CA	1.78	8.35	5.00	6.00
Morgan Hill CA	1.82	7.28	5.00	6.00
Northridge CA	1.88	6.94	5.00	6.00
Oakland CA	1.78	7.22	5.00	6.00
Palmdale CA	1.53	11.34	**4.09**	**4.75**
Palm Springs CA	1.58	10.03	5.00	6.00
Pasadena CA	1.76	7.54	5.00	6.00
Redding CA	1.83	13.83	**4.18**	**4.45**
Riverside CA	1.73	9.33	5.00	6.00
Sacramento CA	2.02	10.80	5.00	6.00
Santa Barbara CA	1.72	7.20	5.00	6.00
Santa Cruz CA	1.75	8.81	5.00	6.00
Santa Rosa CA	1.68	7.34	5.00	6.00
San Bernardino CA	1.53	11.33	**4.19**	**4.75**
San Diego CA	1.78	5.15	5.00	6.00
San Francisco CA	1.64	10.26	5.00	6.00
San Jose CA	1.86	7.30	5.00	6.00
San Luis Obispo CA	1.81	8.42	5.00	6.00
San Mateo CA	1.54	10.90	**4.41**	**5.10**
San Onofre CA	1.86	8.46	5.00	6.00

Site	975yr Sa_{Ratio}	975yr $Ds_{5\text{-}75}$ (sec)	$\mu_D(s/d_b = 6)$	$s/d_b(\mu_D = 5)$
Vallejo CA	1.90	6.00	5.00	6.00
Ventura CA	1.69	7.65	5.00	6.00
Bozeman MT	1.85	5.75	5.00	6.00
Lima MT	1.68	5.16	5.00	6.00
Carson City NV	1.75	5.92	5.00	6.00
Reno NV	1.81	5.34	5.00	6.00
Astoria OR	1.61	31.84	**1.64**	**1.05**
Brookings OR	1.71	24.32	**2.13**	**1.70**
Coos Bay OR	1.68	28.56	**1.78**	**1.30**
Eugene OR	1.66	32.08	**1.57**	**1.10**
Klamath Falls OR	1.69	7.09	5.00	6.00
Medford OR	1.68	30.77	**1.61**	**1.15**
Newport OR	1.72	22.50	**2.32**	**1.95**
Portland OR	1.75	16.45	**3.31**	**3.15**
Salem OR	1.74	26.14	**2.11**	**1.55**
Edgemont SD	2.40	5.26	5.00	6.00
Snyder TX	2.39	5.13	5.00	6.00
Brigham City UT	1.57	5.88	5.00	6.00
Cedar City UT	1.72	5.55	5.00	6.00
Provo UT	1.48	6.76	5.00	6.00
Salt Lake City UT	1.61	5.78	5.00	6.00
Aberdeen WA	1.67	28.83	**1.94**	**1.25**
Bellingham WA	2.10	11.25	5.00	6.00
Everett WA	1.85	10.72	5.00	6.00
Olympia WA	1.92	18.51	**3.48**	**2.95**
Seattle WA	1.85	10.49	5.00	6.00
Tacoma WA	2.05	12.85	**4.81**	**5.55**
Cheyenne WY	2.39	5.30	5.00	6.00
Jackson WY	1.70	5.77	5.00	6.00
Yellowstone WY	1.82	4.88	5.00	6.00
Anchorage AK	1.83	24.08	**2.81**	**1.90**
Fairbanks AK	1.88	17.36	**3.46**	**3.20**
Glennallen AK	1.79	27.45	**2.38**	**1.50**
Haines AK	1.67	13.25	**4.09**	**4.10**
Homer AK	1.87	23.23	**2.88**	**2.05**
Kenai AK	1.95	22.38	**3.10**	**2.30**
Kodiak AK	1.80	25.44	**2.54**	**1.70**
Sitka AK	1.72	14.61	**3.48**	**3.85**
Tok AK	1.81	25.04	**2.08**	**1.75**
Valdez AK	1.67	27.88	**2.38**	**1.35**
Wasilla AK	1.76	18.84	**3.24**	**2.60**
Yakutat AK	1.93	14.42	**4.18**	**4.35**

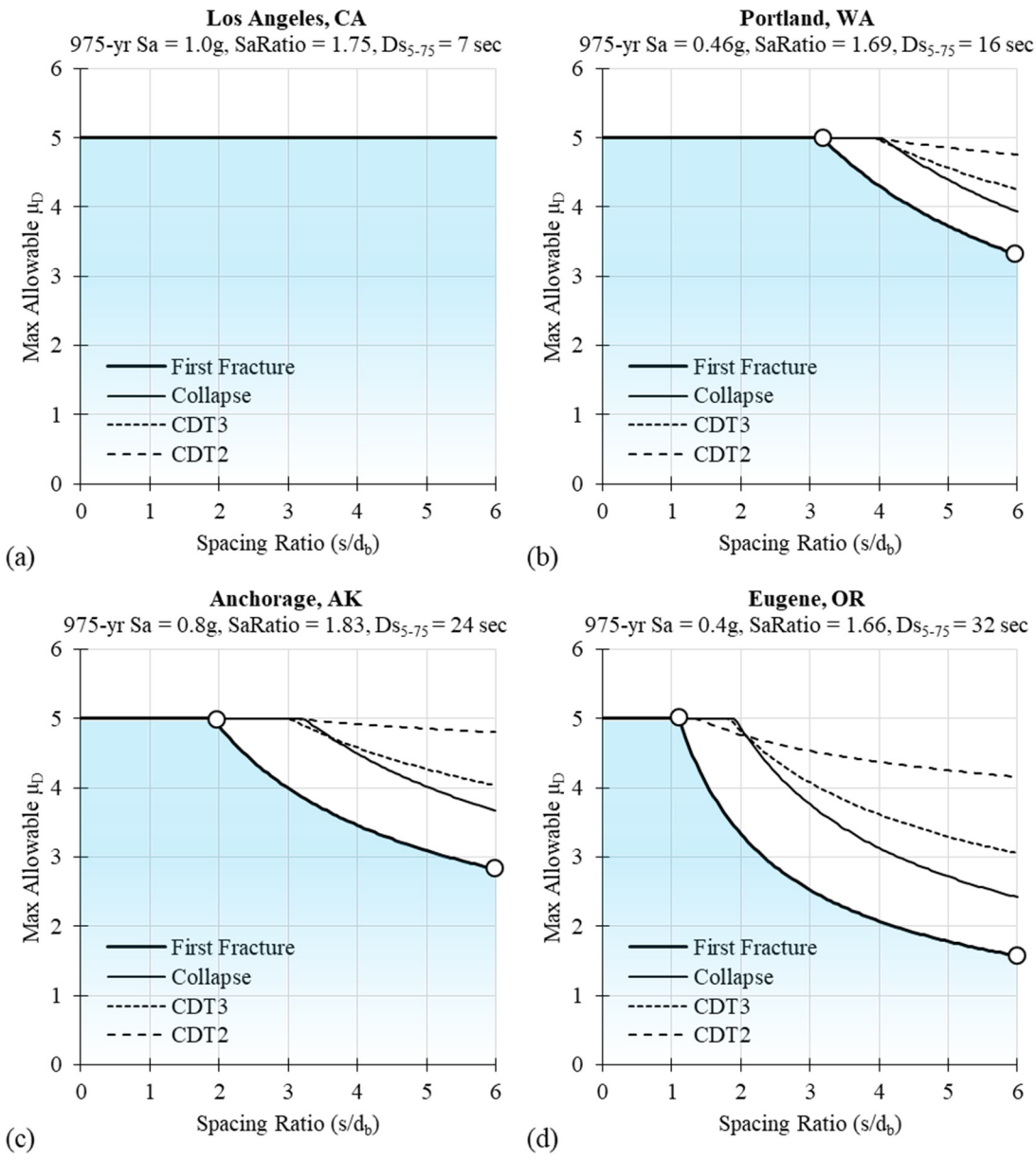

Figure 8.11 **Site-specific design domain considering multiple damage states: (a) Los Angeles; (b) Portland; (c) Anchorage; and (d) Eugene.**

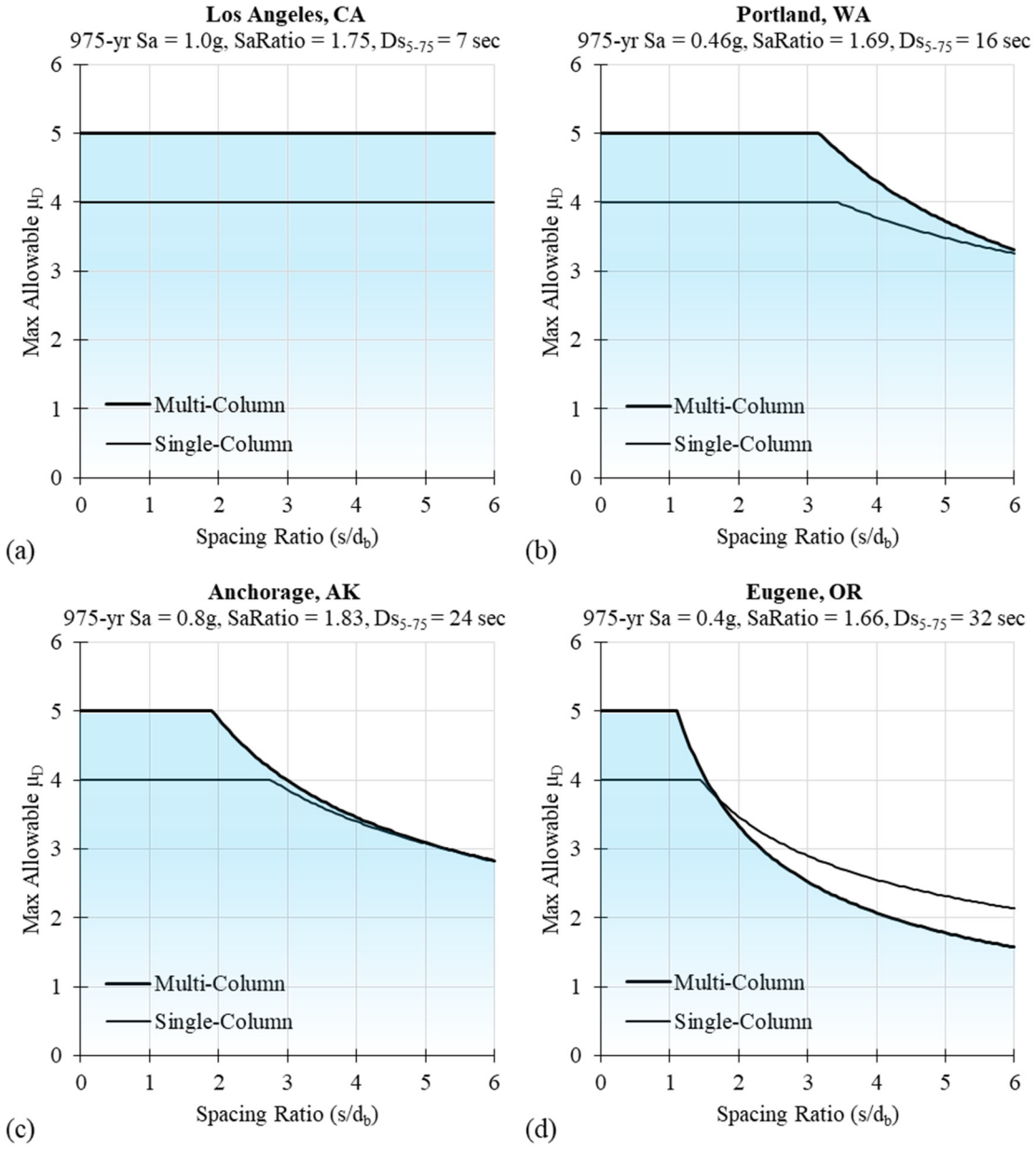

Figure 8.12 **Site-specific design domain considering the first fracture damage state for single-column bent and multi-column bent bridges: (a) Los Angeles; (b) Portland; (c) Anchorage; and (d) Eugene.**

9 Summary and Conclusions

9.1 SUMMARY

Bridge damage caused by long-duration earthquakes along subduction zones around the world have shown the importance of considering the ground-motion duration on the seismic performance of bridges. The current study has demonstrated that earthquake duration can have significant effect on structural performance in terms of decreasing displacement capacity. Thus, it is important to understand the design implications of long-duration earthquakes and provide mitigation strategies that address this scenario. This research comprises analytical and experimental methods to study the effect of different reinforcement (conventional and high-strength reinforcement) and design details (confinement spacing ratio and longitudinal reinforcement debonding) on the seismic response of reinforced concrete (RC) bridge columns under long-duration ground motions.

This study included two experimental phases. First, three 1/3-scale cantilever bridge columns were designed, constructed, and tested on a shake table at UNR. In Phase I, the specimens were designed using conventional Grade 60 (conforming with ASTM 706) reinforcing bars and tested under a sequence of long-duration ground motions adopted from the 2011 Tohoku earthquake main shock and after shock. All three columns had same longitudinal reinforcement ratio. Column #2 had different confinement spacing ratio compared to Column #1. The design of Column #3 included debonding of longitudinal reinforcement at the column–footing interface. Phase I investigated how different design detailing impacts column performance under a long-duration ground motion. The specimens in Phase II were reinforced longitudinally using high-strength Grade 100 (conforming with ASTM A1035) bars. The columns were tested under short- and long-duration motions to study the cyclic deterioration and to help quantify the use of high-strength reinforcement in the seismic design of bridge columns.

All specimens were constructed in following the same construction sequences at the UNR Earthquake Engineering Laboratory fabrication yard. Samples of the materials were taken during construction and were tested to determine mechanical properties of interest for quality assurance (based on the specified and expected properties) and for populating the analytical models. The specimens were instrumented to monitor various aspects of behavior during the tests. The specimens were then placed on a shake table and tested uniaxially in the north–south direction following specified loading protocols. The key observations of the experimental program are summarized in the next section.

A pre-test computational model was developed and initially calibrated against the previous experimental study to be used in the pre-test analysis. The model was then assessed using the shake table test data. Column displacements, base shear, dissipated energy, and strain in the longitudinal bars were compared. Refinements were then applied, and new modeling values / parameters / equations were obtained and summarized in Section 9.3.

The second part of the analytical studies focused on two-span, two-column bent archetype bridges, resulting in recommendations for updating current seismic provisions to consider the duration effect in design of the bridges at sites with potential occurrence of long-duration earthquakes. The seismic performance of the archetype bridges was evaluated using a ground-motion set using IDA. Two main design factors (ductility demand and confinement spacing ratio) and two IMs (conditional Sa_{Ratio} and significant duration) were employed to develop the site-specific safety design domains/criteria. Such design domains considered the duration effects through employing surrogate models that have been developed as another product of the IDA for different bridge performance levels.

9.2 KEY OBSERVATIONS

9.2.1 Experimental Study

The main observations from the experimental study are as follows:

- In Phase I, the seismic performance of the columns was satisfactory. All columns performed in a ductile manner and underwent significant displacements. Good energy dissipation was observed based on the wide hysteresis force-displacement relationship loops. Phase II testing demonstrated that columns with HSS (Grade 100 MMFX) did not exhibit ductile behavior or good energy dissipation. All columns collapsed under 100% of the applied motion.
- As expected for cantilever members, extensive damage was concentrated at the plastic hinges (lower north and south sides of the all columns); the upper two-thirds of all columns remained damage free during the entire test sequence.
- The failure mode was due to the longitudinal bar fracture associated with a combination of bar buckling, strain demand, and low-cycle fatigue. The bar fractures in the Phase I columns were mainly due to low-cycle fatigue; in Phase II, bar fractures were due to induced strain demands.
- Similar damage progression was observed for all columns, which started with flexural cracks and yielding in the longitudinal reinforcement, followed by major spalling of the cover concrete on both the south and north sides of the specimen. Next, longitudinal bars buckled, and the damage expanded into the core concrete, with the exception of the columns with 1.5 in. tie spacing. In that case, minor bar buckling occurred, and core concrete damage was observed. The final damage state of all columns was longitudinal bar fracture.

- The columns reinforced with the high-strength Grade 100 bars (Phase II) showed more bar buckling strength compared to the columns reinforced with conventional Grade 60 bars (Phase I) with the same tie spacing.
- Using smaller spacing for transverse reinforcement significantly improved column performance, with about 55% larger displacement capacity under long-duration ground motions; see Phase I.
- Debonding of the longitudinal bars at the column-footing interface increased the displacement capacity by 24% due to the spread of yielding in the plastic-hinge zone, which demonstrated less improvement compared to increased confinement; see Phase I.
- The measured strains in the debonded bars showed that although the yielding occurred and spread along the debonded length, there was no reduction in peak strains. Thus, debonding would not improve the low-cycle fatigue life of the bar.
- Phase II specimens with HSS bars showed significantly lower displacement capacity by 16% and 47% for those columns with $6d_b$ and $3d_b$ tie spacing, respectively. The result also showed that higher confinement was not effective in increasing the column displacement capacity under long-duration motions.
- All columns in each phase had nearly the same force capacity. Thus, different design details did not dictate major differences between the overall lateral force capacities.
- The response of the columns did not show significant strength degradation prior to bar rupture. The columns did show a lateral-strength degradation due to bar buckling and lost significant strength due to the fracture of longitudinal bars.
- Lower energy dissipation and thinner hysteretic loops for columns with HSS (Grade 100 MMFX) bars were observed and mainly attributed to the following factors: (1) higher effective yield force; (2) lack of a defined yield plateau; (3) lower *T/Y* ratio for the high-strength steel bars; and (4) higher stiffness of the re-loading branch in the column hysteretic behavior.
- Investigation of the high strain-rate effect on the HSS bars demonstrated about 20% increase and 50% reduction on the yield stress and fracture strain, respectively; this effect on the tensile strength was negligible.

9.2.2 Analytical Study

The analytical part of this study had two major components. The first part focused on assessing the modeling assumptions made for seismic bridge columns, especially as related to low-cycle fatigue and emerging types of HSS. The second part was related to the prototype analysis. The main observations from the two-part analytical studies are as follows:

- Comparing the predicted and measured responses showed that the differences in the displacements and base shears were consistently higher for the Phase II columns with

high-strength steel (HSS) bars. The cause of this discrepancy was mainly attributed to the steel material used for HSS bars in the pre-test model (*Steel02*).

- The preliminary low-cycle fatigue model used in the pre-test model underestimated the fatigue life of the conventional Grade 60 bars and overestimated that of HSS (Grade 100 MMFX) bars.
- The correlation between the measured and predicted displacement histories were somewhat closer in the Phase I columns; however, the model did not predict the residual displacements that occurred during the tests, which is mainly related to the bond-slip model.
- The first bar fracture was demonstrated to be the critical damage state (which is very close to the CDT-3 damage state) and is most sensitive to the earthquake duration.
- The main factors that affected the bridge collapse capacity were Sa_{Ratio} and Ds_{5-75}. The IDA results showed that for Sa_{Ratio} greater than 1.8, the sensitivity of the median *Sa* to the spectral shape is decreased. In the same manner, the effect of Ds_{5-75} when it is greater than 10 sec is more significant.
- Typically, the bridge would not fail directly after the first bar fracture, and the median Sa_{col} is found about 30% higher than the median Sa_{FF}.
- The developed site-specific design criteria for the studied sites demonstrated that most sites in Oregon and Alaska—and some sites in Washington—require more restrictive design criteria for multi-column bent bridges. The limited μ_D values for these sites range from 1.6 to 4.8, and the limited s/d_b ranges from 1.0 to 5.6.
- The design domain for multi-column bent bridges—especially the maximum allowable μ_D—appears to be more sensitive to the duration effect compared to that for single-column bent bridges, requiring more restrictive design criteria for multi-column bent bridges at sites with significant long-duration shaking (longer than 30 sec).

9.3 CONCLUSIONS

The following conclusions were drawn from the experimental and analytical studies:

- Both higher concrete confinement (i.e., smaller tie spacing) and longitudinal bars debonding improve the column performance under long-duration earthquakes; greater confinement has a more significant effect.
- The use of high-strength steel Grade 100 ASTM A1035 should be avoided in the critical/ductile members (e.g., bridge columns) due to premature failure in the plastic hinges.
- The bridges were found to be capable of withstanding several bar ruptures because the first few bar ruptures do not cause significant loss of strength and stiffness.

- For a specific site, structural response is dependent on the duration effect and the spectral shape (Sa_{Ratio}). Therefore, both effects should be considered in assessing bridge performance.
- Decreasing the design displacement ductility demand factor (μ_D) and/or the confinement spacing ratio (s/d_b) would be reasonable mitigation design strategies when considering the effect of earthquake duration and spectral shape. Thus, the new site-specific design criteria were developed for multi-column bent bridges considering the sites in the U.S. Pacific Northwest region and Alaska.
- Modeling recommendations:
  - To model the bond-slip effect, it is recommended to develop the moment-rotation backbone curve using three points: one point in the elastic range and two points in the nonlinear range at $M_1 = 0.2 \sim 0.3M_u$, $M_2 = 0.75 \sim 0.85M_u$, and $M_3 = M_u$.
  - Debonding of the longitudinal bars helped to improve the column displacement capacity due to spread of yielding, and subsequently larger bond-slip rotation at the base of the column. Thus, it is recommended to simulate the effect of bar debonding by modifying the bond-slip model.
  - The *RambergOsgoodSteel* uniaxial material may simulate more accurately the stress–strain behavior of HHS bars rather than the commonly used *ReinforcingSteel* and *Steel02* in OpenSees. Further studies on the cyclic behavior of this steel are needed to develop more accurate material models.
  - For modeling and design of structures reinforced by HSS-Grade 100 MMFX bars, it is recommended to consider the differences in the stress–strain behavior of this steel (as described above).
  - It is also recommended to consider the effect of high strain rates (larger than 4000 $\mu\varepsilon$/sec) on the HSS-grade 100 MMFX characteristics, especially for developing the low-cycle fatigue model using the new developed equation reported herein to modify the yield stress: $\text{SRF}_{100\text{MMFX}} = 0.134\ln(\text{strain rate}) - 0.111$.

REFERENCES

AASHTO (2002). *Standard Specifications for Highway Bridges*, American Association of State Highway and Transportation Officials, Washington, D.C.

AASHTO (2014). *AASHTO LRFD Bridge Design Specifications.* American Association of State Highway and Transportation Officials, Washington, D.C.

Abbasi M., Moustafa M.A. (2019). Time-dependent seismic fragilities of older and newly designed multi-frame reinforced concrete box-girder bridges in California, *Earthq. Spectra*, 35(1):233–266, https://doi.org/10.1193/102317EQS220M.

Aboukifa M., Moustafa M.A., Itani A. (2020). Comparative structural response of UHPC and normal strength concrete columns under combined axial and lateral cyclic loading, American Concrete Institute, *Special Publication*, 341: 71–96.

ACI Committee 318. (2014). *Building Code Requirements for Structural Concrete* (ACI 318-14), American Concrete Institute, Farmington Hills, MI.

ACI Committee 318. (2019). *Building Code Requirements for Structural Concrete* (ACI 318-19), American Concrete Institute, Farmington Hills, MI.

Alian S.M., Moustafa M.A., Sanders D.H. (2019). Fragility analysis of reinforced concrete bridge columns under short and long duration ground motions, *Proceedings, International Conference on Earthquake Engineering and Seismology* (5ICEES), Vol. 8, Ankara, Turkey.

Ancheta T.D., Darragh R.B., Stewart J.P., Seyhan E., Silva W.J., Chiou B.S.-J., Wooddell K.E., Graves R.W., Kottke A., Boore D.M., Kishida T., Donahue J.L. (2013). PEER NGA-West2 database, *PEER Report No. 2013/03*, Pacific Earthquake Engineering Research Center, University of California, Berkeley, CA.

Aoyama H. (2001). *Design of Modern Highrise Reinforced Concrete Structures*, Vol. 3, World Scientific, 490 pgs, https://doi.org/10.1142/p204.

Aviram A., Stojadinovic B., Parra-Montesinos G.J. (2014). High-performance fiber-reinforced concrete bridge columns under bidirectional cyclic loading, *ACI Struct. J.*, 111(2):303–312, https://www.doi.org/10.14359/51686522.

Baker J.W. (2007). Probabilistic structural response assessment using vector-valued intensity measures, *Earthq. Eng. Struct. Dyn*., 36(13):1861–1883, https://doi.org/10.1002/eqe.700.

Baker J.W., Cornell C.A. (2006). Spectral shape, epsilon and record selection, *Earthq. Eng. Struct. Dyn*., 35(9):1077–1095, https://doi.org/10.1002/eqe.571

Barbosa A., Link T., Trejo D. (2015). Seismic performance of high-strength steel RC bridge columns, *J. Bridge Eng*., 21(2), https://doi.org/10.1061/(ASCE)BE.1943-5592.0000769.

Bommer J.J., Martinez-Pereira A. (1999). The effective duration of earthquake strong motion, *J. Earthq. Eng*., 3(2):127–172, https://doi.org/10.1080/13632469909350343.

Boore D.M. (2005). On pads and filters: Processing strong-motion data, *Bull. Seismol. Soc. Am*., 95(2):745–750.

Boore D.M., Bommer J.J. (2005). Processing of strong-motion accelerograms: needs, options and consequences, *Soil Dyn. Earthq. Eng*., 25(2):93–115, https://doi.org/10.1016/j.soildyn.2004.10.007.

Caltrans (2013). *Seismic Design Criteria*, Version 1.7, California Department of Transportation, Sacramento, CA.

Caltrans (2019). *Seismic Design Criteria*, Version 2.0. California Department of Transportation, Sacramento, CA.

Chandramohan R. (2016). *Duration of Earthquake Ground Motion: Influence on Structural Collapse Risk and Integration in Design and Assessment Practice*, PhD thesis, Stanford University. Stanford, CA.

Chandramohan R., Baker J.W., Deierlein G.G., Lin T. (2013). Influence of ground motion spectral shape and duration on seismic collapse risk, *Proceedings, 10th International Conference on Urban Earthquake Engineering*, Tokyo Institute of Technology, Tokyo, Japan.

Chandramohan R., Baker J.W., Deierlein G.G., (2016). Quantifying the influence of ground motion duration on structural collapse capacity using spectrally equivalent records, *Earthq. Spectra*, 32(2):927–950, https://doi.org/10.1193/122813eqs298mr2.

Chang G.A., Mander J.B. (1994). Seismic energy-based fatigue damage analysis of bridge columns: Part 1– evaluation of seismic capacity, *Technical Report No. NCEER-94-0006*, National Center for Earthquake Engineering Research, SUNY, Buffalo, NY, 239 pgs.

Coffin Jr. L.F. (1962). Low cycle fatigue--a review, *Report No. 62-RL-3069M*, General Electric Co. Research Lab., Schenectady, NY.

Cosenza E., Manfredi G., Ramasco R. (1993). The use of damage functionals in earthquake engineering: A comparison between different methods, *Earthq. Eng. Struct. Dyn.*, 22(10):855–868, https://doi.org/10.1002/eqe.4290221003.

Eads L., Miranda, E., Lignos, D. G. (2015). Average spectral acceleration as an intensity measure for collapse risk assessment, *Earthq. Eng. Struct. Dyn.*, 44(12):2057–2073, https://doi.org/10.1002/eqe.2575.

Fajfar P. (1992). Equivalent ductility factors, taking into account low-cycle fatigue, *Earthq. Eng. Struct. Dyn.*, 21(10):837–848, https://doi.org/10.1002/eqe.4290211001.

Foschaar J.C., Baker J.W., Deierlein G.G. (2012). Preliminary assessment of ground motion duration effects on structural collapse, *Proceedings, 15th World Conference on Earthquake Engineering*. Lisbon, Portugal.

Ghannoum W.M., Slavin C.M. (2016). Low-cycle fatigue performance of high-strength steel reinforcing bars, *ACI Mat. J.,* 113(6):803–814.

Hamblin W.K., Christiansen E.H. (2003). *Earth's Dynamic Systems*, 10th ed., Pearson Education Englewood Cliffs, NJ.

Hammad A., Moustafa M.A. (2019). Shake table tests of special concentric braced frames under short and long duration earthquakes, *Eng. Struct*., Vol. 200, https://doi.org/10.1016/j.engstruct.2019.109695.

Hammad A., Moustafa M.A. (2020a). Modeling sensitivity analysis of special concentrically braced frames under short and long duration ground motions, *Soil Dyn. Earthq. Eng*., Vol. 128, https://doi.org/10.1016/j.soildyn.2019.105867.

Hammad A., Moustafa M.A. (2020b). Numerical analysis of special concentric braced frames using experimentally-validated fatigue and fracture model under short and long duration earthquakes, *Bull. Earthq. Eng.*, 19:287–316.

Hancock J., Bommer J. J. (2005). The effective number of cycles of earthquake ground motion, *Earthq. Eng. Struct. Dyn.*, 34(6):637–664, https://doi.org/10.1002/eqe.437.

Hancock J., Bommer J. J. (2007). Using spectral matched records to explore the influence of strong-motion duration on inelastic structural response, *Soil Dyn. Earthq. Eng*., 27(4):291–299, https://doi.org/10.1016/j.soildyn.2006.09.004.

Heaton T.H., Kanamori H. (1984). Seismic potential associated with subduction in the northwestern United States, *Bull. Seismol. Soc. Am.,* 74(3):933–941.

Hognestad E. (1961). High strength bars as concrete reinforcement, Part 1—introduction to a series of experimental reports, *J. PCA Res. Devel. Lab*., 3(3):23–29.

Johnson N., Ranf R.T., Saiidi M.S., Sanders D., Eberhard M. (2008). Seismic testing of a two-span reinforced concrete bridge, *J. Bridge Eng*., 13(2):173-182, https://doi.org/10.1061/(ASCE)1084-0702(2008)13:2(173).

Kani G.N.J. (1964, April). The riddle of shear failure and its solution, American Concrete Institute, *Proceedings*, 61(4):441-468, Farmington Hills, MI.

Karim K.R., Yamazaki F. (2001). Effect of earthquake ground motions on fragility curves of highway bridge piers based on numerical simulation, Earthq. Eng. Struct. Dyn., 30(12):1839–1856, https://doi.org/10.1002/eqe.97.

Kawashima K., Hosoiri K., Shoji G., Sakai J.-I. (2001). Effect of unbonding of main reinforcements at plastic hinge region for enhancing ductility of reinforced concrete bridge columns, *J. Stage*, 2001(689):45–64, https://doi.org/10.2208/jscej.2001.689_45.

Kennedy, B. (2015). Rocking connection between a precast bridge column and cap beam. Master's thesis, Dept. of Civil and Environmental Engineering, Univ. of Washington, Seattle. Kircher C., Deierlein G., Hooper J., Krawinkler H., Mahin S., Shing B., Wallace J. (2010). *Evaluation of the FEMA P-695 Methodology for Quantification of Building Seismic Performance Factors*, National Institute of Standards and Technology, Gaithersburg, MD.

Kishida, T., Contreras, V., Bozorgnia, Y., Abrahamson, N. A., Ahdi, S. K., Ancheta, T. D., ... & Youngs, R. R. (2018). NGA-Sub ground motion database.

Kramer S.L., Silva W.J., Baska D.A. (1998). Ground motions due to large magnitude subduction zone earthquakes, *No. WA-RD 450.1*, Washington State Department of Transportation, Olympia, WA.

Kulkarni S.M., Shah S.P. (1998). Response of reinforced concrete beams at high strain rates, *Struct. J.*, 95(6):705–715.

Kunnath S.K., El-Bahy A., Taylor A., Stone W. (1997). Cumulative seismic damage of reinforced concrete bridge piers, *NISTIR Report No. 6075*, National Institute of Standards and Technology, Gaithersburg, MD, https://doi.org/10.6028/NIST.IR.6075.

Laplace P.N., Sanders D., Saiidi M.S., Douglas B. (1999). Shake table testing of flexure dominated reinforced concrete bridge columns, Center for Earthquake Engineering, University of Nevada, Reno, NV.

Lin T., Baker J.W. (2013). Introducing adaptive incremental dynamic analysis: a new tool for linking ground motion selection and structural response assessment, *Proceedings, International Conference on Structural Safety and Reliability*, New York, NY.

Macchi G., Pinto P.E., Sanpaolesi L. (1996). Ductility requirements for reinforcement under Eurocodes, *Struct. Eng. Inter.*, pp. 249–254, https://doi.org/10.2749/101686696780496148.

Mander J.B., Priestley M.J., Park R. (1988). Theoretical stress-strain model for confined concrete, *J. Struct. Eng.*, 114(8):1804–1826, https://doi.org/10.1061/(ASCE)0733-9445(1988)114:8(1804).

Mangalathu Sivasubramanian Pillai, S. (2017). *Performance Based Grouping and Fragility Analysis of Box-Girder Bridges in California*, PhD thesis, School of Civil and Environmental Engineering, Georgia Institute of Technology, Atlanta, GA.

Manson S.S., Hirschberg M.H. (1963). Fatigue behavior in strain cycling in the low and intermediate-cycle range, *Proceedings, The 10th Sagamore Army Research Conference: Fatigue—An Interdisciplinary Approach*, New York, pp. 13–16.

Marafi N.A., Berman J.W., Eberhard M.O. (2016). Ductility-dependent intensity measure that accounts for ground-motion spectral shape and duration, *Earthq. Eng. Struct. Dyn.*, 45(4):653–672, https://doi.org/10.1002/eqe.2678.

Marsh M.L., Gianotti C.M. (1994). Structural response to long-duration earthquakes, *Report WA-RD 340.1*, Washington State Department of Transportation, Olympia, WA.

Massey Jr. F.J. (1951). The Kolmogorov-Smirnov test for goodness of fit, *J. Am. Stat. Assoc.*, 46(253):68–78.

Mazzotti S., Adams J. (2004). Variability of near-term probability for the next great earthquake on the Cascadia subduction zone, *Bull. Seismol. Soc. Am.,* 94(5):1954–1959, https://doi.org/10.1785/012004032.

McGann C. R., Arduino P., Mackenzie-Helnwein P. (2011). Applicability of conventional *py* relations to the analysis of piles in laterally spreading soil, *J. Geotech. Geoenviro. Eng.*, 137(6):557–567, https://doi.org/10.1061/(ASCE)GT.1943-5606.0000468.

McKenna F. (2011). OpenSees: a framework for earthquake engineering simulation, *Comp. Sci. Eng.*, 13(4):58–66, https://doi.org/10.1109/MCSE.2011.66.

Megally S., Silva P., Seible F. (2001). Seismic response of sacrificial shear keys in bridge abutments, *Report No. SSRP–2001/23*, Department of Structural Engineering, University of California, San Diego, CA.

Mehraein M. (2016). *Seismic Performance of Bridge Column-Pile-Shaft Pin Connections for Application in Accelerated Bridge Construction*, PhD Thesis, Department of Civil and Environmental Engineering, University of Nevada, Reno, NV.

Mehrsoroush A. (2014). *Experimental and Analytical Seismic Studies of Bridge Piers with Innovative Pipe Pin Column-Footing Connections and Precast Cap Beams*, PhD Thesis, Department of Civil and Environmental Engineering, University of Nevada, Reno, NV.

Miner M.A. (1945). Cumulative fatigue damage, *J. Appl. Mech.*, 12(3):A159–A164.

Mohammed M.S. (2016). *Effect of Earthquake Duration on Reinforced Concrete Bridge Columns*, PhD Thesis, Department of Civil and Environmental Engineering, University of Nevada, Reno, NV.

Mohammed M.S., Sanders D.H., Buckle I.G. (2017). Reinforced concrete bridge columns tested under long and short duration ground motions, *Proceedings, 16th World Conference on Earthquake Engineering*, Santiago, Chile.

Moustafa M.A., Mosalam K.M. (2015). Seismic response of bent caps in as-built and retrofitted reinforced concrete box-girder bridges, *Eng. Struct.*, 98:59–73, https://doi.org/10.1016/j.engstruct.2015.04.028.

Naeimi N., Moustafa M.A. (2020). Numerical modeling and design sensitivity of structural and seismic behavior of UHPC bridge piers, *Eng. Struct.*, Vol. 219, https://doi.org/10.1016/j.engstruct.2020.110792.

Nikoukalam M.T., Sideris P. (2017). Experimental performance assessment of nearly full-scale reinforced concrete columns with partially debonded longitudinal reinforcement, *J. Struct. Eng.,* 143(4), https://doi.org/10.1061/(ASCE)ST.1943-541X.0001708.

Ou, Y.C., Fan H.D., Nguyen N.D. (2013). Long-term seismic performance of reinforced concrete bridges under steel reinforcement corrosion due to chloride attack, *Earthq. Eng. Struct. Dyn.*, 42(14):2113–2127, https://doi.org/10.1002/eqe.2316.

Ou Y.C., Song J., Wang P.H., Adidharma L., Chang K.C., Lee G.C. (2013). Ground motion duration effects on hysteretic behavior of reinforced concrete bridge columns, *J. Struct. Eng.,* 140(3), https://doi.org/10.1061/(ASCE)ST.1943-541X.0000856.

Pandey G.R., Mutsuyoshi H. (2005). Seismic performance of reinforced concrete piers with bond-controlled reinforcements, *ACI Struct. J.*, 102(2): 295–298, 300–304.

Pandey G.R., Mutsuyoshi H., Maki T. (2008). Seismic performance of bond controlled RC columns, *Eng. Struct.*, 30(9):2538–2547, https://doi.org/10.1016/j.engstruct.2008.02.001.

Park Y., Ang. A.H. (1985). "Mechanistic seismic damage model for reinforced concrete, *J. Struct. Eng.,* 111(4),:40–757, https://doi.org/10.1061/(ASCE)0733-9445(1985)111:4(722).

Phan V., Saiidi M.S., Anderson J. (2005). Near fault (near field) ground motion effects on reinforced concrete bridge columns, *Technical Report No. CCEER-05-07*, Center for Civil Engineering Earthquake Research, University of Nevada, Reno, NV.

Raghunandan M., Liel A.B. (2013). Effect of ground motion duration on earthquake-induced structural collapse, Struct. Safety, 41:119–133, https://doi.org/10.1016/j.strusafe.2012.12.002.

Ramberg W., Osgood W.R. (1943). Description of stress-strain curves by three parameters, *NACA-TN-902*, NASA, Washington, D.C.

Ramanathan K.N. (2012). *Next Generation Seismic Fragility Curves for California Bridges incorporating the Evolution in Seismic Design Philosophy*, PhD thesis, School of Civil and Environmental Engineering, Georgia Institute of Technology, Atlanta, GA.

Ranf R.T., Nelson J.M., Price Z., Eberhard M.O., Stanton J.F. (2005). Damage accumulation in lightly confined reinforced concrete bridge columns, *PEER Report No. 2005/08*, Pacific Earthquake Engineering Research Center, University of California, Berkeley, CA.

Rautenberg J.M. (2013). *Drift Capacity of Concrete Columns Reinforced with High-Strength Steel*, PhD thesis, Department of Civil Engineering, Purdue University, Lafayette, IN.

Richart F.E., Brown R.L. (1943). An investigation of reinforced concrete columns, *Bulletin No. 267*, University of Illinois Engineering Experiment Station, Champaign, IL, 91 pgs.

Roeder C., Stanton J., Taylor, A. (1987). Performance of elastomeric bearings, *NCHRP Report No. 298*, Transportation Research Board, Washington, DC.

Salmon M.W., Short S.A., Kennedy R.P. (1992). Strong motion duration and earthquake magnitude relationships, *No. UCRL-CR-117769*. Lawrence Livermore National Laboratory, University of California, Livermore, CA.

Schoettler M.J., Restrepo J.I., Guerrini G., Duck D.E., Carrea F. (2012). A full-scale single-column bridge bent tested by shake table excitation. *Report No. CCEER-258*, Center for Civil Engineering Earthquake Research, Department of Civil and Environmental Engineering, University of Nevada, Reno, NV.

Shoushtari E. (2019a). *Shake Table Studies of a Steel Girder Bridge System with ABC Connections*, PhD thesis, Department of Civil and Environmental Engineering, University of Nevada, Reno, NV.

Shoushtari E., Saiidi M.S., Itani A., Moustafa M. A. (2019b). Design, construction, and shake table testing of a steel girder bridge system with ABC connections, *J. Bridge Eng.*, 24(9), https://doi.org/10.1061/(ASCE)BE.1943-5592.0001464.

Shoushtari E., Saiidi M.S., Itani A.M., Moustafa M.A. (2019c). Analytical investigations and design implications of seismic response of a two-span abc bridge system, *No. ABC-UTC-2013-C3-UNR05-Final*, Accelerated Bridge Construction University Transportation Center, Florida International University, Miami, FL.

Shoushtari E., Saiidi M.S., Itani A., Moustafa M.A. (2020). Pretest analysis of shake table response of a two-span steel girder bridge incorporating accelerated bridge construction connections, *Front. Struct. Civ. Eng.*, 14 (1):169–184, https://doi.org/10.1007/s11709-019-0590-y.

Slavin C.M., Ghannoum W.M. (2015). Defining structurally acceptable properties of high-strength steel bars through material and column testing. Part I: Material testing report, *Grant No. 05-14*, University of Texas, Austin, TX.

Smith R.W., Hirschberg M.H., Manson S.S. (1963). Fatigue behavior of materials under strain cycling in low and intermediate life range, *Technical Note D-1574*, NASA, Lewis Research Center, Cleveland, OH.

Sokoli D. (2014). *Seismic Performance of Concrete Columns Reinforced with High Strength Steel,* Master's thesis, Department of Civil, Architectural and Environmental Engineering, University of Texas, Austin, TX.

Sokoli D. (2018). *Fracture of High-Strength Bars in Concrete Frame Members under Earthquake Loads*, PhD thesis, Department of Civil, Architectural and Environmental Engineering, University of Texas, Austin, TX.

Sokoli D., Ghannoum W.M. (2016). High-strength reinforcement in columns under high shear stresses, *ACI Struct. J.*, 113(3)605–614.

Sokoli D., Limantono A., Ghannoum M.W. (2017). Defining structurally acceptable properties of high-strength steel bars through material and column testing, Part II: Column testing report, *Research Grant Agreement #05-14*, Charles Pankow Foundation, Vancouver, WA, 214 pgs.

Stapleton S.E. (2004). *Performance of Poorly Confined Reinforced Concrete Columns in Long-Duration Earthquakes*, PhD Thesis, Washington State University, Pullman, WA.

Thoen B.K., Laplace P.N. (2004). Offline tuning of shaking tables, *Proceedings, 13th World Conference on Earthquake Engineering*, Paper No. 960, Vancouver, B.C., Canada.

To D.V (2018). *Seismic Performance Characterization of Beams with High-Strength Reinforcement*, PhD Thesis, Department of Civil and Environmental Engineering, University of California, Berkeley, CA.

Todeschini C.E., Bianchini A.C., Kesler C.E. (1964). Behavior of concrete columns reinforced with high strength steels, *ACI J.*, 61(6):701–716.

Trifunac M.D., Brady A.G. (1975). A study on the duration of strong earthquake ground motion, *Bull. Seismol. Soc. Am.,* 65(3):581–626.

Vamvatsikos D., Cornell C.A. (2002). Tracing and post-processing of IDA curves: Theory and software implementation, *Report No. RMS-44*, RMS Program, Stanford University, Stanford, CA.

Varum H. (2003). *Seismic Assessment, Strengthening and Repair of Existing Buildings*, PhD Thesis, University of Aveiro, Aveiro, Portugal.

Wehbe N., Saiidi M.S., Sanders D. (1997). Effects of confinement and flares on the seismic performance of reinforced concrete bridges columns, *Technical Report No. CCEER-97-2*, Center for Civil Engineering Earthquake Research, University of Nevada Reno, Reno, NV.

Zadeh M.S., Saiidi M.S. (2007). Pre-test analytical studies of NEESR-SG 4-span bridge model using OpenSees, *Technical Report No. CCEER-07*, Center of Civil Engineering Earthquake Research, Department of Civil Engineering, University of Nevada, Reno, Reno, NV.

Zhao J., Sritharan S. (2007). Modeling of strain penetration effects in fiber-based analysis of reinforced concrete structures, *ACI Struct. J.*, 104(2):133–141.

Zhong K. (2020). *Influence of Reinforcing Steel Fracture on Seismic Performance of Concrete Structures: Fracture Simulation, Earthquake Duration Effects, and Design Strategies*, PhD thesis, Department of Civil and Environmental Engineering, Stanford University, Stanford, CA.

Zhong K., Deierlein G.G. (2018). Assessing earthquake loading demands and reliability of high strength reinforcing steel, *Proceedings, 11th U.S. National Conference on Earthquake Engineering*, Los Angeles, CA.

Zhong K. and Deierlein G. G. (2019). Low-cycle fatigue effects on the seismic performance of concrete frame and wall systems with high strength reinforcing steel. Charles Pankow Foundation, Research Grant, Stanford University, Stanford, CA.

APPENDIX A GROUND-MOTION SETS (GROUP A AND GROUP B)

This appendix includes group A and group B of the spectrally equivalent long- and short-duration ground-motion sets used in the preliminary analysis explained in Chapter 2.

Table A.1 Long-duration ground-motion set from Group A.

#	Earthquake	Station	$Ds_{5\text{-}75}$ (sec)	$Ds_{5\text{-}95}$ (sec)
1	2011 Tohoku, Japan	FKS004 EW (IITATE)	76	99
2	2011 Tohoku, Japan	FKS004 NS (IITATE)	78	98
3	2011 Tohoku, Japan	FKS006 EW (KATSURAO)	67	96
4	2011 Tohoku, Japan	FKS006 NS (KATSURAO)	63	88
5	2011 Tohoku, Japan	FKS007 EW (OHKUMA)	55	74
6	2011 Tohoku, Japan	FKS007 NS (OHKUMA)	59	75
7	2011 Tohoku, Japan	FKS020 EW (INAWASHIRO)	80	119
8	2011 Tohoku, Japan	FKS020 NS (INAWASHIRO)	80	117
9	2011 Tohoku, Japan	FKS023 EW (AIDUWAKAMATSU)	57	79
10	2011 Tohoku, Japan	FKS023 NS (AIDUWAKAMATSU)	69	87
11	2011 Tohoku, Japan	FKSH11 EW (YABUKI)	60	73
12	2011 Tohoku, Japan	FKSH11 NS (YABUKI)	59	74
13	2011 Tohoku, Japan	FKSH16 EW (FUKUSHIMA)	77	98
14	2011 Tohoku, Japan	FKSH16 NS (FUKUSHIMA)	77	95
15	2011 Tohoku, Japan	FKSH17 EW (KAWAMATA)	81	100
16	2011 Tohoku, Japan	FKSH17 NS (KAWAMATA)	85	98
17	2011 Tohoku, Japan	FKSH20 EW (NAMIE)	61	86
18	2011 Tohoku, Japan	FKSH20 NS (NAMIE)	64	94
19	2011 Tohoku, Japan	MYG003 EW (TOHWA)	55	88
20	2011 Tohoku, Japan	MYG003 NS (TOHWA)	55	95
21	2011 Tohoku, Japan	MYG005 EW (NARUKO)	71	134
22	2011 Tohoku, Japan	MYG005 NS (NARUKO)	71	127
23	2011 Tohoku, Japan	MYG006 EW (FURUKAWA)	58	115
24	2011 Tohoku, Japan	MYG006 NS (FURUKAWA)	64	122
25	2011 Tohoku, Japan	MYG011 EW (OSHIKA)	57	76
26	2011 Tohoku, Japan	MYG011 NS (OSHIKA)	56	75
27	2011 Tohoku, Japan	MYG015 NS (IWANUMA)	81	116
28	2011 Tohoku, Japan	MYG015 EW (IWANUMA)	71	116
29	2011 Tohoku, Japan	MYG016 EW (SHIROISHI)	77	107
30	2011 Tohoku, Japan	MYG016 NS (SHIROISHI)	68	107
31	2011 Tohoku, Japan	MYG017 EW (KAKUDA)	69	105
32	2011 Tohoku, Japan	MYG017 NS (KAKUDA)	71	110
33	2011 Tohoku, Japan	MYGH08 EW (IWANUMA)	70	113
34	2011 Tohoku, Japan	MYGH08 NS (IWANUMA)	66	112
35	2011 Tohoku, Japan	IWT010 EW (ICHINOSEKI)	48	68
36	2011 Tohoku, Japan	IWT010 NS (ICHINOSEKI)	52	71
37	2011 Tohoku, Japan	IWTH26 EW (ICHINOSEKI-E)	56	87
38	2011 Tohoku, Japan	IWTH26 NS (ICHINOSEKI-E)	54	85
39	2011 Tohoku, Japan	YMT007 EW (HIGASHINE)	73	109
40	2011 Tohoku, Japan	YMT007 NS (HIGASHINE)	69	109
41	2011 Tohoku, Japan	YMT011 EW (KAMINOYAMA)	86	116
42	2011 Tohoku, Japan	YMT011 NS (KAMINOYAMA)	81	119
43	2011 Tohoku, Japan	YMT015 EW (YONEZAWA)	78	104
44	2011 Tohoku, Japan	YMT015 NS (YONEZAWA)	75	106
45	2011 Tohoku, Japan	YMTH01 EW (TENDOU)	71	110

#	Earthquake	Station	Ds_{5-75} (sec)	Ds_{5-95} (sec)
46	2011 Tohoku, Japan	YMTH01 NS (TENDOU)	64	108
47	2011 Tohoku, Japan	YMTH02 EW (YAMAGATA)	79	120
48	2011 Tohoku, Japan	YMTH02 NS (YAMAGATA)	85	119
49	2011 Tohoku, Japan	YMTH06 EW (TAKAHATA)	82	109
50	2011 Tohoku, Japan	YMTH06 NS (TAKAHATA)	80	104
51	2014 Inquique, Chile	Chusmiza 90	30	59
52	2014 Inquique, Chile	Chusmiza 360	25	49
53	2015 Illapel, Chile	El Pedregal 90	22	47
54	2015 Illapel, Chile	El Pedregal 360	21	42
55	2015 Illapel, Chile	Tololo Obs., Vicuna 90	27	58
56	2015 Illapel, Chile	Tololo Obs., Vicuna 360	28	59
57	2015 Illapel, Chile	San Esteban 90	45	74
58	2015 Illapel, Chile	San Esteban 360	44	71
59	2015 Illapel, Chile	Cerro Colorado-Renca 90	40	73
60	2015 Illapel, Chile	Cerro Colorado-Renca 360	45	75
61	2015 Illapel, Chile	Torpederas 90	53	81
62	2015 Illapel, Chile	Torpederas 360	54	82
63	2015 Illapel, Chile	Santo Domingo 90	56	88
64	2015 Illapel, Chile	Santo Domingo 360	59	88
65	2015 Illapel, Chile	Talagante 90	46	76
66	2015 Illapel, Chile	Talagante 360	48	78
67	2010 Maule, Chile	Angol EW	30	50
68	2010 Maule, Chile	Angol NS	23	51
69	2010 Maule, Chile	Concepcion San Pedro EW -97	32	74
70	2010 Maule, Chile	Concepcion San Pedro NS -7	36	70
71	2010 Maule, Chile	Constitucion (long.)	32	60
72	2010 Maule, Chile	Constitucion (Tran.)	32	65
73	2010 Maule, Chile	Curico EW	38	52
74	2010 Maule, Chile	Curico NS	37	50
75	2010 Maule, Chile	Haulane Long.	34	62
76	2010 Maule, Chile	Haulane Tran.	34	56
77	2010 Maule, Chile	Santiago La Florida EW	28	41
78	2010 Maule, Chile	Santiago La Florida NS	26	40
79	2010 Maule, Chile	Talca Long.	51	70
80	2010 Maule, Chile	Talca Tran.	52	72
81	2010 Maule, Chile	Cerro Santa Lucia 360	25	38
82	2010 Maule, Chile	Cerro Santa Lucia 91	30	41
83	2007 Sumatra, Indonesia	West Sumatra 90	36	53
84	2007 Sumatra, Indonesia	West Sumatra 360	36	50
85	1974 Lima, Peru	Arequipa H1	35	48
86	1974 Lima, Peru	Arequipa H2	33	48
87	2012 Kamaishi, Japan	TCG014 EW (MOTEGI)	39	55
88	2012 Kamaishi, Japan	TCG014 NS (MOTEGI)	41	58
89	2012 Kamaishi, Japan	IWT012 EW (KITAKAMI)	35	48
90	2012 Kamaishi, Japan	IWT012 NS (KITAKAMI)	29	44
91	2004 Southeast of Kii Peninsula, Japan	NAR006 EW (KAWAKAMI)	25	32
92	2004 Southeast of Kii Peninsula, Japan	NAR006 NS (KAWAKAMI)	24	30
93	1979 Imperial Valley, USA	Delta H1 (NGA0169)	24	51

#	Earthquake	Station	$Ds_{5\text{-}75}$ (sec)	$Ds_{5\text{-}95}$ (sec)
94	1979 Imperial Valley, USA Delta H2 (NGA0169)	Delta H2 (NGA0169)	22	51
95	1992 Landers, USA	Mission Creek Fault H1 (NGA0880)	23	36
96	1992 Landers, USA	Mission Creek Fault H2 (NGA0880)	31	41
97	1992 Landers, USA	Thousand Palms Post Office H1 (NGA 3758)	26	39
98	1992 Landers, USA	Thousand Palms Post Office H2 (NGA 3758)	26	38
99	2008 Wenchuan, China	051SFB EW	24	90
100	2008 Wenchuan, China	051SFB NS	22	80
101	2008 Wenchuan, China	51SFB EW	15	42
102	2008 Wenchuan, China	51SFB NS	22	80
103	2008 Wenchuan, China	51WCW EW	22	52
104	2008 Wenchuan, China	51WCW NS	27	56
105	2008 Wenchuan, China	51MZQ EW	12	33
106	2008 Wenchuan, China	51MZQ NS	14	34
107	2008 Wenchuan, China	051AXT EW	27	79
108	2008 Wenchuan, China	051MZQ NS	12	33
109	2008 Wenchuan, China	051WCW EW	22	52
110	Cascadia M9.2	Seattle H1	142	197
111	Cascadia M9.2	Seattle H3	62	137
112	Cascadia M9.2	Seattle H4	59	132

Table A.2 Short-duration ground-motion set from Group A.

#	Earthquake	Station	Scale	$Ds_{5\text{-}75}$ (sec)	$Ds_{5\text{-}95}$ (sec)
1	1971 San Fernando	RSN56 H1, Carbon Canyon Dam	4.75	9	19
2	1976 Friuli, Italy-02	RSN132 H1, Forgaria Cornino	2.34	2	5
3	1976 Friuli, Italy-01	RSN125 H1, Tolmezzo	1.67	3	6
4	1975 Northern Calif-07	RSN103 H1, Petrolia, General Store	3.61	2	6
5	1976 Gazli, USSR	RSN126 H1, Karakyr	0.96	5	6
6	1976 Gazli, USSR	RSN126 H1, Karakyr	0.8	5	6
7	1979 Imperial Valley-06	RSN158 H1, Aeropuerto Mexicali	1.36	6	10
8	1952 Kern County	RSN14 H2, Santa Barbara Courthouse	2.23	11	34
9	1984 Morgan Hill	RSN448 H2, Anderson Dam (Downstream)	1.54	2	5
10	1984 Morgan Hill	RSN461 H1, Halls Valley	2.73	9	15
11	1971 San Fernando	RSN70 H2, Lake Hughes #1	4.63	7	17
12	1984 Morgan Hill	RSN461 H2, Halls Valley	1.71	9	11
13	1999 Chi-Chi, Taiwan-06	RSN3264 H1, CHY024	1.77	7	14
14	1978 Santa Barbara	RSN135 H1, Cachuma Dam Toe	3.28	1	5
15	2000 Yountville	RSN3830 H2, Napa - Napa College	1.69	2	6
16	1987 Whittier Narrows-01	RSN592 H1, Arcadia - Campus Dr	0.95	1	3
17	1954 Northern Calif-03	RSN20 H1, Ferndale City Hall	2.81	7	17
18	1999 Chi-Chi, Taiwan	RSN1504 H2, TCU067	1.03	8	23
19	1971 San Fernando	RSN72 H1, Lake Hughes #4	4.32	4	13
20	1971 San Fernando	RSN81 H2, Pearblossom Pump	3.92	7	14
21	1980 Irpinia, Italy-01	RSN294 H2, Tricarico	4.92	14	21
22	1999 Chi-Chi, Taiwan-06	RSN3500 H2, TCU118	4.82	25	52
23	1980 Irpinia, Italy-01	RSN289 H2, Calitri	3.53	14	24
24	1999 Chi-Chi, Taiwan	RSN56 H1, Carbon Canyon Dam	4.73	9	19
25	1971 San Fernando	RSN132 H1, Forgaria Cornino	3.01	5	11
26	1971 San Fernando	RSN125 H1, Tolmezzo	3.78	5	11
27	1999 Chi-Chi, Taiwan	RSN103 H1, Petrolia, General Store	1.13	8	23
28	1999 Chi-Chi, Taiwan	RSN126 H1, Karakyr	3.71	11	26
29	1976 Gazli, USSR	RSN126 H1, Karakyr	0.72	5	6
30	1992 Landers	RSN158 H1, Aeropuerto Mexicali	3.62	8	12
31	1999 Chi-Chi, Taiwan	RSN14 H2, Santa Barbara Courthouse	1.35	7	30
32	1999 Hector Mine	RSN448 H2, Anderson Dam (Downstream)	4.91	13	25
33	2009 L'Aquila, Italy	RSN461 H1, Halls Valley	3.52	4	8
34	1999 Chi-Chi, Taiwan	RSN70 H2, Lake Hughes #1	1.97	9	18
35	1972 Managua, Nicaragua-01	RSN461 H2, Halls Valley	1.36	4	8
36	1972 Managua, Nicaragua-01	RSN3264 H1, CHY024	1.7	5	10
37	1971 San Fernando	RSN135 H1, Cachuma Dam Toe	4.12	7	21
38	1967 Northern Calif-05	RSN3830 H2, Napa - Napa College	3.83	1	15
39	1994 Northridge-01	RSN592 H1, Arcadia - Campus Dr	1.32	8	19
40	1955 Imperial Valley-05	RSN20 H1, Ferndale City Hall	4.85	8	20
41	1989 Loma Prieta	RSN1504 H2, TCU067	0.49	3	9
42	1989 Loma Prieta	RSN72 H1, Lake Hughes #4	1.16	6	14
43	1999 Chi-Chi, Taiwan	RSN81 H2, Pearblossom Pump	4.82	13	26
44	1999 Chi-Chi, Taiwan	RSN294 H2, Tricarico	2.6	10	29
45	1971 San Fernando	RSN3500 H2, TCU118	2.68	4	7
46	1999 Chi-Chi, Taiwan-05	RSN289 H2, Calitri	3.09	11	37

#	Earthquake	Station	Scale	Ds_{5-75} (sec)	Ds_{5-95} (sec)
47	2010 Darfield, New Zealand	RSN1280 H1, HWA031	0.87	12	26
48	1976 Friuli, Italy-01	RSN68 H2, LA - Hollywood Stor FF	2.54	10	20
49	1938 Northwest Calif-01	RSN87 H2, Santa Anita Dam	3.68	4	12
50	1984 Morgan Hill	RSN1504 H2, TCU067	2.31	13	21
51	1971 San Fernando	RSN1269 H2, HWA019	1.65	6	11
52	1976 Fruili, Italy-03	RSN126 H1, Karakyr	4.06	3	5
53	1966 Parkfield	RSN841 H1, Boron Fire Station	2.09	4	11
54	1971 San Fernando	RSN1201 H2, CHY034	2.12	5	11
55	1984 Morgan Hill	RSN1835 H2, Temecula - 6th & Mercedes	1.05	9	11
56	1999 Chi-Chi, Taiwan	RSN4472 H2, Celano	0.34	7	22
57	1984 Morgan Hill	RSN1436 H2, TAP052	4.84	5	8
58	1971 San Fernando	RSN95 H2, Managua, ESSO	2.09	7	14
59	1966 Parkfield	RSN95 H1, Managua, ESSO	0.47	2	6
60	1971 San Fernando	RSN93 H2, Whittier Narrows Dam	1.52	3	7
61	1979 Imperial Valley-06	RSN34 H1, Ferndale City Hall	0.44	5	15
62	1979 Imperial Valley-06	RSN1035 H2, Manhattan Beach - Manhattan	0.43	7	20
63	1971 San Fernando	RSN21 H2, El Centro Array #9	2.9	5	10
64	1974 Hollister-03	RSN783 H1, Oakland - Outer Harbor Wharf	1.85	5	10
65	1971 San Fernando	RSN785 H2, Olema - Point Reyes Station	3.59	6	10
66	1980 Mammoth Lakes-03	RSN2967 H1, CHY063	0.27	3	6
67	1980 Irpinia, Italy-01	RSN1267 H2, HWA016	3.37	4	10
68	1987 Whittier Narrows-02	RSN65 H1, Gormon - Oso Pump Plant	3.47	1	6
69	1987 Whittier Narrows-01	RSN2958 H1, CHY054	3.64	3	7
70	1987 Whittier Narrows-01	RSN6966 H1, Shirley Library	4.64	6	11
71	1979 Imperial Valley-06	RSN125 H19, Tolmezzo	3.04	6	11
72	1999 Chi-Chi, Taiwan	RSN5 H2, Ferndale City Hall	1.07	4	6
73	1979 Imperial Valley-06	RSN472 H2, San Justo Dam (R Abut)	1.95	5	7
74	1983 Coalinga-01	RSN87 H1, Santa Anita Dam	4.96	6	10
75	1971 San Fernando	RSN128 H2, Forgaria Cornino	2.97	7	17
76	1999 Chi-Chi, Taiwan-06	RSN31 H2, Cholame - Shandon Array #8	4	8	15
77	1986 Chalfant Valley-01	RSN68 H2, LA - Hollywood Stor FF	1.46	9	20
78	1994 Northridge-01	RSN461 H2, Halls Valley	1.49	9	20
79	1981 Taiwan SMART1(5)	RSN1231 H1, CHY080	4.53	4	10
80	2011 Christchurch, New Zealand	RSN454 H2, Gilroy - Gavilan Coll.	1.81	4	9
81	1999 Chi-Chi, Taiwan	RSN81 H2, Pearblossom Pump	3.9	9	18
82	1971 San Fernando	RSN30 H1, Cholame - Shandon Array #5	3.34	3	7
83	1978 Tabas, Iran	RSN65 H2, Gormon - Oso Pump Plant	0.29	7	12
84	1975 Northern Calif-07	RSN172 H1, El Centro Array #1	4.35	2	6
85	1980 Mammoth Lakes-08	RSN172 H2, El Centro Array #1	2.18	2	6
86	1979 Imperial Valley-06	RSN58 H2, Cedar Springs Pumphouse	0.71	5	7
87	1957 San Francisco	RSN100 H1, San Juan Bautista, 24 Polk St	1.31	1	4
88	1975 Oroville-03	RSN59 H1, Cedar Springs, Allen Ranch	2.08	1	5
89	1980 Irpinia, Italy-02	RSN236 H1, Convict Creek	2.74	9	19
90	1979 Imperial Valley-07	RSN288 H1, Brienza	3.77	2	6

#	Earthquake	Station	Scale	Ds_{5-75} (sec)	Ds_{5-95} (sec)
91	1970 Lytle Creek	RSN3735 H2, Santa Fe Springs - E. Joslin	0.56	1	2
92	1970 Lytle Creek	RSN691 H2, San Marino - SW Academy	1.91	1	3
93	1999 Chi-Chi, Taiwan	RSN642 H2, LA - W 70th St	4.07	11	21
94	1980 Irpinia, Italy-02	RSN162 H1, Calexico Fire Station	1.43	8	20
95	1979 Norcia, Italy	RSN1197 H2, CHY028	3.82	8	15
96	1999 Chi-Chi, Taiwan-04	RSN158 H2, Aeropuerto Mexicali	4.12	8	18
97	1999 Chi-Chi, Taiwan-03	RSN357 H2, Parkfield - Stone Corral 3E	1.7	10	63
98	1986 Taiwan SMART1(45)	RSN70 H2, Lake Hughes #1	0.62	10	22
99	1972 Managua, Nicaragua-01	RSN3503 H1, TCU122	1.75	4	8
100	1980 Irpinia, Italy-01	RSN544 H1, Bishop - LADWP South St	4.41	4	10
101	1979 Coyote Lake	RSN1000 H1, LA - Pico & Sentous	3.94	2	6
102	1999 Chi-Chi, Taiwan-03	RSN3559 H1, SMART1 I03	4.65	10	61
103	1999 Chi-Chi, Taiwan	RSN8099 H2, Kaiapoi North School	1.4	8	10
104	1974 Hollister-03	RSN1275 H2, HWA026	4.01	2	10
105	1979 Imperial Valley-06	RSN65 H2, Gormon - Oso Pump Plant	1.18	3	6
106	1999 Chi-Chi, Taiwan	RSN139 H1, Dayhook	3.1	12	18
107	1999 Chi-Chi, Taiwan	RSN104 H1, Shelter Cove, Sta A	3.04	9	17
108	1979 Imperial Valley-08	RSN262 H1, Mammoth Elem School	3.94	4	12
109	1983 Coalinga-01	RSN158 H2, Aeropuerto Mexicali	4.48	5	13
110	1995 Kozani, Greece-01	RSN23 H2, Golden Gate Park	4.68	15	28
111	1979 Imperial Valley-06	RSN117 H2, Oroville Airport	1.14	6	17
112	1979 Imperial Valley-06	RSN301 H1, Mercato San Severino	1.07	5	15

Table A.3 Short-duration ground-motion set (FEMA far-field set) from Group B.

#	Earthquake	Station	$Ds_{5\text{-}75}$ (sec)	$Ds_{5\text{-}95}$ (sec)
1	1990 Manjil, Iran	ABBARL	7.4	28.3
2	1990 Manjil, Iran	ABBART	11.5	30.6
3	1999 Kocaeli, Turkey	ARCELIK000	7.6	11.0
4	1999 Kocaeli, Turkey	ARCELIK090	5.1	10.3
5	1999 Duzce, Turkey	BOLU000	2.6	8.5
6	1999 Duzce, Turkey	BOLU090	1.5	9.3
7	1989 Loma Prieta,	CAPITOLA000	5.7	11.9
8	1989 Loma Prieta,	CAPITOLA090	5.6	13.2
9	1999 Chi-Chi, Taiwan	CHY101E	13.5	30.4
10	1999 Chi-Chi, Taiwan	CHY101N	10.3	26.5
11	1992 Landers, USA	COOLWATERLN	5.9	10.4
12	1992 Landers, USA	COOLWATERTR	3.8	8.2
13	1979 Imperial Valley, USA	DELTA262	24.2	51.0
14	1979 Imperial Valley, USA	DELTA352	22.4	50.3
15	1999 Kocaeli, Turkey	DUZCE180	6.1	11.8
16	1999 Kocaeli, Turkey	DUZCE270	2.1	10.6
17	1979 Imperial Valley, USA	ELCENTRO140	4.5	8.7
18	1979 Imperial Valley, USA	ELCENTRO230	4.6	7.9
19	1989 Loma Prieta, USA	GILROY000	1.7	6.4
20	1989 Loma Prieta, USA	GILROY090	3.1	11.4
21	1999 Hector Mine, USA	HECTOR000	6.4	11.6
22	1999 Hector Mine, USA	HECTOR090	7.6	9.7
23	1971 San Fernando, USA	HOLLYWOOD090	5.1	10.5
24	1971 San Fernando, USA	HOLLYWOOD180	4.8	11.2
25	1987 Superstition Hills, USA	ICC000	7.0	16.1
26	1987 Superstition Hills, USA	ICC090	7.6	19.0
27	1994 Northridge, USA	LOSTCANYON000	3.1	6.3
28	1994 Northridge, USA	LOSTCANYON270	2.9	5.6
29	1994 Northridge, USA	MULHOLLAND009	6.1	9.2
30	1994 Northridge, USA	MULHOLLAND279	5.0	8.4
31	1995 Kobe, Japan	NISHI000	4.0	9.7
32	1995 Kobe, Japan	NISHI090	4.5	11.2
33	1987 Superstition Hills, USA	POE270	9.8	13.8
34	1987 Superstition Hills, USA	POE360	11.2	13.6
35	1992 Cape Mendocino, USA	RIODELL270	4.3	15.3
36	1992 Cape Mendocino, USA	RIODELL360	1.9	10.9
37	1995 Kobe, Japan	SHIN000	3.6	10.3
38	1995 Kobe, Japan	SHIN090	4.5	11.8
39	1999 Chi-Chi, Taiwan	TCU045E	7.4	11.3
40	1999 Chi-Chi, Taiwan	TCU045N	8.7	10.8
41	1976 Friuli, Italy	TOLMEZZO000	2.5	4.2
42	1976 Friuli, Italy	TOLMEZZO270	2.5	4.9
43	1992 Landers, USA	YERMO270	7.1	17.6
44	1992 Landers, USA	YERMO360	10.9	18.9

Table A.4 Long-duration ground-motion set from Group B.

#	Earthquake	Station	Scale	Ds_{5-75} (sec)	Ds_{5-95} (sec)
1	1985 Valparaiso, Chile	CAUQUENESL	5.00	25.2	40.4
2	1985 Valparaiso, Chile	LLOLLEO10	0.61	27.5	35.8
3	1985 Valparaiso, Chile	VALPARAISOELALMENDRAL50	1.11	31.1	47.9
4	1985 Michoacan, Mexico	VILC8509191_H2	1.16	33.6	43.3
5	2003 Hokkaido, Japan	HKD1330309260450_H1	4.14	28.4	53.3
6	2010 Maule, Chile	ANGOLEW	0.77	30.2	49.7
7	2011 Tohoku, Japan	AKT0141103111446_H1	5.00	53.8	90.2
8	2011 Tohoku, Japan	AOMH131103111446_H2	1.51	62.7	146.8
9	2011 Tohoku, Japan	AOMH171103111446_H2	2.76	53.2	90.6
10	2011 Tohoku, Japan	FKS0181103111446_H2	0.48	67.5	83.6
11	2011 Tohoku, Japan	FKSH031103111446_H2	1.78	66.5	96.5
12	2011 Tohoku, Japan	FKSH041103111446_H2	1.53	66.6	86.6
13	2011 Tohoku, Japan	FKSH201103111446_H2	0.97	63.5	94.1
14	2011 Tohoku, Japan	GNMH111103111446_H1	4.16	44.6	73.4
15	2011 Tohoku, Japan	IBR0021103111446_H2	1.30	38.9	54.3
16	2011 Tohoku, Japan	IBR0071103111446_H1	0.59	34.4	49.7
17	2011 Tohoku, Japan	IBR0171103111446_H1	0.41	27.8	45.8
18	2011 Tohoku, Japan	IBRH201103111446_H2	1.13	28.7	54.2
19	2011 Tohoku, Japan	IWT0021103111446_H1	2.25	53.1	112.2
20	2011 Tohoku, Japan	IWT0221103111446_H2	2.29	54.4	91.2
21	2011 Tohoku, Japan	KNG0091103111446_H2	3.02	48.1	67.3
22	2011 Tohoku, Japan	MYG0131103111446_H1	0.58	55.4	106.5
23	2011 Tohoku, Japan	MYGH091103111446_H2	1.60	70.3	104.7
24	2011 Tohoku, Japan	SIT0021103111446_H1	2.23	43.7	67.8
25	2011 Tohoku, Japan	SIT0111103111446_H2	1.08	45.7	82.2
26	2011 Tohoku, Japan	SIT0121103111446_H2	3.53	45.9	66.5
27	2011 Tohoku, Japan	SITH081103111446_H2	5.00	37.7	51.0
28	2011 Tohoku, Japan	SZOH421103111446_H2	5.00	57.0	84.5
29	2011 Tohoku, Japan	TKY0181103111446_H1	1.14	40.5	85.7
30	2011 Tohoku, Japan	TKY0221103111446_H2	1.88	42.0	78.8
31	2011 Tohoku, Japan	TKY0261103111446_H1	0.94	44.8	85.5
32	2011 Tohoku, Japan	TKYH121103111446_H2	3.84	46.0	61.1
33	2011 Tohoku, Japan	YMT0051103111446_H2	4.73	68.8	112.5
34	2011 Tohoku, Japan	YMT0101103111446_H1	5.00	70.1	107.8
35	2011 Tohoku, Japan	YMTH011103111446_H1	2.07	71.2	110.1
36	2011 Tohoku, Japan	YMTH021103111446_H1	1.79	78.8	119.7
37	2011 Tohoku, Japan	YMTH151103111446_H2	2.43	71.7	115.0
38	1999 Chi-Chi, Taiwan	CHICHI.04_CHY116W	4.43	35.5	59.3
39	1999 Chi-Chi, Taiwan	CHICHI_CHY058-N	5.00	30.8	44.9
40	2007 Chuetsu-oki, Japan	CHUETSU_NIG011EW	4.04	25.7	74.5
41	2002 Denali, USA	DENALI_FAIGO360	5.00	27.7	104.0
42	2010 El Mayor-Cucapah, USA	SIERRA.MEX_SAL090	1.85	33.3	53.9
43	2008 Wenchuan, China	WENCHUAN_UA0965	4.37	38.2	97.0
44	2009 Wenchuan, China	WENCHUAN_UA1040	2.95	38.8	79.1

APPENDIX B DRAWINGS

This appendix includes the drawing of the specimens tested in this study.

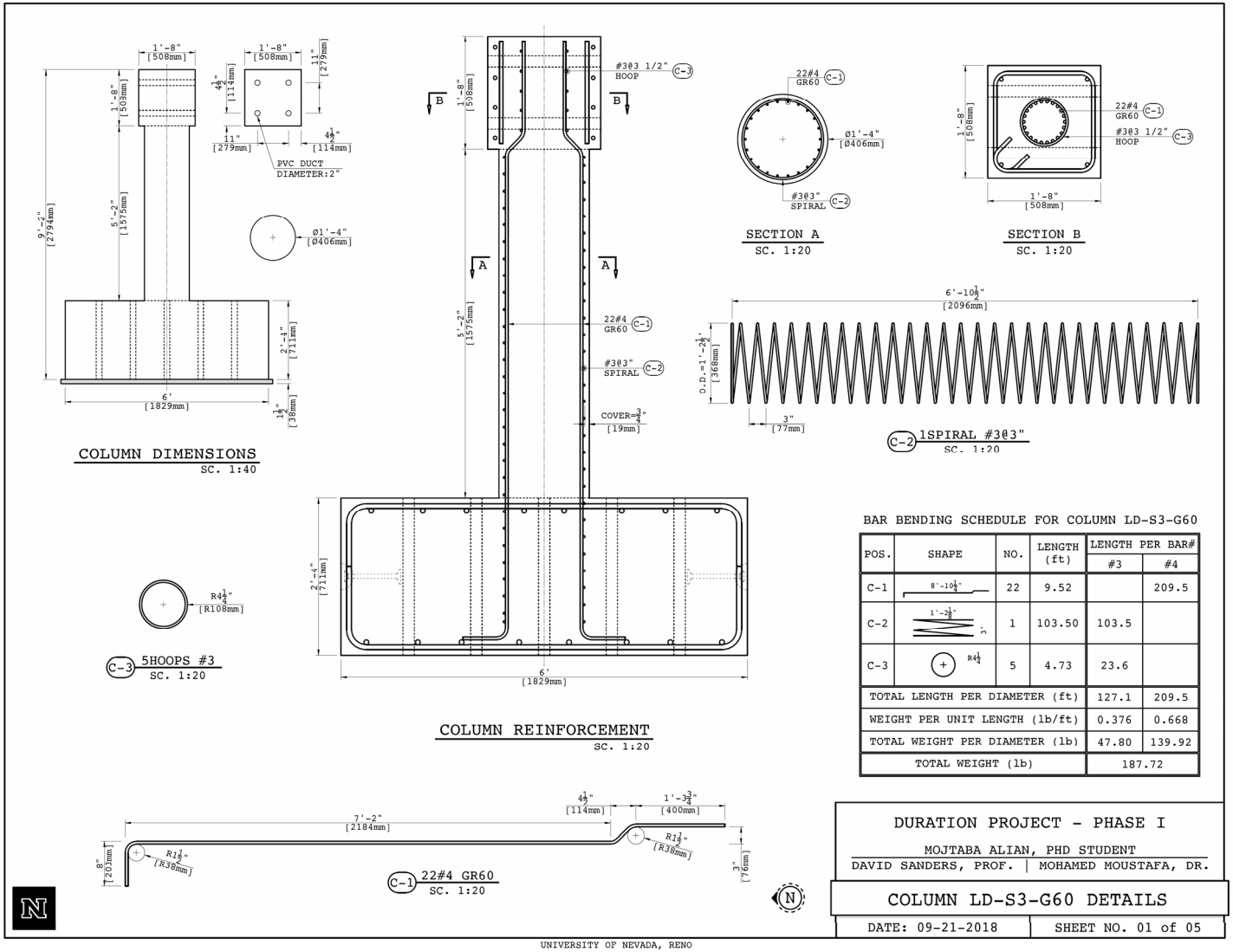

POS.	SHAPE	NO.	LENGTH (ft)	LENGTH PER BAR#	
				#3	#4
C-1	8'-10½"	22	9.52		209.5
C-2	1'-2⅞" 3"	1	103.50	103.5	
C-3	R4¼"	5	4.73	23.6	
TOTAL LENGTH PER DIAMETER (ft)				127.1	209.5
WEIGHT PER UNIT LENGTH (lb/ft)				0.376	0.668
TOTAL WEIGHT PER DIAMETER (lb)				47.80	139.92
TOTAL WEIGHT (lb)				187.72	

Figure A.1 Phase I: Details Column LD-S3-G60.

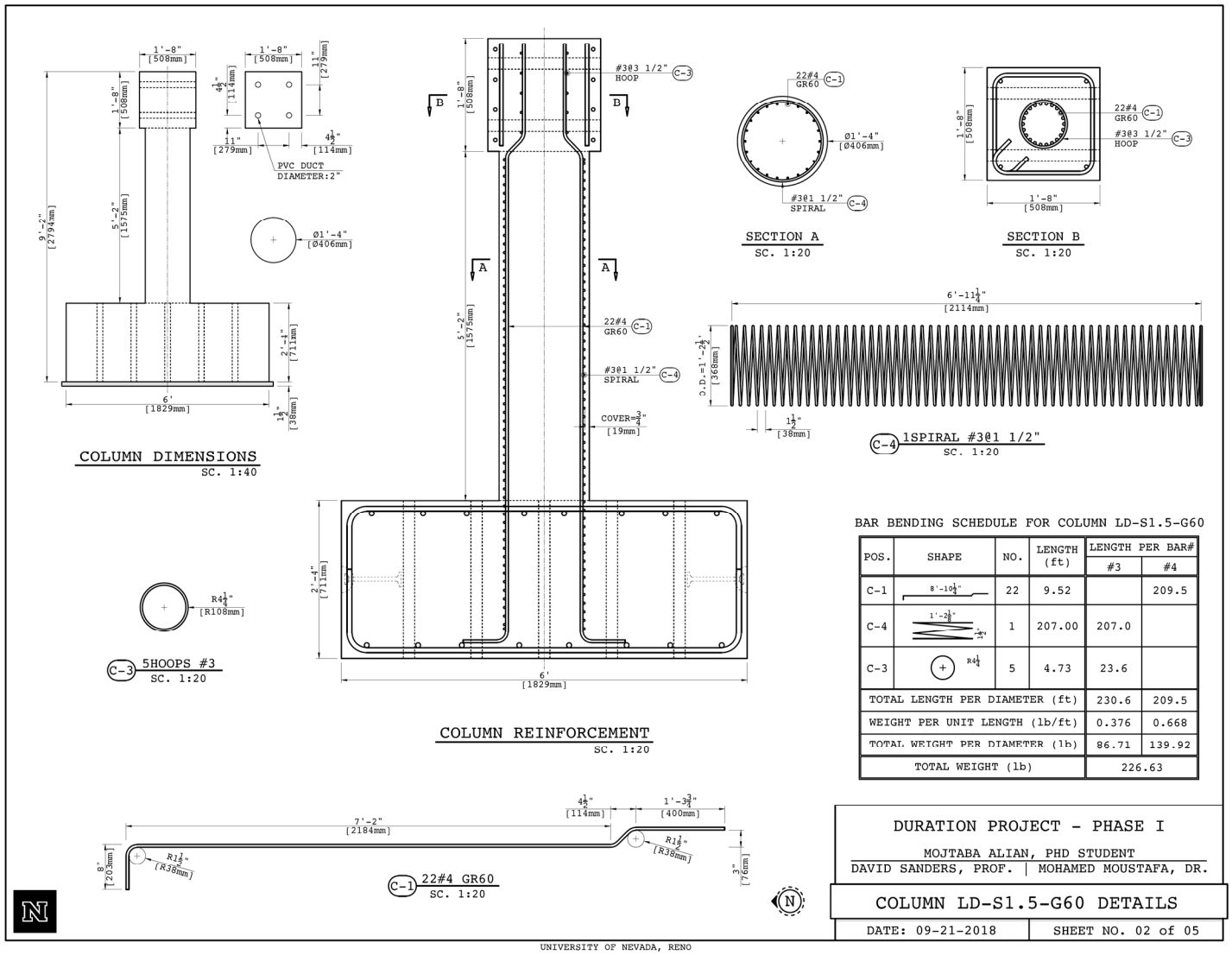

Figure A.2 Phase I: Details Column LD-S1.5-G60.

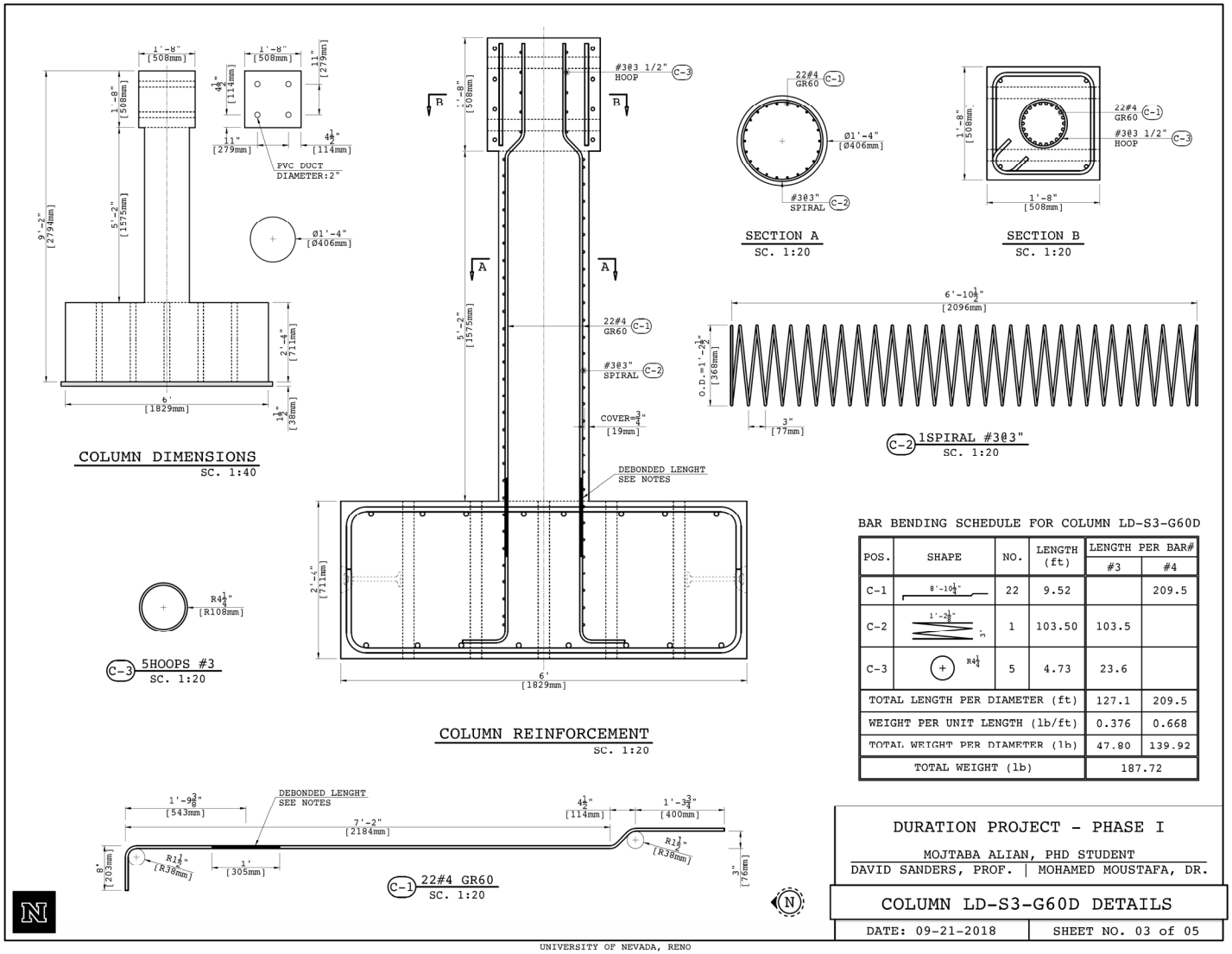

Figure A.3 Phase I: Details Column LD-S3-G60D.

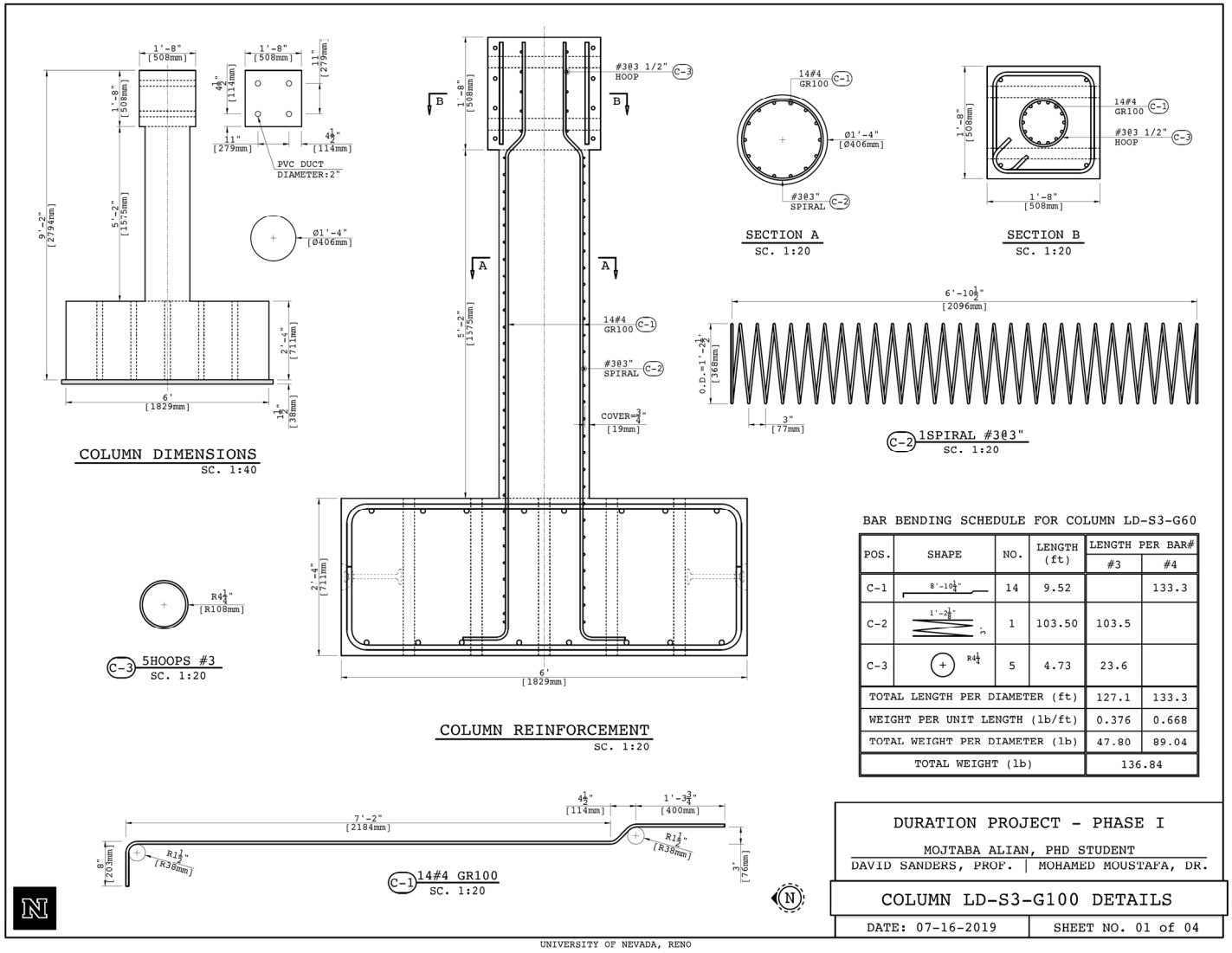

POS.	SHAPE	NO.	LENGTH (ft)	LENGTH PER BAR#	
				#3	#4
C-1	8'-10½"	14	9.52		133.3
C-2	1'-2⅞" 3"	1	103.50	103.5	
C-3	R4¼"	5	4.73	23.6	
TOTAL LENGTH PER DIAMETER (ft)				127.1	133.3
WEIGHT PER UNIT LENGTH (lb/ft)				0.376	0.668
TOTAL WEIGHT PER DIAMETER (lb)				47.80	89.04
TOTAL WEIGHT (lb)				136.84	

Figure A.4 Phase I: Details Column LD-S3-G100.

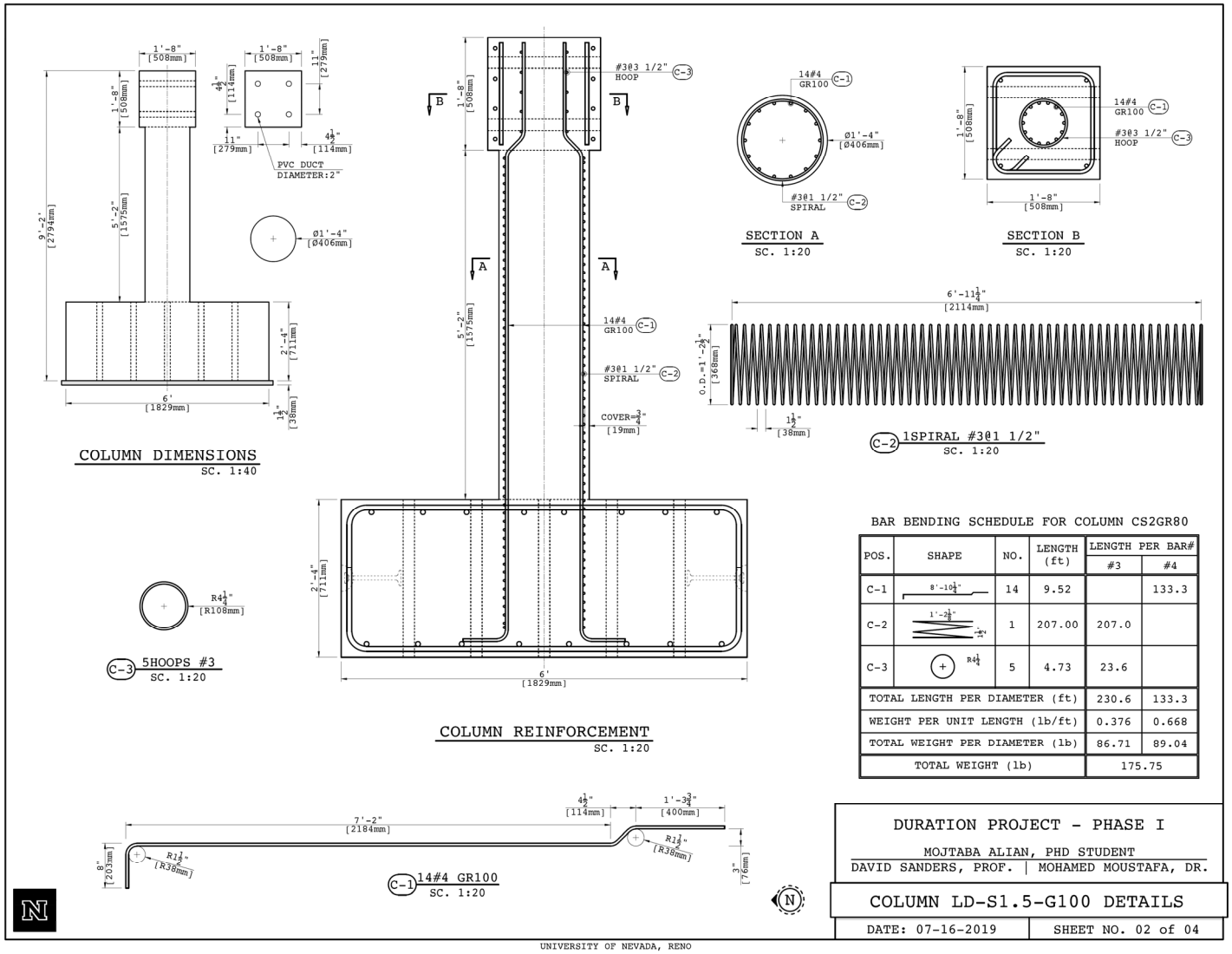

Figure A.5 Phase I: Details Column LD-S1.5-G100.

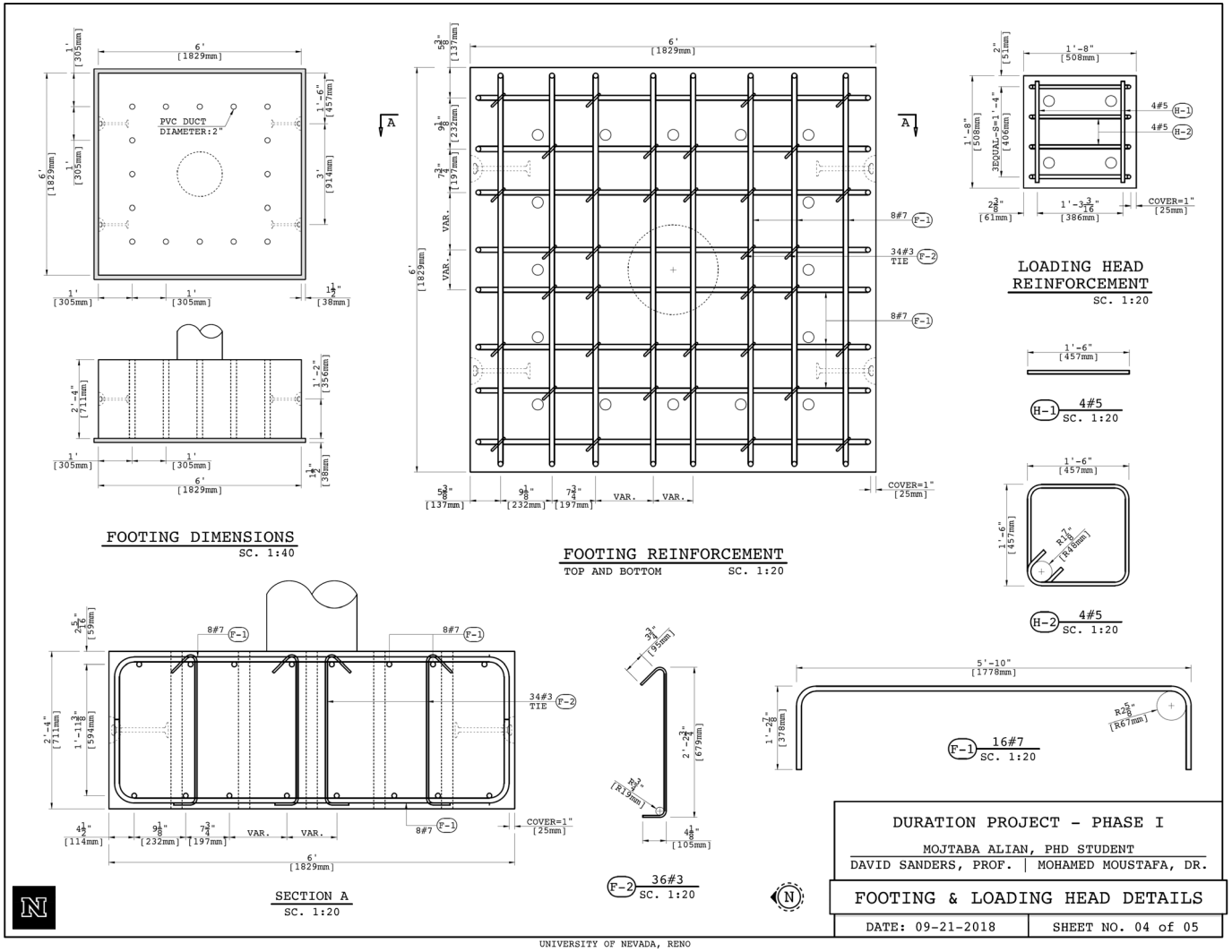

Figure A.6 Phase I: Footing and loading head details.

The Pacific Earthquake Engineering Research Center (PEER) is a multi-institutional research and education center with headquarters at the University of California, Berkeley. Investigators from over 20 universities, several consulting companies, and researchers at various state and federal government agencies contribute to research programs focused on performance-based earthquake engineering.

These research programs aim to identify and reduce the risks from major earthquakes to life safety and to the economy by including research in a wide variety of disciplines including structural and geotechnical engineering, geology/seismology, lifelines, transportation, architecture, economics, risk management, and public policy.

PEER is supported by federal, state, local, and regional agencies, together with industry partners.

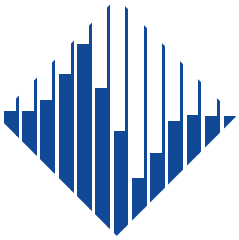

PEER Core Institutions

University of California, Berkeley (Lead Institution)
California Institute of Technology
Oregon State University
Stanford University
University of California, Davis
University of California, Irvine
University of California, Los Angeles
University of California, San Diego
University of Nevada, Reno
University of Southern California
University of Washington

PEER reports can be ordered at https://peer.berkeley.edu/peer-reports or by contacting

Pacific Earthquake Engineering Research Center
University of California, Berkeley
325 Davis Hall, Mail Code 1792
Berkeley, CA 94720-1792
Tel: 510-642-3437
Email: peer_center@berkeley.edu

ISSN 1547-0587X